

# **High Precision Spin Tune Determination at the Cooler Synchrotron in Jülich**

Der Fakultät für Mathematik, Informatik und Naturwissenschaften der  
RWTH Aachen University vorgelegte Dissertation zur Erlangung des  
akademischen Grades eines Doktors der Naturwissenschaften

vorgelegt von  
Master of Science Physiker  
Dennis Eversmann  
aus  
Tönisvorst.

## High Precision Spin Tune Determination at the Cooler Synchrotron in Jülich

Additional sources of the violation of the CP symmetry are required in order to explain the predominance of the matter in our universe. This mechanism is directly interlinked to physics beyond the Standard Model and it is one of the most relevant questions in modern particle physics. Prominent candidates to solve this problem are the permanent electric dipole moments (EDMs) of elementary particles like electrons, neutrons or protons. Experiments with neutral particles already started in the middle of the past century and the current results do not differ significantly from a zero EDM. For charged particles like protons and deuterons, an experimental setup at an electrostatic storage ring is proposed. Corresponding feasibility studies are performed by the JEDI (Jülich Electric Dipole moments Investigation) collaboration at the Cooler Synchrotron (COSY) in order to estimate essential requirements and systematic limitations.

In the scope of this thesis two important quantities are discussed, the spin tune and the spin coherence time. The first one is defined as the number of spin rotations during one turn of the particle bunch in the storage ring. It is shown, that the quantity can be determined in real time with a high statistical precision, which allows the investigation of systematic effects with unprecedented accuracy. The spin coherence time denotes a statistical limitation. It is a measure of how long the spins of the particles are in phase, while they precess in the horizontal plane. In order to reach a statistical limit of an EDM measurement in the order of  $10^{-29} e \text{ cm}$ , the quantity is needed to be larger than 1 000 s. This work demonstrates how this requirement is met by reducing the spin tune spread using sextupole magnets.

The main focus of this thesis is on establishing a theoretical foundation of the related data analysis. Therefore, a naive Bayes approach is used in order to determine the relevant observables, like the phase or the amplitude of the polarization. In addition, a statistical model is developed, which describes the time depending decoherence of the particle spins and the drift of spin tune. This leads to a better understanding of the electromagnetic components in the storage ring and the orbit of the particle beam.

---

# Contents

---

<b>1</b>	<b>Introduction</b>	<b>1</b>
1.1	Baryon Asymmetry . . . . .	3
1.2	Electric Dipole Moments . . . . .	3
1.3	CP violation and EDMs . . . . .	4
1.4	EDM Experiments . . . . .	5
1.4.1	Charged Particle Experiment . . . . .	6
<b>2</b>	<b>Fundamental Statistic and Accelerator Concepts</b>	<b>9</b>
2.1	Statistics . . . . .	9
2.1.1	Central Limit Theorem . . . . .	9
2.1.2	Bayes Theorem . . . . .	9
2.1.3	Estimator . . . . .	10
2.1.4	Fisher Information and Cramer-Rao Bound . . . . .	12
2.1.5	Maximum Likelihood Estimator . . . . .	13
2.1.6	Directional Statistics . . . . .	14
2.2	Beam and Spin Dynamics in Storage Rings . . . . .	16
2.2.1	Coordinate System and Phase Space . . . . .	16
2.2.2	Equations of Motion . . . . .	18
2.2.3	Transverse and Longitudinal Motion . . . . .	19
2.2.4	Beam Emittance and Betatron Tune . . . . .	20
2.2.5	Dispersion and Chromaticity . . . . .	22
2.2.6	Spin and Polarization Formalism . . . . .	24
2.2.7	Thomas-BMT Equation . . . . .	27
2.2.8	Vertical and Horizontal Polarization . . . . .	28
<b>3</b>	<b>Experimental Setup and Data Acquisition</b>	<b>31</b>
3.1	The COSY Storage Ring . . . . .	32
3.2	Data Acquisition . . . . .	35
3.2.1	Time Stamping System . . . . .	35
3.2.2	Frequency of the RF Cavity . . . . .	35
3.3	Event Rate . . . . .	37
3.4	Vertical Asymmetry . . . . .	38
3.4.1	Two Polarization States . . . . .	39

<b>4</b>	<b>Data Analysis</b>	<b>41</b>
4.1	Mapping Method . . . . .	42
4.1.1	Spin Phase Advance $\varphi_s$ . . . . .	42
4.1.2	Up-Down Asymmetries . . . . .	44
4.2	Discrete Turn Fourier Transform . . . . .	47
4.2.1	Fourier Transform . . . . .	47
4.2.2	Discrete Fourier Transform . . . . .	47
4.3	Parameter Estimation . . . . .	51
4.3.1	Standard Error Estimation . . . . .	53
4.3.2	Conclusion . . . . .	55
4.4	Probability Density Function . . . . .	56
4.4.1	Marginal Probability Density Function of Spin Tune and Phase . . . . .	57
4.4.2	Joint Bivariate Probability Density Function . . . . .	59
4.4.3	Marginal Probability Density Function of Turn Number . . . . .	60
4.5	Conclusion . . . . .	62
<b>5</b>	<b>Amplitude Determination</b>	<b>65</b>
5.1	Rice Distribution . . . . .	66
5.1.1	Moments of Rice Distribution . . . . .	68
5.2	Maximum Likelihood Estimator . . . . .	70
5.3	Feldmann-Cousin Algorithm . . . . .	71
5.4	Comparison of Estimators . . . . .	75
5.5	Efficiency of Estimators . . . . .	76
5.6	Amplitude Spectrum . . . . .	78
5.6.1	Main Lobe . . . . .	80
5.6.2	Maximum Likelihood Fit . . . . .	80
5.7	Conclusion . . . . .	81
<b>6</b>	<b>Phase Determination</b>	<b>83</b>
6.1	Wrapped Probability Density Function . . . . .	84
6.1.1	Maximum Likelihood Estimator . . . . .	86
6.1.2	Circular Moment Estimator . . . . .	86
6.1.3	Confidence Interval of Estimated Phase . . . . .	88
6.1.4	Conclusion . . . . .	90
6.1.5	Confidence Interval of True Phase . . . . .	91
6.2	Phase Spectrum . . . . .	93
6.2.1	Maximum Likelihood Fit . . . . .	95
6.3	Combination of Individual Detectors . . . . .	98
6.3.1	Weighted Average . . . . .	98
6.3.2	Discrete Fourier Transform of two Sinusoidal Functions . . . . .	99
6.3.3	Asymmetry (Mapping Method) . . . . .	100
6.4	Conclusion . . . . .	100
6.5	Spin Tune Determination . . . . .	101
6.5.1	Global Maximum Likelihood Fit . . . . .	101

<b>7</b>	<b>Results</b>	<b>107</b>
7.1	Systematics of the Phase Estimation . . . . .	108
7.1.1	Assumed Spin Tune . . . . .	109
7.1.2	Number of Bins of the Asymmetry Distribution . . . . .	111
7.1.3	Pull Distribution . . . . .	112
7.1.4	Conclusion . . . . .	115
7.2	General Experimental Considerations . . . . .	116
7.2.1	Resonant Spin Flip . . . . .	116
7.2.2	Beam Revolution Period . . . . .	117
7.2.3	RF Cavity Period . . . . .	119
7.2.4	Event Arrival Time . . . . .	121
7.3	Extraction Methods . . . . .	124
7.3.1	Vertical and Horizontal Bump Extraction . . . . .	124
7.3.2	White Noise Extraction . . . . .	127
7.3.3	Conclusion . . . . .	128
7.4	Spin Tune Investigations (Beam time June/May 2015) . . . . .	129
7.4.1	Variation within a Cycle . . . . .	129
7.4.2	Long Term Stability . . . . .	137
7.4.3	Long Cycle . . . . .	141
<b>8</b>	<b>Conclusion</b>	<b>143</b>
<b>A</b>	<b>Appendix</b>	<b>145</b>
A.1	List of Runs . . . . .	145
A.2	Integrals for Fisher Information for Spin Precession . . . . .	146
A.3	Integral of the bivariat Probability Density Function . . . . .	149
A.4	Derivation of the Rician Distribution . . . . .	149
A.5	Probability Density Distribution of the Sum of Squared Random Variables . . . . .	150
A.6	Integral of the Circular Moment Cosinus Term . . . . .	151
A.7	Probability Density Function of the True Phase . . . . .	153
	<b>Bibliography</b>	<b>155</b>
	<b>List of Figures</b>	<b>161</b>
	<b>List of Tables</b>	<b>167</b>



---

## Introduction

---

This thesis is written at the Chair of the III. Physikalisches Institut B of the RWTH Aachen university. Moreover, it is established in the section FAME<sup>1</sup> of the Jülich Aachen Research Alliance<sup>2</sup>. The objective of this cooperation is concerned to a better understanding of the matter-antimatter asymmetry in the universe by performing basic physical research in the field of nuclear and particle physics. Solving the puzzle of the observed asymmetry is exceedingly relevant since it holds the key to our very existence.

The focus of this thesis is the investigation of permanent electric dipole moments<sup>3</sup> of charged elementary particles in the context of a storage ring experiment. The existence of those is postulated in the Standard Model<sup>4</sup> of particle physics by the violation of the symmetry of charge-conjugation-parity<sup>5</sup>. Yet, the prediction of the EDMs based on the SM are small and not experimentally measurable. Consequently, the measurement of an EDM enables the possibility to evolve physics beyond the SM. If the charge-parity-time-theorem<sup>6</sup> holds, permanent EDMs of elementary particles violate CP, since they are generated by processes that violate time reversal transformations. According to one of the Sakharov conditions, CP violation is ultimately required for the creation of an asymmetry between the matter and the antimatter in the universe. This chapter addresses the physical preconditions and the resulting consequences of the relevant processes.

The consideration of the three discrete symmetries (parity, charge and time reversal) play an important role in modern physics. The search for their violation has been addressed in plenty of experiments [1] and they can be described as follows

1. **Parity Violation:** The physical process performs equally as its mirror image, i.e. under the transformation  $\vec{x} \rightarrow -\vec{x}$
2. **Charge Conjugation Violation:** Under charge conjugation transformation each particle converts into its antiparticle.
3. **Time Reversal Violation:** The rates of all physical processes are equal, independent of the direction of the time  $t \rightarrow -t$ .

---

<sup>1</sup> Forces and Matter Experiments: FAME (founded in 2011)

<sup>2</sup> Jülich Aachen Research Alliance: JARA

<sup>3</sup> permanent Electric Dipole Moments: EDM

<sup>4</sup> Standard Model of particle physics: SM

<sup>5</sup> Charge Conjugation Parity violation: CP

<sup>6</sup> Charge-Parity-Time-theorem: CPT

The pion decay

$$\pi^- \rightarrow \mu^- + \bar{\nu}_\mu, \quad (1.1)$$

$$\pi^+ \rightarrow \mu^+ + \nu_\mu \quad (1.2)$$

denotes a prominent example of a P and C violating process. However, it conserves CP symmetry.

The first violation of the CP symmetry was observed in the kaon sector [2] and most recently in the B meson sector [3]. The former process is based on the idea that the neutral kaon can transform into its antiparticle by the interchange of two virtual W-bosons. The kaon states are given by the  $K_S$  and  $K_L$  eigenstates, which yield different lifetimes. In 1964 the Fitch-Cronin experiment measured the decay rates of  $K_L$  into two and three pions. The decay into two pions would not be possible if  $K_L$  had been a pure eigenstate. Consequently, the CKM-Matrix (Cabibbo-Kobayashi-Maskawa) has been introduced to explain the observed CP violation. However, the CKM mechanism is not sufficient to explain the baryogenesis, which makes a permanent EDM of elementary particles a proper candidate for additional CP violating sources.

## 1.1 Baryon Asymmetry

The baryon asymmetry is one of the unsolved puzzles in cosmology. Since there is no evidence for primordial antimatter, the excess of matter can be measured by the baryon-to-photon density ratio

$$\eta_{\text{BAU}} = \frac{\eta_B - \eta_{\bar{B}}}{\eta_\gamma} = (6.047 \pm 0.074) \times 10^{-10}, \quad (1.3)$$

where the photon density is given by  $\eta_\gamma = 305/\text{cm}^3$ . The variables  $\eta_B$  and  $\eta_{\bar{B}}$  correspond to the baryon and anti-baryon density, respectively. The latter is measured to zero  $\eta_{\bar{B}} = 0$ .

A quantitative measurement of the asymmetry was realized by the Cosmic Background Explorer<sup>7</sup> satellite, which recorded data in order to determine the angular distribution of the cosmic microwave background. An additional measurement is given by the data of the primordial big-bang-nucleosynthesis. The Standard Model of Cosmology predicts an asymmetry in the order of  $\eta_{\text{BAU}}^{\text{SM}} = 10 \times 10^{-18}$ , which is more than 8 orders of magnitude below the observed one. The unexpectedly large number of baryons of the universe is called baryogenesis. In 1967 Sakharov proved three criteria, which allow the dynamic generation of a baryon asymmetry.

1. **Violation of baryon number:** There must be a process, which violates the baryon number conservation. Otherwise, no asymmetry could be generated
2. **Violation of C and CP symmetries:** In order to produce an imbalance in the production of baryons and anti-baryons, the charge conjugation symmetry C and in addition the parity transformation symmetry has to be violated
3. **The universe is out of thermal equilibrium:** In thermal equilibrium particle production reactions yield the same rate as the inverse process. Thus, the asymmetry generating processes must take place far from thermal equilibrium.

The determination of a permanent EDM of elementary particles is an additional source of CP violating processes.

## 1.2 Electric Dipole Moments

In electrodynamics the classical definition of an EDM describes the charge separation of the centers of gravity of positive and negative charges

$$\vec{d}^{\text{EDM}} = \int_V \vec{x} \cdot \rho(\vec{x}) d\vec{x}, \quad (1.4)$$

where  $\rho(\vec{x})$  denotes the continuous charge density. In analogous the magnetic dipole moment yields

$$\vec{\mu}^{\text{MDM}} = \frac{1}{2} \int_V \vec{x} \times \vec{j}(\vec{x}) d\vec{x}, \quad (1.5)$$

<sup>7</sup> Cosmic Background Explorer: COBE

with the current density  $\vec{j}(\vec{x})$ .

The EDMs and MDMs are fundamental properties of the particles

$$\vec{d} = \eta_{\text{EDM}} \frac{q}{2mc} \vec{S}, \quad (1.6)$$

$$\vec{\mu} = g \frac{q}{2m} \vec{S} \quad (1.7)$$

and they are either aligned parallel or anti-parallel with respect to the spin quantization axis [4]. Here, the mass and the charge of the particle are indicated by  $m$  and  $q$ , respectively. In addition, the speed of light is denoted as  $c$ . The g-factor  $g$  and the scaling parameter  $\eta_{\text{EDM}}$  are dimensionless quantities.

The non-relativistic Hamiltonian of a particle with EDM and MDM reads

$$H = -\vec{\mu}\vec{B} - \vec{d}\vec{E}. \quad (1.8)$$

In the case of a T transformation, only the dipole moments and the magnetic field  $B$  are inverted and for the P transformation, only the electric field flips its sign. Consequently, both symmetries are violated assuming  $d \neq 0$ . In addition, CP is violated, if the CPT theorem is valid [5].

### 1.3 CP violation and EDMs

The already mentioned CKM-Matrix is considered as the only known source of CP violation in the quark sector of the SM [6]. An analogous is the PMNS-Matrix (Pontecorvo-Maki-Nakagawa-Sakata), which describes the CP violation in the lepton sector [7]. The predicted EDMs due to CKM mixing are extremely small since they are generated by a three-loop level Feynman diagram [8]

$$d_q^{\text{CKM}} \approx 10 \times 10^{-34} e \text{ cm} - 10 \times 10^{-35} e \text{ cm}. \quad (1.9)$$

In the case of the electron even four-loop diagrams are needed, which yields [9]

$$d_e^{\text{CKM}} \leq 10 \times 10^{-38} e \text{ cm}. \quad (1.10)$$

For the nucleon EDM, the CP-odd pion-nucleon coupling based on the effective field theory at one-loop level are most relevant and an estimate leads to [9]

$$d_n^{\text{CKM}} \leq 10 \times 10^{-32} e \text{ cm}. \quad (1.11)$$

All numbers are way too small in order to be covered by the sensitivity of current EDM experiments. However, the investigation of an additional source of CP violation caused for example by the strong sector of the SM or by physics beyond the SM is of major interest in modern physics. In the first case, the dimensionless  $\bar{\theta}$ -term, which cannot be computed, is directly

connected to the neutron and proton EDM [10]

$$d_n^{\bar{\theta}} = \bar{\theta}(-2.9 \pm 0.9) \times 10^{-16} e \text{ cm}, \quad (1.12)$$

$$d_n^{\bar{\theta}} = \bar{\theta}(1.1 \pm 1.1) \times 10^{-16} e \text{ cm}. \quad (1.13)$$

The order of the  $\bar{\theta}$ -term is expected to be  $\mathcal{O}(1)$ , however the present neutron EDM limits constrains it to

$$\bar{\theta} < 10^{-10}, \quad (1.14)$$

which is known as the strong CP problem.

Furthermore, another contribution of the EDM caused by CP violation is generated by loops, which include hypothetical supersymmetric particles. These quark- and chromo-EDMs are effectively increasing the limits. Consequently, an EDM measured in current experimental approaches will be a clear sign of new physics.

## 1.4 EDM Experiments

The first EDM experiment was performed in 1949, where the idle spin precession frequency of neutrons in static electromagnetic fields was determined. By aligning the electric field parallel or anti-parallel to the quantization axis, the spin starts to precess perpendicular to the polarization of the particle

$$\omega = \frac{2|\mu B \pm dE|}{\hbar}. \quad (1.15)$$

The sign indicates the flip of the electric fields. After subtracting the two frequencies the magnetic term cancels out and the EDM signal yields

$$d = \frac{\Delta\omega\hbar}{4E}. \quad (1.16)$$

This basic measurement idea is used as the general method in neutron beams experiments. Moreover, the current neutron EDM limit is reached in ultracold experimental setups and yields [11]

$$|d_n| < 2.9 \times 10^{-26} e \text{ cm} \quad (90\% \text{ CL}). \quad (1.17)$$

The limit of the electron EDM is derived from experiments with the paramagnetic atom  $^{205}\text{Tl}$ , whereas the atomic limit is measured on the diamagnetic atom  $^{199}\text{Hg}$

$$|d_e| < 1.6 \times 10^{-27} e \text{ cm} \quad (90\% \text{ CL}), \quad (1.18)$$

$$|d_{\text{atom}}| < 3.1 \times 10^{-29} e \text{ cm} \quad (90\% \text{ CL}). \quad (1.19)$$

### 1.4.1 Charged Particle Experiment

In the case of charged particles, the experimental principle has to be changed since the particles are accelerated due to the electromagnetic fields. Therefore, storage rings represent an ideal starting point, since the particles can be kept circulating for a long time interval.

The generic idea of an experimental setup is shown in Fig. 1.1. A particle is deflected by a radial electric field. An appropriate field strength keeps the particle on a stable circular orbit. Additionally, its spin is tilted into the vertical direction. According to the Thomas-BMT equation this process is proportional to the applied electric field and the electric dipole moment of the particle. One observes that the highest sensitivity is given if the spin is permanently aligned with the momentum. Consequently, the spin manipulation in the horizontal plane is of major interest.



Figure 1.1: Count sums  $N_{U,D}^+(\varphi_s)$  and differences  $N_{U,D}^-(\varphi_s)$  of Eq. 4.5 with  $\varphi_s \in [0, 2\pi)$  using the counts  $N_U(\varphi_s)$  and  $N_D(\varphi_s)$ , shown in Fig. 4.1. The vertical error bars show the statistical uncertainties, the horizontal bars indicate the bin width.

This thesis is part of a feasibility study to investigate the spin motion in a pure magnetic storage ring (COSY). This leads to a better understanding of the statistical limitations and the systematic requirements of an EDM storage ring experiment. It is divided into 7 additional chapters:

- **Chapter 2** elaborates the mathematical basis of the analysis used in this thesis. In addition, it gives a theoretical foundation of the particle and the spin motion in the electromagnetic fields of storage rings.
- **Chapter 3** shows the experimental setup and the basic technical elements, which are required to perform the feasibility studies.
- **Chapter 4** discusses the analysis methods for the polarization measurement. In addition, probability density functions are derived to describe time dependent depolarization effects and the spin tune drift.

- **Chapter 5** examines the determination of the polarization amplitude and its systematic implications.
- **Chapter 6** concentrates on the spin tune phase measurement by making use of circular statistics. It closes with the description of the method of the spin tune determination.
- **Chapter 7** shows mainly the results of the beamtime in 2015. Here, general systematic effects are discussed. In addition, the spin coherence time and the spin tune are investigated.
- **Chapter 8** concludes the achievements of this thesis and gives an outlook about its implications.



---

# Fundamental Statistic and Accelerator Concepts

---

## 2.1 Statistics

In this thesis the estimation of two relevant observables (spin coherence time and spin tune) of a polarization experiment at a storage ring is discussed. Therefore, a mathematical model is derived, which is based on a naive Bayesian approach and yields estimators for the phase and the amplitude of the polarization vector. The relevant theoretical requirements are discussed at the beginning of this chapter.

Furthermore, the time dependency of the two observables is described by a statistical model. For this, the knowledge of the particle and the spin motion are of major interest, which is characterized in the second part of this chapter.

### 2.1.1 Central Limit Theorem

The central limit theorem (CLT) is of fundamental importance in the field of statistical theory and applied probability. Suppose a sequence of independent and identically distributed random variables  $x_1, x_2, \dots, x_n$  with expectation value  $E[x_i] = \mu$  and variance  $\text{var}[x_i] = \sigma^2$ . Then the Lindberg-Lévy CLT states, that the difference between the sample average and the expectation value converges in distribution ( $\xrightarrow{D}$ ) to a Normal distribution [12]

$$\sqrt{n} \left( \left( \sum_{i=1}^n x_i \right) - \mu \right) \xrightarrow{D} N(0, \sigma^2), \quad (2.1)$$

The remarkable property of the CLT consists in the fact, that in Eq. 2.1 no assumption is made about the shape of the distribution of the individual  $x_i$ .

### 2.1.2 Bayes Theorem

The Bayes theorem is another fundamental law in probability theory. Mathematically it can be written as [13]

$$P(A|B) = \frac{P(B|A)P(A)}{P(B)}, \quad (2.2)$$

where  $P(A)$  and  $P(B)$  are the probabilities that  $A$  respectively  $B$  is observed. The conditional probability  $P(A|B)$  represents the probability of observing  $A$  given that  $B$  is true and vice versa for  $P(B|A)$ . In terms of Bayesian interpretation, the probability corresponds to a degree of belief, which is linked to a state before and after taking into account the evidence. In this sense  $P(A)$  is called the *prior*, which represents the initial degree of belief in  $A$ , whereas  $P(A|B)$  denotes the *posterior*, which corresponds to the degree of belief taking into account  $B$ . The ratio  $P(B|A)/P(B)$  is considered as the support  $B$  provides for  $A$ .

### 2.1.3 Estimator

A statistic estimator corresponds to a criterion for determining an estimate of a quantity based on observed data. In the case of a fixed parameter  $\theta$ , which needs to be estimated, the estimator is given by a function, which connects the sample space to a set of sample estimates. In general, it is denoted by a hat above the symbol  $\hat{\theta}$ . If a random variable  $X$  corresponds to the observed data, the estimator becomes a function of that random variable itself  $\hat{\theta}(X)$ . The estimate of a particular data set ( $x = X$ ) is given by  $\hat{\theta}(x)$ , which is a fixed value.

#### Mean Squared Error, Variance and Bias

Three important quantities, i.e. definitions, are related to a statistic estimator. The mean squared error (MSE) is given by the expectation value  $E[\ ]$  of the squared errors

$$\text{MSE}(\hat{\theta}) = E[(\hat{\theta}(x) - \theta)^2]. \quad (2.3)$$

It corresponds to a measure how far, on average, the estimates  $\hat{\theta}(x)$  are from a single true parameter  $\theta$ .

The variance is simply given by

$$\text{var}(\hat{\theta}) = E[(\hat{\theta}(x) - E(\hat{\theta}))^2], \quad (2.4)$$

which indicates how far the estimates are from the expected value of the estimates.

Finally, the bias is defined as  $B(\hat{\theta}) = E(\hat{\theta}) - \theta$ , which corresponds to the distance between the average of the estimates and the single true parameter. The quantities are related by

$$\text{MSE}(\hat{\theta}) = \text{var}(\hat{\theta}) + (B(\hat{\theta}))^2. \quad (2.5)$$

If  $B(\hat{\theta}) = 0$  the estimator  $\hat{\theta}$  is called an unbiased estimator of  $\theta$ . It is important to note, that the bias is a property of the estimator and not of the estimates.

The theory of statistics provides four relevant properties of an estimator, which are defined for a given set of independent and identically distributed random variables.

### Consistency

An estimator  $t_n$  of  $\theta$  is said to be consistent if it converges in probability to the true value of the parameter [14]

$$\text{plim}_{n \rightarrow \infty} t_n = \theta, \quad (2.6)$$

where  $n$  denotes the number of observations of a given sample  $x = (x_1, \dots, x_n)$ . In fact, this behavior is connected to the limit theorems.

### Asymptotic Normality

A consistent estimator is asymptotically normal if its distribution around the true parameter  $\theta$  represents a Normal distribution with a standard deviation decreasing proportional to  $1/\sqrt{n}$  for an increasing sample size  $n$ . Let the symbol  $\xrightarrow{D}$  denotes the convergence in distribution, then  $t_n$  is asymptotically normal if

$$\sqrt{n}(t_n - \theta) \xrightarrow{D} N(0, V), \quad (2.7)$$

where  $V$  or  $V/n$  are called the asymptotic variance. The distribution of  $t_n$  converges weakly to a Dirac distribution for  $n \rightarrow \infty$ , which corresponds to the central limit theorems.

### Efficiency

Efficiency represents a measure of the goodness of an estimator with respect to an experimental design [15] or to a testing of a hypothesis [16]. Loosely speaking, a more efficient unbiased estimator  $t_n$  needs less observations  $n$  to achieve a given performance. It is convenient to define a relative efficiency, which is given by the ratio of two efficiencies obtained for different procedures. The numerator of the ratio is often chosen as the notional best efficiency of the estimator, which corresponds to the Cramér-Rao bound. Thus, one gets

$$e(t) = \frac{1}{\text{var}(t)} \leq 1, \quad (2.8)$$

where  $\mathcal{I}(\theta)$  denotes the Fisher information of the sample, which is defined in the upcoming section. An estimator is called efficient, if the ratio of the efficiency becomes unity  $e(t_n) = 1$ . Additionally, this case corresponds to the minimum variance unbiased estimator (MVUE). Note that a MVUE estimator is not necessarily efficient since the minimum variance does not mean equality holds on the Cramér-Rao inequality.

### Robustness

An estimator is called robust, if the existence of outliers or of other small deviations from model assumptions provide more or less the same result [17]. Hence, a breakdown point is

defined as the proportion of incorrect observations an estimator can handle until its result becomes incorrect.

### 2.1.4 Fisher Information and Cramer-Rao Bound

The Fisher information indicates the amount of information, that a measurable random variable  $X$  carries with respect to an unknown parameter  $\theta$  upon the probability of  $X$  depends. The likelihood function for  $\theta$ , i.e. the probability function for  $X$ , is given by  $f(X; \theta)$  and is called the probability density function pdf (or probability mass function) of the random variable  $X$  conditional on the value of  $\theta$ . The score function is defined as the partial derivative with respect to  $\theta$  of the natural logarithm of the likelihood function and its expectation value (first moment) is 0 [18]

$$E \left[ \frac{\partial}{\partial \theta} \log(f(X; \theta)) \middle| \theta \right] = \int \frac{\frac{\partial}{\partial \theta} f(x; \theta)}{f(x; \theta)} f(x; \theta) dx = \frac{\partial}{\partial \theta} \int f(x; \theta) dx = 0. \quad (2.9)$$

The interchange of the differential operators is valid as long as the bounds of the space of the random variable are independent of the parameter. The second moment of the score function represents the Fisher information and it is given by [18]

$$\mathcal{I}(\theta) = E \left[ \frac{\partial}{\partial \theta} \log(f(X; \theta))^2 \middle| \theta \right] = \int \left( \frac{\partial}{\partial \theta} \log f(x; \theta) \right)^2 f(x; \theta) dx, \quad (2.10)$$

$$\mathcal{I}(\theta) = -E \left[ \frac{\partial^2}{\partial \theta^2} \log(f(X; \theta)) \middle| \theta \right], \quad \text{if } E \left[ \frac{\partial^2}{\partial \theta^2} \log(f(X; \theta)) \middle| \theta \right] = 0. \quad (2.11)$$

Intuitively the Fisher information can be understood as the variability of the gradient of the score function  $\frac{\partial}{\partial \theta} \log(f(X; \theta))$ . Probability density functions, for which the score function has high variability, provide an easier estimation of the parameter and vice versa.

In case of a multivariate parameter space the Fisher information is written in the matrix form

$$\begin{aligned} (\mathcal{I}(\theta))_{ij} &= E \left[ \left( \frac{\partial}{\partial \theta_i} \log(f(X; \theta)) \right) \left( \frac{\partial}{\partial \theta_j} \log(f(X; \theta)) \right) \middle| \theta \right] \\ &= E \left[ \left( \frac{\partial^2}{\partial \theta_i \partial \theta_j} \log(f(X; \theta)) \right) \middle| \theta \right], \end{aligned} \quad (2.12)$$

where the latter transformation is valid, if the parameters are independent of each other.

The Cramér-Rao (CRB) bound defines the minimum variance of an estimator and it is given by the inverse of the Fisher information [19]. This can easily be shown for an unbiased estimator by the mathematical expression of its expectation value

$$E \left[ (\hat{\theta}(X) - \theta) \middle| \theta \right] = \frac{\partial}{\partial \theta} \int (\hat{\theta}(x) - \theta) f(x; \theta) dx = \int (\hat{\theta} - \theta) \frac{\partial}{\partial \theta} f dx - \int f dx = 0. \quad (2.13)$$

The latter integral yields 1 and with the substitution  $\partial f / \partial \theta = f \partial \log f / \partial \theta$  one gets

$$1 = \int (\hat{\theta} - \theta) f \frac{\partial \log f}{\partial \theta} dx = \int \left( (\hat{\theta} - \theta) \sqrt{f} \right) \left( \sqrt{f} \frac{\partial \log f}{\partial \theta} \right) dx. \quad (2.14)$$

The Cauchy-Schwartz inequality leads to the required statement after squaring down the upper equation

$$\left[ \int (\hat{\theta} - \theta)^2 f dx \right] \left[ \int \left( \frac{\partial \log f}{\partial \theta} \right)^2 f dx \right] \geq 1, \quad (2.15)$$

where the right hand side corresponds to the Fisher information and the left-most factor denotes the MSE respectively the variance of the unbiased estimator  $\hat{\theta}$ . Thus, the precision to estimate  $\theta$  is limited by the Fisher information of the likelihood function

$$\text{var}(\hat{\theta}) \geq \frac{1}{\mathcal{I}(\theta)}. \quad (2.16)$$

In the case of multiple parameters  $\boldsymbol{\theta} = [\theta_1, \dots, \theta_n]^T \in \mathbb{R}^d$ , the Cramér-Rao bound corresponds to the covariance matrix of the estimator  $\hat{\boldsymbol{\theta}} = [\hat{\theta}_1, \dots, \hat{\theta}_n]^T$

$$\text{cov}(\hat{\boldsymbol{\theta}}) \geq \frac{\partial \boldsymbol{\psi}(\boldsymbol{\theta})}{\partial \boldsymbol{\theta}} \mathcal{I}(\boldsymbol{\theta})^{-1} \left( \frac{\partial \boldsymbol{\psi}(\boldsymbol{\theta})}{\partial \boldsymbol{\theta}} \right)^T, \quad (2.17)$$

where  $\boldsymbol{\psi}(\boldsymbol{\theta}) = E[\hat{\boldsymbol{\theta}}]$  is the expectation vector of the estimator and  $\partial \boldsymbol{\psi}(\boldsymbol{\theta}) / \partial \boldsymbol{\theta}$  denotes the Jacobian matrix with its elements  $\partial \psi_i(\boldsymbol{\theta}) / \partial \theta_j$ . In the case of an unbiased estimator ( $\partial \boldsymbol{\psi}(\boldsymbol{\theta}) / \partial \boldsymbol{\theta} = 0$ ), the CRB reduces to

$$\text{cov}(\hat{\boldsymbol{\theta}}) \geq \mathcal{I}(\boldsymbol{\theta})^{-1}. \quad (2.18)$$

### 2.1.5 Maximum Likelihood Estimator

The method of maximum likelihood is one of the most discussed and outlined estimation methods in statistical theory. The principle is based on assuming the observations as fixed parameters, whereas the model dependent parameter  $\theta$  is allowed to vary freely as a variable of the likelihood function. The true value of the parameter is given by  $\theta_0$  and it is *a priori* unknown. Thus, the objective is to find an estimator  $\hat{\theta}$ , which is as close as possible to the true value.

For a given set of  $n$  independent and identically distributed observations  $x_1, x_2, \dots, x_n$  the joint density function is specified

$$f(x_1, x_2, \dots, x_n | \theta) = f(x_1 | \theta) \times f(x_2 | \theta) \times \dots \times f(x_n | \theta), \quad (2.19)$$

in order to obtain the likelihood [20]

$$\mathcal{L}(\theta; x_1, x_2, \dots, x_n) = f(x_1, x_2, \dots, x_n | \theta) = f(x_1 | \theta) \times f(x_2 | \theta) \times \dots \times f(x_n | \theta) \quad (2.20)$$

$$= \prod_{i=1}^n f(x_i | \theta). \quad (2.21)$$

Note that  $x_1, x_2, \dots, x_n$  are the fixed parameters of  $\mathcal{L}$ , which is a function of the parameter  $\theta$  or even a vector of parameters  $\boldsymbol{\theta}$ . In order to simplify subsequent calculations, the product is transformed into a sum by taking the natural logarithm

$$\log \mathcal{L}(\theta; x_1, x_2, \dots, x_n) = \sum_{i=1}^n \log f(x_i | \theta). \quad (2.22)$$

The maximum likelihood estimator (MLE) corresponds to the value which maximizes the likelihood  $\log \mathcal{L}$

$$\hat{\theta}_{\text{ML}} = \arg \left\{ \max_{\theta} (\log \mathcal{L}) \right\}. \quad (2.23)$$

Under some conditions, which are discussed and specified in [20], the MLE is consistent and asymptotically normal.

### 2.1.6 Directional Statistics

The theory of directional statistics deals with probability density functions, which are defined in a periodic interval (in the case of a circle it is  $2\pi$ ). More generally spoken, it describes a distribution of unit vectors in  $\mathcal{R}^n$  and of axes through the origin in  $\mathcal{R}^n$  or rotations in  $\mathcal{R}^n$ . In this thesis, it will be applied with respect to angular data, where the angles  $0^\circ$  and  $360^\circ$  are identical.

Suppose a probability density function  $p(x)$  on the line. Furthermore, it is wrapped on the line around the circumference of a unit circle. Then, the random variable is given by

$$\varphi = x_w = x \pmod{2\pi} \in (-\pi, \pi]. \quad (2.24)$$

The wrapped probability density function yields [21]

$$p_w(\varphi) = \sum_{k=-\infty}^{\infty} p(\varphi + 2\pi k) = \frac{1}{2\pi} \sum_{n=-\infty}^{\infty} \phi(n) e^{-in\varphi}, \quad (2.25)$$

where  $\phi(n)$  denotes the characteristic function of the unwrapped distribution at the integer value  $n$ . Thus, the Fourier coefficients of the Fourier transform of the wrapped distribution corresponds to the Fourier coefficients of the Fourier series obtained for the unwrapped distribution at integer values.

For a circular random variable defined in the interval  $(-\pi, \pi]$ , the  $m$ -th vector moment of

the circular distribution is specified as [22]

$$m_n = E(z^n) = \int_{-\pi}^{\pi} p(\varphi) \mathrm{d}\varphi = \phi(m). \quad (2.26)$$

Hence, the first moment is called the mean resultant vector  $\rho = m_1$  and its length is given by  $R = |m_1|$ . The mean angle yields  $\varphi_\mu = \arg(m_1)$ . Note, that the  $m$ -th moment is equal to the characteristic function of the unwrapped distribution for integer arguments. Thus, if  $\phi(n)$  is known, the moments of the wrapped distribution can easily be calculated.

## 2.2 Beam and Spin Dynamics in Storage Rings

A storage ring experiment which aims for a very precise determination of the electric dipole moment of charged particles requires a detailed knowledge of the spin motion in electromagnetic fields. Consequently, it is of fundamental interest to understand the coupling between the beam and the spin motion. At the beginning of this section, the beam dynamics are discussed. The generic description of the particle motion is based on the Lorentz force

$$F_L = q \left( \vec{E} + \vec{v} \times \vec{B} \right), \quad (2.27)$$

where  $q$  is the particle charge,  $\vec{E}$  and  $\vec{B}$  denotes the electric respectively the magnetic field and  $\vec{v}$  represents the velocity of the particle. Subsequently, an introduction of the formalism of polarized particles is given. In addition, the equation of motion of the spin is derived and discussed.

### 2.2.1 Coordinate System and Phase Space

The equation of motion of the particles, which form an ensemble, are parametrized by their spatial coordinates  $\vec{r}$  and their momenta  $\vec{p}$ . Consequently, the trajectories of the particles are described by a six-dimensional phase space. Since the storage ring is composed of deflectors with static electromagnetic fields, the particle motion is time-independent and the arc length  $s$  is chosen as the independent variable.

In addition, it is more convenient to define a Cartesian coordinate system based on curvilinear coordinates, whose origin moves exactly on the reference orbit  $\vec{r}_{\text{ref}}$  with the reference momentum  $\vec{p}_{\text{ref}}$ . In the case of a planar ring, the basis vectors  $\vec{e}_s$  and  $\vec{e}_x$  span a plane which is defined by its orthogonal vector  $\vec{e}_y = \vec{e}_s \times \vec{e}_x$ . Note that  $\vec{e}_s$  is parallel to the momentum vector of the reference orbit  $\vec{p}_{\text{ref}}$ . Consequently, the coordinate transformation from  $s_i$  to  $s_f$ , which is shown in Fig. 2.1, is described by a rotation

$$\vec{e}_{x,f} = \cos(\theta) \vec{e}_{x,i} + \sin(\theta) \vec{e}_{s,i}, \quad (2.28)$$

$$\vec{e}_{y,f} = \vec{e}_{y,i}, \quad (2.29)$$

$$\vec{e}_{z,f} = -\sin(\theta) \vec{e}_{x,i} + \cos(\theta) \vec{e}_{s,i}. \quad (2.30)$$

The angle  $\theta$  is given by

$$\theta = \int_{s_i}^{s_f} \frac{ds}{\rho(s)} = \int_{s_i}^{s_f} \kappa(s) ds, \quad (2.31)$$

where  $\rho(s)$  is the bending radius and  $\kappa(s)$  denotes the curvature.

The transverse motion can be described by the projections of the position  $x$  and  $y$  respectively of the momenta  $p_x$  and  $p_y$  on  $\vec{e}_x$  and  $\vec{e}_y$  with respect to the reference particle  $\vec{r} - \vec{r}_{\text{ref}}$  and  $\vec{p} - \vec{p}_{\text{ref}}$ . In addition, the momenta are normalized by the reference momentum  $p_0 = |\vec{p}_{\text{ref}}|$  yielding  $a = p_x/p_0$  and  $b = p_y/p_0$ . Thus, the transverse motion is given by four coordinates. The longitudinal phase-space of a particle can be specified by its relative momentum deviation

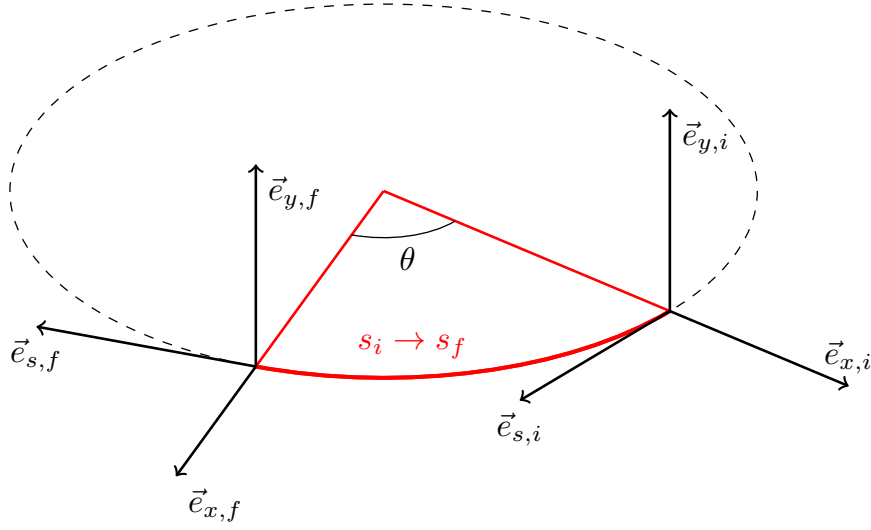


Figure 2.1: Sketch of a co-moved Cartesian coordinate system, which is used to describe the particle motions in a planar accelerator. Its coordinates are called curvilinear.

from the reference particle  $p_0$

$$\delta = \frac{p - p_0}{p_0}, \quad (2.32)$$

or in terms of the reference energy  $K_0$

$$\delta_K = \frac{K - K_0}{K_0}. \quad (2.33)$$

The corresponding space-like variables are given by

$$l = -v_0 \Delta t \quad \text{and} \quad l_K = -v_0 \frac{\gamma_0}{1 + \gamma_0} (t - t_0), \quad (2.34)$$

where  $v_0$  denotes the velocity and  $\gamma_0$  the Lorentz factor of the reference particle. Consequently, the six dimensional phase space yields

$$\vec{z} = (x, a, y, b, l_K, \delta_K)^T. \quad (2.35)$$

Additionally, the coordinate evolution can be expressed in terms of the matrix formalism by a transfer map of the system

$$\vec{z}(s_f) = \mathcal{M}(s_f, s_i)(\vec{z}(s_i)) \approx \hat{M}(s_f, s_i) \cdot \vec{z}(s_i). \quad (2.36)$$

The hat indicates the first order Taylor expansion of  $\mathcal{M}$ , which leads to a simple matrix multiplication by the transfer matrix  $\hat{M}$  with the phase space vector.

### 2.2.2 Equations of Motion

One way of deriving the equations of motion is given by using the Lagrangian and Hamiltonian in curvilinear coordinates. In the following, they are determined based on the transformation of Lorentz force law Eq. 2.27

$$\frac{d\vec{r}}{dt} = \vec{v}, \quad (2.37)$$

$$\frac{d\vec{p}}{dt} = F_L = q \left( \vec{E} + \vec{v} \times \vec{B} \right), \quad (2.38)$$

into curvilinear coordinates with  $s$  as the independent variable. In this case, the derivative of the path length  $L$  with respect to  $s$  is given by

$$L' = \frac{dL}{ds} = 1 + \kappa(s)x, \quad (2.39)$$

where  $\kappa$  corresponds to the curvature of the trajectory. Based on that the two equations of transverse motion yield

$$x' = \frac{dx}{ds} = \frac{dL}{ds} \frac{dx}{dL} = (1 + \kappa(s)) \frac{p_x}{p_s}, \quad (2.40)$$

$$y' = \frac{dy}{ds} = \frac{dL}{ds} \frac{dy}{dL} = (1 + \kappa(s)) \frac{p_y}{p_s}. \quad (2.41)$$

In order to describe the longitudinal phase space the energy change due to electric fields

$$qV = - \int \vec{E}(x, y, s, t) \cdot \vec{v} dt, \quad (2.42)$$

has to be taken into account. In addition, a new variable

$$\eta = 1 - \gamma = \eta_0(1 + \delta_K) - \frac{qV}{mc^2}, \quad (2.43)$$

is introduced, which denotes the ratio of kinetic energy to the energy equivalent of the rest mass. Consequently, the derivative of  $l_K$  2.34 with respect to  $s$  yields

$$l'_K = \frac{dl_K}{ds} = -v_0 \frac{\gamma_0}{1 + \gamma_0} (t' - t'_0) = -\frac{1 + \eta_0}{2 + \eta_0} \left[ (1 + \kappa(s)x) \frac{1 + \eta}{1 + \eta_0} \frac{p_0}{p_s} - 1 \right], \quad (2.44)$$

where the time derivative

$$t' = \frac{dt}{ds} = \frac{1}{v} \sqrt{(x')^2 + (y')^2 + (L')^2} = \frac{1}{v} (1 + \kappa(s)x) \frac{p}{p_s}, \quad (2.45)$$

is used. The momentum-like variables are determined in a similar way. Here, only the solutions are given, due to reasons of simplicity. The exact derivations can be found for example

in [23].

$$a' = \frac{da}{ds} = (1 + \kappa(s)) \left[ \frac{1 + \eta}{1 + \eta_0} \frac{\vec{E} p_0^2}{\chi_{e,0} p_s} + \frac{B_s p_0}{\chi_{m,0} p_s} - \frac{B_y}{\chi_{m,0}} \right] + \kappa(s) \frac{p_0}{p_s}, \quad (2.46)$$

$$b' = \frac{db}{ds} = (1 + \kappa(s)) \left[ \frac{1 + \eta}{1 + \eta_0} \frac{\vec{E} p_0^2}{\chi_{e,0} p_s} + \frac{B_s p_0}{\chi_{m,0} p_s} - \frac{B_x}{\chi_{m,0}} \right], \quad (2.47)$$

where  $\chi_{e,0}$  and  $\chi_{m,0}$  are the electric respectively magnetic rigidity

$$\chi_{e,0} = \frac{pv}{q} \quad \text{and} \quad \chi_{m,0} = \frac{p}{q}. \quad (2.48)$$

The energy difference is independent of the position in the ring, thus its derivative yields

$$\frac{d\delta_K}{ds} = \delta'_K = 0. \quad (2.49)$$

### 2.2.3 Transverse and Longitudinal Motion

In this section the dynamic of the particle bunch in a pure magnetic ring is discussed in linear order. Consequently, the horizontal and vertical motion decouples, which simplifies Eq. 2.40 and Eq. 2.46 to

$$x' = a, \quad (2.50)$$

$$\begin{aligned} a &= (1 + \kappa(s)) - \frac{B_y}{\chi_{m,0}} + \kappa(s) \left( 1 + \frac{1 + \eta_0}{2 + \eta_0} \delta_K \right) \\ &= -(\kappa(s)^2 - k)x + \kappa(s)\delta, \end{aligned} \quad (2.51)$$

where  $\delta_K$  is expressed by  $\delta$ , since it is more convenient in the case of only magnetic fields. Latter can be written in curvilinear coordinates by expanding the normal components in terms of normalized fields

$$\frac{B_x(x, y)}{\chi_{m,0}} = 0 - k \cdot y + k_2 \cdot xy + \dots, \quad (2.52)$$

$$\frac{B_y(x, y)}{\chi_{m,0}} = \kappa(s) - k \cdot y + k_2 \cdot (x^2 - y^2) + \dots, \quad (2.53)$$

where  $k$  and  $k_2$  represents the quadrupole and the sextupole strength, respectively. In order to describe the transversal motion Eq. 2.50 and Eq. 2.51 are combined to an inhomogeneous differential equation of second order

$$\text{horizontal: } \kappa(s)\delta = x'' + (\kappa(s)^2 - k(s))x, \quad (2.54)$$

$$\text{vertical: } 0 = y'' + k(s)y. \quad (2.55)$$

In case of a horizontal focusing ( $k \geq 0$ ) the beam is simultaneously defocused in the vertical plane. The horizontal DGL becomes homogeneous for a vanishing momentum deviation  $\delta = 0$

and it transforms into an equation of Hill's type. Its solution is similar to a harmonic oscillator except of the term which depends on the periodic variable  $s$

$$K(s + C_0) = K(s) \quad \text{with} \quad K(s) = \kappa(s)^2 - k(s), \quad (2.56)$$

where  $C_0$  denotes the length of the storage ring. The solution reads

$$x(s) = \sqrt{\epsilon\beta(s)} \cos(\Psi(s) + \Psi_0), \quad (2.57)$$

where  $\beta(s)$  and  $\Psi(s)$  denote the betatron function respectively the betatron phase. The parameter  $\epsilon$  is called emittance and it will be discussed in the following section. Inserting the solution into Eq. 2.54 leads to

$$\frac{1}{2}\beta(s)\beta''(s) - \frac{1}{4}(\beta'(s))^2 + K(s)\beta(s) = 1, \quad \text{and} \quad \Psi(s) = \int_{s_0}^s \frac{1}{\beta(\tilde{s})} d\tilde{s}. \quad (2.58)$$

Taking into account just linear order effects the longitudinal motion in a pure magnetic storage ring can be derived by considering Eq. 2.44 and Eq. 2.49

$$l'_K = -\kappa(s) \frac{1 + \eta_0}{2 + \eta_0} x + \frac{1}{(2 + \eta_0)^2} \delta_K, \quad (2.59)$$

$$\delta'_K = 0. \quad (2.60)$$

where Eq. 2.59 describes the change of the orbit length given a radial offset and a momentum deviation. A new quantity is introduced, which describes the relation between the momentum deviation and the radial offset  $x = D \cdot \delta$ . It is called the dispersion. With the transformation  $\delta_K = (2 + \eta_0)/(1 + \eta_0)\delta$  one gets

$$l'_K = \left[ -\kappa(s) \frac{1 + \eta_0}{2 + \eta_0} D + \frac{1}{(2 + \eta_0)^2} \frac{2 + \eta_0}{1 + \eta_0} \right] \delta. \quad (2.61)$$

## 2.2.4 Beam Emittance and Betatron Tune

By making use of Eq.2.57 and its first derivative and taking into account only conservative forces the betatron phase  $\Psi$  drops out, which leads to the ellipse equation

$$\gamma(s) = x^2(s) + 2\alpha(s)x(s)x'(s) + \beta(s)x'(s) = \epsilon_{CS} = \text{const.}, \quad (2.62)$$

where the area of the ellipse  $F = \pi\epsilon_{CS}$  is time invariant. Thus, the parameter  $\epsilon_{CS}$  is called the Courant-Snyder-Invariant and it reflects the Liouville theorem, which states that the six-dimensional phase space is conserved. This also holds for the individual phase spaces in the

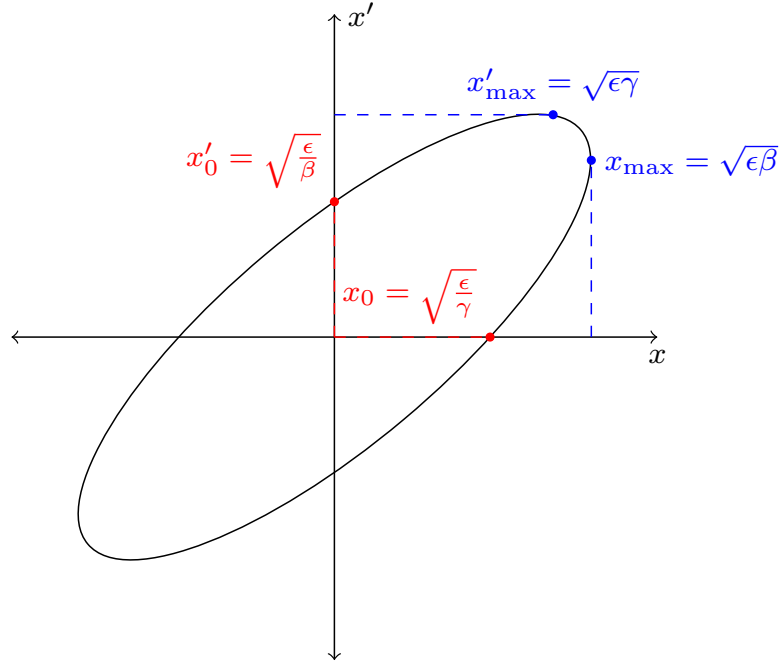


Figure 2.2: Transverse linear particle motion specified by a phase space ellipse. The zero crossings and the extrema are expressed by the optical functions of the investigated particle

case of a vanishing coupling between them. The parameters

$$\alpha(s) = -\frac{\beta'(s)}{2}, \quad (2.63)$$

$$\gamma(s) = \frac{1 + \alpha^2(s)}{\beta(s)}, \quad (2.64)$$

are called the optical functions or Twiss parameters. They describe the emittance of a single particle with position  $x$  and angle  $x'$  at a particular location  $s$ . An example of a linear particle motion expressed by a phase space ellipse is given in Fig. 2.2.

In the case of a particle ensemble of  $N$  particles the particle distribution can often be estimated by a Gaussian function

$$\rho(x, x') = N \cdot \exp\left(-\frac{\sigma_{22}x^2 - 2\sigma_{12}xx' + \sigma_{11}x'^2}{2\epsilon_x^1\sigma}\right), \quad (2.65)$$

where the beam matrix is given by  $\hat{\sigma}_x$

$$\hat{\sigma}_x = \begin{pmatrix} \sigma_{11} & \sigma_{12} \\ \sigma_{12} & \sigma_{22} \end{pmatrix} = \begin{pmatrix} \text{Var}(x) & \text{Cov}(x, x') \\ \text{Cov}(x, x') & \text{Var}(x') \end{pmatrix}, \quad (2.66)$$

which is defined by the phase space ellipse of multiple particles with different Courant-Snyder-

Invariants

$$\hat{\sigma}_x = \begin{pmatrix} x & x' \end{pmatrix} \hat{\sigma}_x \begin{pmatrix} x \\ x' \end{pmatrix} = 1. \quad (2.67)$$

The parameter  $\epsilon_x^{1\sigma}$  in Eq. 2.65 is called the r.m.s beam emittance. That is 39.3% of the particles are localized in the phase space ellipse specified by  $\epsilon_x^{1\sigma}$ .

$$\epsilon_x^{1\sigma} = \det(\hat{\sigma}_x) = \sqrt{\sigma_{11}\sigma_{22} - \sigma_{12}^2}. \quad (2.68)$$

In the case of acceleration or deceleration, the r.m.s. beam emittance varies, which is called adiabatic damping. Thus, a normalized emittance is defined

$$\epsilon_N = \beta\gamma\epsilon, \quad (2.69)$$

where  $\beta$  and  $\gamma$  denote the relativistic Lorentz parameters.

An additional important quantity is the betatron tune, which describes the phase advance of the particle per turn divided by  $2\pi$

$$Q = \frac{\mu}{2\pi}. \quad (2.70)$$

The phase advance depends on the circumference of the accelerator  $C$  and it is given by

$$\mu(C) = \int_s^{s+C} \frac{d\tilde{s}}{\beta(\tilde{s})}. \quad (2.71)$$

Accordingly, the transfer matrix can be expressed by

$$\hat{M} = \begin{pmatrix} \cos(\mu) + \alpha \sin(\mu) & \beta \sin(\mu) \\ -\gamma \sin(\mu) & \cos(\mu) - \alpha \sin(\mu) \end{pmatrix}. \quad (2.72)$$

In the case of no coupling and taking into Liouville's theorem, the two-dimensional phase space volume is conserved and the eigenvalues of the matrix equal unity. In order to provide stable solutions they have to be complex, which yields to

$$\lambda_{1,2} = \left| \cos(\mu) \pm \sqrt{(\cos \mu)^2 - 1} \right| = 1, \quad (2.73)$$

$$\rightarrow \lambda_{1,2} = e^{\pm i\mu} = e^{\pm i2\pi Q}. \quad (2.74)$$

## 2.2.5 Dispersion and Chromaticity

The solution of the inhomogeneous differential equation, which describes the transverse particle motion, can be expressed by a full set of homogeneous solution and one particular solution of the inhomogeneous partial

$$x_g(s) = x(s) + x_D(s). \quad (2.75)$$

For a magnetic ring the latter (dispersive) term corresponds to the momentum deviation of a particle

$$x_D(s) = D(s)\delta, \quad (2.76)$$

where  $D(s)$  is called the dispersion function, which is periodic and its solution is given by

$$D(s) = \frac{\sqrt{\beta(s)}}{2 \sin(\frac{\mu}{2})} \int_s^{s+C} \kappa(\tilde{s}) \sqrt{\beta(\tilde{s})} \cos\left(\Psi(\tilde{s}) - \Psi(s) - \frac{\mu}{2}\right) d\tilde{s}. \quad (2.77)$$

In addition, the momentum-dependent path-length change of the particle with respect to the reference orbit  $C_0$  can be described by the momentum compaction factor  $\alpha_p$

$$\frac{\Delta C}{C_0} = \alpha_p \delta = \alpha_p \frac{\Delta p}{p}. \quad (2.78)$$

Thus, the relation between the dispersion and momentum compaction factor is given by

$$\alpha_p = \frac{1}{C_0} \int_s^{s+C_0} D(\tilde{s}) \kappa(\tilde{s}) d\tilde{s}. \quad (2.79)$$

The dispersion depends on the curvature  $\kappa(s)$  of the particle and it is based on the varying bending powers of the main dipoles for particles with different momenta.

Another momentum depending effect is the chromaticity, which takes into account the momentum-dependent focusing strength of the focusing elements in the ring. In fact, the quadrupole strength are changed by

$$k(p) = -\frac{q}{p} \frac{\partial B_y}{\partial x} = -\frac{q}{p_0} \frac{\partial B_y}{\partial x} \frac{1}{1+\delta} \approx k_0(1-\delta). \quad (2.80)$$

This induces a tune change and the so called natural chromaticity is given by  $Q'^n$

$$\Delta Q_{\text{quad}} = Q'^n \cdot \delta \pm \frac{1}{4\pi} \oint \beta(\tilde{s}) \kappa(\tilde{s}) d\tilde{s} \cdot \delta, \quad (2.81)$$

where the plus and the minus sign correspond to the vertical and radial motion, respectively. In order to compensate this tune changes sextupole magnets can be used, which add an additional tune variation

$$\Delta Q_{\text{sext}} = Q'_{\text{sext}} \cdot \delta = \pm \frac{1}{4\pi} \oint \beta(\tilde{s}) k_2(\tilde{s}) D(\tilde{s}) d\tilde{s} \cdot \delta. \quad (2.82)$$

Note that two sextupole families are required in order to correct chromaticities in both planes, where they act only in the dispersive regions. Since the curvature in the vertical direction is relatively small in a planar ring, the vertical dispersion almost vanishes. A definition of the

chromaticity is given by the relative tune change

$$\xi = \frac{Q'}{Q}. \quad (2.83)$$

## 2.2.6 Spin and Polarization Formalism

The theoretical description of the beam polarization is based on the spin formalism. In the following, latter is discussed for the spin- $\frac{1}{2}$ - and spin-1-particles.

### Spin-1/2-particles

In order to describe the state of a single spin- $\frac{1}{2}$ -particle, the two component Pauli spinor is used

$$\psi = \begin{pmatrix} u \\ d \end{pmatrix}, \quad (2.84)$$

where  $u$  and  $d$  denote the two complex amplitudes, which satisfy the normalization  $|u|^2 + |d|^2 = 1$ . Assuming a Cartesian coordinate system  $(\vec{e}_1, \vec{e}_2, \vec{e}_3)$ , the two components of the spinor correspond to the two different spin states along the quantization axis  $\vec{e}_3$ . In the case of a spin- $\frac{1}{2}$ -particle the associated hermitian operators are given by the Pauli spin operators

$$\hat{S} = \frac{\hbar}{2} \vec{\sigma}, \quad (2.85)$$

where  $\hbar$  denotes Planck's constant divided by  $2\pi$ . The four matrices

$$\sigma_0 = \begin{pmatrix} 1 & 0 \\ 0 & 1 \end{pmatrix}, \quad \sigma_1 = \begin{pmatrix} 0 & 1 \\ 1 & 0 \end{pmatrix}, \quad \sigma_2 = \begin{pmatrix} 0 & -i \\ i & 0 \end{pmatrix}, \quad \sigma_3 = \begin{pmatrix} 1 & 0 \\ 0 & -1 \end{pmatrix}. \quad (2.86)$$

form a complete basis of the hermitian  $2 \times 2$ -matrices. The expectation value of the operator  $\hat{A}$  is equivalent to the observable

$$\langle \hat{A} \rangle = \langle \phi | \hat{A} | \psi \rangle = \psi^\dagger \hat{A} \psi, \quad (2.87)$$

where the density matrix yields

$$\rho = |\psi \rangle \langle \psi| = \begin{pmatrix} |u|^2 & ud^* \\ u^*d & |d|^2 \end{pmatrix}. \quad (2.88)$$

The star indicates the complex conjugated of the variable. Consequently, the expectation value can be expressed by the trace of the product of the density matrix and the corresponding operator

$$\langle \hat{A} \rangle = \text{Tr} \rho \hat{A}, \quad (2.89)$$

which simplifies to

$$\vec{S} = \langle \hat{S} \rangle = \frac{\hbar}{2} \text{Tr} \rho \vec{\sigma} = \frac{\hbar}{2} \begin{pmatrix} 2\text{Re}(ud^*) \\ \text{Im}(ud^*) \\ |u|^2 - |d|^2 \end{pmatrix} \quad (2.90)$$

for a single particle

In a storage ring experiment, more than  $10^9$  particles are usually investigated. Thus, the expectation value of the spin observables for the whole ensemble is measured, which yields the density matrix

$$\rho = \frac{1}{N} \begin{pmatrix} \sum_{i=1}^N |u^{(i)}|^2 & \sum_{i=1}^N u^{(i)} d^{(i)*} \\ \sum_{i=1}^N u^{(i)*} d^{(i)} & \sum_{i=1}^N |d^{(i)}|^2 \end{pmatrix}. \quad (2.91)$$

It can be written in terms of the Pauli spin operators

$$\rho = \frac{1}{2} (\sigma_0 + \vec{P} \vec{\sigma}), \quad (2.92)$$

where  $\vec{P}$  denotes the polarization vector of the particle ensemble, which is given by the sum of the spin operators

$$\vec{P} = \frac{1}{N} \sum_{i=1}^N \vec{S}_i. \quad (2.93)$$

Consequently, the vertical polarization along the quantization axis is specified by

$$P_v = \frac{N^{m=\frac{1}{2}} - N^{m=-\frac{1}{2}}}{N^{m=\frac{1}{2}} + N^{m=-\frac{1}{2}}}, \quad (2.94)$$

where  $N^{m=\frac{1}{2}}$  and  $N^{m=-\frac{1}{2}}$  denote the number of particles in the particular quantization state.

### Spin-1-particles

The formalism of a spin-1-particle takes into account a third component of the spinor in order to describe the state of an individual particle

$$\psi = \begin{pmatrix} a_1 \\ a_2 \\ a_3 \end{pmatrix}, \quad (2.95)$$

where the states along the quantization axis are given by  $m = -1, 0, 1$ . The basic spin operators yield

$$\hat{S}_1 = \frac{\hbar}{\sqrt{2}} \begin{pmatrix} 0 & 1 & 0 \\ 1 & 0 & 1 \\ 0 & 1 & 0 \end{pmatrix}, \quad \hat{S}_2 = \frac{\hbar}{\sqrt{2}} \begin{pmatrix} 0 & -i & 0 \\ i & 0 & -i \\ 0 & i & 0 \end{pmatrix}, \quad \hat{S}_3 = \hbar \begin{pmatrix} 1 & 0 & 0 \\ 0 & 0 & 0 \\ 0 & 0 & -1 \end{pmatrix}. \quad (2.96)$$

Consequently, nine independent hermitian matrices are required to characterize a spin-1-system. Therefore, a second-rank tensor is constructed by the outer product of the spin operators. In order to express the nine operators exclusively in terms of  $\hat{S}_1, \hat{S}_2, \hat{S}_3$  and the identity matrix  $I$ , the tensor is split into a symmetric and an asymmetric contribution. Subsequently, in standard Cartesian notation, a set of ten operators is constructed by

$$\hat{S}_{ij} = \frac{3}{2} (\hat{S}_i \hat{S}_j + \hat{S}_j \hat{S}_i) - 2I \delta_{ij}, \quad i, j \in 1, 2, 3, \quad (2.97)$$

where  $\delta_{ij}$  denotes the Kronecker delta. Nine operators are independent, because of the dependency relation

$$\hat{S}_{11} + \hat{S}_{22} + \hat{S}_{33} = 0. \quad (2.98)$$

The density matrix for a spin-1-particle ensemble can be written as

$$\rho = \frac{1}{3} \left[ I + \frac{3}{2} \sum_{i=1}^3 P_i S_i + \frac{1}{3} \sum_{i=1}^3 \sum_{j=1}^3 P_{ij} S_{ij} \right], \quad \text{with } P_{ij} = P_{ji}, \quad (2.99)$$

where  $P_i$  and  $P_{ij}$  specify the polarization states. In the case of an axial symmetry about the quantization axis, the density can be expressed by

$$\rho = \frac{1}{3} \left[ I + \frac{3}{2} P_3 \hat{S}_3 + \frac{1}{2} P_{33} \hat{S}_{33} \right]. \quad (2.100)$$

In Cartesian notation the vector  $P_V$  and tensor  $P_T$  polarization yield

$$P_V = \frac{N^{m=1} - N^{m=-1}}{N^{m=1} + N^{m=0} + N^{m=-1}}, \quad (2.101)$$

$$P_T = \frac{N^{m=1} + N^{m=-1} - 2N^{m=0}}{N^{m=1} + N^{m=0} + N^{m=-1}}. \quad (2.102)$$

### 2.2.7 Thomas-BMT Equation

The non-relativistic Hamiltonian of the spin interaction in electromagnetic fields is given by

$$\mathcal{H} = -\vec{\mu} \cdot \vec{B} - \vec{d} \cdot \vec{E}, \quad (2.103)$$

where  $\mu$  and  $d$  denote the magnetic and electric dipole moment, respectively. They are fundamental properties of the particle and are aligned with the spin axis

$$\vec{\mu} = g \frac{q}{2m} \vec{S}, \quad (2.104)$$

$$\vec{d} = \eta_{\text{EDM}} \frac{q}{2mc} \vec{S}. \quad (2.105)$$

Here,  $m$  and  $q$  are the mass and the charge of the particle, respectively. The speed of light is given by  $c$  and  $\vec{S}$  denotes the spin. The two dimensionless quantities  $g$  and  $\eta_{\text{EDM}}$  are called the  $g$ -factor and the  $\eta$ -parameter.

particle	spin in $\hbar$	rest energy in MeV	$ \vec{\mu} $ in $\mu_B$ or $\mu_N$	$g$
proton	$\frac{1}{2}$	938.2720813(58)	2.7928473508(85)	5.585695
deuteron	1	1875.612928(12)	0.8574382311(48)	1.714025
electron	$\frac{1}{2}$	0.5109989461(31)	1.00115965218091(36)	2.002319
muon	$\frac{1}{2}$	105.6583745(24)	$4.84197048(11) \times 10^{-3}$	2.002332

Table 2.1: Magnetic properties of the proton, deuteron, electron and muon.

In tabular 2.1 the magnetic properties of the proton, deuteron, electron, and muon are presented. In addition, one finds the rest mass and the spin in terms of the Planck constant. All quantities are determined by experimental measurements, whereas the magnetic dipole moment is expressed in terms of the Bohr magneton  $\mu_B$  (leptons) or the nuclear magneton  $\mu_N$  (hadrons).

$$\mu_B = \frac{eh}{m_e c} = 5.7883818012(26) \times 10^{-5} \text{ eV/T}, \quad (2.106)$$

$$\mu_N = \frac{eh}{m_N c} = 3.1524512550(15) \times 10^{-8} \text{ eV/T}. \quad (2.107)$$

The anomalous gyromagnetic  $g$ -factor is defined as

$$G = a = \frac{g - 2}{2}, \quad (2.108)$$

where the variable  $G$  is commonly used for the hadron and  $a$  for lepton sector. In the non-relativistic case, it yields  $a = 0$ . However, corrections based on higher orders provide a small deviation from this. In the work of [24] a relative precision of  $10^{-9}$  is realized for the Deuteron.

The according non-relativistic equation of motion for the spin vector  $\vec{S}$  in electric  $\vec{E}$  and

magnetic  $\vec{B}$  fields reads

$$\frac{d\vec{S}}{dt} = \vec{\Omega} \times \vec{S} = \vec{\mu} \times \vec{B} + \vec{d} \times \vec{E}. \quad (2.109)$$

Consequently, the spin starts to precess with the angular frequency  $|\vec{\Omega}|$  perpendicular to  $\vec{\Omega}$  in the presence of electromagnetic fields. Note, that in Eq 2.109 the fields are defined in the rest frame of the particle. However, in an accelerator, the fields are mostly known in the curvilinear laboratory reference frame, which leads to the Thomas-BMT equation. The latter describes the spin motion in the relativistic case. A generalized form, which also takes into account the electric dipole moment, is given by

$$\frac{d\vec{S}}{dt} = \vec{\Omega}_{\text{MDM}} \times \vec{S} + \vec{\Omega}_{\text{EDM}} \times \vec{S}, \quad (2.110)$$

$$\vec{\Omega}_{\text{MDM}} = -\frac{q}{m} \left[ \left( G + \frac{1}{\gamma} \right) \vec{B} - \frac{G\gamma}{\gamma+1} (\vec{\beta} \cdot \vec{B}) \vec{\beta} - \left( G + \frac{1}{1+\gamma} \right) \vec{\beta} \times \frac{\vec{E}}{c} \right], \quad (2.111)$$

$$\vec{\Omega}_{\text{EDM}} = -\frac{q}{mc} \frac{\eta_{\text{EDM}}}{2} \left[ \vec{E} - \frac{\gamma}{1+\gamma} (\vec{\beta} \cdot \vec{E}) \vec{\beta} + c\vec{\beta} \times \vec{B} \right], \quad (2.112)$$

where the electric and magnetic fields are defined in the curvilinear laboratory reference frame and the spin vector in the rest frame of the particle.

### 2.2.8 Vertical and Horizontal Polarization

In the following, the scattering frame as a Cartesian system with  $\vec{e}_z$  pointing along the momentum of the deuteron beam is defined. The unit vector  $\vec{e}_y$  points along the vector specified by the cross product of the momentum of the incident and scattered deuteron  $\vec{p}_{\text{inc}} \times \vec{p}_{\text{out}}$ . Finally, the  $\vec{e}_x$  vector completes a right-handed coordinate frame. The differential cross section for the elastic scattering of polarized deuterons onto an unpolarized target in units of the unpolarized differential cross section  $\sigma_0$  can be written as [25]

$$\begin{aligned} \sigma/\sigma_0 = & 1 + \frac{3}{2}P_Y A_y^d + \frac{2}{3}P_{XZ} A_{xz} \\ & + \frac{1}{3} (P_{XX} A_{xx} + P_{YY} A_{yy} + P_{ZZ} A_{zz}), \end{aligned} \quad (2.113)$$

where  $P_I$  denote the components of the deuteron vector polarization and the  $P_{IK}$  the Cartesian moments of the deuteron tensor polarization given the indices (I, K = X, Y, Z).  $A_y^d$  and  $A_{ik}^d$  are the vector and the tensor analyzing power of the deuteron, respectively. All observables depend on the scattering angle  $\theta(\vartheta, \phi)$ . With the relations

$$P_{XX} + P_{YY} + P_{ZZ} = A_{xx} + A_{yy} + A_{zz} = 0 \quad (2.114)$$

one defines  $\Delta A \equiv A_{xx} - A_{yy}$  to eliminate  $A_{xx} + A_{yy}$ . Further, one can use an additional right-handed coordinate system that is fixed in space, where the z-axis points in beam direction,  $\vec{e}_y$  upwards, and  $\vec{e}_x$  sideways. By measuring the azimuth  $\phi$  of the outgoing deuteron clock-

wise from the positive x-axis looking in the beam direction the scattering frame is given by a rotation of the fixed frame by  $\phi$ .

The polarization of a deuteron beam maintained by the atomic source is specified by the vector polarization  $P_{\xi} = m_{+} - m_{-}$  and the tensor polarization  $P_{\xi\xi} = 1 - 3m_0$ . Here,  $m_x$  denotes the fractional populations of the magnetic sub-states  $x = -1, 0, 1$  with respect to the quantization axis  $\hat{S} = (\Theta, \Phi)$ . The quantity  $\hat{S}$  is called the spin alignment axis and provides symmetry under rotation. In the fixed frame the occurring components of the vector polarization and tensor moments in Eq. 2.113 are given by

$$\begin{aligned}
 P_Y &= P_{\xi} \sin \Theta \sin(\Phi - \phi), \\
 P_{XZ} &= \frac{3}{2} P_{\xi\xi} \sin \Theta \cos \Theta \cos(\Phi - \phi), \\
 P_{\Delta} &= P_{XX} - P_{YY} = \frac{3}{2} P_{\xi\xi} \sin^2 \Theta \cos 2(\Phi - \phi), \\
 P_{ZZ} &= \frac{1}{2} P_{\xi\xi} (3 \cos^2 \Theta - 1). \tag{2.115}
 \end{aligned}$$

Consequently, the differential cross section as a function of  $P_{\xi}$ ,  $P_{\xi\xi}$ ,  $\Theta$ ,  $\Phi$  and  $\phi$  yields

$$\begin{aligned}
 \sigma/\sigma_0 &= 1 + \frac{3}{2} P_{\xi} A_y^d \sin \Theta \sin(\Phi - \phi) \\
 &+ \frac{1}{2} P_{\xi\xi} A_{xz} \sin(2\Theta) \cos(\Phi - \phi) \\
 &+ \frac{1}{8} P_{\xi\xi} A_{\Delta} [1 - \cos(2\Theta)] \cos(2(\Phi - \phi)) \\
 &+ \frac{1}{8} P_{\xi\xi} A_{zz} [3 \cos(2\Theta) + 1]. \tag{2.116}
 \end{aligned}$$

### Vertical Polarization

In the case of a vertically polarized beam, the spin alignment axis becomes  $\hat{S} = (\frac{\pi}{2}, 0)$ . Inserting this values in the equation of the differential cross section of a polarized beam on a unpolarized target Eq. 2.116 leads to

$$\begin{aligned}
 \sigma_{\text{ver}}/\sigma_0 &= 1 \\
 &+ \frac{3}{2} P_{\xi} A_y^d \cos \phi \\
 &+ \frac{1}{4} P_{\xi\xi} A_{\Delta}^d \cos 2\phi \\
 &- \frac{1}{4} P_{\xi\xi} A_{zz}^d. \tag{2.117}
 \end{aligned}$$

### Horizontal Polarization

For a beam polarization aligned to the vertical axis of the fixed frame the spin alignment axis becomes  $\hat{S} = (\frac{\pi}{2}, \frac{\pi}{2})$  and the differential cross section is given by

$$\begin{aligned} \sigma/\sigma_0 = & 1 + \frac{3}{2}P_{\zeta}^d A_y^d \cos \phi \\ & + \frac{1}{4}P_{\zeta\zeta} A_{\Delta} \cos 2\phi \\ & - \frac{1}{4}P_{\zeta\zeta} A_{zz} . \end{aligned} \quad (2.118)$$

$$\Theta(t) = \Omega_s t , \quad (2.119)$$

where  $\Omega_s = 2\pi f_{\text{rev}} \nu_s$  denotes the angular frequency of the horizontal spin precession for a reference particle in an ideal ring. The azimuthal angle of the spin alignment axis for vanishing imperfections is  $\Phi = 0$ . This results in  $\hat{S} = (\Omega_s t, 0)$  and the following differential cross section

$$\begin{aligned} \sigma/\sigma_0 = & 1 - \frac{3}{2}P_{\zeta}^d A_y^d \sin \Omega_s t \sin(\phi) \\ & + \frac{1}{2}P_{\zeta\zeta} A_{xz} \sin(2\Omega_s t) \cos(\phi) \\ & - \frac{1}{8}P_{\zeta\zeta} A_{\Delta} [1 - \cos(2\Omega_s t)] \cos(2\phi) \\ & + \frac{1}{8}P_{\zeta\zeta} A_{zz} [3 \cos(2\Omega_s t) + 1] . \end{aligned} \quad (2.120)$$

## Experimental Setup and Data Acquisition

The results, which are discussed in this work, are based on experimental data provided by the COler SYnchrotron (COSY) facility at the Forschungszentrum Jülich. A sketch of the accelerator is shown in Fig. 3.1. It provides a beam momentum range from 0.3 GeV to 3.7 GeV and its circumference is 184.3 m. The unique feature of the apparatus is the ability to store and accelerate polarized protons and deuterons. In addition, several devices are assembled in order to manipulate the polarization of the particle bunch. Thus, COSY represents an ideal machine to study systematic effects on the road to a final electric dipole moment experiment. At the beginning of this chapter, the individual components and devices of the storage ring are introduced. After that, the principle of the data processing is discussed.

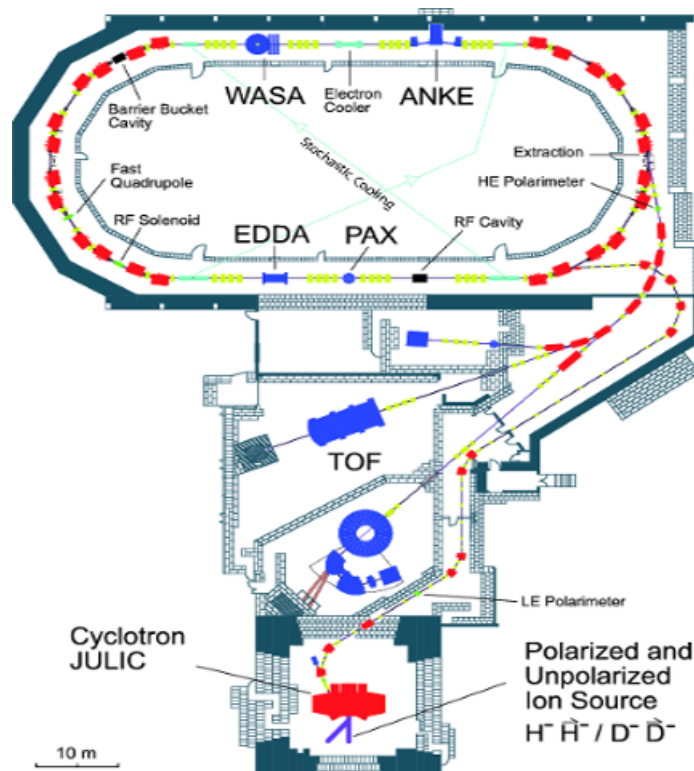


Figure 3.1: Sketch of the COSY facility

Initially, the atomic source provides vector or tensor polarized  $H^-$  or  $D^-$  [26]. After pre-accelerating the particles in the cyclotron JULIC they pass the low-energy polarimeter for first diagnostics. The injection of the particle ensemble into the storage ring takes place via a charge exchanging stripper carbon foil. The RF-cavity specifies the revolution frequency and thus the momentum of the ions. In the case of a deuteron beam, it is set to  $p_D = 0.97 \text{ GeV}/c$ . The beam emittance can be reduced by the operation of the 100 keV electron cooler. An radio-frequency solenoid allows to manipulate the spins of the particles. The EDDA detector allows determining the polarization and the spin tune of the particle ensemble.

In particular, the RF solenoid tilts the initially vertical polarization into the horizontal plane. The polarization starts to precess once it has an horizontal component. The frequency of the precession divided by the frequency of the beam stored in the ring is called the spin tune. It can be measured by extracting the particles onto a carbon target. The particle spin can be determined by using the formalism for spin-1 particles 2.2.6 The extraction is provided by a white noise electric field, which is generated by a superposition of different sinusoidal signals. The detection of each particle is counted as an event and it is analyzed independently.

### 3.1 The COSY Storage Ring

In the following the devices, which are relevant in the context of this thesis, are discussed.

#### EDDA Detector

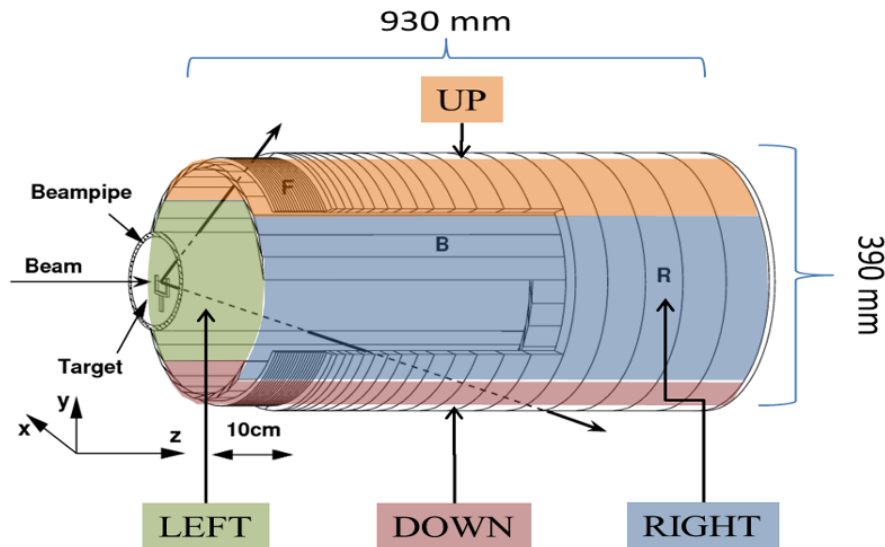


Figure 3.2: Sketch of the EDDA polarimeter

The EDDA detector was originally designed for the determination of proton-proton elastic scattering excitation functions for momentums from  $0.5 \text{ GeV}/c$  to  $2.5 \text{ GeV}/c$  [27]. A schematic overview of EDDA is given in Fig. 3.2. The detector is composed of ring and bar scintillators in an arrangement that wraps completely around the beam pipe downstream of the carbon

target. The latter is movable in the vertical direction. For the current experimental setup the polarimeter is divided into four parts (up, right, down, left). This allows forming asymmetries of the counting rates of the detected events. The spin depending signal is induced by an elastic scattering of the ion beam onto the unpolarized carbon target.

### RF Solenoid

The radio-frequency (RF) solenoid, which is shown in Fig. 3.3, provides a sinusoidal magnetic field parallel to the beam momentum vector. According to the Thomas-BMT Eq. 2.110 the spins of the particles are kicked as soon as they possess a component perpendicular to the magnetic field. The solenoid can be operated on resonance, i.e. on the spin precession frequency. Latter is specified by the spin tune, which is given by the spin revolution per particle turn in the ring. This modus operandi is applied to flip the initial vertical polarization of the beam by means of a half Froissart-Stora scan [28] into the horizontal plane.



Figure 3.3: The RF Solenoid

### 100 keV Electron Cooler

The 100 keV electron cooler reduces the emittance and the momentum spread of the ion beam (deuterons) by providing a coaxial electron beam with the same mean longitudinal velocity but a smaller transverse velocity spread than the ion beam [29]. As soon as the electrons are close to the deuterons the Coulomb interaction leads to an energy transfer between the oppositely charged particles, which reduces the velocity spread of the ion beam. In addition, the electron cooler can be used to change the momentum of the deuteron beam by mismatching the mean longitudinal velocities of the electron beam. In this case, the COSY lattice remains unchanged.

### Ion Beam Profile Monitor

The principle of the Ion Beam Profile Monitor (BPM) is based on the measurement of scintillation light induced by the interaction of the beam and residual gas [30]. Evaluating the optical functions at the local interaction position allows the reconstruction of the transverse ion beam widths. Thus, the Ion BPM represents a minimally invasive tool to determine the distribution of the particles of the ensemble.

## 3.2 Data Acquisition

### 3.2.1 Time Stamping System

In order to determine the precession frequency of the spin in the horizontal plane, each event is assigned to a number of particle turns in the storage ring  $n$ . The COSY RF cavity signal is pre-scaled and put on a time-to-digital-converter (TDC) [31]. The precision of the TDC and the system controller is 92.59 ps with a full range of 6.4  $\mu$ s. The system controller and the TDC operate synchronized with a full range of 0.21 s (15 bit) respectively 6.7 s (20 bit). For time measurements beyond this maximum range the corresponding offsets have to be counted within the data analysis, thus the signals on the TDC have to be more frequent than once per 6.7 s and the read out trigger for the DAQ has to come at least every 0.21 s. This method provides a precise time stamp for every signal since the start of the run.

The data are divided into two different data streams within the DAQ using two different sequences of event numbers. The TDC readout is asynchronous, i.e. whenever data are available the system controller reads out these data and send them to the attached readout computer. In addition, whenever a read-out trigger occurs, the system controller reads out the complete crate including the TDC and sends the data to the attached computer, as well. The latter event stream contains a time stamp from the system controller and is synchronized with the rest of the DAQ. Before the data are analyzed, both data streams are merged together by assigning all asynchronous data to the next synchronized event.

### 3.2.2 Frequency of the RF Cavity

The analysis takes the COSY RF as the reference signal in order to determine the horizontal spin precession, because the spin tune is defined as the spin rotations per particle turn in the ring. After each one hundredth period, a signal from the COSY RF system is forwarded to the TDC, which allows the interpolation of the period time  $T_{\text{RF},i}$  of the turns in between

$$T_{\text{RF},i} = \frac{t_{\text{RF},i+1} - t_{\text{RF},i}}{100}, \quad (3.1)$$

$$t_{\text{RF},i,j} = t_{\text{RF},i} + j \cdot T_{\text{RF},i}, \quad j = 0..99, \quad (3.2)$$

where  $t_{\text{RF},i,j}$  is the time after the  $j^{\text{th}}$  turn after the last COSY RF signal  $t_{\text{RF},i}$ .

Each event is assigned to an integer turn number  $n \in \mathbb{Z}$  by comparing the event time  $t_{\text{ev}}$  to the last time stamp delivered by the COSY RF cavity  $t_{\text{RF},i}$ . This happens every  $n_{\text{ps}} = 100$  revolutions of the particle bunch to reduce fluctuations due to the measurement method. However, it is short enough to account for macroscopic variations of the cavity itself. Consequently, the product of the pre-scale factor  $n_{\text{ps}}$  and the number of COSY RF signals  $n_{\text{RF}}$  defines the microscopic turn interval, in which the turn number of the event  $n$  is determined after the last COSY RF signal  $t_{\text{RF},i}$

$$n = n_{\text{ps}} \cdot n_{\text{RF}} + \left\lfloor \frac{t_{\text{ev}} - t_{\text{RF},i}}{T_{\text{RF}}} \right\rfloor. \quad (3.3)$$

Here,  $T_{\text{RF}} \approx 1332$  ns denotes the average time of the COSY period which is *a priori* given by

the user as a constant value and it must be close to the true one. The floor function  $\lfloor \arg \rfloor$  provides the greatest integer value of the argument and it considers that every pass of the bunch through the cavity marks the beginning of a next turn. Note that only the second summand of Eq. 3.3 depends on the period of COSY RF  $T_{\text{RF}}$ . Thus, the turn number of the event  $n$  is independent of  $T_{\text{RF}}$  since the reference time  $t_{\text{RF}}$  is read out every 100 turns.

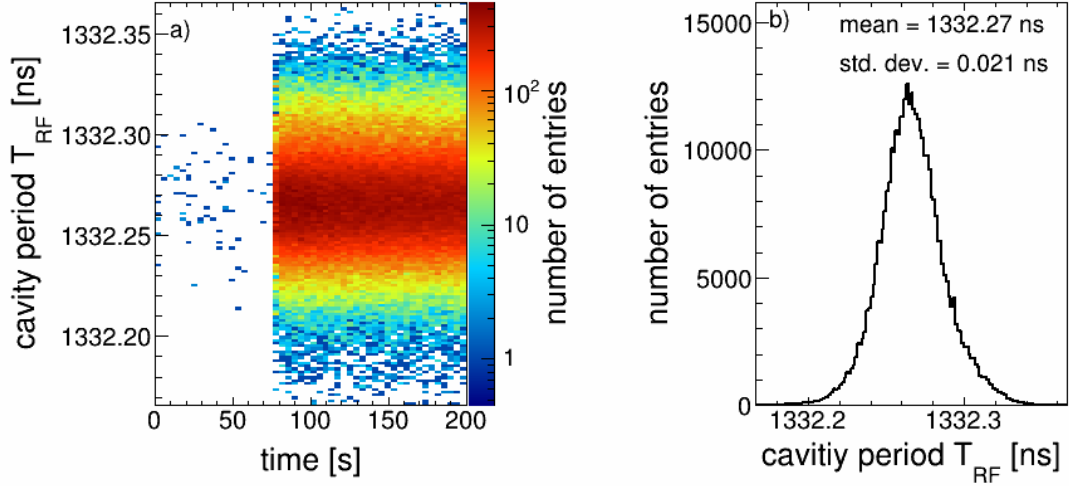


Figure 3.4: a) Distribution of the period time of the RF cavity signal for a run of 200 s. b) Projection of the y-axis for the whole run.

In Fig. 3.4 a) the time distribution of the COSY RF period  $T_{\text{RF}}$ , which is determined for every 100 periods of the RF cavity, is shown in nanoseconds for an entire run of 200 s. It is given by the time difference of two consecutive time signals of the COSY RF divided by the prescale factor

$$T_{\text{RF},i} = \frac{t_{\text{RF},i+1} - t_{\text{RF},i}}{n_{\text{ps}}}. \quad (3.4)$$

In addition, the y-axis projection for the whole run is given in Fig. 3.4 b). One observes a Gaussian distribution with the mean value  $\mu_{T_{\text{RF}}} = 1332.27 \text{ ns}$  and a standard deviation of  $\sigma_{T_{\text{RF}}} = 0.021 \text{ ns}$ . The width could either originate from a true fluctuation of the frequency of the RF cavity or from the measuring method of the time signals. Latter is performed by a discriminator which converts the analog sine wave signal of the cavity into a logical signal. Since the period of the COSY RF is approximately given by  $1.3 \mu\text{s}$ , the slope of the analog signal is quite flat. This leads to a fluctuation of the timing signals determined by the discriminator. Additionally, an unstable baseline of the discriminator could induce a similar effect. However, it is reduced by averaging out the COSY period by taking just every hundredth period. The main principle of the spin tune analysis is based on assigning each recorded event a turn number  $n$ , which is guaranteed by the unambiguous determination of particle turn number.

### 3.3 Event Rate

The event rates  $R_X = \dot{N}_X = dN_X/dn$  are measured in each detector quadrant  $X = (L, U, R, D)$  in order to determine the horizontal and vertical polarization. The centers of the quadrants are located at  $\phi_L \approx 0^\circ$ ,  $\phi_U \approx 90^\circ$ ,  $\phi_R \approx 180^\circ$  and  $\phi_D \approx 270^\circ$ , covering polar angles from  $\vartheta = 9^\circ$  to  $13^\circ$ , and an azimuthal range of  $\Delta\phi_X \approx 90^\circ$ . The event rates in each detector quadrant are obtained by the integration over the solid angle

$$R_X = I d_t \int_X a_X(\vartheta, \phi) \sigma(\vartheta, \phi) d\Omega. \quad (3.5)$$

Here,  $a_X(\vartheta, \phi)$  denotes the combined detector efficiency and acceptance,  $I$  [ $s^{-1}$ ] the beam intensity and  $d_t$  [ $cm^{-2}$ ] the target density,  $\sigma(\vartheta, \phi)$  the spin-dependent cross section. Equation 2.116 represents the cross section depending on the polarization, the azimuthal  $\phi$  and the polar angle  $\vartheta$ . Hence, the event rates in each detector are coupled to the polarization, which is described in the upcoming sections in more detail.

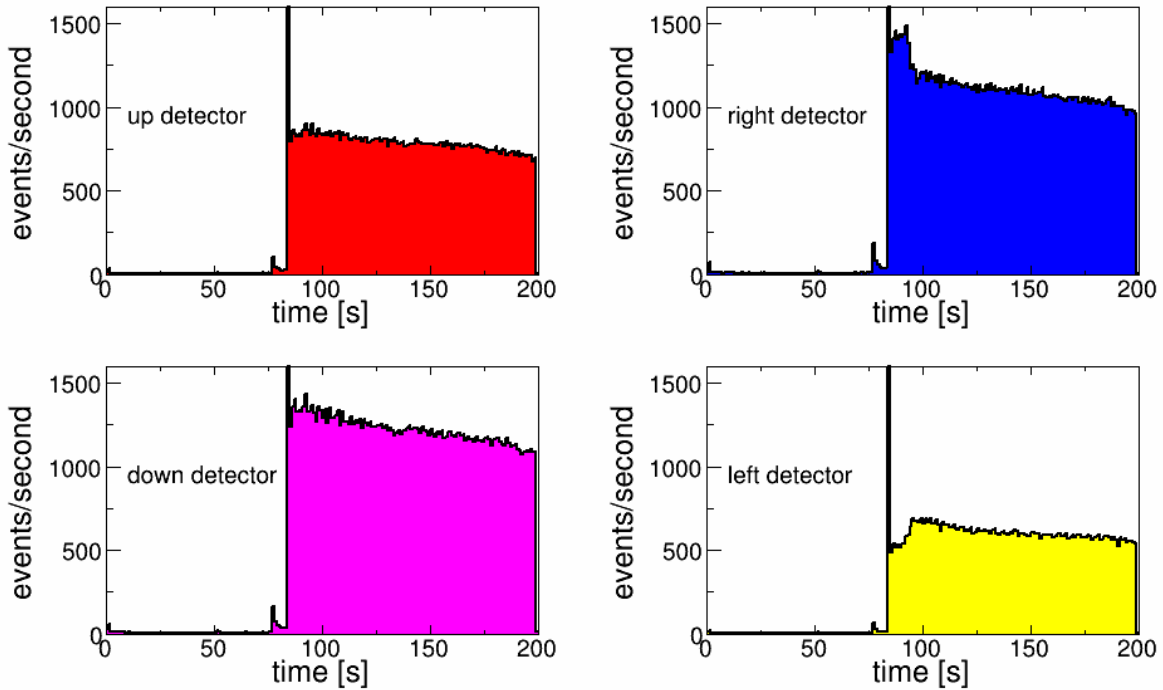


Figure 3.5: Counting rates of each detector quadrant for a 200 s cycle.

In Fig. 3.5 the counting rates of the four detector quadrants are shown for a 200 s cycle. Very few events are detected during the first 80 s because the beam is prepared by bunching and cooling. As soon as the white noise extraction of the beam onto the carbon target starts the event rates increase, which corresponds to the first little bump at 80 s. The larger second bump at 90 s represents the moment in time where the RF solenoid is switched on for 4 650 ms in order to flip the spin into the horizontal plane. This indicates that the transverse magnetic field of the RF solenoid is not perfectly aligned to the momentum of the particles, which results

in a displacement of their trajectory due to the Lorentz force. Consequently, particles will be kicked to another orbit, which leads to a higher extraction rate.

In addition, the RF solenoid induces the spin to be tilted from the initial vertical direction into the horizontal plane. This process is illustrated by the decreasing rate in the right detector and the increasing rate in the left one after switching on the RF solenoid. After the flip, the counting rates stay roughly constant for the rest of the cycle. This is achieved by the operation of a feedback system (Schneider box). It adjusts the voltage of the white noise extraction such that a constant extraction rate is maintained. The absolute value of the counting rates of each detector are different since the acceptances of the individual detectors are not identical. Additionally, the beam is not exactly going through the geometric center of the detector, which also yields to asymmetric counting rates.

### 3.4 Vertical Asymmetry

For two point-like detectors placed at  $\phi_L = 0^\circ$  and  $\phi_R = 180^\circ$  the number of detected events  $N_L, N_R$  during a macroscopic time interval  $\Delta t_{\text{mac}}$  yields

$$N_R = Id_t \bar{\sigma}_{0R} \Delta t_{\text{mac}} \left( 1 - \frac{3}{2} P_\zeta^d A_{yR}^d + \frac{1}{4} P_{\zeta\zeta}^d A_{\Delta R}^d - \frac{1}{4} P_{\zeta\zeta}^d A_{zzR}^d \right), \quad (3.6)$$

$$N_L = Id_t \bar{\sigma}_{0L} \Delta t_{\text{mac}} \left( 1 + \frac{3}{2} P_\zeta^d A_{yL}^d + \frac{1}{4} P_{\zeta\zeta}^d A_{\Delta L}^d - \frac{1}{4} P_{\zeta\zeta}^d A_{zzL}^d \right). \quad (3.7)$$

The analyzing powers  $A_y^d, A_\Delta^d$  and  $A_{zz}^d$  are assumed to be the same for all detectors quadrants  $A_y^d = A_{yX}^d, A_\Delta^d = A_{\Delta X}^d$  and  $A_{zz}^d = A_{zzX}^d$ , with  $X = (L, U, R, D)$ . In order to determine the vertical polarization and to cancel out variations of the beam intensity a conventional calculation of the left-right asymmetry  $\epsilon_{LR}$  yields

$$\begin{aligned} \epsilon_{LR} &= \frac{N_R - N_L}{N_R + N_L} \\ &= \frac{\bar{\sigma}_{0L} \left( 1 + \frac{3}{2} P_\zeta^d A_y^d + \frac{1}{4} P_{\zeta\zeta}^d (A_\Delta^d - A_{zz}^d) \right) - \bar{\sigma}_{0R} \left( 1 - \frac{3}{2} P_\zeta^d A_y^d + \frac{1}{4} P_{\zeta\zeta}^d (A_\Delta^d - A_{zz}^d) \right)}{\bar{\sigma}_{0L} \left( 1 + \frac{3}{2} P_\zeta^d A_y^d + \frac{1}{4} P_{\zeta\zeta}^d (A_\Delta^d - A_{zz}^d) \right) + \bar{\sigma}_{0R} \left( 1 - \frac{3}{2} P_\zeta^d A_y^d + \frac{1}{4} P_{\zeta\zeta}^d (A_\Delta^d - A_{zz}^d) \right)} \\ &= \frac{(\bar{\sigma}_{0L} - \bar{\sigma}_{0R}) \left( 1 + \frac{1}{4} P_{\zeta\zeta}^d (A_\Delta^d - A_{zz}^d) \right) + (\bar{\sigma}_{0L} + \bar{\sigma}_{0R}) \frac{3}{2} P_\zeta^d A_y^d}{(\bar{\sigma}_{0L} + \bar{\sigma}_{0R}) \left( 1 + \frac{1}{4} P_{\zeta\zeta}^d (A_\Delta^d - A_{zz}^d) \right) + (\bar{\sigma}_{0L} - \bar{\sigma}_{0R}) \frac{3}{2} P_\zeta^d A_y^d}. \end{aligned} \quad (3.8)$$

$$\sigma_{\epsilon_{LR}} = \sqrt{\frac{4N_R^2 N_L + 4N_R N_L^2}{(N_R + N_L)^4}} = \sqrt{\frac{4N_L N_R}{(N_R + N_L)^3}}. \quad (3.9)$$

Thus, for a vanishing tensor polarization  $P_{\zeta\zeta} = 0$  the left-right asymmetry of the counting rates is proportional to the vector polarization  $\epsilon_{LR} \propto P_\zeta$ . If the integrated spin-independent differential cross sections are exactly the same  $\bar{\sigma}_{0L} = \bar{\sigma}_{0R}$  the left-right asymmetry simplifies to  $\epsilon_{LR} = \frac{3}{2} P_\zeta^d A_y^d$ . However, for  $\bar{\sigma}_{0L} \neq \bar{\sigma}_{0R}$  the left-right asymmetry is not simply given by the product of the analyzing power and the polarization but is biased and distorted. In order to reduce the systematic shift of this effect the so-called cross-ratio method is applied.

### 3.4.1 Two Polarization States

The experimental setup provides an initial vertical polarization of the particle ensemble, which alternates between the cycles from the up  $p_{+\zeta}$  to the down  $p_{-\zeta}$  state. The notation plus and minus in front of the variable  $\zeta$  corresponds to the respective state. The cross-ratio  $\epsilon_{LR}^{CR}$  allows a cancellation of geometric misalignments and the detector acceptances. The concept of the cross-ratio is based on dividing the product of the counting rates of two different detector rates measured for two different polarization states by the product of the other detectors for the opposite polarization states

$$\begin{aligned}\epsilon_{LR}^{CR} &= \frac{1-r}{1+r} = |A_y^d| P_\zeta, \\ r^2 &= \frac{N_R^{p_{+\zeta}} N_L^{p_{-\zeta}}}{N_R^{p_{-\zeta}} N_L^{p_{+\zeta}}},\end{aligned}\quad (3.10)$$

where  $N_X^{p_{+\zeta}}$  denotes the counting rate of the polarization state  $p_{+\zeta}$  and  $N_X^{p_{-\zeta}}$  of the polarization state  $p_{-\zeta}$  for the detector quadrants  $X = L, R$ . Note that the term in front of the brackets in Eq. 3.7 drops out by calculating the cross-ratio  $r^2$ . However, the statement  $\epsilon_{LR}^{CR} = |A_y^d| P_\zeta$  is just valid, if both polarization states have the same amplitude  $p_{+\zeta} = p_{-\zeta}$ , which is not necessarily provided by the atomic source.

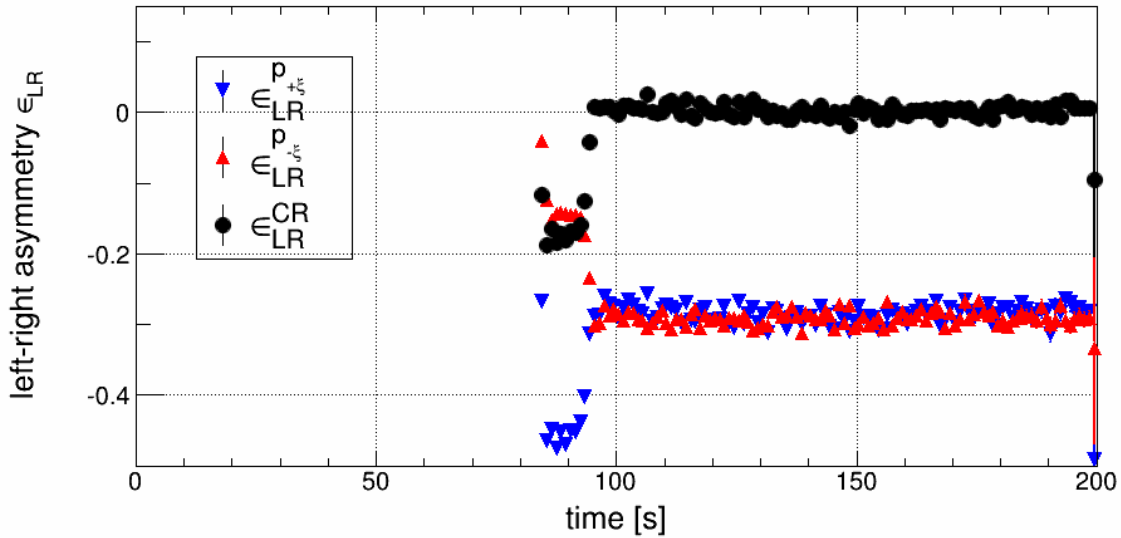


Figure 3.6: Left-right asymmetry of individual polarization states and their cross-ratio for a typical 200 s cycle.

In Fig. 3.6 a typical example of the left-right asymmetries for each of the two polarization states  $\epsilon_{LR}^{p_{+\zeta}}, \epsilon_{LR}^{p_{-\zeta}}$  and the cross-ratio  $\epsilon_{LR}^{CR}$  for a  $\pi/2$  flip are shown. The extraction onto the carbon target starts at 80 s. Shortly after the operation of the RF solenoid, the initial value  $\epsilon_{LR}^{CR} \approx -0.2$  jumps to zero at around 90 s. Additionally, the asymmetries of each polarization state are presented. They show a larger absolute initial polarization value of the up-state  $p_{+\zeta} = \epsilon_{LR,i}^{p_{+\zeta}} -$

$\epsilon_{\text{LR},f}^{p_{+\xi}} \approx -0.26$  (blue) compared to down-state  $p_{-\xi} = \epsilon_{\text{LR},i}^{p_{-\xi}} - \epsilon_{\text{LR},f}^{p_{-\xi}} \approx 0.17$  (red). The indices  $i$  and  $f$  represent the initial respectively the final value of the left-right asymmetry. Subsequently, the cross-ratio in Eq. 3.10 becomes more complicated because of  $p_{+\xi} \neq p_{-\xi}$ . However, it represents an ideal method to specify the moment in time where the polarization is flipped completely into the horizontal plane  $p_{+\xi} = p_{-\xi} = 0$  since  $\epsilon_{\text{LR}}^{\text{CR}} = 0$  is independent of the absolute values of the individual initial polarization amplitudes.

In fact, the quantities  $\epsilon_{\text{LR}}^{p_{+\xi}}$  and  $\epsilon_{\text{LR}}^{p_{-\xi}}$  are proportional to the fraction of the number of vector polarized particles  $N^{\uparrow,\downarrow}$  compared to the total number of particles of the ensemble  $N_{\text{tot}}$

$$\epsilon_{\text{LR}}^{p_{+,-\xi}} = |A_y^{\text{d}}| P_{\xi} = |A_y^{\text{d}}| \frac{N^{\uparrow,\downarrow}}{N_{\text{tot}}}. \quad (3.11)$$

Thus, the atomic source ensures a higher percentage of vector polarized particles for the up-state than for the down-state. A deeper understanding of this and additional information about the operation of the atomic source can be found in [32].

Once the spin vector provides a component in the horizontal plane, it starts to precess. The frequency  $f_s$  is given by the spin tune  $\nu_s$  times the RF cavity frequency  $f_{\text{RF}}$

$$f_s = \nu_s f_{\text{RF}} \approx 0.1609 \cdot 750 \text{ kHz} \approx 120 \text{ kHz}. \quad (3.12)$$

In order to realize a complete spin flip the frequency of the RF solenoid has to be close to the spin precession frequency to fulfill the resonant condition. Additionally, it is crucial that the solenoid is switched off at the right moment. This ensures a maximally statistical sensitivity since the vertical polarization vanishes. In the upcoming sections, two analysis methods are discussed in order to unfold the horizontal spin precession.

---

# Data Analysis

---

At the beginning of this chapter two different analysis methods are introduced, which are implemented to determine the spin tune  $\nu_s$  and the amplitude  $\epsilon$  of the spin precession in the horizontal plane. In a simplified model, the probability density function of recording an event at the turn number  $n$  can be written as

$$p_s(n; \epsilon, \varphi_s, \nu_s) = \frac{1}{\Delta n} (1 + \epsilon \sin(2\pi\nu_s n + \varphi_s)) , \quad (4.1)$$

where  $\Delta n$  denotes the macroscopic turn interval and  $\varphi_s$  is the phase shift of the spin precession.

The first analysis method cancels out acceptance and flux variations during a macroscopic measurement interval by forming asymmetries mapping the counts of the Left(L), Up (U), Right (R) and Down (D) detector quadrants. An initial overview of this technique can be found in [33] and a more detailed discussion is given in this thesis. The second analysis method is based on the discrete turn Fourier transform, which provides Fourier coefficients as estimators of the parameters in Eq. 4.1.

Afterward, the statistical properties of the estimators are discussed. In particular, it is shown that the estimator of the amplitude parameter is biased. In addition, the Cramér-Rao bound of each parameter is determined in order to specify a lower bound of the statistical error of the estimated parameter.

At the end of this chapter, a more sophisticated probability density function based on a Rayleigh distributed spin tune of the particles is derived.

## 4.1 Mapping Method

In order to determine the spin tune given in Eq. 4.1 the time depending horizontal polarization has to be determined. For this purpose, asymmetries are formed using the counts of the Up (U) and Down (D) detector quadrants to cancel out possible acceptance and flux variations during the measurement. The quadrants are centered at  $\phi_U \approx 90^\circ$ , and  $\phi_D \approx 270^\circ$ , covering polar angles from  $\vartheta = 9^\circ$  to  $13^\circ$ , and an azimuthal range of  $\Delta\phi_U \approx \Delta\phi_D \approx 90^\circ$ .

It is not possible to determine the spin precession frequency  $f_s$  directly from the observed event rates by a simple least squares fit with  $\nu_s$  as a parameter using Eq. (3.5), because at a detector rate of  $\approx 5000 \text{ s}^{-1}$  and a spin precession frequency of  $f_s = |\nu_s| \cdot f_{\text{RF}} \approx 0.16 \cdot 750 \text{ kHz} = 120 \text{ kHz}$ , only about one event is detected per 25 spin revolutions. Hence, as described below, an algorithm is applied that maps all events into one oscillation period to accumulate enough statistics to extract properly the amplitude, the frequency and the phase of the precession. The algorithm generates asymmetries, which are largely independent of variations of acceptance or flux, and yields to a distribution of the polarization that oscillates around zero.

### 4.1.1 Spin Phase Advance $\varphi_s$

The main problem of unfolding the idle spin precession in the horizontal plane is based on the fact that approximately every 25th turn of the bunch only one event is detected in each of the four detector quadrants. Thus it is not possible to calculate up-down asymmetries, which are proportional to the horizontal polarization, in real-time. In the following section, the procedure to accumulate sufficient statistics during a macroscopic time interval  $\Delta T_{\text{mac}}$  is described. If not mentioned explicitly the time interval corresponds to  $\Delta n = 10^6$  turns and accordingly lasts for  $\Delta T_{\text{mac}} \approx 1.3 \text{ s}$ . This corresponds to a period time of the RF cavity of  $T_{\text{RF}} = 1/f_{\text{RF}} \approx 1.3 \mu\text{s}$ .

As described in section 3.2.2 a turn number  $n \in \mathbb{Z}$  is assigned to each recorded event Eq. 3.3. Hence, it is possible to calculate the spin phase advance  $\varphi_s^{\nu_s^0}$  of each event by assuming the number of spin precession in the horizontal plane per particle turn in the ring  $\nu_s^0$  (spin tune)

$$\varphi_s^{\nu_s^0}(n) = 2\pi\nu_s^0 n. \quad (4.2)$$

Each of the macroscopic turn intervals is analyzed independently, and the events are mapped into a  $4\pi$  interval

$$\varphi_{s,\text{map}}^{\nu_s^0}(n) \equiv \varphi_s^{\nu_s^0}(n) \pmod{4\pi}. \quad (4.3)$$

This yields the event counts for the up  $N_U(\varphi_{s,\text{map}}^{\nu_s^0}(n))$  and the down  $N_D(\varphi_{s,\text{map}}^{\nu_s^0}(n))$  detector quadrant, respectively. An example is given in Fig. 4.1. Here,  $N_{\text{tot}} = 10107$  events were recorded in the time interval  $t \in [2.6 \text{ s}, 3.9 \text{ s}]$  after the polarization was tilted into the horizontal plane. In addition, they are mapped within the  $4\pi$  interval and divided into  $N_{\text{bins}} = 20$  bins. Each bin contains between 75 and 200 events depending on the detector quadrant and the mapped spin phase advance  $\varphi_{s,\text{map}}^{\nu_s^0}$ . The statistical error of each bin content is given by the square root of the number of entries  $\sigma_N = \sqrt{N}$  since the underlying process is interpreted as a

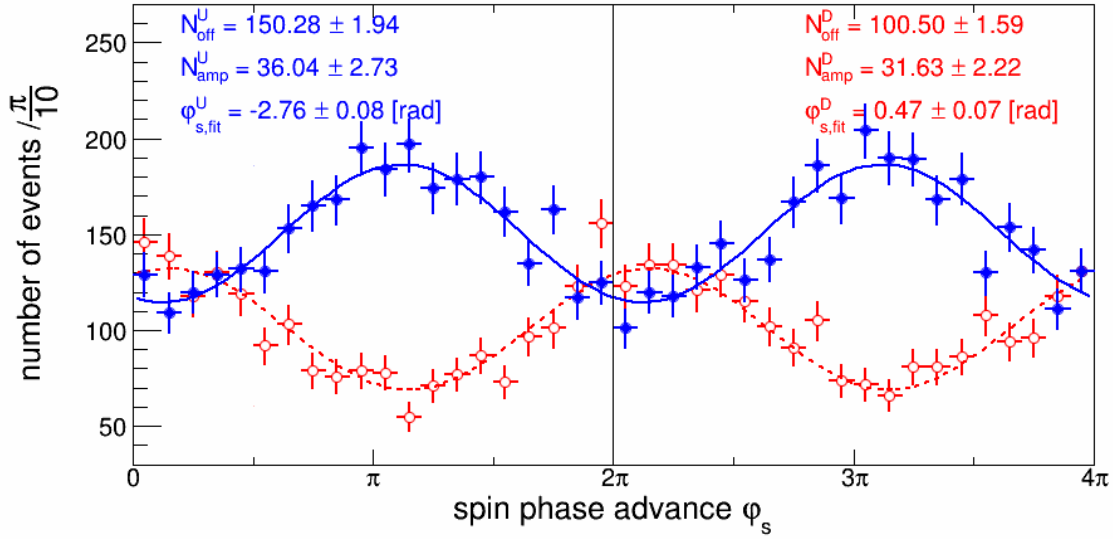


Figure 4.1: (a): Counts  $N_U$  and  $N_D$  after mapping the events recorded during a macroscopic turn interval of  $\Delta n = 10^6$  turns into a spin phase advance interval of  $4\pi$ . The vertical error bars show the statistical uncertainties, the horizontal bars indicate the bin width.

Poisson process. A least squares fit is performed by a sine function with three free parameters

$$N_{\text{fit}}(\varphi_s) = N_{\text{offset}} + N_{\text{amp}} \sin(\varphi_{s,\text{map}}^{\nu_s^0} + \varphi_{s,\text{fit}}^{\nu_s^0}). \quad (4.4)$$

The quantities  $N_{\text{amp}}$  and  $\varphi_{s,\text{fit}}^{\nu_s^0}$  are the amplitude and the phase of the sine.  $N_{\text{offset}}$  denotes the offset of the function.

The spin precession is unfolded as soon as the assumed spin phase advance  $\varphi_s^{\nu_s^0}(n)$  of each detected event is close to the real phase advance of the particle. In other words, the spin phase advance is mapped properly into the  $4\pi$  interval of each macroscopic interval when the assumed spin tune matches the true one  $\nu_s^0 \approx \nu_s$ . The event rates of the up detector quadrants are shifted by  $|\varphi_{s,\text{fit}}^D| + |\varphi_{s,\text{fit}}^U| \approx \pi$  with respect to the down detector. This becomes obvious in Eq. 2.120 where the spin dependent cross section is expressed as a function of the azimuthal scattering angle. Since the argument of the sine is given by the position of the detector quadrants located at  $\varphi_U \approx 90^\circ$  and  $\varphi_D \approx 270^\circ$ , a sign flip is obtained for the spin dependent part of the cross section. Thus, the rate of one detector quadrant becomes maximal whilst the other detector quadrant reaches its minimum.

The rates of the separate detector quadrants are strongly depending on the individual detector acceptance. Thus, the amplitude  $N_{\text{amp}}$  corresponds not directly to the amplitude of the spin precession, but also on the total number of detected events ( $N_{\text{tot}} \approx N_{\text{offset}} \cdot N_{\text{bins}}$ ) and thus on the detector geometry and acceptance, respectively. To cancel out these systematic effects, asymmetries are formed by using both detectors.

## 4.1.2 Up-Down Asymmetries

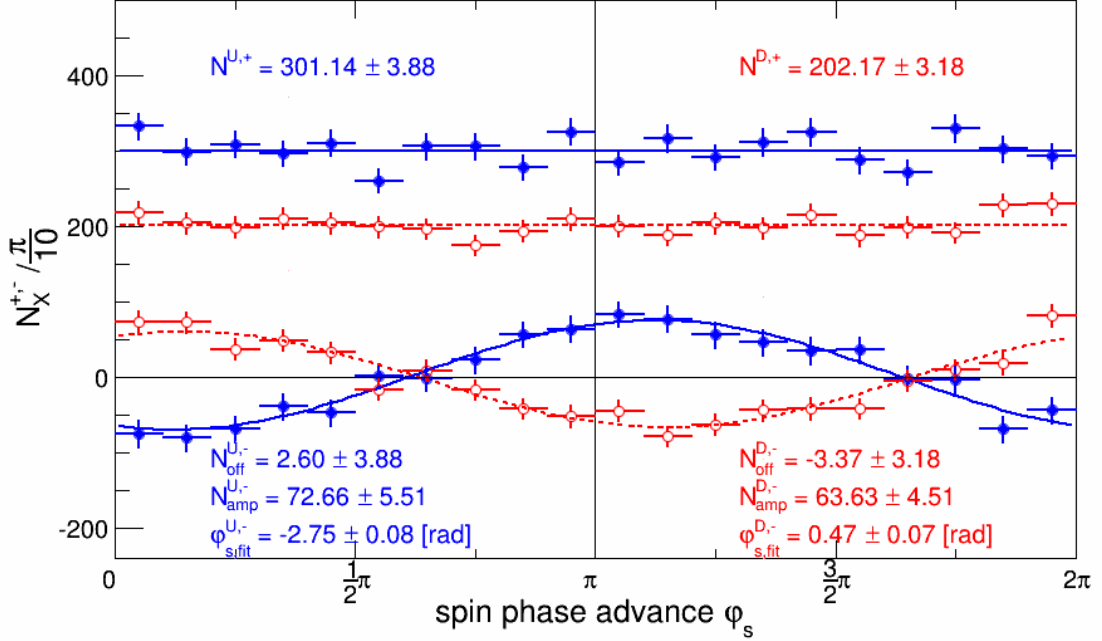


Figure 4.2: Count sums  $N_{U,D}^+(\varphi_s)$  and differences  $N_{U,D}^-(\varphi_s)$  of Eq. 4.5 with  $\varphi_s \in [0, 2\pi)$  using the counts  $N_U(\varphi_s)$  and  $N_D(\varphi_s)$ , shown in Fig. 4.1. The vertical error bars show the statistical uncertainties, the horizontal bars indicate the bin width.

In the following, the spin phase advance  $\varphi_s^{v_s^0}(n)$  depending on the assumed spin tune  $\nu_s^0$  and mapped into a  $4\pi$  interval will be denoted by  $\varphi_s$ . A sinusoidal waveform that oscillates around zero is obtained by defining four new event counts for the two quadrants ( $X = U$  or  $D$ ) are defined,

$$N_X^\pm(\varphi_s) = \begin{cases} N_X(\varphi_s) \pm N_X(\varphi_s + 3\pi) & \text{for } 0 \leq \varphi_s < \pi \\ N_X(\varphi_s) \pm N_X(\varphi_s + \pi) & \text{for } \pi \leq \varphi_s < 2\pi. \end{cases} \quad (4.5)$$

The equations provide sums,  $N_U^+(\varphi_s)$  and  $N_D^+(\varphi_s)$ , and differences,  $N_U^-(\varphi_s)$  and  $N_D^-(\varphi_s)$ , of counts depicted in Fig. 4.2. While the sums are constant, the differences oscillate around zero, and the asymmetry,

$$\begin{aligned} \epsilon(\varphi_s) &= \frac{N_U^-(\varphi_s) - N_D^-(\varphi_s)}{N_U^+(\varphi_s) + N_D^+(\varphi_s)} \\ &= \frac{3}{2} p_\xi \frac{\overline{\sigma}_{0U} \overline{A}_{yU}^d - \overline{\sigma}_{0D} \overline{A}_{yD}^d}{\overline{\sigma}_{0U} + \overline{\sigma}_{0D}} \sin(\varphi_s + \varphi), \end{aligned} \quad (4.6)$$

in the range  $\varphi_s \in [0, 2\pi)$  is independent of beam intensity and target density and is propor-

tional to the sine of the spin phase advance. In Fig. 4.3 the asymmetry  $\epsilon(\varphi_s)$  is shown for a measurement interval between 2.6 s and 3.9 s.

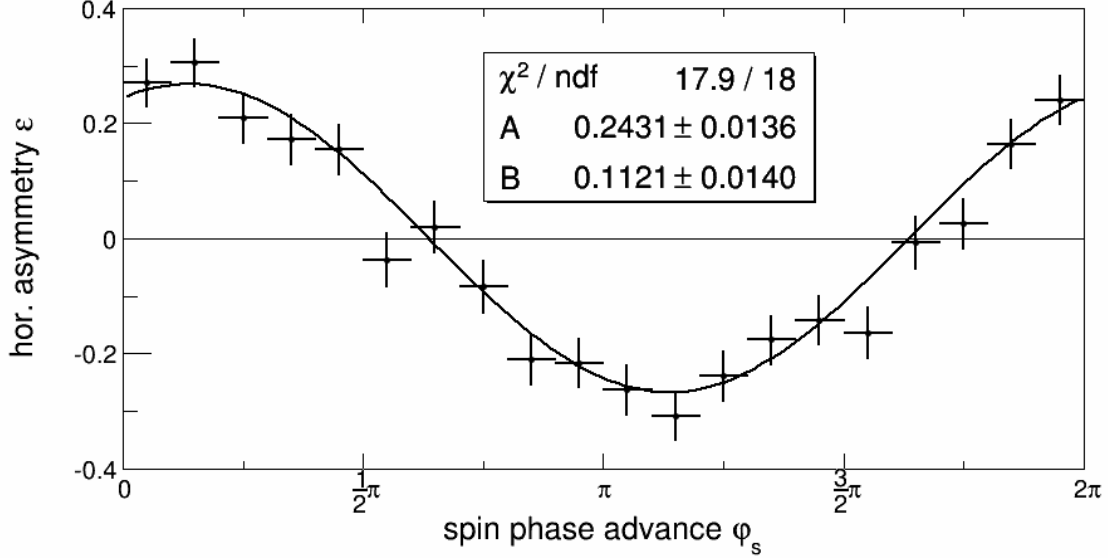


Figure 4.3: Measured asymmetry  $\epsilon(\varphi_s)$  of Eq. 4.6 fitted with  $\epsilon(\varphi_s)$  of Eq. 4.7 to extract amplitude  $\tilde{\epsilon}$  and phase  $\tilde{\varphi}$ , using the yields  $N_{U,D}^{+,-}(\varphi_s)$  of Fig. 4.1 (b) for a single turn interval of  $\Delta n = 10^6$  turns at a measurement time of  $2.6 \text{ s} < t < 3.9 \text{ s}$ .

A least squares fit performed to the data by the function

$$\epsilon_{\text{fit}}(\varphi_s) = A \sin(\varphi_s) + B \cos(\varphi_s), \quad (4.7)$$

yields the black curve in Fig.4.3 and provides an estimator of the amplitude  $\tilde{\epsilon}$  respectively the phase  $\tilde{\varphi}$  parameter. The amplitude is proportional to the horizontal vector polarization  $p_{\xi}$ , which can be determined if the cross section  $\bar{\sigma}_{0X}$  and the analyzing power  $\overline{A_{yX}^d}$  are known for both detectors ( $X=\text{up, down}$ ). A linear combination of both trigonometric functions is chosen in order to provide two parameters ( $A$  and  $B$ ), which are maximal uncorrelated since the two functions are orthogonal to each other. Thus, the amplitude and the phase yield

$$\tilde{\epsilon} = \sqrt{A^2 + B^2} = \sqrt{0.2431^2 + 0.1121^2} = 0.2677 \pm 0.0137, \quad (4.8)$$

$$\tilde{\varphi} = \text{atan2}(B, A) = \text{atan2}(0.1121, 0.2431) = (0.432 \pm 0.052) \text{ rad}, \quad (4.9)$$

where  $\text{atan2}$  denotes the arctangent of the arguments  $A$  and  $B$  [34]. The amplitude corresponds to a typical value for the initial asymmetry of polarization state  $p_{+\xi}$ . The statistical error are

given by

$$\tilde{\sigma}_\epsilon^2 = \frac{A^2\sigma_A^2 + B^2\sigma_B^2}{A^2 + B^2}, \quad (4.10)$$

$$\tilde{\sigma}_\varphi^2 = \frac{B^2\sigma_A^2 + A^2\sigma_B^2}{(A^2 + B^2)^2}. \quad (4.11)$$

They are compatible with the Fisher information  $\sigma_\epsilon^{\text{th}} = \sqrt{2/N} = 0.014$  given the total number of events  $N_{\text{tot}} = 10107$ . A more detailed discussing of the statistical error can be found at end of this chapter.

Two assumptions must hold in order to determine and to unfold the asymmetry properly during a macroscopic time interval  $\Delta T_{\text{mac}}$ :

- The spin tune of the beam has to be stable during  $\Delta T_{\text{mac}}$ , otherwise the sinusoidal functional form of the event distribution would get smeared and thus the amplitude would be underestimated.
- The in-plane vector polarization should not drop too fast during a macroscopic turn interval  $\Delta n$ . This causes a false amplitude estimation because the depolarization effect is not linear. Generally speaking the spin coherence time (SCT) has to be large or the macroscopic time interval small enough.

## 4.2 Discrete Turn Fourier Transform

In this section, another analysis approach of the data is discussed by introducing the discrete time Fourier transform. It is more precise to speak of a discrete turn Fourier Transform (DTFT), since the measurement observable is based on a discrete integer turn number  $n$  and not on a time stamp. After a general overview about Fourier transforms a more detailed implementation of the DTFT regarding the signal processing is given.

### 4.2.1 Fourier Transform

The general principle of the Fourier Transform is well known and it is discussed in manifold topics. The continuous Fourier Transform of an integrable function  $f \in L^1(\mathbb{R}^n)$  is given by

$$\mathbb{F}(f)(t) = \frac{1}{(2\pi)^{\frac{n}{2}}} \int_{\mathbb{R}^n} f(x) e^{-it \cdot x} dx, \quad (4.12)$$

where  $dx$  is an  $n$ -dimensional volume element,  $i$  denotes the imaginary unit and  $x \cdot t$  represents the dot product between the vectors  $x$  and  $t$ . The inverse transformation yields

$$f(x) = \mathbb{F}^{-1} \hat{f}(x) = \int_{\mathbb{R}^n} \hat{f}(t) e^{-it \cdot x} dt, \quad (4.13)$$

Assuming a simple model of the spin motion  $\hat{f}$  corresponds to a 1-dimensional time periodic probability density function  $\hat{f}(t) = A \cos(\omega_s t + \varphi_s)$  (Eq. 4.1), where  $\omega_s$  is the angular spin precession frequency and  $\varphi_s$  denotes the phase of the spin oscillation. Hence the operator  $\mathbb{F}^{-1}$  transforms the signal from the time domain  $t$  into the frequency domain  $\omega$

$$f(\omega) = \int_{-\infty}^{\infty} \hat{f}(t) e^{-it \cdot \omega} dt. \quad (4.14)$$

### 4.2.2 Discrete Fourier Transform

As described in section 3.2.2 each detected event is assigned to a turn number  $n \in \mathbf{N}$ . Thus, the variable of  $\hat{f}$  becomes discrete. Mathematically this is related to the Delta comb, which is constructed by the sum of the Dirac delta functions  $\delta(t - \frac{n}{f_{\text{RF}}})$

$$\begin{aligned} f(\omega) &= \int_{-\infty}^{\infty} \sum_{n=0}^{\infty} \hat{f}(t) \delta\left(t - \frac{n}{f_{\text{RF}}}\right) e^{-it \cdot \omega} dt \\ &= \sum_{n=0}^{\infty} \hat{f}[n] e^{\frac{-in \cdot \omega}{f_{\text{RF}}}} \\ &= \sum_{n=0}^{\infty} \hat{f}[n] e^{\frac{-i2\pi n \cdot \omega}{\omega_{\text{RF}}}}, \end{aligned} \quad (4.15)$$

where the square brackets indicate that the argument of  $\hat{f}$  is discrete and  $f_{\text{RF}}$  represents the RF cavity frequency. With the relation  $\nu = \frac{\omega}{\omega_{\text{RF}}}$  Eq. 4.15 yields

$$f(\nu) = \sum_{n=0}^{\infty} \hat{f}[n] e^{-i2\pi n \cdot \nu} \quad (4.16)$$

$$\text{with } \hat{f}[n] = A \cos(2\pi\nu_s n + \varphi_s), \quad (4.17)$$

where  $\nu_s = \frac{\omega_s}{\omega_{\text{RF}}}$  denotes the spin tune. Given a finite measurement interval, a discrete causal rectangular window function  $w[n]$  is used to describe the data. Since a multiplication in the turn domain  $\hat{g}[n] = \hat{f}[n] \cdot \hat{w}[n]$  corresponds to a convolution in the spin tune domain  $g(\nu) = f(\nu) * w(\nu)$ , one obtains

$$\hat{w}[n] = \begin{cases} 0 & n < 0 \\ 1 & \text{for } 0 \leq n < N \\ 0 & n \geq N \end{cases} \quad (4.18)$$

$$\begin{aligned} g(\nu) &= f(\nu) * w(\nu) = (f * w)(\nu) \\ &= \int_{-\infty}^{\infty} f(\nu - \lambda) w(\lambda) d\lambda \\ &= \sum_{n=0}^{\infty} \hat{f}[n] \hat{w}[n] e^{-i2\pi n \cdot \nu} = \sum_{n=0}^{N-1} \hat{g}[n] e^{-i2\pi n \cdot \nu}, \end{aligned} \quad (4.19)$$

with the number of samples in the measurement interval  $N = \Delta n$ . The discrete Fourier transforms of both functions are well known and the running index of the sum goes from 0 to  $N - 1$  samples

$$f(\nu) = \frac{A}{2} (\delta(\nu - \nu_s) + \delta(\nu + \nu_s)), \quad (4.20)$$

$$w(\nu) = \sum_{n=0}^{N-1} e^{-i2\pi n \cdot \nu} = \frac{1 - e^{-i2\pi\nu N}}{1 - e^{-i2\pi\nu}}, \quad (4.21)$$

$$\begin{aligned} \Rightarrow g(\nu) &= \frac{A}{2} \int_{-\infty}^{\infty} (\delta(\lambda - \nu + \nu_s) + \delta(-\lambda + \nu + \nu_s)) \frac{1 - e^{-i2\pi\lambda N}}{1 - e^{-i2\pi\lambda}} d\lambda \\ &= \frac{A}{2} \left[ \frac{1 - e^{i2\pi(\nu_s - \nu)N}}{1 - e^{i2\pi(\nu_s - \nu)}} + \frac{1 - e^{i2\pi(\nu_s + \nu)N}}{1 - e^{i2\pi(\nu_s + \nu)}} \right]. \end{aligned} \quad (4.22)$$

In practice, it is not possible to generate a continuous distribution of  $g(\nu)$  since the difference between two adjacent values of  $\nu$  cannot be infinitesimally small. As a consequence, the values of  $\nu$  become discrete, and the sampling interval of the spin tune domain is given by  $\Delta\nu_k = \frac{1}{N}$  yielding  $\nu[k] = \nu_k = \Delta\nu_k, k = \frac{k}{N}$ , with  $k \in \mathbb{Z}$ . Thus, the equidistant and discrete sequence of

the turn signals is discretely transformed into the spin tune domain

$$\begin{aligned} g_{v_k} &= \sum_{n=0}^{N-1} \hat{g}[n] e^{-i2\pi n v_k} \\ &= \sum_{n=0}^{N-1} \hat{g}[n] [\cos(2\pi n v_k) - i \sin(2\pi n v_k)] , \end{aligned} \quad (4.23)$$

$$\text{with } v_k = \frac{k}{N} \text{ and } k \in [0, N-1], \quad (4.24)$$

where Euler's formula is used. The granularity of the spin tune values  $\Delta v_k$  depends on the turn number of the measurement interval  $\Delta n = N$ . The interval  $\Delta n$  can be artificially increased by adding zero entries at the beginning and the end. This decrease the spaces in the spin tune domain. The technique is called 'zero padding' and it generates smoother distributions of  $g_{v_k}$ . Thus, it is more likely to hit the true frequency by obtaining the maximal magnitude of the amplitude.

The experiment provides a sequence of signals  $\hat{g}[n]$ , which are based on random processes. The probability of detecting an event per one turn of the bunch is small  $\ll 1$  and consequently, most of the turn entries are zero

$$\hat{g}[n] = \begin{cases} 1 & \text{for } n = n(n_{\text{ev}}) \\ 0 & \text{else} . \end{cases} \quad (4.25)$$

Thus, it is not possible to obtain the exact turn distribution  $\hat{g}[n]$  from the retransformation of  $g_{v_k}$ . Consequently, the summation is given by the sequence of the total number of events  $n_{\text{ev}} \in [1, N_{\text{ev}}]$ . The discrete Fourier coefficients are given by the real and the imaginary part of  $g_{v_k}$

$$a_{v_k} = \Re(g_{v_k}) = \frac{2}{N_{\text{ev}}} \sum_{n_{\text{ev}}=1}^{N_{\text{ev}}} \cos(2\pi v_k n(n_{\text{ev}})) , \quad (4.26)$$

$$b_{v_k} = \Im(g_{v_k}) = \frac{2}{N_{\text{ev}}} \sum_{n_{\text{ev}}=1}^{N_{\text{ev}}} -\sin(2\pi v_k n(n_{\text{ev}})) . \quad (4.27)$$

The factor  $2/N_{\text{ev}}$  takes into account the normalization based on Parseval's theorem for real input data [35]. The amplitude and the phase yield

$$\epsilon_{v_k} = |g_{v_k}| = \sqrt{\Im(g_{v_k})^2 + \Re(g_{v_k})^2} = \sqrt{a_{v_k}^2 + b_{v_k}^2} , \quad (4.28)$$

$$\varphi_{v_k} = \arg(g_{v_k}) = \text{atan2}(\Im(g_{v_k}), \Re(g_{v_k})) = \text{atan2}(b_{v_k}, a_{v_k}) . \quad (4.29)$$

The statistical error of the amplitude is equal to the statistical error of real respectively the

imaginary part of  $g_{v_k}$ . Using Gaussian error propagation one gets

$$\begin{aligned}
 \sigma_{\epsilon_{v_k}} &= \sigma_{a_{v_k}} = \sigma_{b_{v_k}} = \sigma_{\text{DFT}} \\
 &= \frac{2}{N_{\text{ev}}} \sqrt{\sum_{n_{\text{ev}}=1}^{N_{\text{ev}}} (\cos(2\pi v_k n(n_{\text{ev}})))^2} \\
 &= \frac{2}{N_{\text{ev}}} \sqrt{\sum_{n_{\text{ev}}=1}^{N_{\text{ev}}} (\sin(2\pi v_k n(n_{\text{ev}})))^2} \\
 &= \sqrt{\frac{2}{N_{\text{ev}}}}.
 \end{aligned} \tag{4.30}$$

Accordingly, the statistical error of the phase is given by

$$\sigma_{\varphi_{v_k}}^2 = \frac{\sigma_{\text{DFT}}^2}{\epsilon_{v_k}^2}, \tag{4.31}$$

where the identities 4.30 are used. The statistical error scales reciprocally with the amplitude, which is in conformity with the theoretical derivation based on the Cramér-Rao bound of a sinusoidal oscillation. Thus, for larger amplitude values the phase estimation becomes more precise.

### 4.3 Parameter Estimation

Both methods discussed in the previous sections provide two independent parameter estimators  $\tilde{A}(\tilde{a}_{\nu_k})$  and  $\tilde{B}(\tilde{b}_{\nu_k})$ . In the case of the mapping method, the estimators correspond to the orthogonal, i.e. independent, parameters of the asymmetry fit shown in Fig. 4.3. For the discrete turn Fourier transform  $\tilde{A}$  and  $\tilde{B}$  the parameters are simply given by the Fourier coefficients, which are orthogonal, as well. In the following, the estimation of the amplitude, the phase, and the spin tune are discussed in a more general way. Afterwards, a more detailed discussion is addressed by an individual chapter for each parameter, where in particular systematic effects of the estimators are considered.

Suppose two independent and Normally distributed random variables  $A$  and  $B$ . Then the estimated amplitude reads

$$\tilde{\epsilon} = \sqrt{\tilde{A}^2 + \tilde{B}^2} \geq \epsilon = \sqrt{A^2 + B^2}. \quad (4.32)$$

It is biased in the positive direction since it is defined as the square root of the sum of the squares of the variables (Eq. 4.28 and Eq. 4.8). Even though the estimators  $\tilde{A}$  and  $\tilde{B}$  are consistent, asymptotic Normal, efficient and unbiased, the amplitude is systematically overestimated, which becomes more and more significant for small amplitudes and low statistics.

In order to provide a better understanding of this effect, a set of turn numbers  $n$  is generated by Monte Carlo simulations with  $N_0 = 500$  events according to

$$p_n^{\nu_s}(n; \epsilon, \nu_s, \varphi_{\nu_s}) = \frac{1}{\Delta n} [1 \pm \epsilon_0 \sin(2\pi\nu_s n + \varphi_{\nu_s})], \quad n \in (0, \Delta n), \quad (4.33)$$

where  $\nu_s$  denotes the spin tune and  $\Delta n = 2 \times 10^6$  is the measurement interval.

#### Amplitude Estimator

For the simulation, two different true amplitude values ( $\epsilon_{0,\text{red}} = 0.05$  and  $\epsilon_{0,\text{black}} = 0.5$ ) are chosen. The true phase value is fixed to  $\varphi_s = -1$ . The corresponding distributions of 2500 estimators are shown in Fig. 4.4 for the variables  $\tilde{A}$  and  $\tilde{B}$  as well as for the amplitude and the phase.

The randomly generated data is analyzed by the discrete turn Fourier transform 4.2. Note that the spin tunes for the analysis and for the random data generation are exactly the same. The upper plots of Fig. 4.4 show the distributions of the Fourier coefficients. Both distributions correspond to a Normal distribution since the number of randomly generated events for each estimator is large  $N_0 = 500$  (asymptotic normality and consistent 2.1.3). However, the amplitude estimator is biased, which becomes obvious for small true amplitudes. An example is given by the distribution shown in red in the lower left-hand side of Fig. 4.4, where the true amplitude is set to  $\epsilon = 0.05$  and the mean value of  $\tilde{\epsilon}$  yields

$$\hat{\epsilon}_{\text{mean}} = \langle \tilde{\epsilon} \rangle = 0.09 > \epsilon = 0.05. \quad (4.34)$$

Note, that although the amplitude estimator is biased, it is consistent and asymptotic normal,

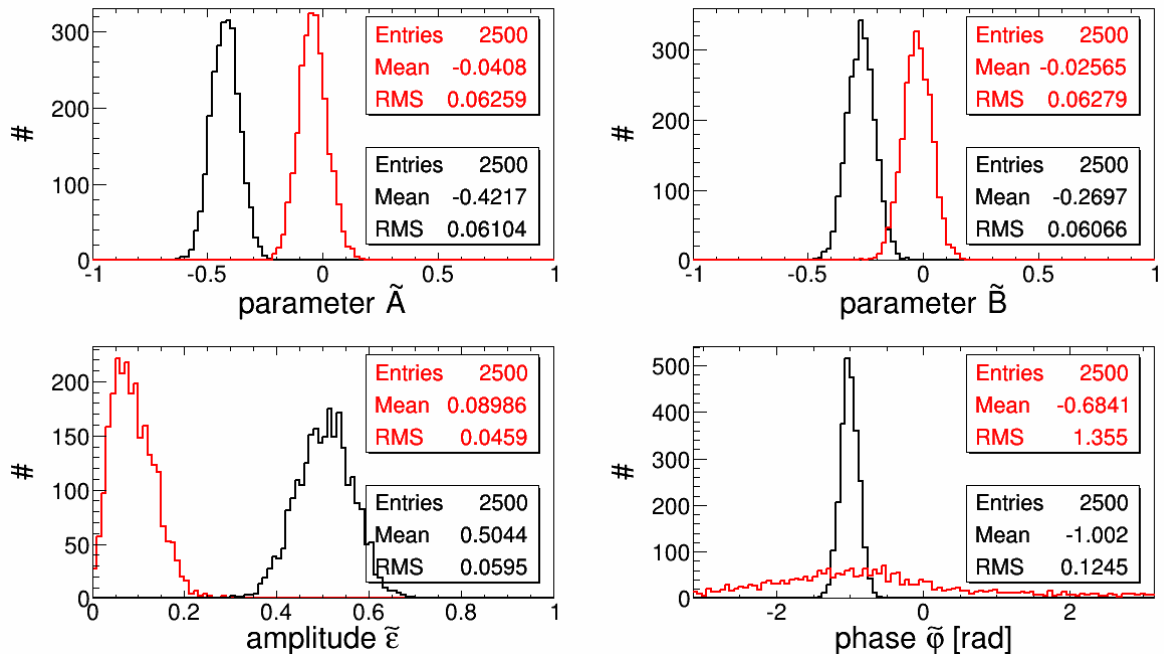


Figure 4.4: Upper two plots: distributions of the estimator of the parameter  $A$  and  $B$  based on random data analyzed by the discrete turn Fourier transform. The true amplitude value is set to  $\epsilon = 0.05$  (red) and  $\epsilon = 0.5$  (black), whereas the phase is fixed to  $\varphi_s = -1$ . Lower plots: distribution of the amplitude and phase estimator obtained by  $\tilde{A}$  and  $\tilde{B}$ .

since it converges to the true value for sufficient large statistics  $\hat{\epsilon}_{\text{mean}} \xrightarrow{N_0 \rightarrow \infty} \epsilon$ . The underlying distribution is called Rice distribution. In chapter 5 its characteristics and implications will be discussed. In particular, several approaches are presented to reduce the systematic bias of the amplitude estimator and to determine a proper confidence interval.

### Phase Estimator

Since the phase is defined on a  $2\pi$  interval ambiguities exists for  $-\pi$  and  $\pi$ . In chapter 6 it is shown that the DTFT phase estimator is unbiased if the theory of directional statistics is taken into account. Latter takes into account the phase jump by wrapping the probability density function around the circumference of a unit circle. In addition, its probability density function yields a non-Gaussian distribution. Thus, in the case of a small true amplitude (lower-right hand side plot), the first moment of the unwrapped distribution represents a biased estimator  $\hat{\varphi}_{\text{mean}} = \langle \tilde{\varphi}_s \rangle \neq \varphi_s$ . However, for large true amplitudes or high statistics, the mean value of the phase distribution becomes consistent, asymptotic normal and unbiased. This is represented by the distributions, which is shown on lower right-hand side plot of Fig. 4.4 in black.

An overview of the amplitude and phase parameters respectively estimators can be found in table 4.1. One observes, that even for relatively large true amplitudes the estimator of the amplitude is biased within its standard error (error on the mean), whereas the phase estimator

becomes unbiased.

$\epsilon$	$\langle \tilde{\epsilon} \rangle$	$\varphi_s$ [rad]	$\langle \tilde{\varphi}_s \rangle$ [rad]
0.05	$0.900 \pm 0.001$	-1	$-0.684 \pm 0.027$
0.5	$0.504 \pm 0.001$	-1	$-1.002 \pm 0.003$

Table 4.1: Mean value and the standard deviation of the estimated amplitude and phase compared to the true ones

Henceforward two different notations are used for the amplitude and the phase estimator, respectively:

- The amplitude estimator obtained by the mapping or the discrete Fourier transform is indicated by  $\tilde{\epsilon}$  (phase  $\tilde{\varphi}_s$ ).
- A more sophisticated estimator, which considers the systematic positive bias or the wrapped probability density function, is denoted by  $\hat{\epsilon}$  (phase  $\hat{\varphi}_s$ ).

### Spin Tune Estimator

The spin tune is determined by taking into account the phase information or rather the turn derivative of the phase. This becomes obvious in Eq. 4.28, where the phase parameter depends on the spin tune, which is chosen to obtain the Fourier coefficients Eq. 4.26. The relation of phase and angular frequency yields

$$\omega_s(n) = 2\pi\nu_s(n) = \frac{d\varphi_s(n)}{dn}, \quad (4.35)$$

where  $n$  denotes the turn number of the bunch. Thus, the spin tune is determined from the interpolation of two consecutive phase estimators. In the case of a known functional form of the turn depending phase, the change of the spin tune is proportional to the turn derivative of this function. A more detailed discussion of the spin tune determination is given in chapter 6.

#### 4.3.1 Standard Error Estimation

The Cramér-Rao bound 2.1.4 represents the lower bound of the standard error of an estimator  $\sigma_\theta$  or a vector of estimators  $\sigma_\theta$ . It is given by the inverse of the Fisher information. For the probability density function of the spin precession it yields

$$\mathcal{I}(\varphi_s, \nu_s, \epsilon) = - \int_0^{\Delta n} \frac{\partial^2}{\partial \theta^2} \log p_s(n; \nu_s, \varphi_s, \epsilon) p_s(n; \nu_s, \varphi_s, \epsilon) dn, \quad (4.36)$$

where  $\epsilon$  denotes the amplitude,  $\varphi_s$  the phase, and  $\nu_s$  the spin tune.

The analytical solution of the integral in Eq. 4.36 is discussed in appendix A.2 and the Fisher

information matrix reads

$$\mathcal{I}(\varphi_s, \nu_s, \epsilon) = \begin{pmatrix} 1 - \sqrt{1 - \epsilon^2} & \frac{\pi}{2} \Delta n \epsilon^2 & 0 \\ \frac{\pi}{2} \Delta n \epsilon^2 & \frac{4\pi^2}{3} \Delta n^2 (1 - \sqrt{1 - \epsilon^2}) & 0 \\ 0 & 0 & \frac{1}{\sqrt{1 - \epsilon^2}} - 1 \end{pmatrix}. \quad (4.37)$$

Furthermore, the covariance matrix is given by the inverse of the Fisher information matrix 2.17

$$\begin{aligned} \text{cov}(\varphi_s, \nu_s, \epsilon) &= (\mathcal{I}(\varphi_s, \nu_s, \epsilon))^{-1} \\ &= \begin{pmatrix} \frac{1 - \sqrt{1 - \epsilon^2}}{2 - 2\sqrt{1 - \epsilon^2} - \epsilon^2 - \frac{3\epsilon^4}{16}} & -\frac{3\epsilon^2}{8\pi\Delta n(2 - 2\sqrt{1 - \epsilon^2} - \epsilon^2 - \frac{3\epsilon^4}{16})} & 0 \\ -\frac{3\epsilon^2}{8\pi\Delta n(2 - 2\sqrt{1 - \epsilon^2} - \epsilon^2 - \frac{3\epsilon^4}{16})} & \frac{3(1 - \sqrt{1 - \epsilon^2})}{4\pi^2\Delta n^2(2 - 2\sqrt{1 - \epsilon^2} - \epsilon^2 - \frac{3\epsilon^4}{16})} & 0 \\ 0 & 0 & \frac{\epsilon^2\sqrt{1 - \epsilon^2}}{1 - \sqrt{1 - \epsilon^2}} \end{pmatrix} \\ &\approx \begin{pmatrix} \frac{8}{\epsilon^2} & -\frac{12}{2\pi\Delta n\epsilon^2} & 0 \\ -\frac{12}{2\pi\Delta n\epsilon^2} & \frac{24}{4\pi^2\Delta n^2\epsilon^2} & 0 \\ 0 & 0 & 2 \end{pmatrix}. \end{aligned} \quad (4.38)$$

The latter transformation takes into account the Taylor series expanded at small amplitudes  $\epsilon \ll 1$ .

One observes, that the lower bound of the standard error of the phase and of the spin tune scale with the inverse of the amplitude. Additionally, latter depends reciprocally on the length of the macroscopic turn interval. Since the estimators are asymptotic Normal, all standard errors scale with the inverse of the square root of the number of events  $N_0$  detected during the macroscopic turn interval  $\Delta n$  (see Eq. 2.7). If the phase nor the spin tune are *a priori* unknown, the lower bounds of the standard errors yield

$$\sigma_{\tilde{\varphi}_s}^{\text{CRB}} = \sqrt{\frac{1 - \sqrt{1 - \epsilon^2}}{N_0(2 - 2\sqrt{1 - \epsilon^2} - \epsilon^2 - \frac{3\epsilon^4}{16})}} \approx \sqrt{\frac{8}{\epsilon^2 N_0}}, \quad (4.39)$$

$$\sigma_{\tilde{\nu}_s}^{\text{CRB}} = \sqrt{\frac{3(1 - \sqrt{1 - \epsilon^2})}{4\pi^2\Delta n^2 N_0(2 - 2\sqrt{1 - \epsilon^2} - \epsilon^2 - \frac{3\epsilon^4}{16})}} \approx \sqrt{\frac{24}{4\pi^2\epsilon^2\Delta n^2 N_0}}, \quad (4.40)$$

$$\sigma_{\tilde{\epsilon}}^{\text{CRB}} = \sqrt{\frac{\epsilon^2\sqrt{1 - \epsilon^2}}{N_0(1 - \sqrt{1 - \epsilon^2})}} \approx \sqrt{\frac{2}{N_0}}. \quad (4.41)$$

In the case of the mapping method or the discrete turn Fourier transform the spin tune is fixed and subsequently, it is assumed to be known. Therefore, the Fisher information matrix 4.37 reduces to 2 dimensions depending on the estimator vector  $\tilde{\boldsymbol{\theta}} = (\tilde{\varphi}_s, \tilde{\epsilon})$ . Thus, the standard

errors become

$$\text{if } \nu_s \text{ is known: } \sigma_{\tilde{\varphi}_s}^{\text{CRB}, \nu_s} = \sqrt{\frac{1}{N_0(1 - \sqrt{1 - \epsilon^2})}} \approx \sqrt{\frac{2}{\epsilon^2 N_0}}, \quad (4.42)$$

$$\text{if } \varphi_s \text{ is known: } \sigma_{\tilde{\nu}_s}^{\text{CRB}, \varphi_s} = \sqrt{\frac{3}{N_0 4\pi^2 \Delta n^2 (1 - \sqrt{1 - \epsilon^2})}} \approx \sqrt{\frac{6}{4\pi^2 \Delta n^2 \epsilon^2 N_0}}. \quad (4.43)$$

Hence, it is possible to compare the lower bounds of the standard errors  $\sigma_{\tilde{\theta}}^{\text{CRB}}$  with the standard deviations of the estimator distributions obtained by the MC data  $\sigma_{\tilde{\theta}}^{\text{MC}}$ . The latter can be found in Fig. 4.4. In other words, it can be tested, if the second moment of the MC distributions represents a biased estimator of the standard error of the respective parameter  $\tilde{\theta} = (\tilde{\varphi}_s, \tilde{\epsilon})$ . The results are shown in table 4.2, where the MC data is compared with the exact evaluation of  $\sigma_{\tilde{\theta}}^{\text{CRB}}$  and with the solution obtained for the Taylor expand ( $\epsilon \ll 1$ ). One sees, that for a true

$\epsilon$	$\sigma_{\tilde{\epsilon}}$			$\sigma_{\tilde{\varphi}_s} [\text{rad}]$		
	MC data	exact	Taylor	MC data	exact	Taylor
0.5	0.060	0.057	0.063	0.125	0.122	0.127
0.05	0.050	0.063	0.063	1.355	1.27	1.27

Table 4.2: First and second of the estimated amplitude and phase compared to the true ones

amplitude of  $\epsilon = 0.5$  the second moment of the MC distribution lies in between the exact and the Taylor solution. Thus, both results  $\sigma_{\tilde{\varphi}_s}^{\text{MC}}$  and  $\sigma_{\tilde{\epsilon}}^{\text{MC}}$  are biased estimators of the standard error of the respective parameters. Additionally, the Taylor series expand provides a significant deviation from the exact value of the standard error.

However, in the case of  $\epsilon = 0.05$  the Taylor solution coincides almost with the exact result. Here, the MC data provides a smaller estimator of the amplitude standard error  $\sigma_{\tilde{\epsilon}}^{\text{MC}} < \sigma_{\tilde{\epsilon}}^{\text{CRB}}$  since the distribution of  $\tilde{\epsilon}$  is asymmetric (lower left plot in Fig. 4.4). The second moment of the MC distribution overestimates the standard error of the phase  $\sigma_{\tilde{\varphi}_s}^{\text{MC}} > \sigma_{\tilde{\varphi}_s}^{\text{CRB}}$  since it is defined in the interval  $\tilde{\varphi}_s \in (-\pi, \pi]$ .

### 4.3.2 Conclusion

In the previous sections, it was shown, that the probability density function of the amplitude  $\tilde{\epsilon}$  and the phase estimator  $\tilde{\varphi}_s$  are not Normally distributed. Thus, their first and second moments are biased estimators of the true value and its standard error, respectively. A more detailed discussion is given in the chapters 5 and 6.

## 4.4 Probability Density Function

In order to describe the probability of a particle being detected in the up or down detector, the probability density function of the turn number  $p_n(n)$  has to be identified. So far, the spin precession frequency is assumed to be the same for all particles, i.e. the conditional probability function of the turn number, which depends on the spin tune  $\nu_s$ , yields

$$p_n^{\nu_s}(n; \epsilon, \nu_s, \varphi_{\nu_s}) = \frac{1}{\Delta n} [1 \pm \epsilon_0 \sin(2\pi\nu_s n + \varphi_{\nu_s})], \quad n \in (0, \Delta n), \Delta n \mathbb{Z}, \quad (4.44)$$

where  $\varphi_{\nu_s}$  denotes the phase of the spin tune and  $\epsilon_0 = |A_y^d| P_{\xi}$  corresponds to the analyzing power times the fraction of the vector polarized particles of the ensemble.

Note that for the probability density function in Eq. 4.44 the spin tune is assumed to be known and it is identical for all particles. Thus,  $p_n^{\nu_s}(n; \epsilon, \nu_s, \varphi_s)$  corresponds to the conditional probability density distribution of the turn number  $n$  given the occurrence of a fixed spin tune  $\nu_s$ . The two detector quadrants are considered by the indices plus and minus and the phase shift between both detectors is assumed to be exactly  $\pi$ . The normalization factor is approximately given by  $1/\Delta n$ , since the measurement interval is large compared to one revolution of the particle bunch. Thus, the contribution of the oscillation term is negligible. In addition, the parameter  $\epsilon_0$  corresponds to the initial vector polarization, which is provided by the atomic source.

### Turn Depending Spin Tune

The turn depending spin tune  $\nu_s(n)$  can be derived by the definition of the angular frequency. Latter is defined as the derivation of the phase with respect to the turn number and it is identical to the spin tune change corrected by the factor  $2\pi$ . Thus, the turn depending variation of the phase of the ensemble  $\delta\varphi_s(n)$  determines the change of the angular frequency

$$\delta\nu_s(n) = \frac{1}{2\pi} \delta\omega_{\nu_s}(n) = \frac{1}{2\pi} \frac{d\delta\varphi_{\nu_s}(n)}{dn}. \quad (4.45)$$

The turn depending spin tune yields

$$\nu_s(n) = \nu_s^0 + \delta\nu_s(n) = \nu_s^0 + \frac{1}{2\pi} \frac{d\delta\varphi_{\nu_s}(n)}{dn}. \quad (4.46)$$

The quantity  $\nu_s^0$  corresponds to the initial spin tune. Note that  $\varphi_{\nu_s}$  corresponds to the phase of the spin tune and not to the phase of the spin precession  $\varphi_s$  since the spin tune is defined by

the ratio of the spin precession frequency  $f_s$  and the RF cavity frequency  $f_{\text{RF}}$

$$\nu_s = \frac{f_s}{f_{\text{RF}}}, \quad (4.47)$$

$$\begin{aligned} \Rightarrow \frac{\Delta \nu_s}{\nu_s} &= \frac{\Delta f_s}{f_s} - \frac{\Delta f_{\text{RF}}}{f_{\text{RF}}} \\ &= \frac{\frac{\partial \varphi_s}{\partial t}}{2\pi f_s} - \frac{\frac{\partial \varphi_{\text{RF}}}{\partial t}}{2\pi f_{\text{RF}}} = \frac{1}{2\pi \nu_s} \frac{\partial \varphi_{\nu_s}}{\partial n} \end{aligned} \quad (4.48)$$

In the following, the phase of the spin tune is denoted by  $\varphi_s$ .

#### 4.4.1 Marginal Probability Density Function of Spin Tune and Phase

Suppose that the spin tunes of the individual particles of the ensemble are distributed. In addition, the spin tune of the particle on the reference orbit is defined as  $\nu_s^{\text{ref}}$ . In good approximation, the marginal probability density distribution of  $\nu_s$  can be described by a Rayleigh distribution [36]

$$p_{\nu_s}(\nu_s; \nu_s^{\text{ref}}, \sigma_{R,\nu_s}) = \frac{\nu_s - \nu_s^{\text{ref}}}{\sigma_{R,\nu_s}^2} e^{-\frac{(\nu_s - \nu_s^{\text{ref}})^2}{2\sigma_{R,\nu_s}^2}}, \quad \text{for } \nu_s \geq \nu_s^{\text{ref}}. \quad (4.49)$$

The scale parameter  $\sigma_{R,\nu_s}$  indicates the width of the distribution, i.e. for larger  $\sigma_{R,\nu_s}$  the spin tune spread of the ensemble is wider. The expectation value of the Rayleigh distribution corresponds to the mean spin tune of the ensemble and it reads

$$\mu_{\nu_s} = E(\nu_s) = \nu_s^{\text{ref}} + \sqrt{\frac{\pi}{2}} \sigma_{R,\nu_s}. \quad (4.50)$$

It is assumed turn invariant if the orbit of each particle and the bending magnets are stable over time. Note that for the time depending drifts the parameters of the spin tune model become turn depending. It is possible to distinguish between a global shift of the spin tunes  $\nu_s^{\text{ref}}(n)$  and a time depending widening of the spin tune distribution  $\sigma_{R,\nu_s}(n)$ . Latter induces a faster depolarization, whereas the global shift has no impact on the amplitude spectrum.

The turn dependent phase shift of the spins between each particle  $i$  and the reference particle is given by

$$\varphi_{s,i}(n) = 2\pi(\nu_{s,i} - \nu_s^{\text{ref}})n, \quad \text{for } \nu_s \geq \nu_s^{\text{ref}}. \quad (4.51)$$

It is important to note that the phase provides an unambiguity at  $2\pi$ . Consequently, the theory

of directional statistics is applied to identify the wrapped probability density function [22]

$$p_{\varphi_s}^w(\varphi_s; \sigma_{R, \nu_s}, n) = \sum_{k=0}^{\infty} \frac{1}{4\pi^2 n^2 \sigma_{R, \nu_s}^2} (\varphi_s + 2\pi k) e^{-\frac{1}{4\pi^2 n^2 2\sigma_{R, \nu_s}^2} (\varphi_s + 2\pi k)^2}, \quad (4.52)$$

$$p_{\varphi_s}^w(\varphi_s; \sigma_{\varphi_s}(n)) = \sum_{k=0}^{\infty} \frac{1}{2\sigma_{\varphi_s}^2(n)} (\varphi_s + 2\pi k) e^{-\frac{1}{4\sigma_{\varphi_s}^2(n)} (\varphi_s + 2\pi k)^2} \quad (4.53)$$

$$\begin{aligned} \Rightarrow p_{\varphi_s}^w(z; \sigma_{\varphi_s}(n)) &= \frac{1}{\pi} \sum_{t=-\infty}^{\infty} \phi_{\text{Ray}}\left(t, \frac{\sigma_{\varphi_s}(n)}{\sqrt{2}}\right) e^{-it\varphi_s} \\ &= \frac{1}{\pi} \sum_{t=-\infty}^{\infty} \left(1 - \sqrt{\pi} \sigma_{\varphi_s}(n) t e^{-\sigma_{\varphi_s}^2(n) t^2} [\operatorname{erfi}(\sigma_{\varphi_s}(n) t) - i]\right) e^{ik\varphi_s}, \end{aligned} \quad (4.54)$$

where  $\operatorname{erfi}$  denotes the imaginary error function and  $z = e^{i\varphi}$  is the circular variable. In fact,  $p_{\varphi_s}^w$  corresponds to a wrapped Rayleigh distribution truncated at  $2\pi$  with the phase scale parameter  $\sigma_{\varphi_s}(n) = \sqrt{2\pi n} \sigma_{R, \nu_s}$ . It can be expressed by the characteristic function of its unwrapped distribution  $\phi_{\text{Ray}}$  [22] (Eq.2.26).

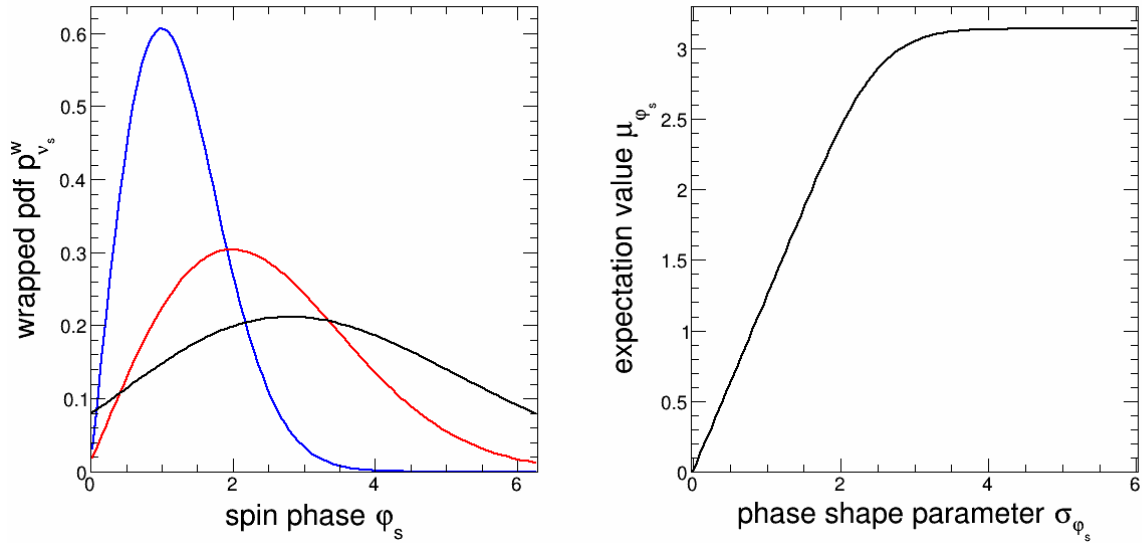


Figure 4.5: Left: wrapped probability density function of the phase for three different phase scale parameters (blue:  $\sigma_{\varphi_s} = 1$ ; red:  $\sigma_{\varphi_s} = 2$ ; black:  $\sigma_{\varphi_s} = 3$ ). Right: average phase of the ensemble as a function of the phase scale parameter.

For a larger scale parameter, the particle spins are distributed more uniformly since they are wrapped at  $2\pi$ . Consequently, the average phase of the ensemble increases. Latter can be

identified by the first moment of the wrapped Rayleigh distribution [22]

$$\begin{aligned}
 \langle z^{k=1} \rangle &= \int_0^{2\pi} p_{\varphi_s}^w(z; \sigma_{\varphi_s}(n)) e^{i\varphi_s} d\varphi_s \\
 &= \phi_{\text{Ray}}(k=1, \sigma_{\varphi_s}(n)) \\
 &= 1 - \sqrt{\pi} \sigma_{\varphi_s}(n) e^{-\sigma_{\varphi_s}^2(n)} [\operatorname{erfi}(\sigma_{\varphi_s}(n)) - i], \quad (4.55)
 \end{aligned}$$

which can be expressed in terms of the characteristic function evaluated at the integer parameter  $k = 1$ . Taking the argument of 4.55 leads to the mean phase of the ensemble

$$\begin{aligned}
 \mu_{\varphi_s}(\sigma_{\varphi_s}(n)) = \arg(\langle z^{k=1} \rangle) &= \frac{\pi}{2} - \arctan\left(\frac{1 - \sqrt{\pi} \sigma_{\varphi_s}(n) e^{-\sigma_{\varphi_s}^2(n)} \operatorname{erfi}(\sigma_{\varphi_s}(n))}{\sqrt{\pi} \sigma_{\varphi_s}(n) e^{-\sigma_{\varphi_s}^2(n)}}\right) \\
 &= \frac{\pi}{2} - \arctan\left(\frac{1}{\sqrt{\pi}} \frac{e^{\sigma_{\varphi_s}^2(n)}}{\sigma_{\varphi_s}(n)} - \operatorname{erfi}(\sigma_{\varphi_s}(n))\right), \quad (4.56)
 \end{aligned}$$

which is plotted on the right hand side of Fig. 4.5. One observes that the expectation value of the phase starts at zero, is strictly monotonically increasing and converges to  $\pi$  for large phase scale parameter. Thus, the phase of the ensemble performs a half rotation in the horizontal plane.

The analytical expression of the expectation value of the phase as a function of the turn number and the spin tune scale parameter can be derived by using joint bivariate probability density functions. This is presented in the following sections.

#### 4.4.2 Joint Bivariate Probability Density Function

The joint bivariate probability density function based on the turn number and the spin tune is given by the product of the conditional probability distribution  $p_n^{v_s}$  and the marginal pdf of the spin tune  $p_{v_s}$  (Bayes' theorem)

$$\begin{aligned}
 p_{n, v_s}(n, v_s; \epsilon, \varphi_s, \sigma_{R, v_s}, v_s^{\text{ref}}) &= p_n^{v_s}(n; \epsilon, v_s, \varphi_s) \cdot p_{v_s}(v_s; \sigma_{R, v_s}, v_s^{\text{ref}}) \\
 &= \frac{(v_s - v_s^{\text{ref}})}{\Delta n \sigma_{R, v_s}^2} e^{-\frac{(v_s - v_s^{\text{ref}})^2}{2\sigma_{R, v_s}^2}} \cdot (1 \pm \epsilon \sin[2\pi v_s n + \varphi_s]), \quad (4.57) \\
 &\text{with } n \in (0, \Delta n) \text{ and } v_s \geq v_s^{\text{ref}}.
 \end{aligned}$$

An example of Eq. 4.57 is given in Fig 4.6 for the parameters  $\Delta n = 10^6$  turns,  $v_s^{\text{ref}} = 0.1609$ ,  $\sigma_{R, v_s} = 10^{-4}$ ,  $\epsilon = 0.25$  and  $\varphi_s = 0$ . The values of the y-axis are shifted by the reference spin tune  $v_s^{\text{ref}}$ . The turn axis is cut into three pieces and each interval covers 50 turns and each gap corresponds to 25000 turns.

For small turn numbers, the probability density function shows a sinusoidal pattern weighted by the Rayleigh distribution. The period of this structure is given by  $1/v_s^{\text{ref}} \approx 6.2$  turns. In the second interval, the initial vertical elliptical-like bands are tilted towards the left side, since the spin tune increases in the direction of the y-axis. Consequently, the period of the spin

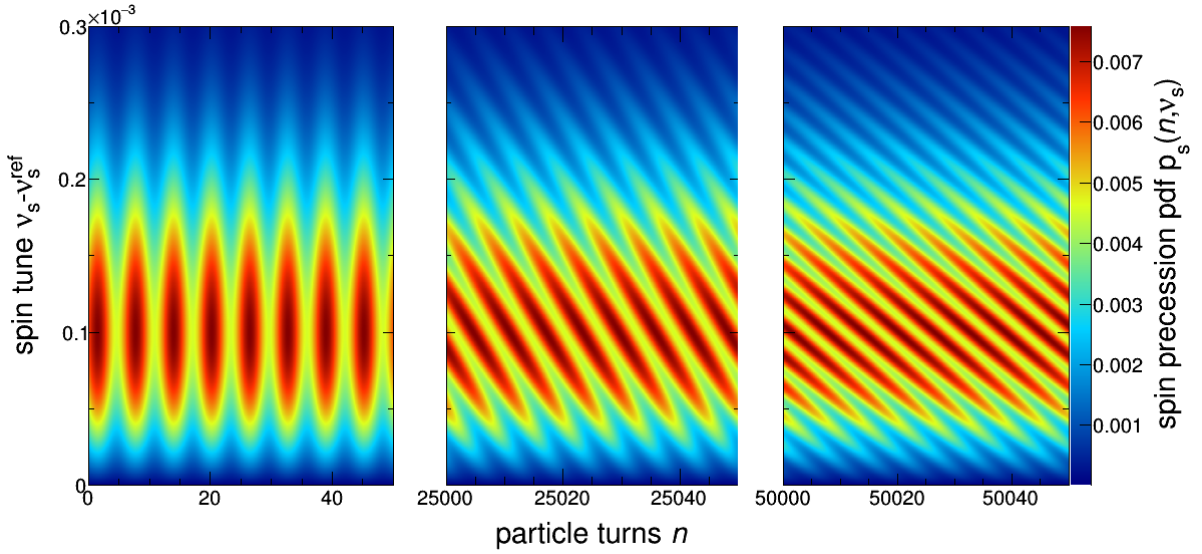


Figure 4.6: Joint bivariate probability density function of the turn number and the spin tune  $p_{n,\nu_s}$  (4.57). The x-axis (number of particle turns) is cut into three intervals and each lasts for 50 turns. The size of the gaps is set to 25000 turns. The parameters are set to  $\Delta n = 10^6$  turns,  $\nu_s^{\text{ref}} = 0.1609$ ,  $\sigma_{R,\nu_s} = 10^{-4}$ ,  $\epsilon = 0.25$  and  $\varphi_s = 0$ . The values on the y-axis are shifted by the reference spin tune  $\nu_s^{\text{ref}}$ .

precession decreases

$$T_s(\nu_s) = \frac{1}{f_{\text{cyc}}(\nu_s^{\text{ref}} + \nu_s)} \leq T_s^{\text{ref}} = \frac{1}{f_{\text{cyc}}\nu_s^{\text{ref}}}, \quad \text{for } \nu_s \geq 0, \quad (4.58)$$

which leads to a smooth rotation towards the left direction. In the last interval of Fig. 4.57 this process is further advanced.

#### 4.4.3 Marginal Probability Density Function of Turn Number

Since the observable of the experiment is given by the turn number  $n$ , it is of major interest to identify its marginal probability density function  $p_n(n)$ , which corresponds to the probability of a particle being detected at a given turn number. The integration of  $p_{n,\nu_s}$  with respect to the spin tune is derived in appendix A.3 yielding

$$p_n(n) = \int_0^\infty p_{n,\nu_s}(n, \nu_s) d\nu_s \quad (4.59)$$

$$= \frac{1}{\Delta n} \left[ 1 + \epsilon_0 \left( \left[ 1 - \sqrt{\pi} \gamma_s(n) e^{-\gamma_s^2(n)} \text{erfi}(\gamma_s(n)) \right]^2 + \pi \gamma_s^2(n) e^{-2\gamma_s^2(n)} \right)^{\frac{1}{2}} \times \right. \\ \left. \sin \left[ \Omega_s(n) + \frac{\pi}{2} - \arctan \left( \frac{e^{\gamma_s^2(n)}}{\sqrt{\pi} \gamma_s(n)} - \text{erfi}(\gamma_s(n)) \right) \right] \right], \quad (4.60)$$

where  $\text{erfi}$  denotes the imaginary error function. The fundamental oscillation is given by the spin tune  $\nu_s$  and the phase  $\varphi_s$

$$\Omega_s(n) = 2\pi\nu_s n + \varphi_s. \quad (4.61)$$

The turn depending damping term is defined by the spin tune spread  $\sigma_{R,\nu_s}$

$$\gamma_s(n) = \sqrt{2\pi}\sigma_{R,\nu_s} n. \quad (4.62)$$

For a vanishing width of the spin tune distribution  $\sigma_{R,\nu_s} = \gamma_s(n) = 0$ , the marginal pdf reduces to  $p_n^{\nu_s}(n)$  (Eq. 4.44), which makes perfect sense. For large turn numbers, the perturbation term converges to  $-\epsilon_0 \sin(2\pi\nu_s n)$  because of the infinity limit identity

$$\sqrt{\pi} x e^{-x^2} \text{erfi}(x) \underset{x \rightarrow \infty}{=} 1. \quad (4.63)$$

Consequently, the probability density function becomes constant  $p_n(n) = \frac{1}{\Delta n}$  and the oscillation vanishes since the individual spins are distributed Uniformly. In fact,  $p_n(n)$  corresponds to the integral of the vertical projections of the joint bivariate probability function given in Fig. 4.6. An example of the marginal pdf of the turn number is shown in Fig. 4.7 with the same parameters used in Fig 4.6. In this representation, the oscillations are not visible since the precession is fast. The marginal pdf oscillates around the reciprocal of the macroscopic turn interval  $1/\Delta n$ , which coincides with the infinite limit.

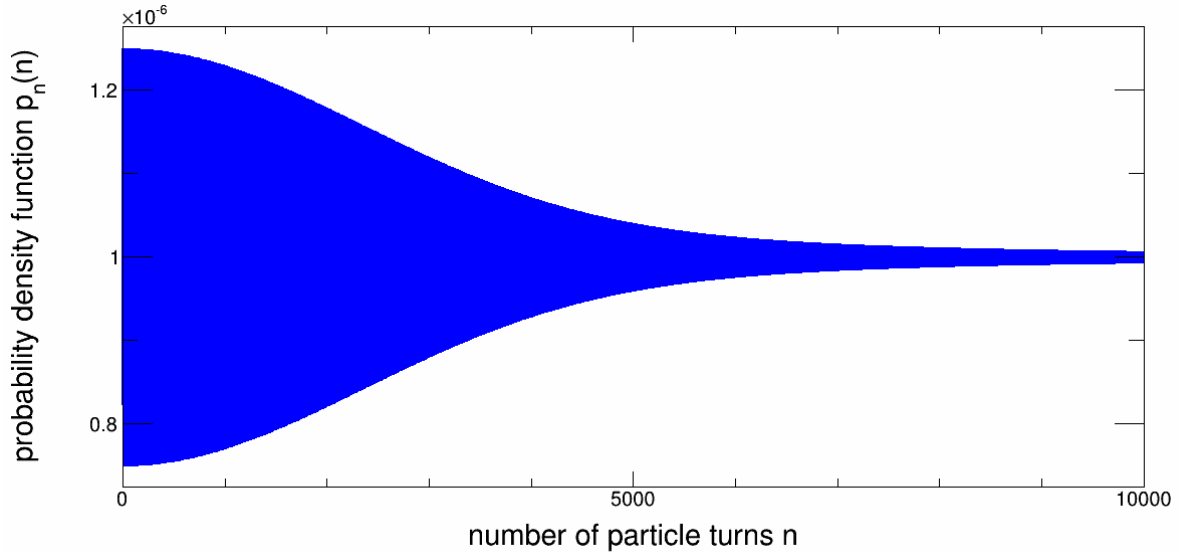


Figure 4.7: Marginal probability density function of the turn number  $p_n(n)$  for the first 10000 particle turns with the parameters  $\Delta n = 10^6$  turns,  $\nu_s^{\text{ref}} = 0.1609$ ,  $\sigma_{R,\nu_s} = 10^{-4}$ ,  $\epsilon_0 = 0.25$  and  $\varphi_s = 0$ .

Furthermore, one observes a decreasing amplitude of the oscillation, since the particle spins decohere. The envelope is simply given by the amplitude term in Eq. 4.60. It's turn depending

functional form yields

$$\epsilon(\gamma_s(n)) = \epsilon_0 \left( \left[ 1 - \sqrt{\pi} \gamma_s(n) e^{-\gamma_s^2(n)} \operatorname{erfi}(\gamma_s(n)) \right]^2 + \pi \gamma_s^2(n) e^{-2\gamma_s^2(n)} \right)^{\frac{1}{2}}. \quad (4.64)$$

This allows to specify the spin coherence time  $\tau_{\text{SCT}}$  as a function of the spin tune spread  $\sigma_{R,\nu_s}$ . Former is defined as the moment in time where the amplitude reaches  $1/e$  of its initial value. The relation between  $\tau_{\text{SCT}}$  and  $\sigma_{R,\nu_s}$  is obtained by solving numerically the equation

$$\begin{aligned} \epsilon(\gamma_s(\tau_{\text{SCT}})) &= \frac{1}{e} \\ \Leftrightarrow \gamma_s(\tau_{\text{SCT}}) &= \sqrt{2\pi} \sigma_{R,\nu_s} \tau_{\text{SCT}} \approx 1.571 \\ \Leftrightarrow \tau_{\text{SCT}} &\approx \frac{1.571}{\sqrt{2\pi}} \frac{1}{\sigma_{R,\nu_s}} = \frac{0.3536}{\sigma_{R,\nu_s}}, \end{aligned} \quad (4.65)$$

since the damping factor is proportional to the product of the turn number and the scale parameter in Eq. 4.62. Thus, the spin coherence time depends reciprocally on the scale parameter, where the constant of proportionality yields  $A_{\sigma_{R,\nu_s}} = 0.353603$ .

Another ansatz in order to identify the functional form of the turn depending amplitude is based on the theory of directional statistics. In Eq. 4.52 it is shown that the wrapped probability density function of the phase can be expressed in terms of the characteristic function of the Rayleigh distribution. In addition, the length of the mean resultant vector, which corresponds in this case to the amplitude of the polarization, is given by the absolute value of the first moment of the circular distribution [22], which is derived in Eq. 4.55

$$\begin{aligned} | \langle z^{k=1} \rangle | &= | \phi_{\text{Ray}}(k=1, \sigma_{\varphi_s}(n)) | \\ &= \left| 1 - \sqrt{\pi} \sigma_{\varphi_s}(n) e^{-\sigma_{\varphi_s}^2(n)} [\operatorname{erfi}(\sigma_{\varphi_s}(n)) - i] \right| \\ &= \left( \left[ 1 - \sqrt{\pi} \sigma_{\varphi_s}(n) e^{-\sigma_{\varphi_s}^2(n)} \operatorname{erfi}(\sigma_{\varphi_s}(n)) \right]^2 + \pi \sigma_{\varphi_s}^2(n) e^{-2\sigma_{\varphi_s}^2(n)} \right)^{\frac{1}{2}} \\ &= \left( \left[ 1 - \sqrt{\pi} \gamma_s(n) e^{-\gamma_s^2(n)} \operatorname{erfi}(\gamma_s(n)) \right]^2 + \pi \gamma_s^2(n) e^{-2\gamma_s^2(n)} \right)^{\frac{1}{2}}. \end{aligned} \quad (4.66)$$

The latter representation corresponds exactly to the one derived based on the integration of the joint bivariate probability density function (Eq. 4.59 and Eq. 4.64). Thus, both theoretical concepts provide the same result of the turn depending amplitude model function, since the parameters  $\sigma_{\varphi_s} = \gamma_s = \sqrt{2\pi} \sigma_{R,\nu_s} n$  are defined identically.

## 4.5 Conclusion

In this chapter, a two parameter model, which is based on the width of the spin tune distribution  $\sigma_{R,\nu_s}$  and the spin tune of the particle on the reference orbit  $\nu_s^{\text{ref}}$ , was derived for the turn depending phase and amplitude. Both, the theory of directional statistics and the

integration of the joint bivariate probability density function, leads to the same results. Furthermore, the relation between the spin coherence time  $\tau_{\text{SCT}}$  and the scale parameter of the spin tune distribution was identified. On the left-hand side of Fig. 4.8 the distributions of the

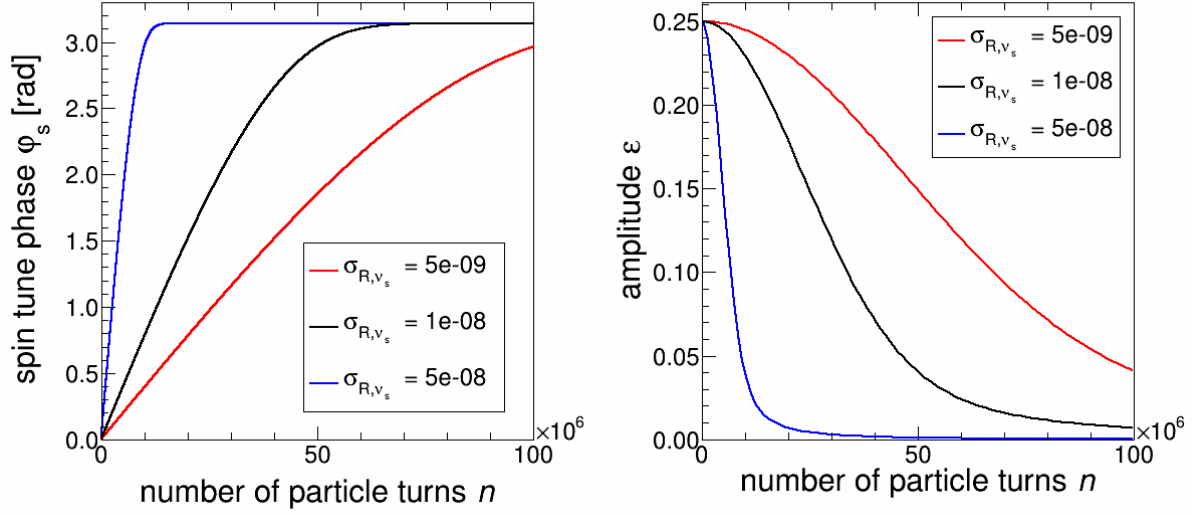


Figure 4.8: Left: turn depending phase deviation of the ensemble from the reference particle for different spin tune spread parameters and the amplitude parameter  $\epsilon = 0.25$ . Right: amplitude distribution

turn depending phase are shown for three different spin tune scale parameters (blue:  $\sigma_{R,\nu_s} = 5 \cdot 10^{-8}$ ; black:  $\sigma_{R,\nu_s} = 1 \cdot 10^{-9}$ ; red:  $\sigma_{R,\nu_s} = 5 \cdot 10^{-9}$ ). In all cases, the initial phase starts at zero and afterwards, it increases strictly monotonically until it converges to  $\pi$ . In fact, the distribution corresponds to the first circular moment of the phase pdf (Eq. 4.56) shown in Fig. 4.5. In addition, the distribution of the amplitude is displayed on the right-hand side based on the amplitude parameter  $\epsilon = 0.25$ .



---

# Amplitude Determination

---

In the previous chapter, it was shown, that the mapping method and the discrete turn Fourier transform provide an estimator of the phase  $\tilde{\varphi}$  and of the amplitude  $\tilde{\epsilon}$  for each macroscopic turn interval. However, the estimator of the amplitude is biased. Consequently, a more sophisticated estimator  $\hat{\epsilon}$  is introduced based on the measurement of  $\tilde{\epsilon}$  and the standard deviation  $\sigma$ . In fact, the moments of the probability density function are discussed, which describes the distribution of the estimator given a true amplitude value and its standard deviation  $p_R(\tilde{\epsilon}; \epsilon, \sigma)$ . Latter is called the Rice distribution. After the comparison of the different estimators, the results of a typical amplitude distribution are discussed.

## 5.1 Rice Distribution

Suppose that in the case of a vanishing true amplitude signal  $\epsilon = \sqrt{A^2 + B^2} = 0$  the two uncorrelated parameters  $A \sim N(0, \sigma^2)$  and  $B \sim N(0, \sigma^2)$  are normal random variables, with mean value 0 and a standard deviation, which is specified by the number of detected events  $\sigma = \sqrt{\frac{2}{N}}$  (4.30). The central limit theorem (2.1) ensures that for a large number of detected events  $N$  this assumption holds. It follows that the estimated magnitude  $\tilde{\epsilon} = \sqrt{\tilde{A}^2 + \tilde{B}^2}$  is Rayleigh distributed [37]

$$p_R(\tilde{\epsilon}; \epsilon = 0, \sigma) = \frac{\tilde{\epsilon}}{\sigma^2} \exp\left(-\frac{\tilde{\epsilon}}{2\sigma^2}\right), \quad (5.1)$$

with the most probable value  $\sigma$ . The quantities  $\tilde{A}$  and  $\tilde{B}$  are estimated according to the two methods described in chapter 4. They are both consistent, asymptotic normal and unbiased. However, the probability that  $\tilde{\epsilon}$  reaches very high or low values is not null, even if the analyzed signal has zero amplitude. Consequently, the estimated amplitude  $\tilde{\epsilon}$  is positively biased.

If the signal provides a non-zero amplitude  $\epsilon > 0$  the probability density function of  $\tilde{\epsilon}$  follows a Rice distribution

$$p_R(\tilde{\epsilon}; \epsilon, \sigma) = \frac{\tilde{\epsilon}}{\sigma^2} \exp\left(-\frac{\tilde{\epsilon}^2 + \epsilon^2}{2\sigma^2}\right) I_0\left(\frac{\epsilon\tilde{\epsilon}}{\sigma^2}\right), \quad (5.2)$$

where  $I_0$  is the modified Bessel function of the first kind of order 0. In fact, the Rice distribution corresponds to the integral over the estimated phase  $\tilde{\varphi}$  of a joint probability density function of two Normal distributed random variables  $\tilde{A}$  and  $\tilde{B}$  with mean value  $A$  and  $B$  and the same standard deviation  $\sigma$

$$f(\tilde{A}; A) f(\tilde{B}; B) d\tilde{A} d\tilde{B} = \frac{1}{2\pi\sigma^2} e^{-\frac{(\tilde{A}-A)^2}{2\sigma^2}} \cdot e^{-\frac{(\tilde{B}-B)^2}{2\sigma^2}} d\tilde{A} d\tilde{B}. \quad (5.3)$$

Note that the transformation into polar coordinates ( $\tilde{A} = \tilde{\epsilon} \sin(\tilde{\varphi})$  and  $\tilde{B} = \tilde{\epsilon} \cos(\tilde{\varphi})$ ) and the Jacobian  $J = \tilde{\epsilon}$  has to be taken into account. A derivation of  $p_R$  is given in appendix A.4. One should highlight that the Rice distribution is independent of the phase parameter  $\varphi$ .

It is helpful to define a signal-to-noise ratio (SNR)  $\gamma_{\text{SNR}} = \epsilon/\sigma$  and  $\tilde{\gamma}_{\text{SNR}} = \tilde{\epsilon}/\sigma$ , respectively. Considering the Jacobian of the latter transformation  $\frac{d\tilde{\epsilon}}{d\tilde{\gamma}_{\text{SNR}}} = \sigma$  the Rician distribution can also be written as

$$p_R(\tilde{\gamma}_{\text{SNR}}; \gamma_{\text{SNR}}) d\tilde{\gamma}_{\text{SNR}} = \tilde{\gamma}_{\text{SNR}} e^{-\frac{\tilde{\gamma}_{\text{SNR}}^2 + \gamma_{\text{SNR}}^2}{2}} I_0(\gamma_{\text{SNR}} \tilde{\gamma}_{\text{SNR}}) d\tilde{\gamma}_{\text{SNR}}, \quad (5.4)$$

which is independent of the standard deviation. Note that the term signal-to-noise ratio is used widely in the field of signal processing, where a measured signal is in general disturbed by white noise. However, in the experimental context addressed in this thesis, every event contributes as a noiseless signal. Thus, the present signal-noise-ratio is given as the ratio of the actual signal and the standard deviation, which depends on the number of detected event.

For large  $\gamma_{\text{SNR}}$  the Rice distribution converges to a Normal distribution with mean  $\hat{\epsilon} \approx \tilde{\epsilon}_R$

and standard deviation  $\sigma_{\hat{\epsilon}_R} \approx \sigma$ , where  $\hat{\epsilon}_R$  denotes the Rician amplitude estimator and  $\sigma_{\hat{\epsilon}_R}$  represents its standard deviation. In addition, the positive bias becomes small  $\tilde{\epsilon}_{\text{bias}} \xrightarrow{\gamma_{\text{SNR}} \rightarrow \infty} 0$ . Hereinafter, the parameter  $\sigma$  written down without any index will denote the standard deviation, which depends on the number of detected events  $N$

$$\sigma = \sqrt{\frac{2}{N}}. \quad (5.5)$$

It specifies the standard deviation of the Normal distribution of the random variables  $A$  and  $B$ . According to the central limit theorem, the estimators  $\tilde{A}$  and  $\tilde{B}$  are Normally distributed, as well 2.1.

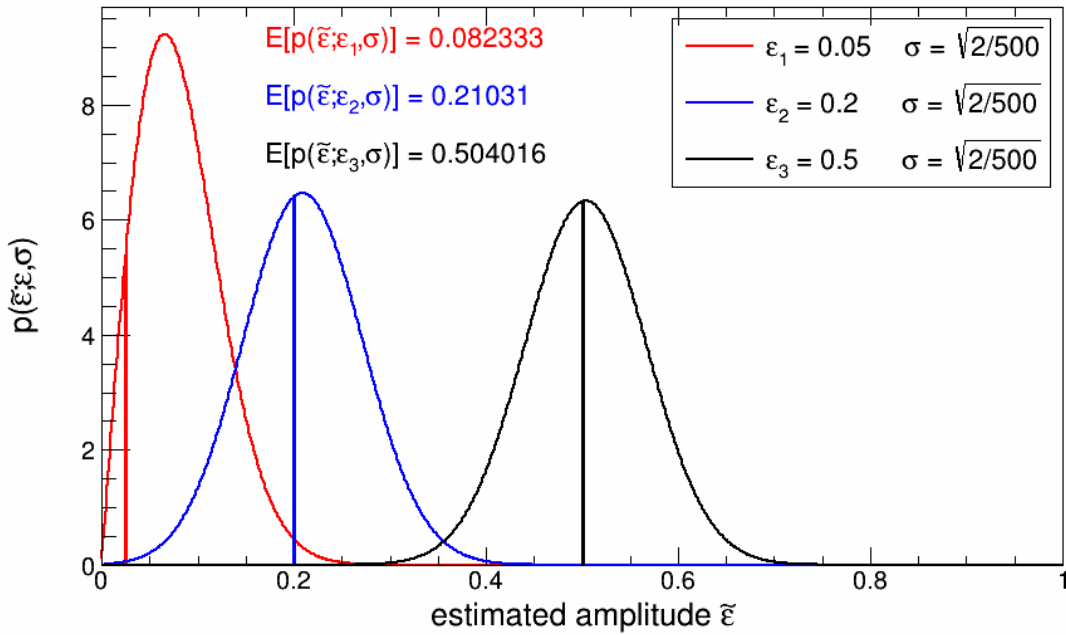


Figure 5.1: Three examples of the Rice distribution with the standard deviation  $\sigma = \sqrt{2/500}$  and different true amplitudes  $\epsilon_1 = 0.05, \epsilon_2 = 0.2, \epsilon_3 = 0.5$ , which are represented by the vertical lines. Additionally, the first moments of each distribution are given.

In Fig 5.1 three examples of the Rice distribution Eq. 5.2 are shown for different true amplitudes  $\epsilon$  but identical standard deviation  $\sigma = \sqrt{2/500}$ . The vertical lines correspond to the true value  $\epsilon$ . It is obvious, that the expectation value  $\hat{\epsilon}_R = E[p_R(\tilde{\epsilon}; \epsilon, \sigma)]$  does not coincide with  $\epsilon$  since  $p_R(\tilde{\epsilon}; \epsilon, \sigma)$  is asymmetric. In fact, the inequality  $\hat{\epsilon}_{\text{Rice}} > \epsilon$  holds for all values of the amplitude  $\epsilon \in (0, \infty)$  and of the standard deviation  $\sigma \in (0, \infty)$ . In the upcoming sections, it will be shown, that the positive bias  $\tilde{\epsilon}_{\text{bias}} = \hat{\epsilon}_R - \epsilon$  increases for smaller true amplitudes  $\epsilon$  and larger standard deviations  $\sigma$ .

In the following, three different approaches, which reduce the positive bias of the amplitude estimator, are discussed. First, the moments of the Rice distribution are taken into consider-

ation, whereas a conventional and a scaled 2nd moment estimator are specified. The second approach is based on a maximum likelihood estimation (MLE) and the last one is connected to the Feldmann-Cousin algorithm.

### 5.1.1 Moments of Rice Distribution

The  $\nu^{\text{th}}$  moment of the Rice distribution Eq. 5.2 can be analytically expressed by [38]

$$\langle \tilde{\epsilon}^\nu \rangle = (2\sigma^2)^{\frac{\nu}{2}} \Gamma\left(1 + \frac{\nu}{2}\right) {}_1F_1\left[-\frac{\nu}{2}; 1; -\frac{\epsilon^2}{2\sigma^2}\right], \quad (5.6)$$

where  $F$  is the hypergeometric function and  $\Gamma$  denotes the gamma function. For integer values of  $\nu/2$ ,  $F$  becomes a polynomial in its arguments and in particular the second moment yields

$$\langle \tilde{\epsilon}^2 \rangle = \epsilon^2 + 2\sigma^2 \quad (5.7)$$

With  $\widehat{\langle \tilde{\epsilon}^2 \rangle} = \langle \tilde{\epsilon}^2 \rangle = \tilde{\epsilon}^2$ , an estimator of  $\epsilon^2$  is given by

$$\hat{\epsilon}_{2\text{nd}}^2 = \tilde{\epsilon}^2 - 2\sigma^2, \quad (5.8)$$

$$\Rightarrow \hat{\epsilon}_{2\text{nd}} = \sqrt{\tilde{\epsilon}^2 - 2\sigma^2}. \quad (5.9)$$

In the case of  $\tilde{\epsilon}^2 < 2\sigma^2$ , the argument of the square root becomes negative. This is physically meaningless since it violates the *a priori* knowledge that the amplitude assumes real positive values. In fact, the probability distribution  $p(\hat{\epsilon}_{2\text{nd}}^2; \epsilon, \sigma)$  follows a non-central  $\chi^2$  distribution, which is derived in appendix: A.5 In particular, it is shown, that the probability of  $p(\hat{\epsilon}_{2\text{nd}}^2 < 0)$  is not zero. Even for large  $\gamma_{\text{SNR}}$  the estimator is biased, which can be seen by expanding  $\hat{\epsilon}$  about  $\epsilon$

$$\hat{\epsilon}_{2\text{nd}} \approx \epsilon \left(1 - \frac{\sigma^2}{2\epsilon^2}\right) = \epsilon \left(1 - \frac{1}{2}\gamma_{\text{SNR}}^2\right). \quad (5.10)$$

A better estimator is established by taking into account the first moment of the Rice distribution, which is given by

$$\langle \tilde{\epsilon} \rangle = (2\sigma^2)^{\frac{1}{2}} \frac{\sqrt{\pi}}{2} {}_1F_1\left[-\frac{1}{2}; 1; -\frac{\epsilon^2}{2\sigma^2}\right] \quad (5.11)$$

$$= \sqrt{\frac{\pi}{2}} \sigma e^{-\frac{\epsilon^2}{4\sigma^2}} \left[ \left(\frac{\epsilon^2}{2\sigma^2} + 1\right) I_0\left(\frac{\epsilon^2}{4\sigma^2}\right) + \frac{\epsilon^2}{2\sigma^2} I_1\left(\frac{\epsilon^2}{4\sigma^2}\right) \right] \quad (5.12)$$

$$= \sqrt{\frac{\pi}{8}} \sigma e^{-\frac{\gamma_{\text{SNR}}^2}{4}} \left[ (\gamma_{\text{SNR}}^2 + 2) I_0\left(\frac{\gamma_{\text{SNR}}^2}{4}\right) + \gamma_{\text{SNR}}^2 I_1\left(\frac{\gamma_{\text{SNR}}^2}{4}\right) \right]. \quad (5.13)$$

Consequently, the variance of the estimated amplitude yields

$$\sigma_{\hat{\epsilon}_{2\text{nd},\text{cor}}}^2 = \langle \tilde{\epsilon}^2 \rangle - \langle \tilde{\epsilon} \rangle^2 \quad (5.14)$$

$$= \zeta(\gamma_{\text{SNR}})\sigma^2, \quad (5.15)$$

where  $\zeta(\gamma_{\text{SNR}})$  is obtained by factoring out  $\sigma^2$  and by the substitution of the signal-to-noise ratio. The correction factor  $\zeta(\gamma_{\text{SNR}})$  is defined as

$$\zeta(\gamma_{\text{SNR}}) = 2 + \gamma_{\text{SNR}}^2 - \frac{\pi}{8} e^{\frac{\gamma_{\text{SNR}}^2}{2}} \left[ (\gamma_{\text{SNR}}^2 + 2) I_0 \left( \frac{\gamma_{\text{SNR}}^2}{4} \right) + \gamma_{\text{SNR}}^2 I_1 \left( \frac{\gamma_{\text{SNR}}^2}{4} \right) \right]^2. \quad (5.16)$$

In Fig. 5.2 the scale factor is shown as a function of the signal-to-noise ratio. It starts at  $\zeta(0) = 2 - \frac{\pi}{2}$  and converges to unity for large  $\gamma_{\text{SNR}}$ . Thus, the corrected standard deviation of the estimated amplitude  $\sigma_{\tilde{\epsilon}, \text{cor}}$  is always smaller than the one based on the number of detected events  $\sigma = \sqrt{\frac{2}{N}}$ . In fact, the scale factor takes into account, that the width of the Rice distribution 5.1 becomes narrower for a decreasing signal-to-noise ratio.

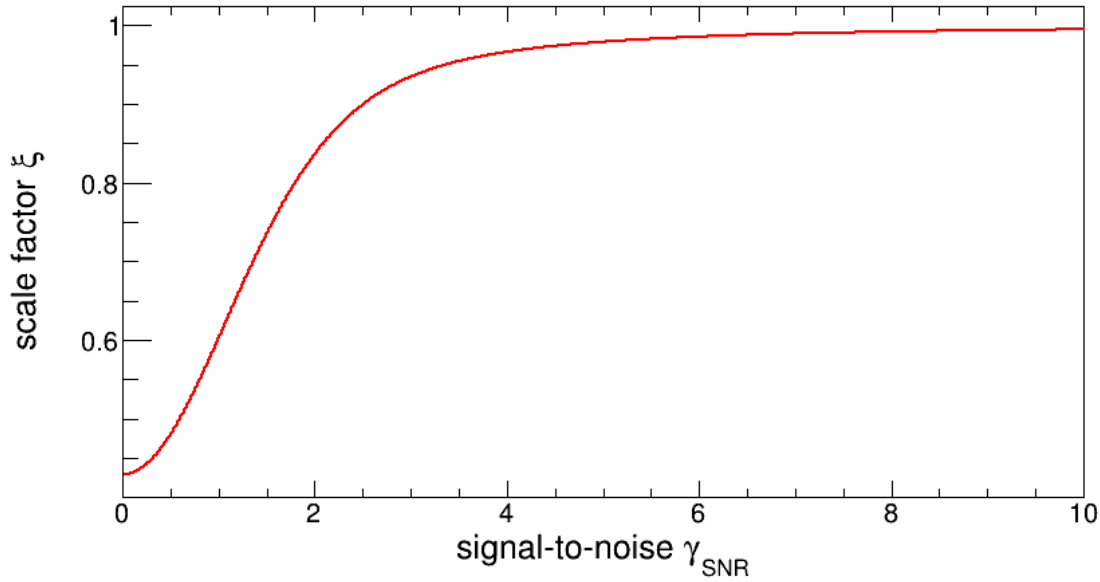


Figure 5.2: The scale factor 5.16 of the amplitude variance as a function of the signal-to-noise ratio  $\gamma_{\text{SNR}}$ .

The Eq. 5.14 can also be written as

$$\langle \tilde{\epsilon}^2 \rangle - \langle \tilde{\epsilon} \rangle^2 = 2\sigma^2 + \epsilon^2 - \tilde{\epsilon}^2 = \zeta(\gamma_{\text{SNR}})\sigma^2 \quad (5.17)$$

$$\Leftrightarrow 2 + \gamma_{\text{SNR}}^2 - \frac{\tilde{\epsilon}^2}{\sigma^2} = \zeta(\gamma_{\text{SNR}}) \quad (5.18)$$

$$\Leftrightarrow \gamma_{\text{SNR}} = \sqrt{\zeta(\gamma_{\text{SNR}}) + \frac{\tilde{\epsilon}^2}{\sigma^2} - 2}. \quad (5.19)$$

This expression has a unique solution for all  $\frac{\tilde{\epsilon}}{\sigma} \geq \sqrt{\frac{\pi}{2}}$  since  $\zeta(0) = 2 - \frac{\pi}{2}$ . The exact result of Eq. 5.19 is obtained iteratively using the definition  $h(\gamma_{\text{SNR}}) = \sqrt{\zeta(\gamma_{\text{SNR}}) + \frac{\tilde{\epsilon}^2}{\sigma^2} - 2}$ . Therefore the iteration  $|h^i(\gamma_{\text{SNR},0}) - \gamma_{\text{SNR},i-1}| \leq \epsilon$  starts with an initial value  $\gamma_{\text{SNR},0}$  and converges until it reaches a lower limit  $\epsilon$ .  $h^m$  denotes the  $m$ -th composition of the function  $h$ , i.e.  $h^m(\gamma_{\text{SNR}}) = h(\dots h(\gamma_{\text{SNR}}))$ . This method is presented in [39] and it is called the Koay inversion fix point

technique. Finally, the corrected 2nd moment amplitude estimator and its standard deviation yields

$$\hat{\epsilon}_{2\text{nd,cor}} = \sqrt{\tilde{\epsilon}^2 + (\zeta(\gamma_{\text{SNR}}) - 2)\sigma^2} \quad (5.20)$$

$$= \sqrt{\tilde{\epsilon}^2 + \sigma_{\hat{\epsilon}_{2\text{nd,cor}}}^2 - 2\sigma^2}, \quad (5.21)$$

$$\sigma_{\hat{\epsilon}_{2\text{nd,cor}}}^2 = \zeta(\gamma_{\text{SNR}})\sigma^2. \quad (5.22)$$

## 5.2 Maximum Likelihood Estimator

In order to avoid an unphysical estimator, the maximum likelihood method is implemented to determine  $\tilde{\epsilon}^2$ . In general, the likelihood function is defined as the product of the joint PDFs of a sample containing  $N$  independent observations  $\tilde{\epsilon}_i$

$$\mathcal{L} = \prod_{i=1}^N p_{\text{R}}(\tilde{\epsilon}_i; \epsilon). \quad (5.23)$$

Here, it is assumed that the standard deviation  $\sigma$  is *a priori* known, thus the function  $\mathcal{L}$  has only one unknown parameter  $\epsilon$ . In the case of one observation  $\tilde{\epsilon}$  per macroscopic turn interval  $\Delta n$ , the sum ends at  $N = 1$ . Taking the logarithm of Eq. 5.23 and making use of Eq. 5.2 one gets

$$\log \mathcal{L} = \log \left[ \frac{\tilde{\epsilon}}{\sigma^2} \exp\left(-\frac{\tilde{\epsilon}^2 + \epsilon^2}{2\sigma^2}\right) \text{I}_0\left(\frac{\epsilon\tilde{\epsilon}}{\sigma^2}\right) \right] \quad (5.24)$$

$$\sim -\frac{\epsilon^2}{2\sigma^2} + \log \text{I}_0\left(\frac{\epsilon\tilde{\epsilon}}{\sigma^2}\right). \quad (5.25)$$

The ML estimator is given by the global maximum of  $\log \mathcal{L}$

$$\hat{\epsilon}_{\text{ML}} = \arg\{\max_{\epsilon}(\log \mathcal{L})\}. \quad (5.26)$$

This is realized numerically, since the parameter  $\epsilon$  enters Eq. 5.25 in a nontrivial way. In Fig. 5.3 the likelihood function in Eq. 5.25 is shown for three measured amplitudes  $\tilde{\epsilon}$  and the standard deviation  $\sigma^2 = 2/500$ . For larger  $\tilde{\epsilon}$  the maxima are located at  $\epsilon > 0$ , whereas for smaller values (here  $\tilde{\epsilon} = 0.05$ ) the function decreases monotonically. In this case the estimator yields  $\hat{\epsilon}_{\text{ML}} = 0$ , which is physically meaningful but obviously biased. Analytically the maximum is given by

$$\frac{d \log \mathcal{L}}{d\epsilon} = -\frac{\hat{\epsilon}_{\text{ML}}}{\sigma^2} + \frac{\tilde{\epsilon} \text{I}_1\left(\frac{\tilde{\epsilon}\hat{\epsilon}_{\text{ML}}}{\sigma^2}\right)}{\sigma^2 \text{I}_0\left(\frac{\tilde{\epsilon}\hat{\epsilon}_{\text{ML}}}{\sigma^2}\right)} \stackrel{!}{=} 0 \quad (5.27)$$

$$\Leftrightarrow \hat{\epsilon}_{\text{ML}} \text{I}_0\left(\frac{\tilde{\epsilon}\hat{\epsilon}_{\text{ML}}}{\sigma^2}\right) = \tilde{\epsilon} \text{I}_1\left(\frac{\tilde{\epsilon}\hat{\epsilon}_{\text{ML}}}{\sigma^2}\right), \quad (5.28)$$

where  $\text{I}_1$  denotes the modified Bessel function of first kind and first order.

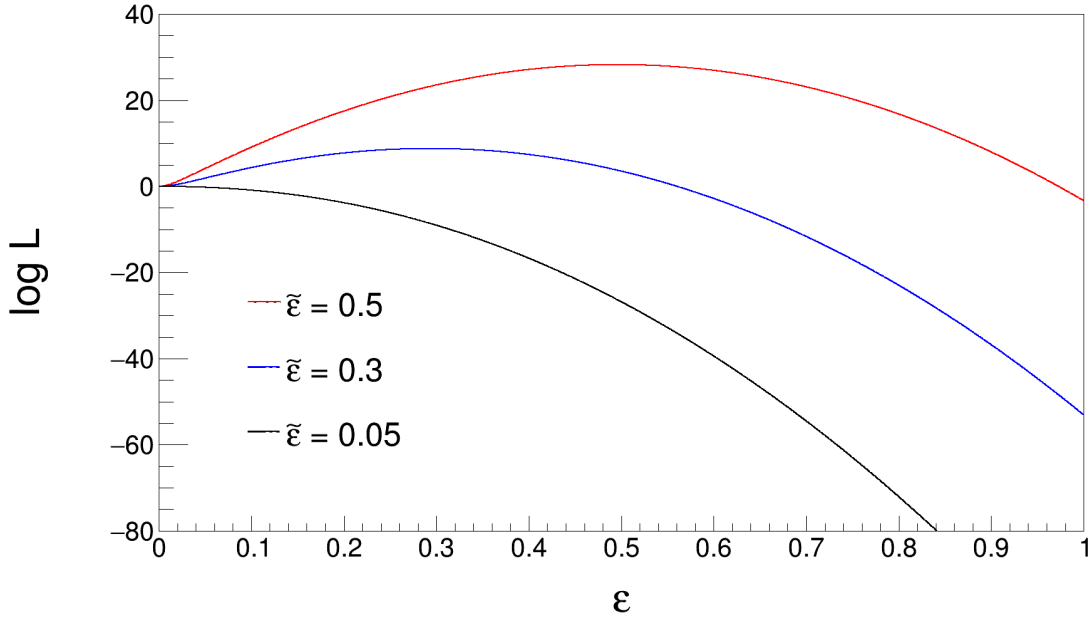


Figure 5.3: Three log-likelihood functions 5.25 for different measured amplitudes  $\tilde{\epsilon}$  with a standard deviation  $\sigma^2 = 2/500$ . For the red and the blue curves, the maxima (best estimator) are located in the region  $\epsilon > 0$ . The black curve decreases monotonically and yields  $\tilde{\epsilon}_{\text{ML}} = 0$

### 5.3 Feldmann-Cousin Algorithm

Another approach obtaining proper confidence intervals of the amplitude estimator is given by the Feldmann-Cousin algorithm [40]. Therefore, the likelihood ratio of the Rician probability density function and its functional value for the most probable value  $\epsilon_{\text{best}}$  is formed

$$R_{\text{R}}(\tilde{\epsilon}, \epsilon) = \frac{p_{\text{R}}(\tilde{\epsilon}; \epsilon)}{p_{\text{R}}(\tilde{\epsilon}; \epsilon_{\text{best}})}. \quad (5.29)$$

Confidence intervals are constructed by selecting all values of  $\tilde{\epsilon}$  for which the ratio is largest until the desired coverage is reached. A better understanding of the method is given in Fig. 5.4. Here, the likelihood ratio 5.29 and the Rician distribution 5.2 are shown as a function of the estimated amplitude for two different true amplitude parameters  $\epsilon = 0.1$  and  $\epsilon = 0.4$  but same conventional standard deviation  $\sigma = 0.2$ . Henceforward, all values of  $R_{\text{R}}(\tilde{\epsilon}_{\text{selected}}, \epsilon)$  are selected until the integral of  $p_{\text{R}}(\tilde{\epsilon}_{\text{selected}}; \epsilon)$  reaches the desired target value. In the case of a 68.3% confidence interval the blue area in Fig. 5.4 corresponds to approximately 68.3%. The blue curve in the upper plot represents the included respectively largest values of the likelihood ratio within the interval.

On the left-hand side of Fig. 5.5 a 2-dimensional map of the Rice distribution 5.2 is shown. The statistical error is set to  $\sigma = \sqrt{2/50}$ . The black curve represents the most probable value  $\epsilon_{\text{best}}(\tilde{\epsilon})$ , which denotes the global maximum of the y-axis projection of the respective bin, as a function of the estimated amplitude. An evident positive bias arises, which increases for

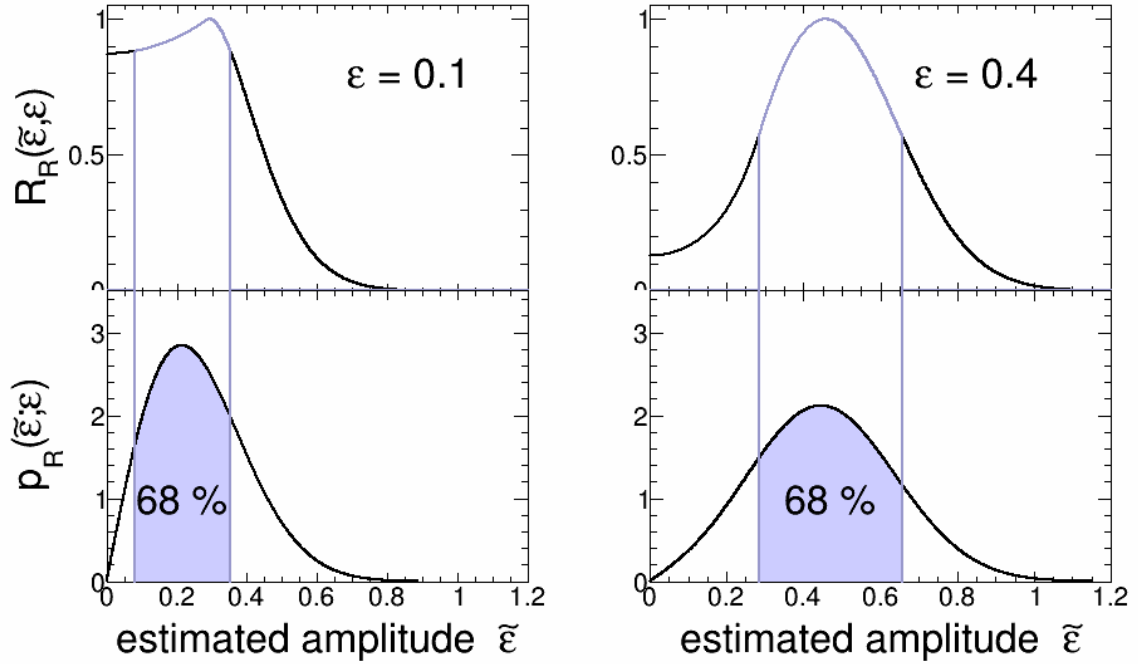


Figure 5.4: Two examples of the construction of the Feldmann-Cousin confidence interval for  $\epsilon = 0.1$ ,  $\epsilon = 0.4$  and  $\sigma = 0.2$ . The blue area in the lower plots corresponds to the 68.3% confidence of the Rician distribution, whereas the colored curve in the upper plots represents the largest values of the likelihood ratio  $R_R$  according to the 68% coverage.

smaller estimated amplitudes.

The right-hand side of Fig. 5.5 shows the corresponding map of the likelihood ratio  $R_R(\tilde{\epsilon}, \epsilon)$  in Eq. 5.29. The two blue curves indicate the 68.3% standard deviation. In other words 68% of the x-axis projection of the map on the left-hand side is covered within this interval. The confidence interval of the true amplitude given for a fixed  $\tilde{\epsilon}$  is enclosed by two horizontal lines. Therefore, a vertical line is drawn at  $\tilde{\epsilon}$ , which intersects the lower and upper bounds (blue curves). The horizontal intersection lines define the confidence interval. This procedure is illustrated by the dotted white lines for  $\tilde{\epsilon}_1 = 0.2$  and  $\tilde{\epsilon}_2 = 0.7$ . The confidence intervals yield  $\epsilon(\tilde{\epsilon}_1) \in [0, 0.28]$  and  $\epsilon(\tilde{\epsilon}_2) \in [0.46, 0.87]$ . The latter result spans approximately the same interval as using Gaussian error (which is biased)  $[\epsilon - \sqrt{\frac{2}{50}} = \epsilon - 0.2, \epsilon + \sqrt{\frac{2}{50}} = \epsilon + 0.2] \rightarrow \Delta\sigma_\epsilon^{\text{gaus}} = 0.4 \approx \Delta\sigma_\epsilon^{\text{FC}}(\tilde{\epsilon}_2) = 0.41$ .

If the estimator of the amplitude represents the final result, the determination of the Feldmann-Cousin interval is sufficient. However, a subsequent analysis demands a probability density function of  $\epsilon$  depending on a given parameter  $\tilde{\epsilon}$ . Therefore, the assumption of a constant prior

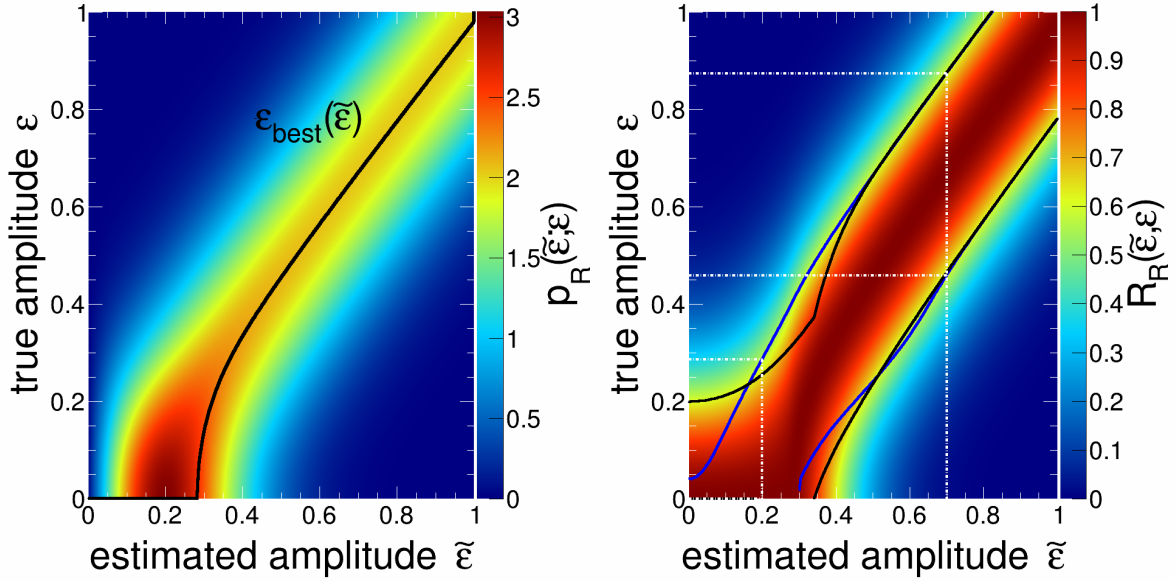


Figure 5.5: Left: Two dimensional map of the Rice distribution 5.2 with standard deviation  $\sigma = \sqrt{2/50}$ . In addition the most probable value of the true amplitude as a function of the estimated amplitude  $\epsilon_{\text{best}}(\tilde{\epsilon})$  is shown in black. Right: Likelihood ratio 5.29 constructed according to the Feldmann-Cousin algorithm. The blue curve indicates the 68.3% confidence interval and the horizontal dashed white lines corresponds to the confidence interval of the respective estimated amplitude  $\tilde{\epsilon}$  (vertical dashed white lines). The black curve represents the 68.3% coverage of the y-axis projection based on the Bayes' theorem.

probability for  $\epsilon$  is used. This yields

$$\begin{aligned}
 \tilde{p}_R(\epsilon; \tilde{\epsilon}) &= \frac{p_R(\tilde{\epsilon}; \epsilon)p(\epsilon)}{p(\tilde{\epsilon})} \\
 &= \frac{p_R(\tilde{\epsilon}; \epsilon)p(\epsilon)}{\int_0^\infty p_R(\tilde{\epsilon}; \epsilon) d\epsilon} \\
 &\sim R_R(\tilde{\epsilon}, \epsilon)
 \end{aligned} \tag{5.30}$$

according to the Bayes' theorem [41]. The constant prior probability  $p(\epsilon)$  ensures the normalization of 5.30  $\int_0^\infty \tilde{p}_R(\epsilon; \tilde{\epsilon}) d\epsilon = 1$ . It is important to note that the probability density function of  $\epsilon$  is proportional to the likelihood ratio  $\tilde{p}_R(\epsilon; \tilde{\epsilon}) \sim R_R(\tilde{\epsilon}, \epsilon)$ . The latter is given by the y-axis projection of the distribution on the right hand-side of Fig. 5.5. Two examples are shown in Fig. 5.6 for the estimated amplitudes  $\tilde{\epsilon} = 0.1$  and  $\tilde{\epsilon} = 0.4$ . The blue area covers 68.3% of the largest values of  $R_R(\tilde{\epsilon}, \epsilon)$ .

Additionally, the probability density function of  $\epsilon$  is shown in red. In the case of  $\tilde{\epsilon} = 0.1$  the x-axis is scaled that both distributions match exactly. This is possible since the distributions are proportional to each other and thus both yield the identical 68.3% confidence interval. The same scale is used for  $\tilde{\epsilon} = 0.4$ . Here, the probability density function becomes lower and wider. However, both distributions provide equivalent results for the 68.3% coverage.

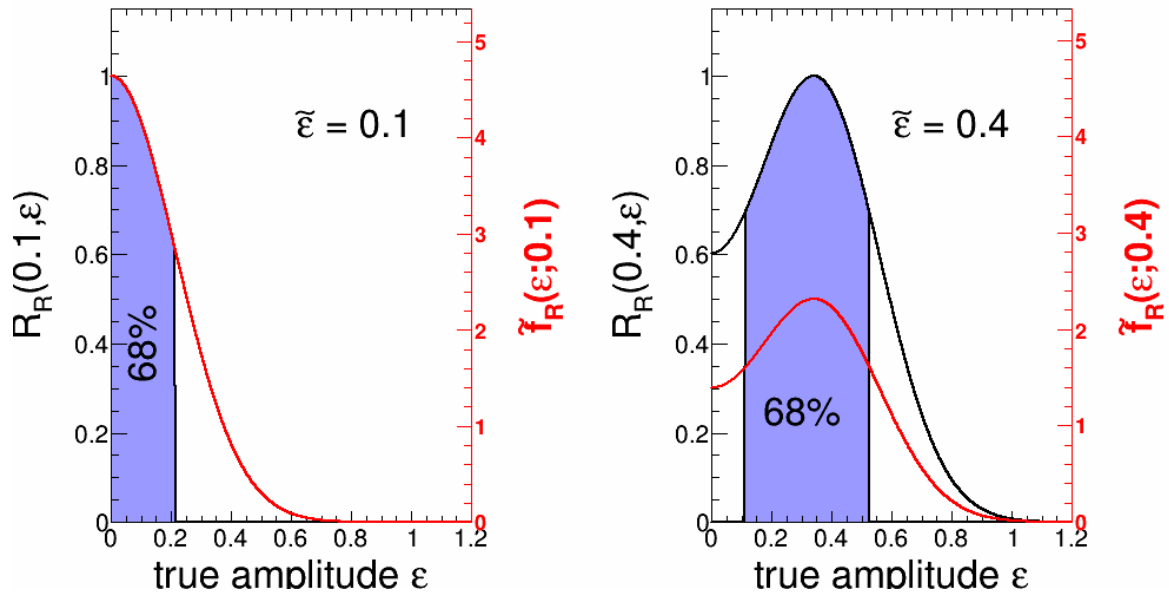


Figure 5.6: Comparison between the amplitude likelihood ratio (black) and the probability density function of the true amplitude (red) obtained for a given  $\tilde{\epsilon} = 0.1$  and  $\tilde{\epsilon} = 0.4$ . The blue area represents 68.3% of the largest values of  $R_R(\tilde{\epsilon}, \epsilon)$ .

On the right-hand side of Fig.5.5 the black curves indicate the 68.3% confidence interval of  $R_R(\tilde{\epsilon}, \epsilon)$  and  $p_R(\epsilon; \tilde{\epsilon})$ , respectively. They are based on the Bayes' theorem and one observes a significant deviation compared to the results from the Feldmann-Cousin algorithm (blue curve).

## 5.4 Comparison of Estimators

The amplitude estimators  $\hat{\epsilon}_{2\text{nd}}$ ,  $\hat{\epsilon}_{2\text{nd,cor}}$  and  $\hat{\epsilon}_{\text{ML}}$  are benchmarked by generating  $n_{\mathcal{E}} = 10^6$  random variables  $\mathcal{E}$  according to the Rice distribution in Eq. 5.2. Again, the signal-to-noise ratio  $\gamma_{\text{SNR}} = \frac{\epsilon}{\sigma}$  is used given a standard deviation of  $\sigma = \sqrt{\frac{2}{500}}$ . Thus, the amplitude, i.e. the reciprocal signal-to-noise ratio is given by

$$\epsilon = \sigma \gamma_{\text{SNR}} = \gamma_{\text{SNR}} \sqrt{\frac{2}{500}} \quad (5.31)$$

$$\frac{1}{\gamma_{\text{SNR}}} = \frac{1}{\epsilon} \sqrt{\frac{2}{500}}. \quad (5.32)$$

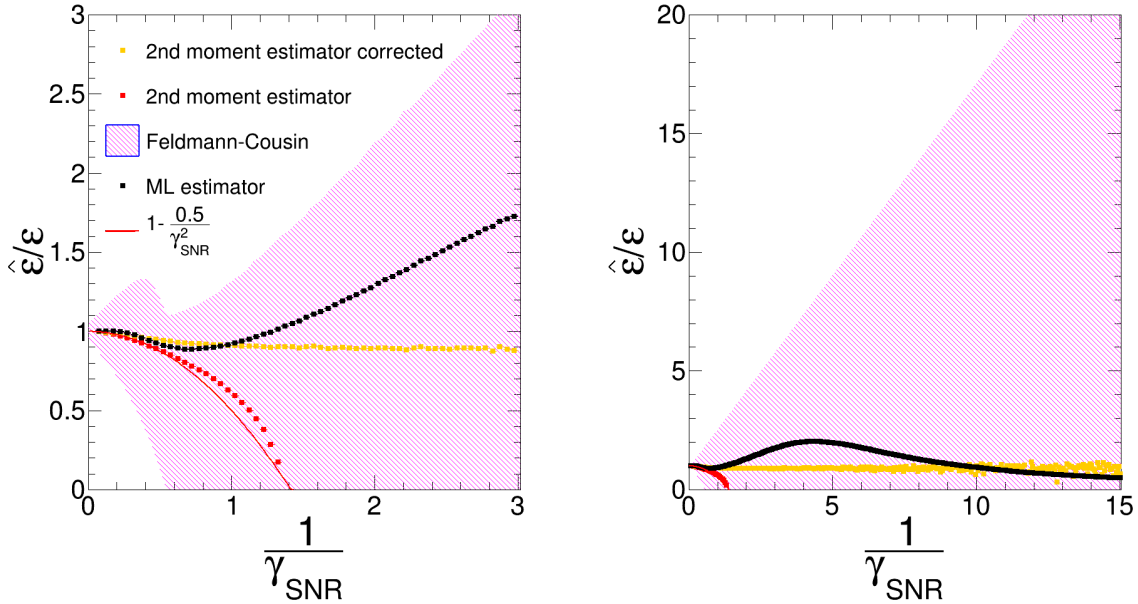


Figure 5.7: Both plots show the different estimators of the amplitude normalized by the true one as a function of the reciprocal signal-to-noise ratio. The left-hand side illustrates a zoom of the plot on the right-hand side. The red data points correspond to the 2nd moment estimator  $\hat{\epsilon}_{2\text{nd}}$  from Eq. 5.9. The yellow ones are corrected by the scaling factor  $\hat{\epsilon}_{2\text{nd,cor}}$  as shown in Eq. 5.20. The red curve represents the second order Taylor estimate of the 2nd moment estimator 5.10. The ML estimator 5.26 is shown in black and the blue band covers the 68.3% Feldmann-Cousin confidence interval 5.3.

For each value of  $\gamma_{\text{SNR}}$  the arithmetic mean of the generated random variables  $\mu_{\mathcal{E}}$  is calculated. The estimators  $\hat{\epsilon}_{2\text{nd}}$  and  $\hat{\epsilon}_{2\text{nd,cor}}$  are determined according to Eq. 5.9 and Eq. 5.20, respectively. The conventional estimator is given by  $\tilde{\epsilon} = \mu_{\mathcal{E}}$ . In order to obtain  $\hat{\epsilon}_{\text{ML}}$ , the likelihood function 5.25 is applied for each  $\mathcal{E}$  to identify the best estimate of the random variable  $\mathcal{E}$ . The arithmetic mean of the maximum likelihood estimators  $\mu_{\mathcal{E}_{\text{ML}}}$  corresponds to the best estimator for a given ratio of  $\epsilon$  and  $\sigma$ .

Figure 5.7 shows the results in red ( $\hat{\epsilon}_{2\text{nd}}$ ), yellow ( $\hat{\epsilon}_{2\text{nd,cor}}$ ) and black ( $\hat{\epsilon}_{\text{ML}}$ ). Here, the nor-

malized estimator  $\hat{\tilde{\epsilon}}$  is plotted against the reciprocal signal-to-noise ratio in order to avoid singularities at  $\gamma_{\text{SNR}} = 0$ . Consequently, an unbiased estimator yields  $\hat{\tilde{\epsilon}} = 1$  and the 68.3% confidence interval of each data point is given by  $\sigma_{\hat{\tilde{\epsilon}}} = \frac{\sigma}{\epsilon \cdot n_{\tilde{\epsilon}}} = \frac{1}{\gamma_{\text{SNR}} \cdot \sqrt{10^6}}$ .

One observes, that the likelihood method provides an unbiased estimator until  $\frac{1}{\gamma_{\text{SNR}}} \approx 0.3$ , while  $\hat{\epsilon}_{2\text{nd}}$  decreases instantaneously. The red curve corresponds to the second order Taylor approximation of the expectation value of the 2nd moment estimator in Eq. 5.9. It describes the red data points in a good agreement until  $\frac{1}{\gamma_{\text{SNR}}} \approx 0.5$ , but drops faster for larger values. For  $\frac{1}{\gamma_{\text{SNR}}} > 1.4$ , the mean of the random variables is larger than the standard deviation. Consequently, the argument of the square root in Eq. 5.9 becomes negative and  $\hat{\epsilon}_{2\text{nd}}$  corresponds to a complex number.

The corrected 2nd moment estimator  $\hat{\epsilon}_{2\text{nd,cor}}$  gives a more stable result. It is almost constant for all signal-to-noise ratios. In addition, it provides a slightly underestimated normalized amplitude ratio  $\frac{\hat{\epsilon}_{2\text{nd,cor}}}{\epsilon} \approx 1$ . However, one still faces the problem of a negative argument of the square root in Eq. 5.20. It occurs, as soon as the inequality  $\tilde{\epsilon}^2 + \zeta(\gamma_{\text{SNR}})\sigma^2 < 2\sigma^2$  is fulfilled. Since the conventionally estimated amplitude can assume all values greater than zero  $\tilde{\epsilon} \geq 0$  and since the minimal scale factor is given by  $\zeta(\gamma_0) = 2 - \frac{\pi}{2}$ , the right-hand side of the inequality becomes dominant for larger standard deviations  $\sigma = \sqrt{\frac{2}{N}}$ . Thus, the probability, that the corrected 2nd moment estimation fails is increased for smaller values of  $\tilde{\epsilon}$  and larger values of  $\sigma$ .

The likelihood estimator  $\hat{\epsilon}_{\text{ML}}$  shows a local minimum at  $\frac{1}{\gamma_{\text{SNR}}} \approx 0.7$ . Afterwards, it increases until the signal-to-noise ratio reaches approximately 5. For larger  $\gamma_{\text{SNR}}$  it converges to zero. The behavior of  $\hat{\epsilon}_{\text{ML}}$  depends on the interplay between the probability to obtain  $\tilde{\epsilon}_{\text{ML}} = 0$  (black curve in Fig. 5.3), which becomes larger for smaller amplitudes  $\epsilon$  (larger  $\frac{1}{\gamma_{\text{SNR}}}$ ), and the simultaneously increasing ratio  $\frac{\tilde{\epsilon}_{\text{ML}}}{\epsilon} > 0$  obtained for a non-zero ML estimator. However, even for small true amplitudes the probability to obtain  $\hat{\epsilon}_{\text{ML}} \neq 0$  does not vanish, since also larger estimated amplitudes  $\tilde{\epsilon}$  are allowed according to the Rice distribution in Eq. 5.2. Thus, for large  $\frac{1}{\gamma_{\text{SNR}}}$  the distribution of the likelihood estimators based on the random variable  $\tilde{\mathcal{E}}_{\text{ML}}$  contains either zero values or relatively large normalized amplitude estimators  $\frac{\hat{\tilde{\epsilon}}}{\epsilon} \gg 1$ .

The blue band indicates the 68.3% Feldmann-Cousin confidence interval. In the representation of Fig. 5.7 it becomes broader with increasing  $1/\gamma_{\text{SNR}}$  since the y-axis corresponds to the normalized estimator. Thus, the upper and lower limits of the confidence interval are divided by  $\epsilon$ . Additionally, the lower bound reaches zero at approximately  $1/\gamma_{\text{SNR}} \approx 0.6$ . This means, that for larger values of  $1/\gamma_{\text{SNR}}$  the 68.3%, confidence interval entirely covers the left part of the white vertical line of the right-hand side plot in Fig. 5.5.

## 5.5 Efficiency of Estimators

In the case of high statistics, i.e. a sufficiently large number of estimators obtained for an identical measurement setup, the corrected 2nd moment estimator  $\hat{\epsilon}_{2\text{nd,cor}}$  yields the most convincing result. However, the experiment provides only one amplitude estimator per macroscopic measurement interval. Thus, besides of the determination of an unbiased estimator, it is of major interest to identify the probability, that  $\tilde{\epsilon}$  and  $\sigma_{\tilde{\epsilon}}$  yield a physically meaningful

result. In other words, an efficiency is defined as

$$\epsilon_{\hat{\epsilon}} = \frac{N_{\text{valid}}}{N_{\text{tot}}}, \quad (5.33)$$

where  $N_{\text{valid}}$  denotes the number of meaningful results and  $N_{\text{tot}}$  is the number of the total number of estimators.

In the case of the 2nd moment estimators  $\hat{\epsilon}_{2\text{nd}}$  and  $\hat{\epsilon}_{2\text{nd,cor}}$  a valid estimator is obtained, when the argument of the square root in Eq. 5.9 respectively Eq. 5.20 is not negative. A deeper understanding of the pdf of  $\hat{\epsilon}_{2\text{nd}}^2$  is given in appendix A.5, where the filled area in Fig. A.1 represents the integrated probability of a non-physical solution. For the maximum likelihood estimator  $\hat{\epsilon}_{\text{ML}}$ , a meaningful result is defined, if the maximum of the likelihood function in Fig. 5.3 assumes numbers not equal to zero.

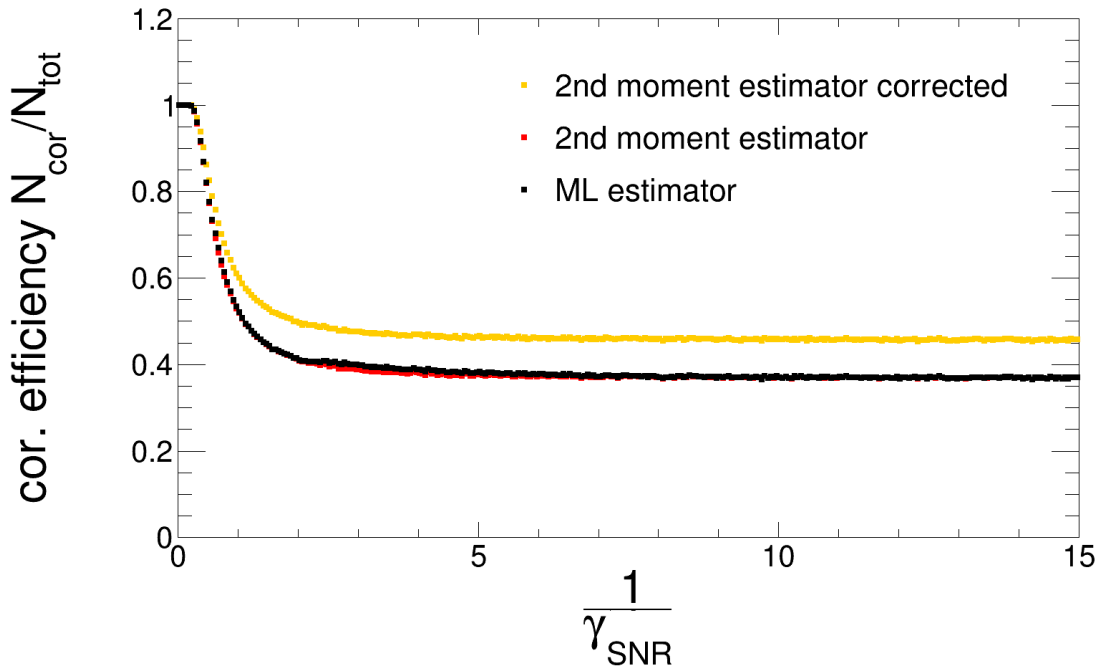


Figure 5.8: The efficiency to obtain a physically meaningful estimator is shown as a function of the reciprocal signal-to-noise ratio for the three different approaches discussed in the previous sections (the 2nd moment in red, the corrected 2nd moment in yellow, the maximum likelihood in black).

In Fig. 5.8 the efficiency of each estimator is shown as a function of the reciprocal signal-to-noise ratio with  $N_{\text{tot}} = 10^5$  and a typical standard deviation of  $\sigma = \sqrt{\frac{2}{500}}$ . For small  $\gamma_{\text{SNR}} < 0.3$  all efficiencies yield unity, i.e. for every estimated amplitude  $\tilde{\epsilon}$  a valid estimator  $\hat{\epsilon}$  is identified. In the case of larger signal-to-noise ratios, the quantity  $\epsilon_{\hat{\epsilon}}$  decreases, whereas the results of the 2nd moment (red) and the maximum likelihood (black) estimator are almost identical. However, once the estimator  $\hat{\epsilon}_{2\text{nd}}$  fails, the maximum likelihood estimator yields  $\hat{\epsilon}_{\text{ML}} = 0$ , which is an appropriate result. Both distributions converge to  $\frac{1}{e}$ , which can be understood by

evaluating the integral of the pdf in Eq. A.32 for large  $\frac{1}{\gamma_{\text{SNR}}} \rightarrow \infty$  or  $\epsilon \rightarrow 0$

$$\begin{aligned} N_{\text{tot}} - N_{\text{valid}}^{\text{min}} &= N_{\text{tot}} \int_{-2\sigma}^0 p(\hat{\epsilon}_{2\text{nd}}^2; \epsilon, \sigma) d\hat{\epsilon}_{2\text{nd}}^2 \\ &= N_{\text{tot}} \int_{-2\sigma}^0 \frac{1}{2\sigma^2} e^{-\frac{\hat{\epsilon}_{2\text{nd}}^2 + 2\sigma^2}{2\sigma^2}} d\hat{\epsilon}_{2\text{nd}}^2 = N_{\text{tot}} \frac{e-1}{e}, \end{aligned} \quad (5.34)$$

from  $-2\sigma$  to 0. The integral represents the probability, that  $\hat{\epsilon}_{2\text{nd}}^2$  assumes negative values and consequently, the minimal number of valid estimators is given by  $N_{\text{valid}}^{\text{min}} = N_{\text{tot}}(1 - \frac{1-e}{e}) = \frac{N_{\text{tot}}}{e}$ , which leads to a minimal efficiency of  $e_{\hat{\epsilon}_{2\text{nd}}^{\text{min}}}^{\text{min}} = e_{\hat{\epsilon}_{\text{ML}}^{\text{min}}}^{\text{min}} = \frac{1}{e}$ .

The efficiency of the corrected 2nd moment estimator  $e_{\hat{\epsilon}_{2\text{nd,corr}}^2}$  is larger, since the argument of the square root is corrected by the scale factor  $\zeta(\gamma_{\text{SNR}})$ . Thus, estimators obtained by the mapping method or the discrete turn Fourier transform, which fulfill the inequality

$$\tilde{\epsilon}^2 > (\zeta(\gamma_{\text{SNR}}) - 2)\sigma^2, \quad (5.35)$$

yield proper results. For large  $\frac{1}{\gamma_{\text{SNR}}}$  the scale factor in Eq.5.16 assumes  $\zeta(0) = 2 - \frac{\pi}{2}$  and the right-hand side of Eq. 5.35 becomes  $-\frac{\pi}{2}\sigma$ . Thus, the maximal number of non-valid estimators is given by

$$N_{\text{tot}} - N_{\text{valid}}^{\text{min}} = N_{\text{tot}} \int_{-\frac{\pi}{2}\sigma}^0 p(\hat{\epsilon}_{2\text{nd,corr}}^2; \epsilon, \sigma) d\hat{\epsilon}_{2\text{nd,corr}}^2 \quad (5.36)$$

$$= N_{\text{tot}} \int_{-\frac{\pi}{2}\sigma}^0 \frac{1}{2\sigma^2} e^{-\frac{\hat{\epsilon}_{2\text{nd,corr}}^2 + \frac{\pi}{2}\sigma^2}{2\sigma^2}} d\hat{\epsilon}_{2\text{nd,corr}}^2 = N_{\text{tot}}(1 - e^{-\frac{\pi}{4}}). \quad (5.37)$$

Consequently, the minimal efficiency yields  $e_{\hat{\epsilon}_{2\text{nd,corr}}^{\text{min}}}^{\text{min}} = e^{-\frac{\pi}{4}} \approx 0.456$ .

## 5.6 Amplitude Spectrum

An example of a turn depending amplitude spectrum  $\tilde{\epsilon}(\nu_s, n)$  is shown in Fig. 5.9 for an idle spin precession in the horizontal plane. On the left-hand side the results obtained by the mapping method are presented. The right-hand side is based on the results obtained by the discrete turn Fourier transform. The scan interval varies from  $\nu_{\text{min}}^{\text{scan}} = 0.1609655$  to  $\nu_{\text{max}}^{\text{scan}} = 0.1609765$ , which yields a total range of  $\Delta\nu^{\text{scan}} = 1.2 \cdot 10^{-5}$ . A protruding maximum of the amplitude  $\tilde{\epsilon}_{\text{max}} = \tilde{\epsilon}(\nu_{\text{max}})$  appears at  $\nu_{\text{max}} \approx 0.160971$ , which leads to a first estimate of the spin tune. The spectra of both methods provide similar results within the given resolution.

In order to evolve a better understanding of the respective distribution, the integral of the y-axis projections over the total cycle length is shown in Fig. 5.10. The error bars  $\sigma_{\tilde{\epsilon}}$  correspond to the 68.3% confidence interval determined by the Feldman-Cousin algorithm introduced in section 5.3. The red data points represent the results obtained by the mapping method, which yields systematically larger values than the discrete turn Fourier transform displayed in blue  $\tilde{\epsilon}^{\text{map}} > \tilde{\epsilon}^{\text{DFT}}$ . The difference occurs mainly due to the fact, that for the former method the number of bins  $N_{\text{bins}}$  has to be chosen for the asymmetry distribution, which yields an additional systematic positive bias. The sum of the y-axis projections forms a spectrum which

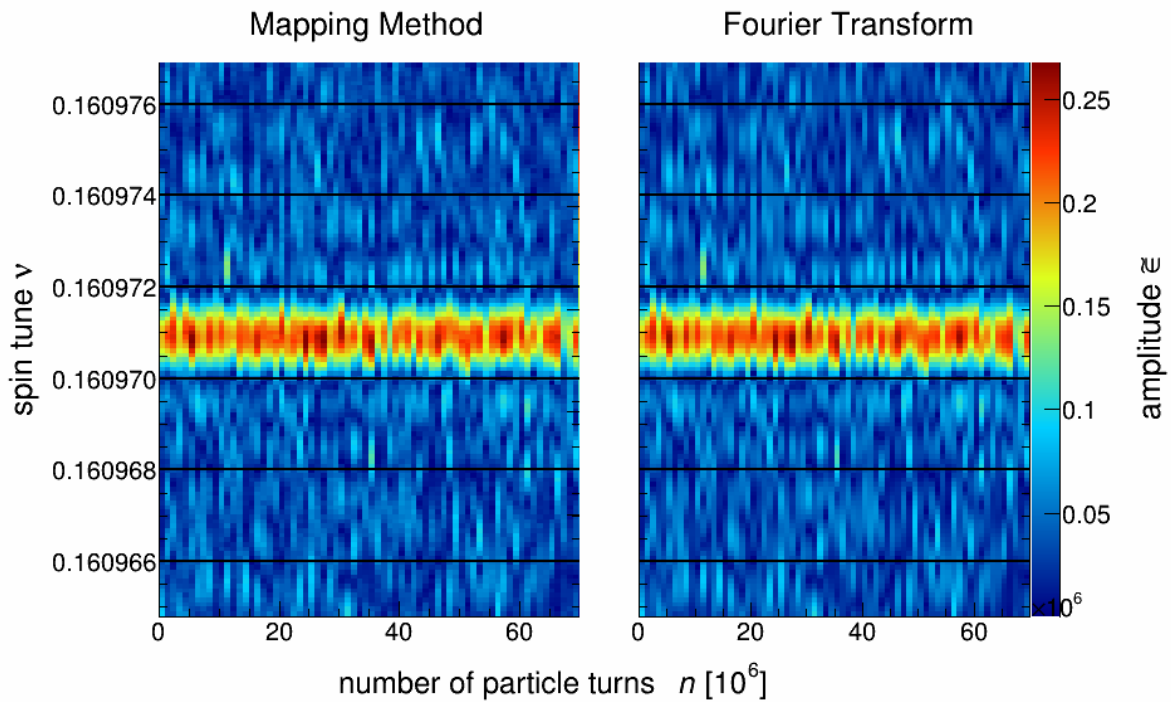


Figure 5.9: Two examples of the turn depending amplitude spectrum  $\tilde{\epsilon}$  for an idle spin precession in the horizontal plane, which lasts for  $n = 70 \cdot 10^6$  turns ( $\approx 90$  s). The spin tune scan is performed from  $\nu_{\min}^{\text{scan}} = 0.1609655$  to  $\nu_{\max}^{\text{scan}} = 0.1609765$ , i.e. in a full range of  $\Delta\nu_s^0 = 1.1 \cdot 10^{-5}$ .

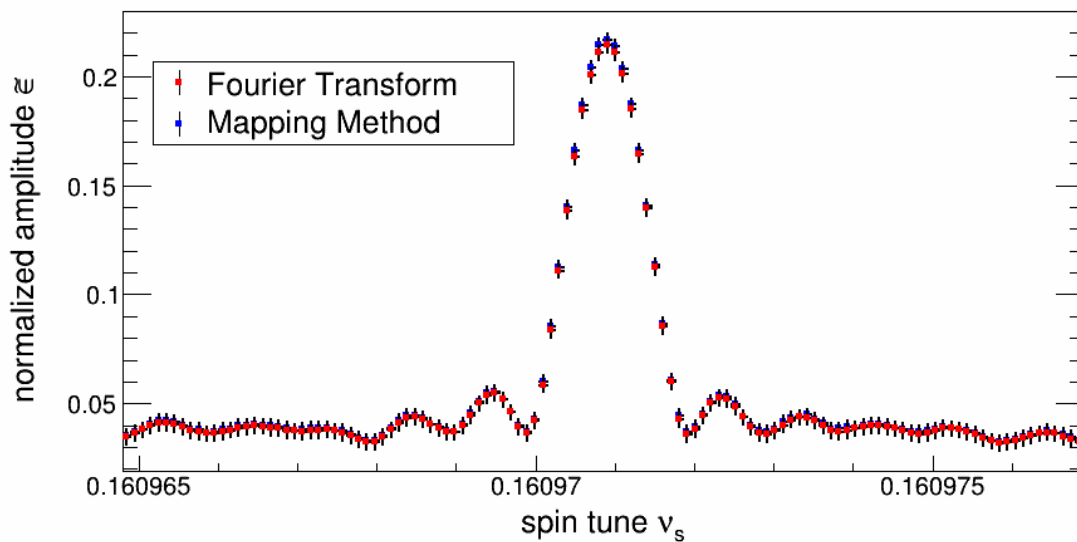


Figure 5.10: The y-axis projection of the 3rd bin of the x-axis of Fig. 5.9. The red data points correspond to the mapping method and the blue ones represent the result obtained by the discrete Fourier transform.

corresponds to a  $\text{sinc}(x) = \sin(x)/x$  distribution. This corresponds to the Fourier transform representation of a sinusoidal function in the frequency domain.

### 5.6.1 Main Lobe

The full width at half maximum (FWHM) of the main lobe in Fig. 5.10 is approximately given by

$$\delta\nu \approx \frac{1}{\Delta n}, \quad (5.38)$$

where  $\Delta n$  denotes the number of particle revolutions in the ring during a macroscopic measurement interval. In the case of  $\Delta n = 10^6$ , the FWHM yields  $\delta\nu = 10^{-6}$ .

This becomes clear by evaluating the Fourier transform  $\mathbb{G}(\nu)$  of a sine-like function  $f(n) = A \cos(2\pi\nu n)$  within a finite turn interval  $\Delta n$ . As mentioned in section 4.2, a multiplication in the turn domain corresponds to a convolution in the spin tune domain.

$$\begin{aligned} \mathbb{G}(\nu) &= \int_{-\infty}^{\infty} \mathbb{F}(\nu - \lambda) * \mathbb{W}(\lambda) d\lambda \\ &= \int_{-\infty}^{\infty} \frac{A}{2} [\delta(\lambda - \nu + \nu_s) + \delta(\lambda + \nu + \nu_s)] \cdot \frac{\sin(2\pi\lambda\Delta n)}{2\pi\lambda} d\lambda \\ &= \frac{A}{2} \left[ \frac{\sin(2\pi(\nu - \nu_s)\Delta n)}{2\pi(\nu - \nu_s)} + \frac{\sin(2\pi(\nu + \nu_s)\Delta n)}{2\pi(\nu + \nu_s)} \right]. \end{aligned} \quad (5.39)$$

Here, the function  $\mathbb{W}$  corresponds the Fourier transform of a rectangular window function  $w(n) = 1$  for  $n < \Delta n$ . The function 5.39 is symmetric about the y-axis and it provides two main peaks at  $\nu = \nu_s$  and  $\nu = -\nu_s$ . To estimate the width of the main lobe the first zero-crossings of the function in Eq. 5.39 are identified, which occurs at

$$\pi(\nu - \nu_s)\Delta n = \delta\nu\Delta n = \pm\pi \quad (5.40)$$

$$\Rightarrow \delta\nu = \frac{1}{\Delta n} \text{ q.e.d.} \quad (5.41)$$

This result represents the uncertainty principle of the Fourier transform, which states that for a more concentrated  $g(n)$  the Fourier transform  $\mathbb{G}(\nu)$  must be more spread out. Or differently spoken: the longer the measurement interval the narrower the main lobe

$$\Delta n\delta\nu \geq 1. \quad (5.42)$$

### 5.6.2 Maximum Likelihood Fit

In Fig. 5.11 the turn depending amplitude is shown for two cycles recorded for different runs. A run is specified by a set of cycles, which were performed with the same settings of the storage ring. Thus, the decoherence of the particle spins should change from run to run. Consequently, both distributions yield a differently decreasing amplitude pattern. The analysis is based on a fixed assumed spin tune  $\nu_s$  for the whole cycle. A better estimation of  $\nu_s$  is discussed

in the upcoming chapters.

In section 4.4.3 an expression for the turn depending amplitude is derived based on the assumption of a Rayleigh distributed spin tune

$$\epsilon(n) = \epsilon_0 \left( \left[ 1 - \sqrt{\pi} \sigma_{\varphi_s} n e^{-(\sigma_{\varphi_s} n)^2} \operatorname{erfi}(\sigma_{\varphi_s} n) \right]^2 + \pi (\sigma_{\varphi_s} n)^2 e^{-2(\sigma_{\varphi_s} n)^2} \right)^{\frac{1}{2}}. \quad (5.43)$$

where  $\sigma_{\varphi_s} = \sqrt{2\pi} \sigma_{R, \nu_s}$  corresponds to the scale parameter of the Rayleigh distribution and  $\epsilon_0$  denotes to the initial vertical vector polarization of the particle ensemble. The red curve in Fig. 5.11 represents a maximum likelihood fit based on the function

$$\mathcal{L} = \prod_{i=1}^N \tilde{p}_R(\epsilon(n_i, \sigma_{R, \nu_s}, \epsilon_0); \epsilon_i). \quad (5.44)$$

Here, the probability density function  $\tilde{p}_R$  derived in the previous sections and the Bayes' theorem stated in Eq. 5.30 are used. The respective pdf of each data point is represented by the underlying scatter plot given by the color scale. Accordingly, the spin coherence times yield

$$\tau_{\text{SCT}}^{\text{long}} = (184.17 \pm 151.55) \times 10^6 \text{ turns}, \quad (5.45)$$

$$\tau_{\text{SCT}}^{\text{short}} = (38.10 \pm 11.91) \times 10^6 \text{ turns}. \quad (5.46)$$

The amplitude parameters  $\epsilon_0$  are compatible with each other within their statistical error since both cycles are performed with the same polarization state.

## 5.7 Conclusion

In the previous sections, it is pointed out, that the amplitude estimator is positively biased. Several techniques are presented in order to minimize the bias. The most stable estimator is given by the corrected 2nd moment estimator  $\epsilon_{\hat{\epsilon}_{2\text{nd}, \text{cor}}}$ . In particular, it provides proper results for small signal-to-noise ratios. However, the probability that  $\epsilon_{\hat{\epsilon}_{2\text{nd}, \text{cor}}}$  becomes physically meaningless increases with decreasing  $\gamma_{\text{SNR}}$  until it reached its minimum at approximately  $1 - 0.456$ . Thus, the Feldmann-Cousin algorithm corresponds to the most convenient method. Note that it provides asymmetric confidence intervals, which have to be taken into account if the data is used for a further analysis.

In fact, the probability density function of the amplitude  $\tilde{p}_R(\epsilon; \tilde{\epsilon}, \sigma)$  can be derived based on the Rice distribution and the Bayes' theorem. Consequently, it is possible to identify the pdf of the true amplitude  $\epsilon$ , which depends on the estimated amplitude  $\tilde{\epsilon}$  and the standard deviation obtained by the discrete Fourier transform  $\sigma$ . Furthermore, the spin coherence time  $\tau_{\text{SCT}}$  is determined by a maximum likelihood fit. The fit function is based on the assumption of a Rayleigh distributed spin tune with the scale parameter  $\sigma_{R, \nu_s}$  and the spin tune on the reference orbit  $\nu_s^{\text{ref}}$ .

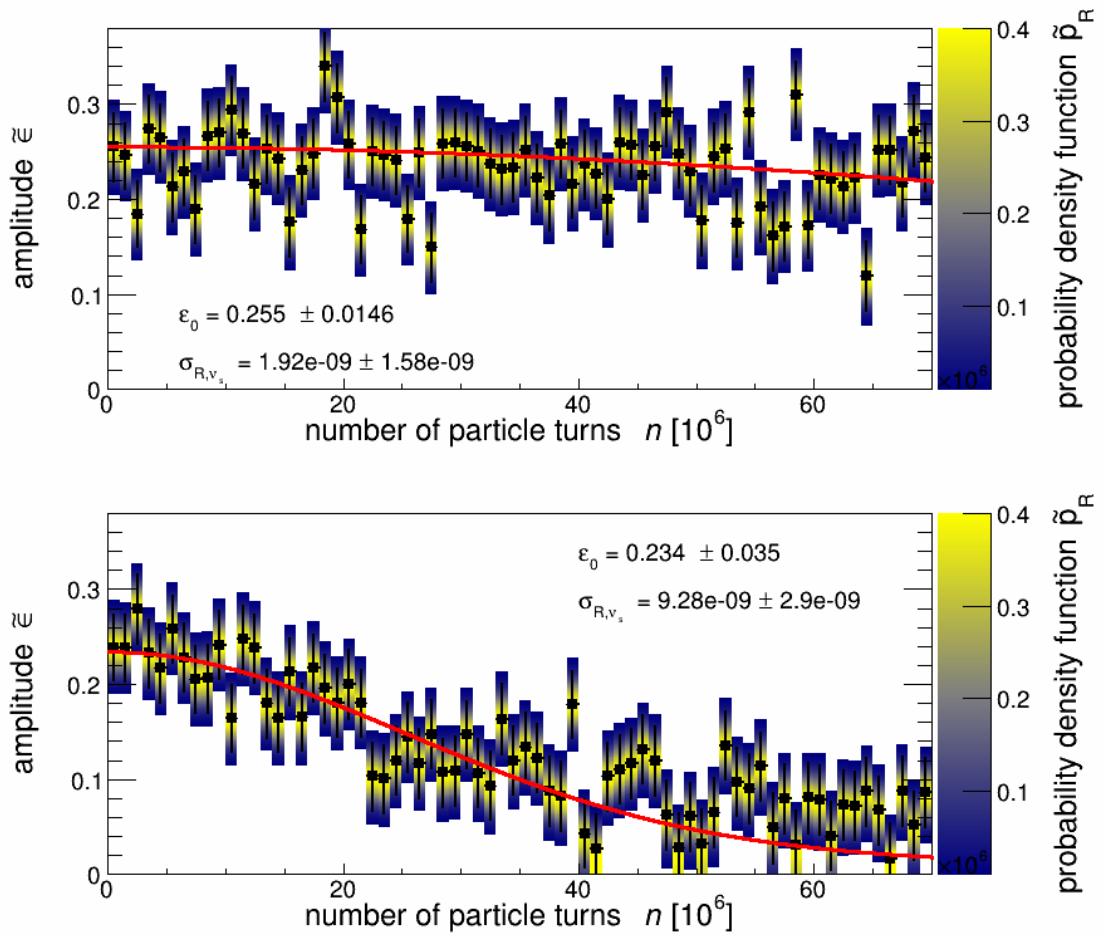


Figure 5.11: Turn depending amplitude for two cycles from runs with different settings of the sextupole magnets. The red curve represents a maximum likelihood fit based on Eq. 5.44. The probability density function of the amplitude based on the measured amplitude is indicated by the color scheme.

## Phase Determination

The spin tune  $\nu_s$  is determined by means of the phase information  $\tilde{\varphi}$  obtained by the asymmetry distribution in Fig. 4.3 or by the discrete Fourier Transform (Eq. 4.28). It is supposed that the assumed spin tune  $\nu_s^0$  is fixed to a constant value for the analysis of the whole cycle. Thus, it acts as a baseline with respect to the turn derivative of the phase  $\partial\varphi_s(n)/\partial n$ . Consequently, the turn depending spin tune can be split into a constant term  $\nu_s^0$  and a part, which specifies the turn depending deviation between the true value  $\nu_s(n)$  and  $\nu_s^0$

$$\begin{aligned}\frac{\nu_s(n)}{\nu_s^0} &= 1 + \frac{\delta\nu_s(n)}{\nu_s^0} \\ &= 1 + \frac{\delta f_s(n)}{f_s} - \frac{\delta f_{\text{RF}}(n)}{f_{\text{RF}}} \\ &= 1 + \frac{1}{2\pi\nu_s^0} \frac{\partial\varphi_s(n)}{\partial n}.\end{aligned}\tag{6.1}$$

Here,  $f_s$  corresponds to frequency of the spin precession and  $f_{\text{RF}}$  denotes the RF cavity frequency. Observing the phase difference  $\varphi_s(n)$  allows the determination of the turn depending spin tune  $\nu_s(n)$ .

$$\nu_s(n) = \nu_s^0 + \frac{1}{2\pi} \frac{\partial\varphi_s(n)}{\partial n},\tag{6.2}$$

Note that Eq. 6.1 is independent of the cavity frequency  $f_{\text{RF}}$ .

In the following, several approaches are discussed in order to provide a proper estimator of the phase parameter  $\tilde{\varphi}_s$  and of its confidence interval  $\sigma_{\tilde{\varphi}_s}$ . First, the wrapped probability density function of the phase is derived. Hereinafter, the maximum likelihood method is used to show that the phase estimator is unbiased. In addition, the confidence interval of the phase estimator is determined based on the Feldmann-Cousin algorithm. Finally, the theory of directional statistic is used to identify a proper confidence interval based on the estimated amplitude  $\tilde{\epsilon}$ .

At the end of this chapter, the interpolation of the spin tune based on the phase estimator is described, which also includes the discussion of its statistical error.

## 6.1 Wrapped Probability Density Function

Up to now, the standard deviation of the phase has been determined conventionally by

$$\sigma_{\tilde{\varphi}} = \frac{\sigma_{\tilde{\epsilon}}}{\tilde{\epsilon}} = \frac{\sqrt{2}}{\tilde{\epsilon}\sqrt{N}} = \frac{\sqrt{2}}{\tilde{\gamma}_{\text{SNR}}}, \quad (6.3)$$

where  $\tilde{\epsilon}$  denotes the estimated amplitude obtained by the mapping method or discrete Fourier transform,  $N$  represents the number of detected events and  $\tilde{\gamma}_{\text{SNR}}$  is the estimated signal-to-noise ratio. In chapter 5 it was shown, that the estimator of the amplitude is biased because it is composed of the square root of the sum of two quadratic independent random variables. Hence, Feldmann-Cousin intervals are constructed, which cover the requested coverage. Accordingly, distributions of the true amplitude  $\epsilon$  are identified depending on  $\tilde{\epsilon}$ . However, no analytical representation exists to describe these distributions. Thus, look-up tables are generated in order to construct proper confidence intervals.

An estimator of the phase standard deviation is obtained in a similar way. Therefore, the joint probability density function of two Normal distributed random variables  $A$  and  $B$  from Eq. 5.3 is evaluated. In comparison to section 5 the integration is performed with respect to the amplitude parameter  $\tilde{\epsilon} \in (0, \infty)$

$$p_{\varphi}(\tilde{\epsilon}, \tilde{\varphi}; \epsilon, \varphi, \sigma) d\tilde{\epsilon} d\tilde{\varphi} = \frac{\tilde{\epsilon}}{2\pi\sigma^2} e^{-\frac{(\tilde{\epsilon}^2 + \epsilon^2)}{2\sigma^2}} \cdot e^{-\frac{2\tilde{\epsilon}\epsilon(\sin(\varphi)\sin(\tilde{\varphi}) + \cos(\varphi)\cos(\tilde{\varphi}))}{2\sigma^2}} d\tilde{\varphi} d\tilde{\epsilon}, \quad (6.4)$$

$$\begin{aligned} p_{\varphi}(\tilde{\varphi}; \epsilon, \varphi, \sigma) d\tilde{\varphi} &= \left[ \int_0^{\infty} \frac{\tilde{\epsilon}}{2\pi\sigma^2} e^{-\frac{(\tilde{\epsilon}^2 + \epsilon^2)}{2\sigma^2}} e^{-\frac{2\tilde{\epsilon}\epsilon\cos(\tilde{\varphi} - \varphi)}{2\sigma^2}} d\tilde{\epsilon} \right] d\tilde{\varphi} \\ &= \frac{e^{-\frac{\epsilon^2}{2\sigma^2}}}{2\pi} \left[ 1 - \frac{\sqrt{\pi}\epsilon\cos(\tilde{\varphi} - \varphi)}{\sqrt{2\sigma^2}} e^{\frac{\epsilon^2\cos^2(\tilde{\varphi} - \varphi)}{2\sigma^2}} \operatorname{erfc} \left( \frac{\epsilon\cos(\tilde{\varphi} - \varphi)}{\sqrt{2\sigma^2}} \right) \right] d\tilde{\varphi}, \end{aligned} \quad (6.5)$$

where  $\operatorname{erfc}$  denotes the complementary error function. The probability density function can be written as a function of two parameters, namely the signal-to-noise ratio  $\gamma_{\text{SNR}} = \frac{\epsilon}{\sigma} = \sqrt{2}\gamma_{\text{SNR}}^{\dagger}$  and the difference between the estimated and the true value  $\Delta\varphi = \tilde{\varphi} - \varphi$ . In addition, the complementary error function  $\operatorname{erfc}$  can be expressed in terms of the Kummer confluent hypergeometric function  ${}_1F_1$  of first kind

$$\begin{aligned} \sqrt{\pi}\cos(x)e^{x^2}\operatorname{erfc}(x) &= \sqrt{\pi}\cos(x)e^{x^2}(1 - \operatorname{erf}(x)) \\ &= \sqrt{\pi}\cos(x)e^{x^2} - {}_1F_1\left(1, \frac{1}{2}, x^2\right) - 1, \end{aligned} \quad (6.6)$$

where  $\operatorname{erf}$  denotes the error function. Accordingly, the probability density function of the phase is given by

$$p_{\varphi}(\tilde{\varphi}; \gamma_{\text{SNR}}^{\dagger}, \Delta\varphi) = \frac{e^{-(\gamma_{\text{SNR}}^{\dagger})^2}}{2\pi} \left( {}_1F_1 \left[ 1; \frac{1}{2}; \left( \gamma_{\text{SNR}}^{\dagger} \cos \Delta\varphi \right)^2 \right] - \sqrt{\pi}\gamma_{\text{SNR}}^{\dagger} \cos \Delta\varphi e^{(\gamma_{\text{SNR}}^{\dagger} \cos \Delta\varphi)^2} \right). \quad (6.7)$$

Apparently, Eq. 6.7 has not been extensively discussed in other scientific work, thus neither

a name nor a proper notation exists, yet. In the following, the subscript  $\varphi$  will indicate the denotation of the probability density function given in Eq. 6.7. The domain of definition of the estimated phase is given by  $\tilde{\varphi} \in (-\pi, \pi]$ . Additionally,  $p_\varphi(\tilde{\varphi}; \gamma_{\text{SNR}}, \varphi)$  represents a wrapped probability density function, which is constructed by wrapping the pdf on the line around the circumference of a unit circle [42]. The normalization is ensured, since the integral from  $-\pi$  to  $\pi$  yields unity  $\int_{-\pi}^{\pi} p_\varphi(\tilde{\varphi}) d\tilde{\varphi} = 1$ .

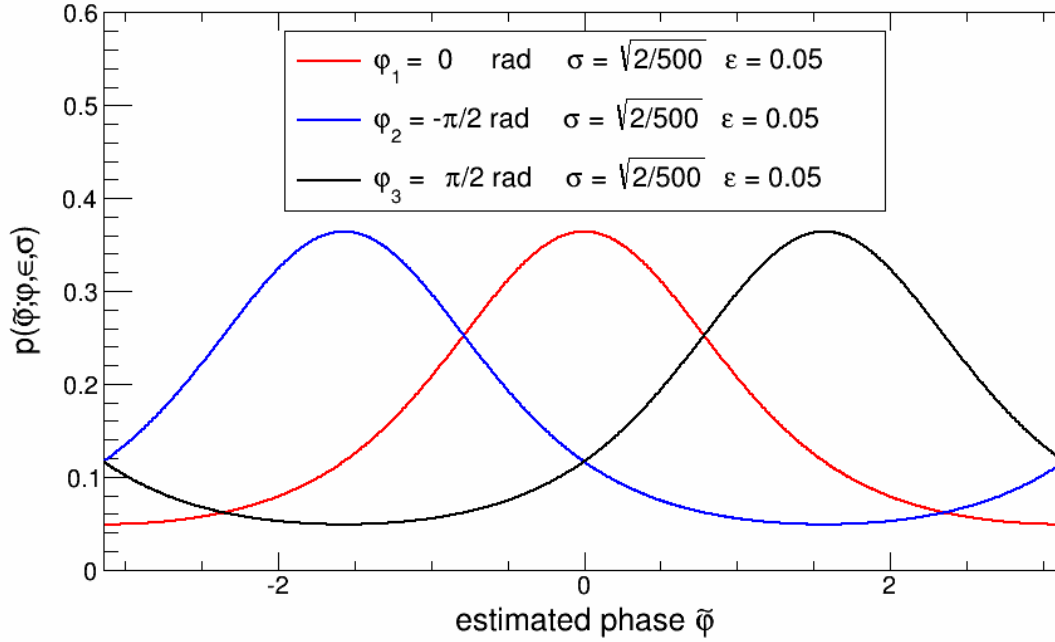


Figure 6.1: Probability distributions for different true phases  $\varphi_1 = 0$ ;  $\varphi_2 = -\frac{\pi}{2}$ ;  $\varphi_3 = \frac{\pi}{2}$ , but same standard deviation  $\sigma^2 = \frac{2}{500}$  and amplitude  $\epsilon = 0.05$

In Fig. 6.1 three examples of  $p_\varphi(\tilde{\varphi}; \epsilon, \varphi)$  are shown for different true phase values  $\varphi_1 = 0$ ;  $\varphi_2 = -\frac{\pi}{2}$ ;  $\varphi_3 = \frac{\pi}{2}$  and the same standard deviation  $\sigma = \sqrt{2/500}$ . The true amplitude is chosen relatively small  $\epsilon = 0.05$  compared to  $\sigma$  ( $\gamma_{\text{SNR}} \ll 1$ ) in order to unfold the characteristic behavior of  $p_\varphi(\tilde{\varphi}; \epsilon, \varphi)$ . The distribution is symmetric about the mean value  $\hat{\varphi}_\varphi = \langle \tilde{\varphi} \rangle$ . Its variance  $\sigma_{\hat{\varphi}_\varphi}^2$  depends on the standard deviation  $\sigma$  and the true amplitude  $\epsilon$ . In the following, three different approaches are discussed to determine a proper estimator of the phase  $\tilde{\varphi}$  and its standard deviation  $\sigma_{\tilde{\varphi}}$ .

### 6.1.1 Maximum Likelihood Estimator

The maximum likelihood estimator  $\hat{\varphi}_{\text{MLE}}$  is obtained by taking the logarithm of Eq. 6.5

$$\log \mathcal{L} = \log \left[ \frac{e^{-\frac{\epsilon^2}{2\sigma^2}}}{2\pi} \left[ 1 - \frac{\sqrt{\pi}\epsilon \cos(\tilde{\varphi} - \varphi)}{\sqrt{2\sigma^2}} e^{\frac{\epsilon^2 \cos^2(\tilde{\varphi} - \varphi)}{2\sigma^2}} \operatorname{erfc} \left( \frac{\epsilon \cos(\tilde{\varphi} - \varphi)}{\sqrt{2\sigma^2}} \right) \right] d\tilde{\varphi} \right] \quad (6.8)$$

$$\sim \log \frac{\epsilon \cos(\tilde{\varphi} - \varphi)}{\sqrt{2\sigma^2}} + \frac{\epsilon^2 \cos^2(\tilde{\varphi} - \varphi)}{2\sigma^2} + \log \operatorname{erfc} \left( \frac{\epsilon \cos(\tilde{\varphi} - \varphi)}{\sqrt{2\sigma^2}} \right). \quad (6.9)$$

The global maximum of  $\log \mathcal{L}$  is given by

$$0 \stackrel{!}{=} \frac{d \log \mathcal{L}}{d\varphi} \quad (6.10)$$

$$0 = \frac{\sin(\tilde{\varphi} - \hat{\varphi}_{\text{MLE}})}{\cos(\tilde{\varphi} - \hat{\varphi}_{\text{MLE}})} + \frac{\epsilon^2}{2\sigma^2} \sin(2[\tilde{\varphi} - \hat{\varphi}_{\text{MLE}}]) + \frac{\epsilon}{\sqrt{2\pi\sigma^2}} \sin(\tilde{\varphi} - \hat{\varphi}_{\text{MLE}}) e^{\frac{\epsilon^2}{2\sigma^2} \cos^2(\tilde{\varphi} - \hat{\varphi}_{\text{MLE}})}. \quad (6.11)$$

The right hand side becomes zero if  $\sin(\tilde{\varphi} - \hat{\varphi}_{\text{MLE}}) \stackrel{!}{=} 2\pi k$  for  $k \in \mathbb{Z}$ . Thus, the estimated value  $\tilde{\varphi} = \hat{\varphi}_{\text{MLE}}$  denotes an unbiased,  $2\pi$ -periodic maximum likelihood estimator of the phase.

### 6.1.2 Circular Moment Estimator

According to the theory of directional statistics, the  $m$ -th moment of a wrapped probability distribution  $p_w(\varphi)$  based on the random variable  $\varphi$  is given by [43]

$$\hat{z}^m = \int_{-\pi}^{\pi} p(z) z^m dz = \int_{-\pi}^{\pi} p(\varphi) e^{im\varphi} d\varphi, \quad (6.12)$$

with  $z = e^{i\varphi} = \cos \varphi - i \sin \varphi$ ,  $\varphi = \arg z, |z| = \sqrt{\Re(z)^2 + \Im(z)^2}$ . Here,  $\Im$  and  $\Re$  denote the imaginary and the real part of  $z$ , respectively.

Consequently, the  $m$ -th moment of  $p_\varphi(\tilde{\varphi}; \epsilon, \varphi)$  in Eq. 6.5 reads

$$\hat{z}^m = \int_{-\pi}^{\pi} \frac{e^{-\frac{\epsilon^2}{2\sigma^2}}}{2\pi} \left[ 1 - \frac{\sqrt{\pi}\epsilon \cos(\tilde{\varphi} - \varphi)}{\sqrt{2\sigma^2}} e^{\frac{\epsilon^2 \cos^2(\tilde{\varphi} - \varphi)}{2\sigma^2}} \operatorname{erfc} \left( \frac{\epsilon \cos(\tilde{\varphi} - \varphi)}{\sqrt{2\sigma^2}} \right) \right] e^{im\tilde{\varphi}} d\tilde{\varphi}. \quad (6.13)$$

There exists no analytical representation of this integral for  $m \in \mathbb{N}$  and  $\varphi \in (-\pi, \pi]$ . Thus, a numerical solution is required to obtain the first circular moment ( $m = 1$ ) of  $p_\varphi(\tilde{\varphi}; \epsilon, \varphi)$  respectively the circular estimator of the phase

$$\hat{\varphi}^{\text{circ}} = \arg \hat{z}^1 = \operatorname{atan2} \left( \Im(\hat{z}^1), \Re(\hat{z}^1) \right). \quad (6.14)$$

In the left part of Fig. 6.3 the true phase  $\varphi$  is shown as a function of  $\hat{\varphi}^{\text{circ}}$  for a given standard deviation  $\sigma = \sqrt{\frac{2}{500}}$  and a true amplitude  $\epsilon = 0.05$ . Evidently,  $\hat{\varphi}^{\text{circ}}$  represents an unbiased estimator of the phase over the full range  $\varphi \in (-\pi, \pi]$ .

In the previous section, it has been shown, that the standard deviation of the phase  $\sigma_{\tilde{\varphi}}$  is

independent of the phase value itself. Thus, the true value can be set to  $\varphi = 0$  without loss of generality:  $\sigma_{\tilde{\varphi}} \equiv \sigma_{\tilde{\varphi}}(\varphi = 0)$ ). Furthermore, the integral is split into a sine and a cosine term. The first circular moment ( $m = 1$ ) yields

$$\hat{z}^1(\varphi = 0) = \int_{-\pi}^{\pi} \frac{e^{-\frac{\epsilon^2}{2\sigma^2}}}{2\pi} \left[ 1 - \frac{\sqrt{\pi}\epsilon \cos \tilde{\varphi}}{\sqrt{2\sigma^2}} e^{-\frac{\epsilon^2 \cos^2 \tilde{\varphi}}{2\sigma^2}} \operatorname{erfc} \left( \frac{\epsilon \cos \tilde{\varphi}}{\sqrt{2\sigma^2}} \right) \right] (\cos \tilde{\varphi} - i \sin \tilde{\varphi}) d\tilde{\varphi}, \quad (6.15)$$

The integral of the sinus vanishes  $\int_{-\pi}^{\pi} p(\tilde{\varphi})_{\varphi} \sin(\tilde{\varphi}) d\varphi = 0$ , since it is an odd function. The solution of the cosine term is more complicated and it is derived in appendix A.6. Subsequently, the following expressions are obtained for the imaginary respectively real part

$$\Im(\hat{z}^1) = 0, \quad (6.16)$$

$$\Re(\hat{z}^1) = \sqrt{\frac{\pi}{2}} \sqrt{\frac{\epsilon^2}{4\sigma^2}} e^{-\frac{\epsilon^2}{4\sigma^2}} \left[ I_0 \left( \frac{\epsilon^2}{4\sigma^2} \right) + I_1 \left( \frac{\epsilon^2}{4\sigma^2} \right) \right], \quad (6.17)$$

$$\begin{aligned} R_{z^1} &= |\hat{z}^1| \\ &= \sqrt{(\Im(\hat{z}^1))^2 + (\Re(\hat{z}^1))^2} \\ &= \sqrt{\frac{\pi}{2}} \sqrt{\frac{\epsilon^2}{4\sigma^2}} e^{-\frac{\epsilon^2}{4\sigma^2}} \left[ I_0 \left( \frac{\epsilon^2}{4\sigma^2} \right) + I_1 \left( \frac{\epsilon^2}{4\sigma^2} \right) \right], \end{aligned} \quad (6.18)$$

where  $R_{z^1} \in (0, 1)$  denotes the length of the mean resultant, which corresponds to the sum of all vectors of the population. The first circular moment of the phase corresponds to the true one  $\hat{\varphi}^{\text{circ}} = \operatorname{atan2} \left( \Im(\hat{z}^1), \Re(\hat{z}^1) \right) = \varphi = 0$ , since the imaginary part yields zero.

### 6.1.3 Confidence Interval of Estimated Phase

The Feldmann-Cousin algorithm, which was already discussed in section 5.3), allows the construction of the confidence interval. Therefore, the wrapped probability density function in Eq. 6.7 is evaluated for different true phase values  $\varphi \in [-\pi, \pi)$  as a function of the estimated phase  $\tilde{\varphi} \in [-\pi, \pi)$ . The horizontal projection on the left-hand side plot of Fig. 6.2 shows the pdf for a given true amplitude  $\epsilon = \sqrt{2} \cdot 0.02$  and standard deviation  $\sigma = \sqrt{2/500}$ . Obviously, the Feldmann-Cousin estimator of the phase is unbiased, since the most probable value coincides with the estimated one  $\varphi_{\text{best}}(\tilde{\varphi}) = \hat{\varphi}_{\text{FC}} = \tilde{\varphi}$ .

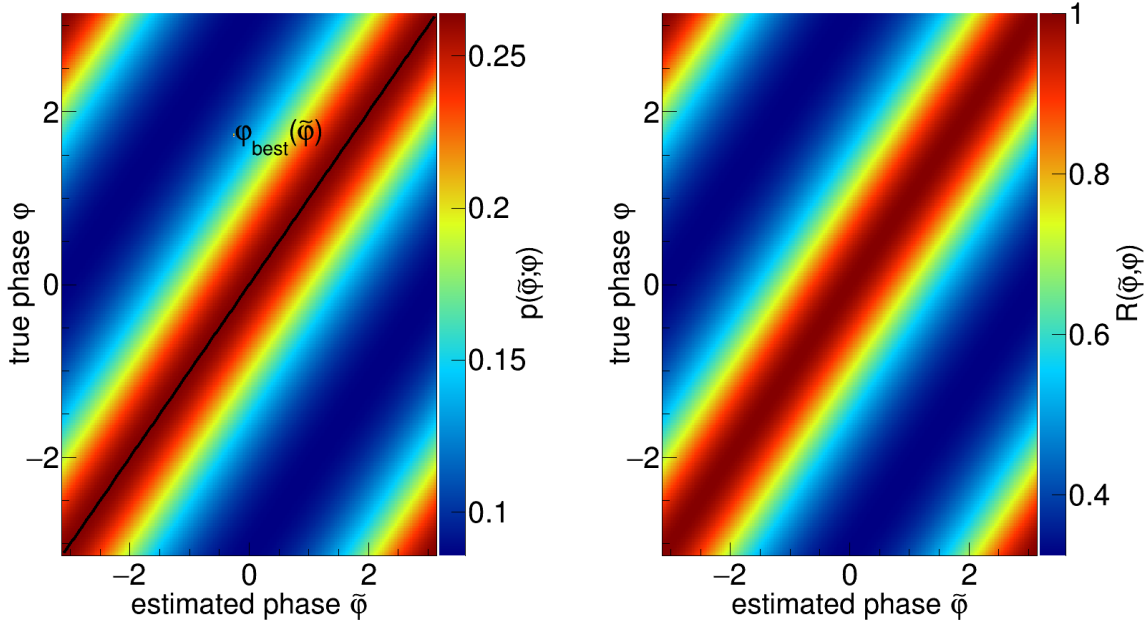


Figure 6.2: The plot on the left-hand side shows the probability density functions of the estimated phase  $p_{\varphi}(\tilde{\varphi}; \epsilon, \varphi)$  for a given true amplitude  $\epsilon = \sqrt{2} \cdot 0.2$  and a standard deviation  $\sigma = \sqrt{2/500}$ . Additionally, the most probable value  $\varphi_{\text{best}}(\tilde{\varphi})$  is given by the black line. On the right-hand side the likelihood ratio  $R(\tilde{\varphi}, \varphi) = p(\tilde{\varphi}; \varphi) / p(\tilde{\varphi}; \varphi_{\text{best}})$  is shown.

On the right-hand side of Fig. 6.2, the likelihood ratio  $R_{\varphi}(\tilde{\varphi}, \varphi) = p_{\varphi}(\tilde{\varphi}; \varphi) / p_{\varphi}(\tilde{\varphi}; \varphi_{\text{best}})$  is shown. It is symmetric about the unbiased estimator  $\hat{\varphi}_{\text{FC}}$ , since the wrapped pdf is invariant under the substitution  $\tilde{\varphi} \leftrightarrow \varphi$ , i.e.  $p_{\varphi}(\tilde{\varphi}; \epsilon, \varphi, \sigma) = p_{\varphi}(\varphi; \epsilon, \tilde{\varphi}, \sigma)$ . Therefore, the confidence interval of the phase is independent of the estimated phase  $\tilde{\varphi}$  itself and the quantity  $\sigma_{\tilde{\varphi}}^{\text{FC}}(\epsilon, \sigma)$  depends only on the true amplitude and its standard deviation.

In order to determine the 68.3 % confidence interval, the following integral is solved

$$\begin{aligned}
 0.683 &\stackrel{!}{=} \int_{-\sigma_{\tilde{\varphi}}^{\text{FC}}(\gamma_{\text{SNR}})}^{\sigma_{\tilde{\varphi}}^{\text{FC}}(\gamma_{\text{SNR}})} p_{\varphi}(\tilde{\varphi}; \epsilon, \varphi) d\tilde{\varphi} \\
 &= \frac{e^{-(\gamma_{\text{SNR}}^{\dagger})^2}}{\pi} \int_0^{\sigma_{\tilde{\varphi}}^{\text{FC}}(\gamma_{\text{SNR}})} \left( {}_1F_1 \left[ 1; \frac{1}{2}; \left( \gamma_{\text{SNR}}^{\dagger} \cos \Delta\varphi \right)^2 \right] - \sqrt{\pi} \gamma_{\text{SNR}}^{\dagger} \cos \Delta\varphi e^{(\gamma_{\text{SNR}}^{\dagger} \cos \Delta\varphi)^2} \right) d\tilde{\varphi} \\
 &= -\frac{\gamma_{\text{SNR}}^{\dagger}}{2\pi} \text{erf}(\gamma_{\text{SNR}}^{\dagger} \sin \sigma_{\tilde{\varphi}}^{\text{FC}}(\gamma_{\text{SNR}})) + \frac{e^{-(\gamma_{\text{SNR}}^{\dagger})^2}}{\pi} \int_0^{\sigma_{\tilde{\varphi}}^{\text{FC}}(\gamma_{\text{SNR}})} {}_1F_1 \left[ 1; \frac{1}{2}; \left( \gamma_{\text{SNR}}^{\dagger} \cos \Delta\varphi \right)^2 \right] d\tilde{\varphi}.
 \end{aligned} \tag{6.19}$$

The results are shown on the right hand side of Fig. 6.3 as the data points in magenta. For a vanishing amplitude  $\gamma_{\text{SNR}} = 0$  one obtains  $\sigma_{\tilde{\varphi}}^{\text{FC}} \approx 0.683 \cdot \pi = 2.14$  since the first term of Eq. 6.19 vanishes and the integrand becomes unity

$${}_1F_1 \left[ 1; \frac{1}{2}; 0 \right] = 1, \tag{6.20}$$

$$\Rightarrow 0.683 = \frac{\sigma_{\tilde{\varphi}}^{\text{FC}}(\gamma_{\text{SNR}} = 0)}{\pi}. \tag{6.21}$$

For relatively large signal-to-noise ratios  $\gamma_{\text{SNR}} > 4$ ,  $\sigma_{\tilde{\varphi}}^{\text{FC}}$  converges towards the conventional estimator  $\sigma_{\tilde{\varphi}}^{\text{conv}} = \frac{1}{\gamma_{\text{SNR}}}$ .

### Circular Standard Deviation of a Wrapped Normal Distribution

One can find two definitions of the standard deviation of a wrapped Normal distribution, which is given by

$$f_{\text{WN}}(\varphi; \mu, \sigma) = \frac{1}{\sigma\sqrt{2\pi}} \sum_{k=-\infty}^{k=\infty} e^{-\frac{(\varphi - \mu + 2\pi k)^2}{2\sigma^2}}. \tag{6.22}$$

Here,  $\mu$  and  $\sigma$  denote the mean and standard deviation of the unwrapped distribution. In fact, it exists a bounded one  $\sigma_{\tilde{\varphi},\text{b}}^{\text{circ}} \in (0, \sqrt{2})$  and an unbounded one  $\sigma_{\tilde{\varphi},\text{ub}}^{\text{circ}} \in (0, \infty)$

$$\sigma_{\tilde{\varphi},\text{b}}^{\text{circ}} = \sqrt{2(1 - |\hat{z}^1|)} = \sqrt{2(1 - R_{z^1})}, \tag{6.23}$$

$$\sigma_{\tilde{\varphi},\text{ub}}^{\text{circ}} = \sqrt{-2 \ln |\hat{z}^1|} = \sqrt{-2 \ln R_{z^1}}. \tag{6.24}$$

Since the pdf of the phase in Eq. 6.5 does not correspond to a wrapped Normal distribution, both approaches yield a biased estimator for the phase standard deviation. Nonetheless, it is helpful to compare the results in order to obtain a deeper understanding of the principle of circular moments.

### 6.1.4 Conclusion

The lower plot of Fig. 6.3 shows the 68.3% confidence interval as a function of the signal to noise ratio  $\gamma_{\text{SNR}} = \frac{\varepsilon}{\sigma}$ . The green and the black curves correspond to the bounded and unbounded case, respectively. In magenta, the results of the Feldmann-Cousin algorithm are shown. The red curve represents the conventional approach given in Eq. 6.3 and the blue

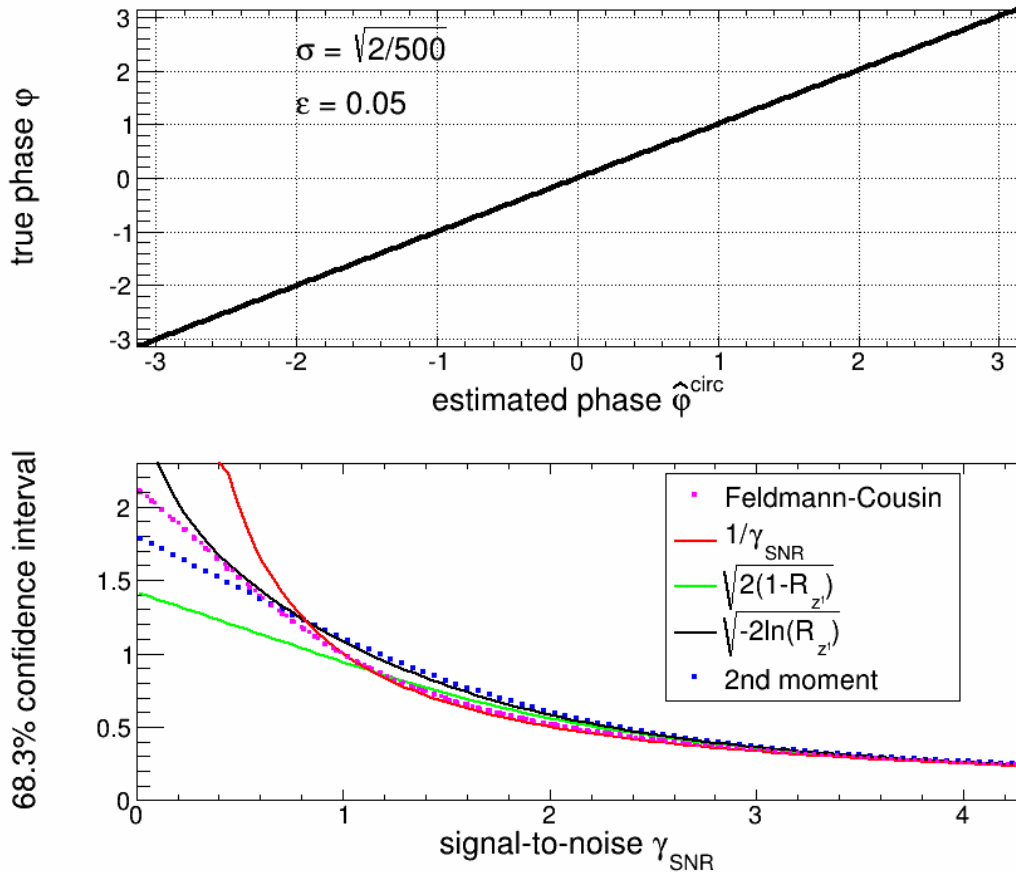


Figure 6.3: Upper plot: the true phase value  $\varphi$  is shown against the estimated one  $\hat{\varphi}^{\text{circ}}$ . Lower plot: The 68.3% confidence interval obtained by the bounded (green) and unbounded (black) 2nd moment estimation based on directional statistics. The blue points represent the 2nd moment of the linear pdf and the red curve corresponds to the conventional estimation of standard deviation  $\sigma_{\varphi}^{\text{con}} = \frac{1}{\gamma_{\text{SNR}}}$ . In magenta the result of the Feldmann-Cousin algorithm is shown.

data points are obtained by evaluating the 2nd central moment of a linear probability density function

$$\sigma_{\hat{\varphi}, 2\text{nd}}^2 = \int_{-\pi}^{\pi} (\tilde{\varphi} - \hat{\varphi})^2 p(\tilde{\varphi}) d\tilde{\varphi}. \quad (6.25)$$

For large SNR all methods coincide. However, for  $\gamma_{\text{SNR}} < 2$  a significant deviation occurs. Especially the results obtained by the conventional and the unbounded estimator becomes physical meaningless for  $\gamma_{\text{SNR}} \ll 1$ , since they assume values larger than  $2\pi$ , which exceeds

the domain of definition of  $\tilde{\varphi}$ . The 2nd moment of the linear pdf starts at  $\sigma_{\tilde{\varphi},2\text{nd}}^{\text{max}} = 1.8138 = \frac{2\pi}{\sqrt{12}}$ , which corresponds to the standard deviation of a Uniform distribution within the interval of  $2\pi$ . However, from the theory of directional statistics, one knows that  $\sigma_{\tilde{\varphi},2\text{nd}}$  represents not a proper estimator. Additionally, the 68.3% confidence interval obtained by the bounded circular 2nd moment  $\sigma_{\tilde{\varphi},b}$  provides incorrect results, since it is based on the assumption of a wrapped Normal distribution. In the following, the Feldmann-Cousin estimator is chosen as the most convenient one. It is defined by the solution of the integral in Eq. 6.19.

Hitherto the probability density function of the phase  $p_{\varphi}(\tilde{\varphi}; \varphi, \epsilon, \sigma)$  and its 68.3% confidence interval  $\sigma_{\tilde{\varphi}}^{\text{CF}}(\epsilon, \sigma)$  has been estimated as a function of the true amplitude and the standard deviation. However, the amplitude  $\tilde{\epsilon}$ , estimated based on the mapping method or discrete Fourier transform, is biased by a positive shift and the true amplitude is *a priori* unknown. A deeper discussion of this subject can be found in chapter 5. In the following, an expression of the probability density function depending on the estimated amplitude  $\tilde{p}_{\varphi}(\varphi; \tilde{\varphi}, \tilde{\epsilon}, \sigma)$  is derived by using the Bayes' theorem.

### 6.1.5 Confidence Interval of True Phase

Based on the Bayes' theorem [44] the joint probability density function of  $\epsilon$  and  $\varphi$  can be written as

$$\begin{aligned} \tilde{p}(\epsilon, \varphi; \tilde{\epsilon}, \tilde{\varphi}, \sigma) &= \frac{p(\tilde{\epsilon}, \tilde{\varphi}; \epsilon, \varphi, \sigma)p(\epsilon)p(\varphi)}{p(\tilde{\epsilon})p(\tilde{\varphi})} \\ &= \frac{p(\tilde{\epsilon}, \tilde{\varphi}; \epsilon, \varphi, \sigma)p(\epsilon)}{p(\tilde{\epsilon})} \\ &= \frac{p(\tilde{\epsilon}, \tilde{\varphi}; \epsilon, \varphi, \sigma)p(\epsilon)}{\int_0^{\infty} p_{\text{R}}(\tilde{\epsilon}; \epsilon, \sigma) d\epsilon}. \end{aligned} \quad (6.26)$$

The first reformation is valid since the symmetry about the phase substitution  $\varphi \Leftrightarrow \tilde{\varphi}$  provides  $p(\tilde{\varphi}) = p(\varphi)$ . For the latter step, the normalized distribution of the y-axis projection of the amplitude likelihood ratio (right-hand side of Fig.5.5) is integrated with respect to  $\epsilon$ . In fact, this corresponds to the denominator in Eq. 5.30, where the probability density function for the true amplitude  $p_{\text{R}}(\epsilon; \tilde{\epsilon}, \sigma)$  has been derived.

The integration of Eq. 6.26 with respect to the true amplitude corresponds to the marginal probability density function of the true phase

$$\begin{aligned} \tilde{p}_{\varphi}(\varphi; \tilde{\epsilon}, \tilde{\varphi}, \sigma) &= \int_0^{\infty} \tilde{p}(\epsilon, \varphi; \tilde{\epsilon}, \tilde{\varphi}, \sigma) d\epsilon \\ &= \frac{1}{2\pi} \int_0^{\infty} \frac{e^{-\frac{2\tilde{\epsilon}\epsilon \cos(\varphi - \tilde{\varphi})}{2\sigma^2}} \tilde{p}_{\text{R}}(\epsilon; \tilde{\epsilon})}{I_0\left(\frac{\tilde{\epsilon}\epsilon}{\sigma^2}\right)} d\epsilon. \end{aligned} \quad (6.27)$$

The exact derivation can be found in appendix A.7. Note that the function  $\tilde{p}_{\text{R}}(\epsilon, \tilde{\epsilon})$  has no analytical solution and the integral is solved numerically.

In section 5.1 it was shown, that the Rician distribution 5.4 can be written as a function of the estimated signal-to-noise ratio  $\tilde{\gamma}_{\text{SNR}}$  with a unique parameter  $\gamma_{\text{SNR}}$ . In this representation,

$p_R(\tilde{\gamma}_{\text{SNR}}; \gamma_{\text{SNR}})$  is independent of the standard deviation  $\sigma$ . Consequently, only one map is given based on the Rician distribution  $p_R(\tilde{\epsilon}; \epsilon, \sigma)$  with  $\sigma = 1$ . In addition, the integrand in Eq. 6.27 can be expressed as a function of the signal-to-noise ratio

$$\tilde{p}_\varphi(\varphi; \tilde{\gamma}_{\text{SNR}}, \tilde{\varphi}) = \frac{1}{2\pi} \int_0^\infty \frac{e^{-\tilde{\gamma}_{\text{SNR}} \gamma_{\text{SNR}} \cos(\varphi - \tilde{\varphi})} \tilde{p}_R(\gamma_{\text{SNR}}; \tilde{\gamma}_{\text{SNR}})}{I_0(\tilde{\gamma}_{\text{SNR}} \gamma_{\text{SNR}})} d\gamma_{\text{SNR}}. \quad (6.28)$$

The corresponding probability density function  $\tilde{p}_R(\gamma_{\text{SNR}}; \tilde{\gamma}_{\text{SNR}})$  is presented on the left-hand side of Fig. 6.4. The black curves indicate the 68.3% confidence interval.

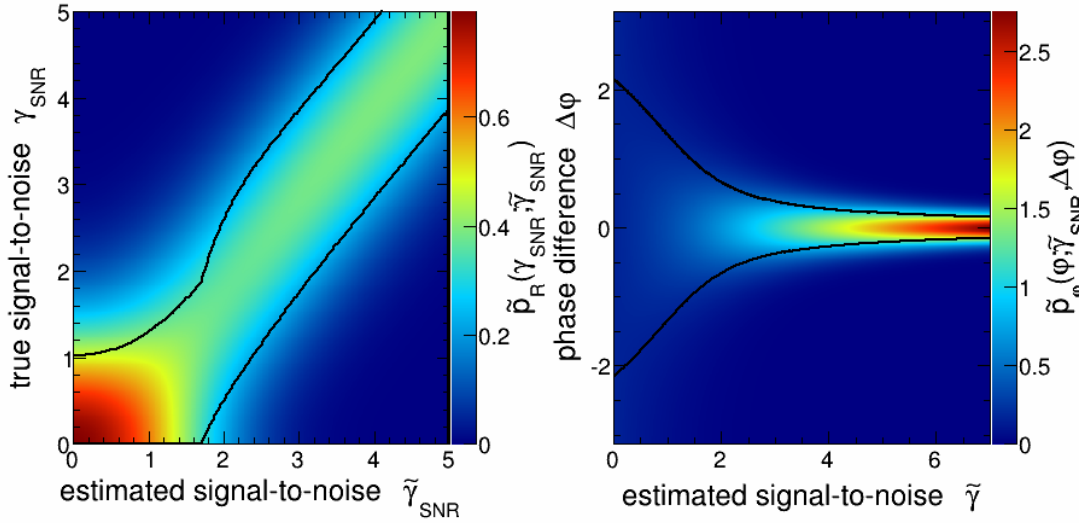


Figure 6.4: Left: probability density function of the true signal-to-noise ratio given a measured one  $\tilde{\gamma}_{\text{SNR}}$ . Right: corresponding pdf of the phase difference  $\Delta\varphi = \varphi - \tilde{\varphi}$  denoted in Eq. 6.28. The black curves indicate the 68.3% confidence interval.

The phase distribution in Eq. 6.28 is shown on the right-hand side of Fig. 6.4. In particular, it is presented for different estimated signal-to-noise ratios and as a function of the difference between the true and the estimated phase value  $\Delta\varphi = \varphi - \tilde{\varphi}$ . Finally, the probability density function of the signal-to-noise ratio and the phase can be determined for each estimated signal-to-noise ratio based on the results presented in Fig. 6.4.

The 68.3% coverage of the y-axis projection is given by the two black curves. Since the probability density function is invariant under phase transformation, the estimator of the confidence interval yields

$$\begin{aligned} 0.683 &\stackrel{!}{=} \int_{-\sigma_{\tilde{\varphi}}^{\text{CF}}(\tilde{\gamma}_{\text{SNR}})}^{\sigma_{\tilde{\varphi}}^{\text{CF}}(\tilde{\gamma}_{\text{SNR}})} \tilde{p}_\varphi(\varphi; \tilde{\gamma}, \Delta\varphi) d\Delta\varphi \\ &= 2 \int_0^{\sigma_{\tilde{\varphi}}^{\text{CF}}(\tilde{\gamma}_{\text{SNR}})} \tilde{p}_\varphi(\varphi; \tilde{\gamma}, \Delta\varphi) d\Delta\varphi. \end{aligned} \quad (6.29)$$

The index CF is meant analogously to the Feldmann-Cousin confidence interval obtained for the phase based on the true signal-to-noise ratio in Eq. 6.19.

In Fig. 6.5 the quantity  $\sigma_{\tilde{\varphi}}^{\text{CF}}(\tilde{\gamma}_{\text{SNR}})$  (black data points) is compared to the standard deviation of the phase  $\sigma_{\tilde{\varphi}}^{\text{conv}} = \frac{1}{\gamma_{\text{SNR}}}$  assuming a Gaussian pdf (red curve). In addition, the confidence interval  $\sigma_{\tilde{\varphi}}^{\text{CF}}(\gamma_{\text{SNR}})$  is shown by the green data points. For the latter, the asymmetric structure of the Rice distribution  $p_R$  is not taken into account. All quantities are independent of the standard deviation  $\sigma$ , since they are expressed as a function of the signal-to-noise ratio. For a vanishing amplitude signal  $\gamma_{\text{SNR}} = 0$  both results yield  $\sigma_{\tilde{\varphi}}(\gamma_{\text{SNR}}) = \sigma_{\tilde{\varphi}}(\tilde{\gamma}_{\text{SNR}}) = 0.683\pi$ . This corresponds to the confidence interval of a Uniform distribution defined on the interval  $[-\pi, \pi)$ . Within the interval  $1 < \gamma_{\text{SNR}} < 4$  one obtains  $\sigma_{\tilde{\varphi}}^{\text{CF}}(\tilde{\gamma}_{\text{SNR}}) > \sigma_{\tilde{\varphi}}^{\text{CF}}(\gamma_{\text{SNR}})$  and for  $\gamma_{\text{SNR}} > 4$  the results of all approaches coincide.

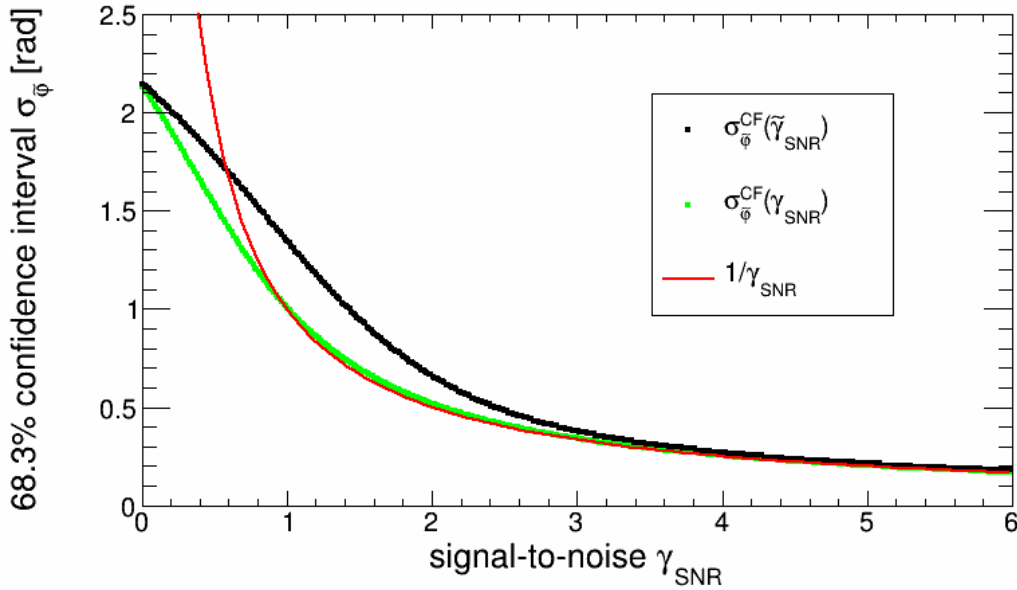


Figure 6.5: Confidence interval depending on the true  $\sigma_{\tilde{\varphi}}(\gamma_{\text{SNR}})$  (green) and the estimated signal-to-noise ratio  $\sigma_{\tilde{\varphi}}(\tilde{\gamma}_{\text{SNR}})$  (black). For comparison, the standard distribution of the discrete Fourier transform is shown in red.

## 6.2 Phase Spectrum

A spin tune phase distribution for a typical cycle ( $70 \cdot 10^6$  turns) based on a spin tune scan is shown in Fig. 6.6. The scan range spans  $\Delta\nu_s^0 = 6 \cdot 10^{-7}$ . In order to obtain a smooth structure of the phase distribution, the initially wrapped phase  $\tilde{\varphi}_s \in [-\pi, \pi)$  is unwrapped by adding  $2\pi$  whenever  $\Delta\tilde{\varphi}_s > \pi$  or subtracting  $2\pi$  whenever  $\Delta\tilde{\varphi}_s < -\pi$ . Here,

$$\Delta\tilde{\varphi}_s(n) = \tilde{\varphi}_s(n+1) - \tilde{\varphi}_s(n) \quad (6.30)$$

represents the difference of two consecutive phase values in the turn domain. The phase wrapping in vertical direction (spin tune domain) is realized by adding or subtracting  $2\pi$ , whenever the difference of two consecutive spin tune bins yield a difference larger than  $\pi$  respectively

$-\pi$ 

$$\Delta\tilde{\varphi}_s(\nu_s^0) = \tilde{\varphi}_s(\nu_s^0 + \Delta\nu_s^0) - \tilde{\varphi}_s(\nu_s^0). \quad (6.31)$$

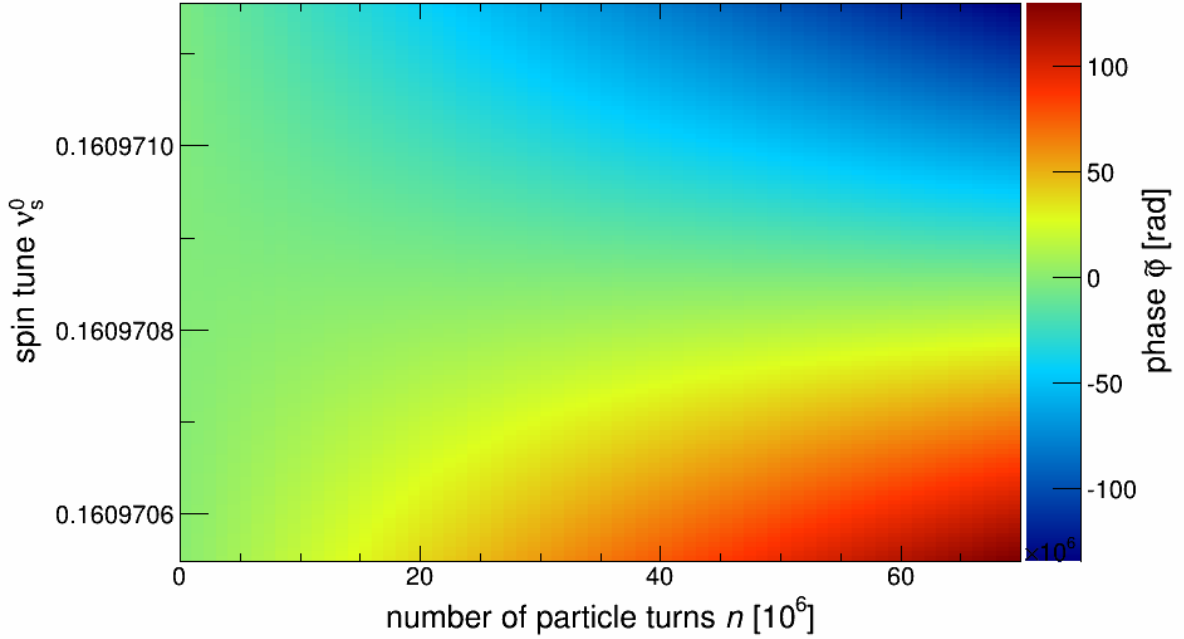


Figure 6.6: Phase spectrum for a typical cycle based on spin tune scan. The initially wrapped phase is unwrapped by subtracting or adding  $2\pi$ , which leads to a smooth phase distribution.

Three vertical projections ( $n_1 = 9.5 \cdot 10^6$ ;  $n_2 = 29.5 \cdot 10^6$ ;  $n_3 = 59.5 \cdot 10^6$ ) of the phase distribution are displayed on the left-hand side of Fig 6.7. In good approximation, the phase is a linear function of the assumed spin tune. The intersection of the straight lines corresponds to the spin tune estimator  $\tilde{\nu}_{s,\text{best}}$ , which is closest to the true value. The linear phase equation as a function of the assumed spin tune reads

$$\tilde{\varphi}(\nu_s^0) = 2\pi(\nu_s^0 - \tilde{\nu}_{s,\text{best}}). \quad (6.32)$$

Three horizontal projections ( $\nu_{s,1}^0 = 0.16097070$ ;  $\nu_{s,2}^0 = 0.16097085$ ;  $\nu_{s,3}^0 = 0.16097100$ ) are presented on the right-hand side of Fig 6.7. Again, the data can be described by a linear function  $\tilde{\varphi}(n)$ , where the slope decreases for an increasing spin tune

$$\tilde{\varphi}(n) = 2\pi n(\tilde{\nu}_{s,\text{best}} - \nu_s^0), \quad (6.33)$$

Note that the slope becomes zero for  $\tilde{\nu}_{s,\text{best}} = \nu_s^0$ .

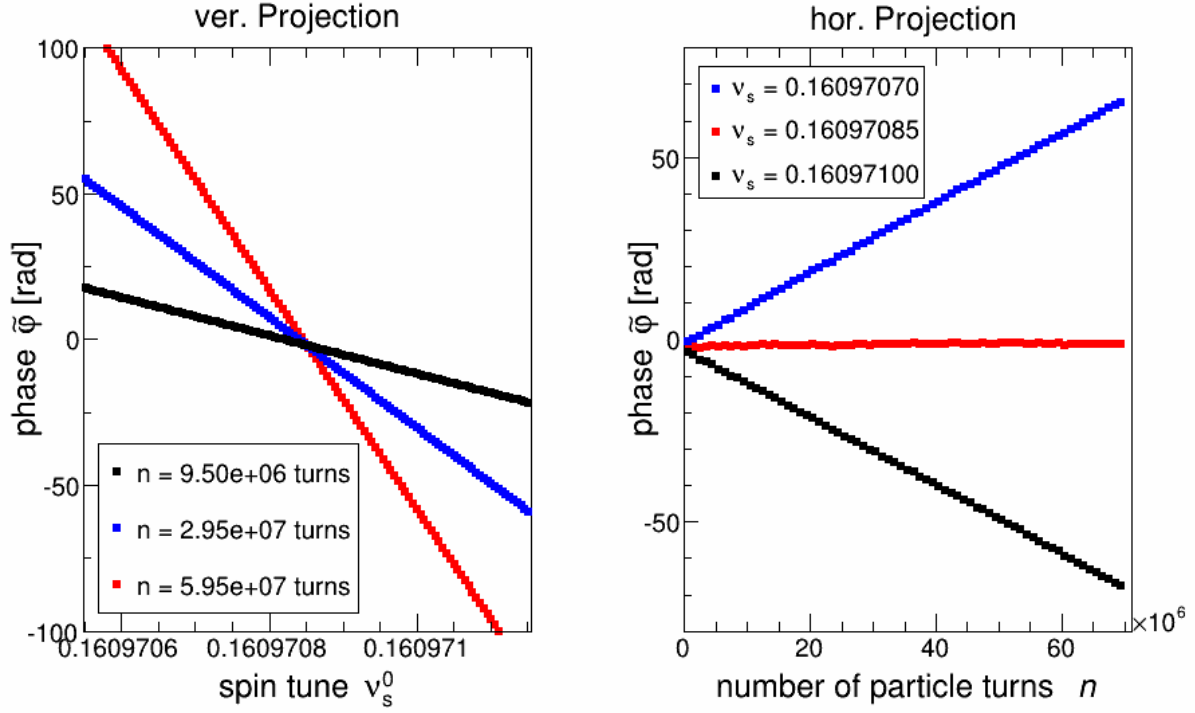


Figure 6.7: Left: vertical projections of the phase spectrum in Fig. 6.6 for different turn numbers. Right: horizontal projections for different assumed spin tune.

### 6.2.1 Maximum Likelihood Fit

An example of a phase distribution is shown in Fig. 6.8. The analysis is performed based on a fixed assumed spin tune for the whole cycle. Note that the error bars do not correspond to a Gaussian probability density function, but are specified by Eq. 6.27 derived in section 6.1.5. In fact, they represent the 68.3% confidence interval of wrapped probability density function. The latter depends on the estimated amplitude  $\tilde{\epsilon}$  and standard deviation  $\sigma$ .

An analytic expression of the turn depending phase  $\varphi_s(n)$  (Eq. 4.56) is derived in section 4.4.1. It is based on the assumption of Rayleigh distributed spin tunes. A linear fit parameter is included in order to take into account the deviation between the fixed assumed spin tune and the true mean spin tune of the ensemble

$$\Delta\omega_s = 2\pi(\nu_s^{\text{ref}} - \nu_s^0), \quad (6.34)$$

where the factor  $2\pi$  considers the transformation from the phase into the spin tune space. A maximum likelihood fit is performed with  $N$  estimated amplitude  $\epsilon_i$  respectively phase  $\varphi_{s,i}$

values based on its probability density function  $p_\varphi(\varphi; \tilde{\epsilon}, \tilde{\varphi})$  (Eq. 6.28)

$$\mathcal{L} = \prod_{i=1}^N \tilde{p}_\varphi(\varphi_s^{\text{fit}}(n_i, \sigma_{R, \nu_s}, \Delta\omega_s, \varphi_s^0); \epsilon_i, \varphi_{s,i}) . \quad (6.35)$$

$$\varphi_s^{\text{fit}}(n, \sigma_{R, \nu_s}, \Delta\omega_s, \varphi_s^0) = \varphi_s^0 + \Delta\omega_s n - \arctan \left( \frac{e^{(\sqrt{2}\pi\sigma_{R, \nu_s} n)^2}}{\sqrt{2\pi}\pi\sigma_{R, \nu_s} n} - \operatorname{erfi}(\sqrt{2}\pi\sigma_{R, \nu_s} n) \right) , \quad (6.36)$$

where  $\varphi_s^0$  is the initial phase and  $\sigma_{R, \nu_s}$  denotes the scale parameter of the spin tune distribution. The parameter  $\Delta\omega_s$  specifies the reference spin tune  $\nu_s^{\text{ref}}$  6.34, which corresponds mathematically to the limit at infinity  $\nu_s(n \rightarrow \infty) = \nu_s^{\text{ref}}$ .

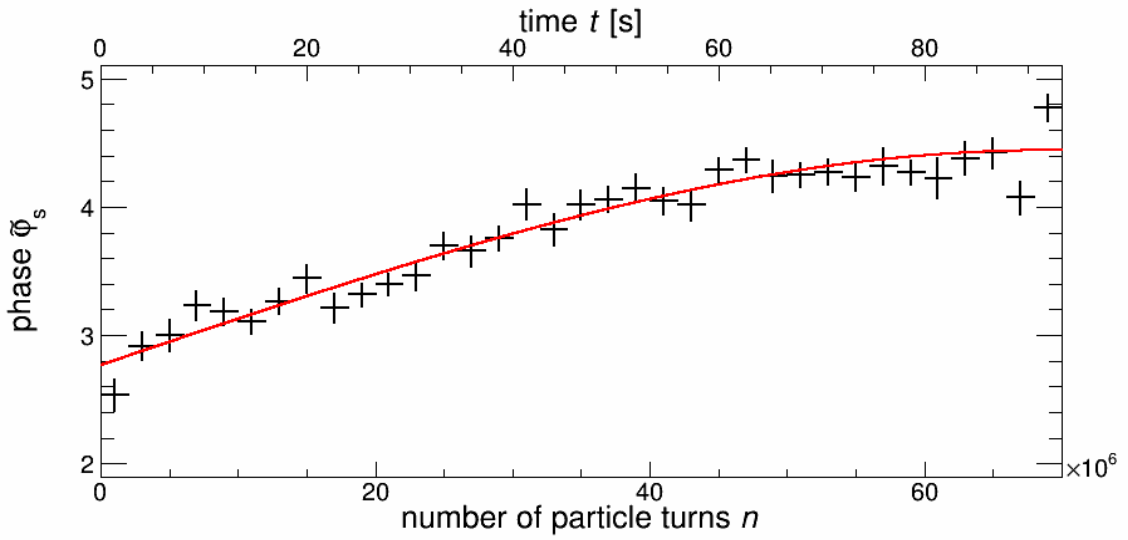


Figure 6.8: Turn depending phase distribution obtained for a fixed assumed spin tune. The red curve represents a maximum likelihood fit of the phase based on Eq. 6.35.

Even though the probability density function is symmetric about the maximum likelihood estimator  $\hat{\varphi}_{s, \text{MLE}}$ , the errors  $\sigma_{\Delta\omega_s}$  and  $\sigma_{\sigma_{R, \nu_s}}$  of the parameters are asymmetric due to the non-linearity of the fit function  $\varphi_s^{\text{fit}}$ . This fact is reflected in Fig. 6.9, where two contour plots are shown for the 2-dimensional parameter space  $\Delta\omega_s$  and  $\sigma_{R, \nu_s}$ . The 68.3% and the 95.4% confidence interval are represented in blue and in black, respectively. Both structures shape an inclined and oval form, which is obviously asymmetric. Thus, the maximum likelihood parameters are listed with their asymmetric 68.3% confidence interval. In addition, the covariance between both parameters is shown, which denotes an important quantity in order to determine the confidence interval of the turn depending spin tune  $\sigma_{\nu_s}$ .

In the example shown in Fig. 6.8, the spin tune of the reference particle is determined to

$$\nu_s^{\text{ref}} = \nu_s^0 + \frac{1}{2\pi} \Delta\omega_s = 0.16097084867 \left( \begin{smallmatrix} +0.39 \\ -0.31 \end{smallmatrix} \times 10^{-9} \right) . \quad (6.37)$$

This yields a precision of the order of  $10^{-10}$ . The scale parameter of the spin tune distribution

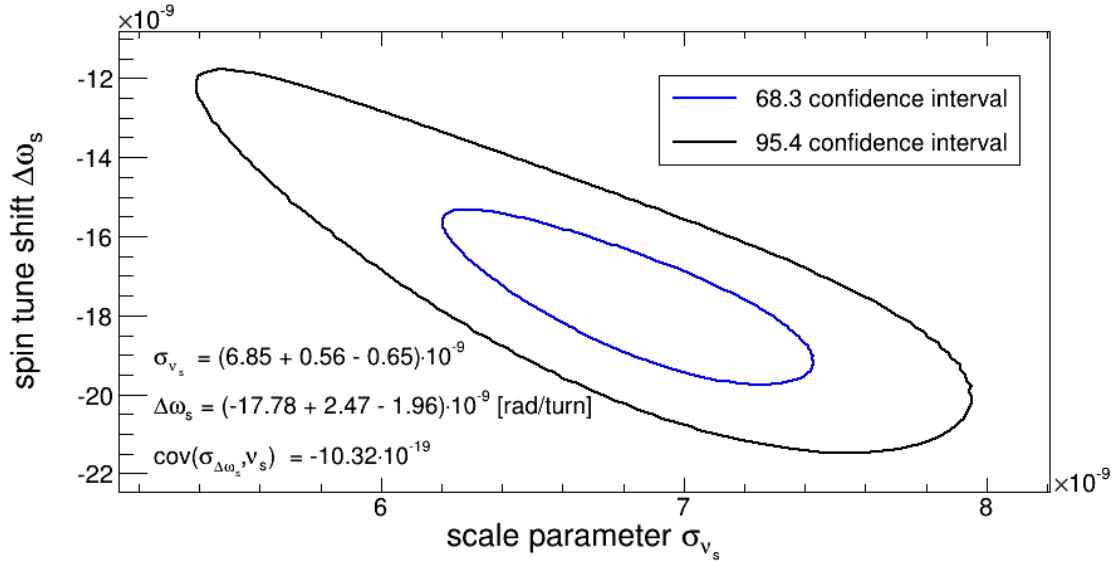


Figure 6.9: Contour plot of the two parameters  $\Delta\omega_s$  and  $\sigma_{R,\nu_s}$ . The 68.3% confidence interval is shown in blue, whereas the black line indicates the 95.4% confidence level.

and the spin coherence time are given by

$$\sigma_{R,\nu_s} = (6.85^{+0.56}_{-0.65}) \times 10^{-9}, \quad (6.38)$$

$$\tau_{\text{SCT}} = \frac{0.2325 \text{ turns}}{\sigma_{R,\nu_s}} = (33.94^{+2.77}_{-3.22}) \times 10^6 \text{ turns}. \quad (6.39)$$

Note that the amplitude spectrum  $\epsilon(n)$  of each cycle provides an estimator of  $\tau_{\text{SCT}}$ , as well. Consequently, the spin coherence time is specified by means of two independent analysis methods (phase and amplitude spectrum). A more detailed discussion of this topic is given in chapter 7, where the results of the beamtime in 2013-2015 are presented.

### 6.3 Combination of Individual Detectors

In this section three procedures are discussed in order to combine the events of the individual detectors. Therefore, it is helpful to define the phase shift between the individual detectors as

$$\Delta\tilde{\varphi} = \tilde{\varphi}_s^U - (\tilde{\varphi}_s^D + \pi). \quad (6.40)$$

For this purpose, it must be ensured that the phase of the up detector is wrapped in the interval  $\tilde{\varphi}_s^U \in [0, \pi]$ , where the down detector possesses  $\tilde{\varphi}_s^D \in [-\pi, 0]$ . Three methods are investigated to determine  $\tilde{\varphi}_s$  for a combined data set

1. The weighted average of  $\tilde{\varphi}_s^U$  and  $\tilde{\varphi}_s^D$  is formed.
2. The discrete Fourier transform of a complete data set, where the events of the up detector are shifted by  $\pi$  with respect to the down detector.
3. The asymmetry determination based on the mapping method explained in section 4.1.2.

#### 6.3.1 Weighted Average

The conventional calculation of the weighted average yields

$$\tilde{\varphi}_{s,\text{wa}} = \frac{\tilde{\varphi}_s^U \cdot \sigma_{\tilde{\varphi}_s^D}^2 + (\tilde{\varphi}_s^D + \pi) \cdot \sigma_{\tilde{\varphi}_s^U}^2}{\sigma_{\tilde{\varphi}_s^U}^2 + \sigma_{\tilde{\varphi}_s^D}^2}, \quad (6.41)$$

where the standard deviation of the phase  $\sigma_{\tilde{\varphi}_s^X}$  ( $X=U, D$ ) is given by the estimated amplitude  $\tilde{\epsilon}$  and the number of detected events  $N$  in the macroscopic measurement interval  $\Delta n$

$$\sigma_{\varphi_s} = \frac{1}{\tilde{\epsilon}\sqrt{2N}}. \quad (6.42)$$

Without loss of generality, the phase of the up detector is set to  $\tilde{\varphi}_s^U = 0$ , which yields

$$\tilde{\varphi}_{s,\text{wa}} = -\frac{\Delta\tilde{\varphi}}{1 + \left(\frac{\sigma_{\tilde{\varphi}_s^D}}{\sigma_{\tilde{\varphi}_s^U}}\right)^2} \quad (6.43)$$

$$= -\frac{\Delta\tilde{\varphi}}{1 + \frac{N_U}{N_D} \cdot \left(\frac{\tilde{\epsilon}_U}{\tilde{\epsilon}_D}\right)^2}, \quad (6.44)$$

with the standard deviation

$$\sigma_{\tilde{\varphi}_{s,\text{wa}}}^2 = \frac{\sigma_{\tilde{\varphi}_s^D}^2 \sigma_{\tilde{\varphi}_s^U}^2}{\sigma_{\tilde{\varphi}_s^D}^2 + \sigma_{\tilde{\varphi}_s^U}^2} \quad (6.45)$$

$$= \frac{2}{(N_U \tilde{\epsilon}_U^2 + N_D \tilde{\epsilon}_D^2)}. \quad (6.46)$$

In the case of  $\tilde{\epsilon}_U = \tilde{\epsilon}_D$  and  $N_U = N_D$ , the phase is given by  $\tilde{\varphi}_{s,wa} = -\frac{\Delta\tilde{\varphi}}{2}$ , which becomes null if the phase difference yields  $\tilde{\varphi}_s^U = \tilde{\varphi}_s^D + \pi$ . Thus, if the phase shift between both detectors matches exactly  $\pi$ , the weighted average is coherent with the up detector and shifted by  $\pi$  with respect to the results of the down detector.

### 6.3.2 Discrete Fourier Transform of two Sinusoidal Functions

The linearity of the Fourier transform  $\mathcal{F}(a \cdot f + b \cdot g) = a\mathcal{F}(f) + b\mathcal{F}(g)$  and the time shift  $\mathcal{F}(f(n-a)) = e^{-iav_s} \mathcal{F}(f(n))$  are used to determine the arithmetic mean of the Fourier transform of two sinusoidal functions with a tiny phase shift and different amplitudes but same frequencies

$$f(n) = \frac{1}{2} [P_U(n) - P_D(n)] \quad (6.47)$$

$$= \frac{1}{2} \left[ \epsilon_U \cos(2\pi\nu_s n + \tilde{\varphi}_s^U) + \epsilon_D \cos(2\pi\nu_s n + \tilde{\varphi}_s^D) \right] \quad (6.48)$$

$$= \frac{1}{2} \left[ \epsilon_U \cos(2\pi\nu_s n) - \epsilon_D \cos(2\pi\nu_s n - \Delta\tilde{\varphi}) \right]. \quad (6.49)$$

For the latter transformation, the phase of the up detector is set to zero and the definition of the phase difference from Eq. 6.40 is used. Thus, the Fourier transform is given by

$$\mathcal{F}(f(n)) = \frac{1}{2} \left[ \epsilon_U \mathcal{F}(\cos(2\pi\nu_s n)) - \epsilon_D \mathcal{F}(\cos(2\pi\nu_s n - \Delta\tilde{\varphi})) \right] \quad (6.50)$$

$$= \frac{1}{2} \left[ \epsilon_U \mathcal{F}(\cos(2\pi\nu_s n)) - \epsilon_D e^{-i\Delta\tilde{\varphi}} \mathcal{F}(\cos(2\pi\nu_s n)) \right] \quad (6.51)$$

$$= \frac{1}{2} \left[ \mathcal{F}(\cos(2\pi\nu_s n)) (\epsilon_U - \epsilon_D e^{-i\Delta\tilde{\varphi}}) \right]. \quad (6.52)$$

Consequently, the phase yields

$$\tilde{\varphi}_{s,DFT} = \text{atan2}(\epsilon_D \sin \Delta\tilde{\varphi}, \epsilon_U - \epsilon_D \cos \Delta\tilde{\varphi}) \quad (6.53)$$

$$= \text{atan2} \left( \sin \Delta\tilde{\varphi}, \frac{\epsilon_U}{\epsilon_D} - \cos \Delta\tilde{\varphi} \right), \quad (6.54)$$

since it is defined as the arctangent of the ratio of the imaginary and the real part. For  $\epsilon_U = \epsilon_D$ , one obtains  $\tilde{\varphi}_s = \text{atan2}(\sin \Delta\tilde{\varphi}, 1 - \cos \Delta\tilde{\varphi}) = -\frac{\Delta\tilde{\varphi}}{2}$ , which corresponds to the result of the weighted average approach. However, the combined DFT solution is independent of the counting rates, because every event is weighted equivalently. This reflects the *a priori* assumption of the  $\pi$  difference between the detectors. The standard deviation is given by

$$\sigma_{\tilde{\varphi}_{s,DFT}}^2 = \frac{2}{\epsilon^2 N} \quad (6.55)$$

$$= \frac{2}{\frac{1}{4}(\epsilon_U^2 + \epsilon_D^2 - 2\epsilon_U\epsilon_D \cos \Delta\tilde{\varphi})(N_U + N_D)}, \quad (6.56)$$

with  $\epsilon^2 = \frac{1}{4}(\epsilon_U^2 + \epsilon_D^2 - 2\epsilon_U\epsilon_D \cos \Delta\tilde{\varphi})$ . Thus, for a phase shift, different from  $-\pi$ , the statistical error increases, because both amplitudes do not combine in a maximal positive way anymore. Hence, this approach takes into account the phase shift  $\Delta\tilde{\varphi}$  and it will be equal or larger than  $\sigma_{\tilde{\varphi}_{s,wa}}$ . However, the  $\pi$  shift constraint is prejudicial, since it precludes the possible systematic phase deviation between both quadrants. Thus, it is more convenient to use the weighted average approach in order to determine the phase by merging the results of both detectors.

### 6.3.3 Asymmetry (Mapping Method)

For the asymmetry approach, the counting rates of both detectors are combined with regard to the technique described in section 4.1.2. The results of the individual detector quadrants are merged in terms of minimizing systematic effects like the variation of the particle flux or time depending geometric misalignments. Since the phase is determined by the arctangent of two independent amplitude parameters it is not possible to find an analytic representation of the quantity  $\tilde{\varphi}_{s,map}$ . However, the  $\pi$ -shift assumption between both detectors holds, as well. Consequently, the statistical error can be handled in a similar way as discussed in the previous section.

## 6.4 Conclusion

In this chapter, the wrapped probability density function of the phase parameter based on the discrete turn Fourier transform was derived. It was shown, that the first circular moment is unbiased. In addition, confidence intervals were estimated using Bayes' theorem. Finally, a maximum likelihood fit was performed with the model function of the phase derived in chapter 4 and based on the wrapped pdf. This allows the measurement of the spin coherence time and the difference between the assumed spin tune used for the analysis and the true value. In the following section, the determination of the turn depending spin tune will be investigated based on the estimated phase and amplitude value.

## 6.5 Spin Tune Determination

In this section the determination of the turn depending spin tune is discussed for the same cycle which is shown in Fig. 6.8. Assuming a Rayleigh distributed spin tune distribution the turn depending spin tune yields

$$\nu_s(n) = \nu_s^{\text{ref}}(n) + \sqrt{\frac{\pi}{2}} \sigma_{R,\nu_s}(n), \quad (6.57)$$

where  $\nu_s^{\text{ref}}$  denotes the spin tune of the particle on the reference orbit and  $\sigma_{R,\nu_s}$  corresponds to the width of the spin tune distribution. In the following both parameters become turn dependent in order to account for linear time depending drifts of the magnetic elements, of the RF cavity or of the orbit

$$\nu_s^{\text{ref}}(n) = \nu_{s,0}^{\text{ref}} + \nu_{s,1}^{\text{ref}} n, \quad (6.58)$$

$$\sigma_{R,\nu_s}(n) = \sigma_{R,\nu_s,0} + \sigma_{R,\nu_s,1} n. \quad (6.59)$$

A change of the reference spin tune corresponds to a global spin tune drift, which does not affect the amplitude but the phase spectrum. However, both observables are sensitive to a change of the width of the spin tune distribution. Consequently, a global maximum likelihood fit of both distribution allows to distinguish between both effects.

### 6.5.1 Global Maximum Likelihood Fit

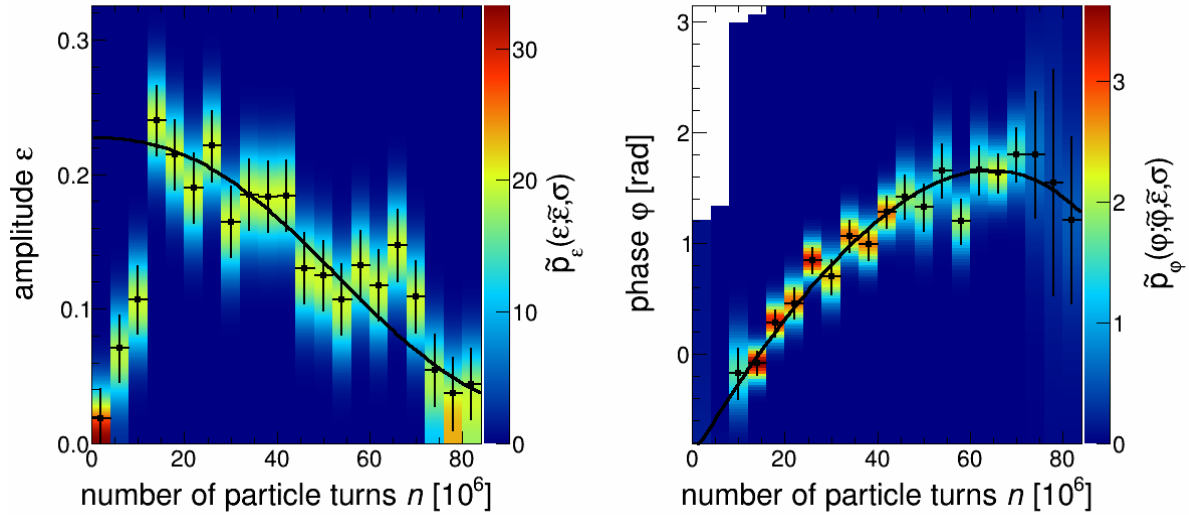


Figure 6.10: Global maximum likelihood fit for the amplitude and phase spectrum based on the probability density functions derived in the previous chapters. The fit function provides turn depending parameters of the spin tune distribution.

An example of a global maximum likelihood fit is shown by the black curves in Fig. 6.10.

The data points represent the estimated values ( $\tilde{\epsilon}$  and  $\tilde{\varphi}_s$ ) obtained by the discrete turn Fourier transform and the error bars denote the respective standard deviation  $\sigma$ . The color scheme shows the corresponding probability density functions derived in the previous chapters ( $\tilde{p}_\varphi$  and  $\tilde{p}_\epsilon$ ). One observes, that the initial vertical polarization of the beam is tilted into the horizontal plane during the first  $13 \times 10^6$  turns. The likelihood, which has to be minimized, reads

$$\mathcal{L} = \prod_{i=1}^N \tilde{p}_\varphi(\varphi_s(n_i; \boldsymbol{\theta}_\varphi); \tilde{\epsilon}_i, \tilde{\varphi}_{s,i}, \sigma_i) + \prod_{i=1}^N \tilde{p}_R(\epsilon(n_i; \boldsymbol{\theta}_\epsilon); \tilde{\epsilon}_i, \sigma_i), \quad (6.60)$$

$$\boldsymbol{\theta}_\varphi \in \left\{ \sigma_{R,\nu_s,0}; \sigma_{R,\nu_s,1}; \nu_{s,0}^{\text{ref}}; \nu_{s,1}^{\text{ref}}; \varphi_s^0 \right\} \quad \text{and} \quad \boldsymbol{\theta}_\epsilon \in \left\{ \sigma_{R,\nu_s,0}; \sigma_{R,\nu_s,1}; \epsilon_0 \right\}. \quad (6.61)$$

The two global parameters  $\sigma_{R,\nu_s,0}$  and  $\sigma_{R,\nu_s,1}$  consider the turn depending width of the spin tune distribution. The initial phase and amplitude are given by  $\varphi_s^0$  and  $\epsilon_0$ , respectively. A turn depending spin tune drift is regarded by the parameters  $\nu_{s,0}^{\text{ref}}$  and  $\nu_{s,1}^{\text{ref}}$ , which are exclusively determinable in the phase spectrum.

The results of the maximum likelihood fit are shown in table 6.1. One observes a linear spin tune drift, which is specified by the parameter  $\nu_{s,1}^{\text{ref}} = (-1.89 \pm 0.67) \times 10^{-16}$ . The assumed spin tune used for the analysis  $\nu_{s,0}$  deviates from the reference spin tune by  $\nu_{s,0}^{\text{ref}} = (6.45 \pm 2.55) \times 10^{-9}$ . In addition, the linear change of the spin tune width yields  $\sigma_{R,\nu_s,1} = (2.66 \pm 1.61) \times 10^{-17}$ . The initial width is given by  $\sigma_{R,\nu_s,0} = (3.71 \pm 1.10) \times 10^{-9}$ .

Phase	Amplitude
$\varphi_s^0 = (-2.48 \pm 0.23) \text{ rad}$	$\epsilon_0 = 0.2396 \pm 0.0223$
$\sigma_{R,\nu_s,0} = (3.71 \pm 1.10) \times 10^{-9}$	
$\sigma_{R,\nu_s,1} = (2.66 \pm 1.61) \times 10^{-17}$	
$\nu_{s,0}^{\text{ref}} = (6.45 \pm 2.55) \times 10^{-9}$	
$\nu_{s,1}^{\text{ref}} = (-1.89 \pm 0.67) \times 10^{-16}$	

Table 6.1: Parameters obtained by the global maximum likelihood fit based on the data shown in Fig. 6.10.

Consequently, the turn depending mean value of the spin tune yields

$$\Delta\mu_{\nu_s}(n) = \nu_s(n) - \nu_{s,0} = \nu_{s,0}^{\text{ref}} + \nu_{s,1}^{\text{ref}}n + \sqrt{\frac{\pi}{2}} (\sigma_{R,\nu_s,0} + \sigma_{R,\nu_s,1}n). \quad (6.62)$$

In the latter equation the assumed spin tune is subtracted. The result of the mean spin tune is presented by the red color in Fig. 6.11. One observes a linear decreasing behavior since the sum  $\nu_{s,1}^{\text{ref}} + \sigma_{R,\nu_s,1} = -1.6 \times 10^{-16}$  is negative. The corresponding error band is calculated by Gaussian error propagation and its minimum  $\sigma_{\mu_{\nu_s}}^{\text{min}} \approx 8.9 \times 10^{-10}$  is reached at approxim-

ately  $n_{\min} \approx 32 \times 10^6$  turns. The Cramér-Rao bound based on the Fisher information yields (Eq. 4.40)

$$\begin{aligned} \sigma_{\nu_s}^{\text{CRB}} &\approx \sqrt{\frac{24}{4\pi^2 \epsilon^2 (\Delta n)^2 N_0}} \\ &= 3.27 \times 10^{-10}, \end{aligned} \quad (6.63)$$

where the average amplitude is assumed to be  $\epsilon = 0.1$ . In addition, approximately  $N_0 \approx 10^5$  particles were detected during the measurement interval of

$$\Delta n = n_{\text{fit},f} - n_{\text{fit},i} = (84 - 14) \times 10^6 = 72 \times 10^6 \text{ turns}. \quad (6.64)$$

The minimal statistical error based on the maximum likelihood fit is more than 2 times larger than the Cramér-Rao bound

$$\Delta \sigma_{\nu_s} = \sigma_{\mu_{\nu_s}}^{\min} - \sigma_{\nu_s}^{\text{CRB}} = 5.32 \times 10^{-10}. \quad (6.65)$$

Note that the Cramér-Rao bound is calculated for a spin tune based on a Delta distribution, i.e. all particles of the ensemble exhibit the same spin tune. However, the parameters  $\sigma_{R,\nu_s,0}$  and  $\sigma_{R,\nu_s,1}$  take into account the Rayleigh distributed particle spins. Thus, the statistical error of the mean spin tune value increases for larger spin tune distribution widths. In first order, the latter quantity corresponds to the chromaticity of the ring, i.e. it is a measure of the energy dependence of the focusing strength, which can be manipulated by sextupole magnets.

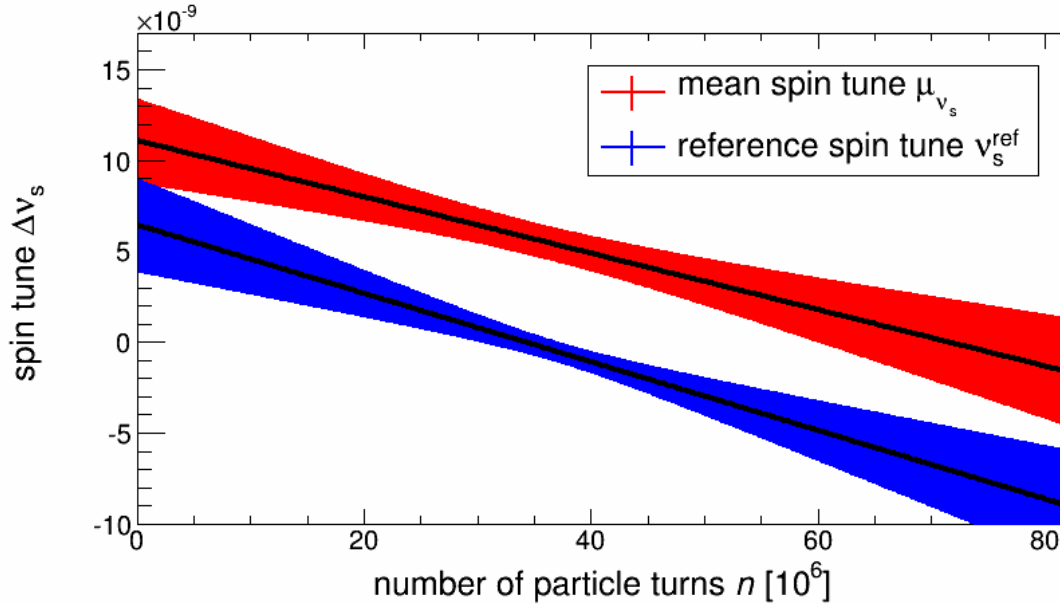


Figure 6.11: Turn depending spin tune interpolation. The red color corresponds to the mean value of the spin tune and the blue color indicates the reference spin tune.

The turn depending spin tune of the reference particle reads

$$\Delta v_s^{\text{ref}}(n) = v_{s,0}^{\text{ref}} + v_{s,1}^{\text{ref}} n. \quad (6.66)$$

This observable depends mainly on the magnetic configuration of the bending dipoles and the beam orbit. The result is shown by the blue error band in Fig. 6.11. It is shifted by  $\sigma_{R,\nu_{s,0}}$  and not exactly parallel to the mean spin tune value (blue band), because the mean value drifts additionally by  $\sigma_{R,\nu_{s,1}}$ . The minimal statistical error of the reference spin tune is reached at  $n_{\text{min}} = 37 \times 10^6$  and yields  $\sigma_{v_s^{\text{ref}}}^{\text{min}} = 5.42 \times 10^{-10}$ .

The turn depending error is presented in Fig. 6.12 and it is calculated by

$$(\sigma_{v_s^{\text{ref}}}(n))^2 = (\sigma_{v_{s,0}^{\text{ref}}})^2 + n^2 \cdot (\sigma_{v_{s,1}^{\text{ref}}})^2 + n \cdot \text{cov}(v_{s,0}^{\text{ref}}, v_{s,1}^{\text{ref}}), \quad (6.67)$$

where  $\text{cov}(v_{s,0}^{\text{ref}}, v_{s,1}^{\text{ref}})$  denotes the covariance between the constant  $v_{s,0}^{\text{ref}}$  and the linear  $v_{s,1}^{\text{ref}}$  parameter. The minimum of the function yields

$$\frac{d(\sigma_{v_s}(n_{\text{min}}))^2}{dn} = 2n_{\text{min}}(\sigma_{v_{s,1}^{\text{ref}}})^2 + \text{cov}(v_{s,0}^{\text{ref}}, v_{s,1}^{\text{ref}}) \stackrel{!}{=} 0 \quad (6.68)$$

$$\Rightarrow n_{\text{min}} = -\frac{1}{2} \frac{\text{cov}(v_{s,0}^{\text{ref}}, v_{s,1}^{\text{ref}})}{(\sigma_{v_{s,1}^{\text{ref}}})^2} = -\frac{1}{2} \rho(v_{s,0}^{\text{ref}}, v_{s,1}^{\text{ref}}) \frac{\sigma_{v_{s,0}^{\text{ref}}}}{\sigma_{v_{s,1}^{\text{ref}}}}. \quad (6.69)$$

where  $\rho(v_{s,0}^{\text{ref}}, v_{s,1}^{\text{ref}}) \in (0, 1)$  indicates the correlation between  $v_{s,1}^{\text{ref}}$  and  $v_{s,2}^{\text{ref}}$ . In case of a minimal correlation  $\rho(p_1, p_2) = 0$  the smallest error is obtained at the beginning of the cycle  $n_{\text{min}} = 0$ . For a stronger correlation  $n_{\text{min}}$  increases until the ratio  $0.5\sigma_{v_{s,0}^{\text{ref}}}/\sigma_{v_{s,1}^{\text{ref}}}$  is reached. The covariance yields to  $\rho = -0.977$ , which represents a strong negative correlation between the two parameters. Thus, the turn number, for which  $\sigma_{v_s^{\text{ref}}}$  becomes minimal, is given by  $n_{\text{min}} = 37.01 \times 10^6$  turns.

The minimal statistical error of the reference spin tune differs from the Cramér-Rao bound, as well. Following reasons are proposed to explain this deviation:

- The spin tune is not stable over time and it drifts by approximately  $\Delta v_s \approx 10 \times 10^{-9}$  during the cycle.
- The spins are distributed according to a Rayleigh distribution, which causes a different Cramér-Rao bound of the spin tune.
- The amplitude decreases within a cycle due to the decoherence of the spins.
- Gaussian error propagation is not the proper method in order to handle asymmetric errors.

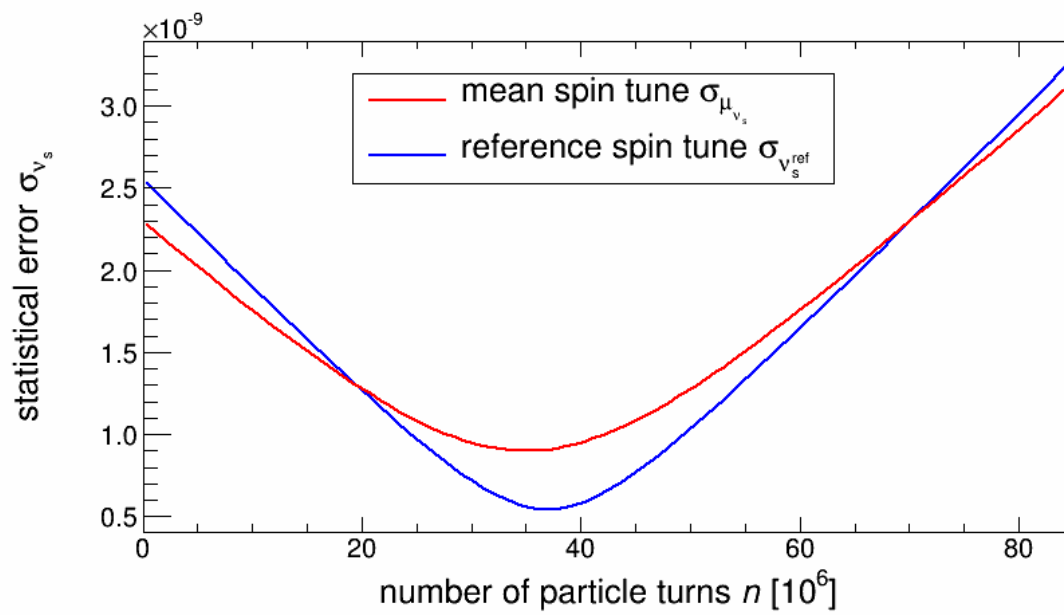


Figure 6.12: Statistical error of the interpolated spin tune as a function of the turn number  $n$ . The red color corresponds to the mean value of the spin tune and the blue color indicates the reference spin tune.



At the beginning of this chapter systematic effects of the turn discrete Fourier transform are discussed based on the assumed spin tune or by analyzing the results of the individual detectors. Here, mainly the results of the beamtime in May 2015 are discussed. The motivation for this experiment was to increase the spin coherence time by varying the strength of different sextupole magnets in the ring. This setup allowed to determine the spin tune parasitically since the polarization was tilted into the horizontal plane and the spin underwent an idle precession. Thus, it was possible to study several systematic effects like different extraction methods or the impact of the electron cooler. Furthermore, long cycle times ( $\approx 1\,000$  s) were realized to demonstrate the feasibility of very long polarization lifetimes. The long-term measurements should also lead to a better understanding of the spin tune drifts. A summary of the relevant runs discussed in this chapter is given in appendix A.1.

## 7.1 Systematics of the Phase Estimation

In this section, systematic effects of the analysis based on the mapping method and discrete Fourier transform will be discussed. The estimation of the systematic error of the phase determination  $\sigma_{\varphi_s}^{\text{sys}}$  implies the discussion of three different aspects.

1. The assumed fixed spin tune chosen for the analysis.
2. The number of bins of the asymmetry distribution in the case of the mapping method.
3. The comparison of the results obtained by the individual detectors.

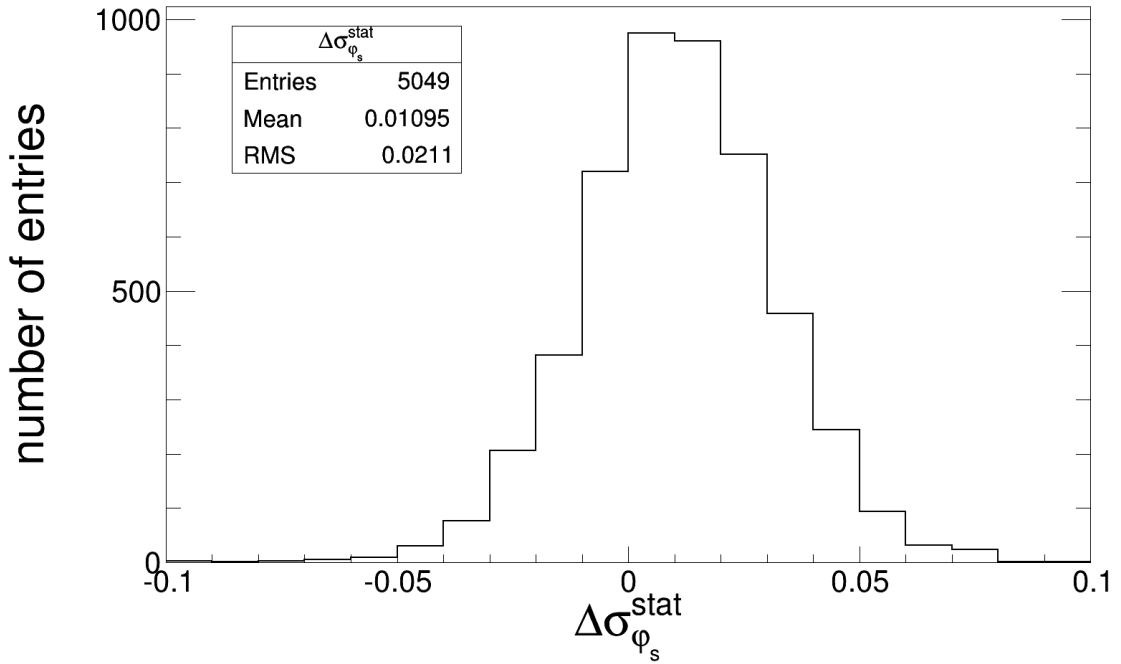


Figure 7.1: The difference of the statistical error obtained by the mapping and the Fourier method.

The results of the phase standard deviation obtained by both methods  $\sigma_{\varphi_s}^{\text{map,stat}}$  and  $\sigma_{\varphi_s}^{\text{DFT,stat}}$  are not identical. In fact, the width of the distribution, normalized by the statistical error of the mapping method

$$\Delta\sigma_{\varphi_s}^{\text{stat}}(n) = \frac{\sigma_{\varphi_s}^{\text{DFT,stat}}(n) - \sigma_{\varphi_s}^{\text{map,stat}}(n)}{\sigma_{\varphi_s}^{\text{map,stat}}(n)}, \quad (7.1)$$

yields  $\sigma_{\Delta\sigma_{\varphi_s}^{\text{stat}}} = 0.021$ . The results of 5049 cycles are presented in Fig. Fig. 7.1. Hence, the estimations of the statistical error differ between both methods. In particular, the mean value of the distribution  $\mu_{\Delta\sigma_{\varphi_s}^{\text{stat}}} = 0.011$  indicates that on average the Fourier transform provides significantly greater statistical errors compared to the mapping method

$$\sigma_{\varphi_s}^{\text{DFT,stat}} = \mu_{\Delta\sigma_{\varphi_s}^{\text{stat}}} \cdot \sigma_{\varphi_s}^{\text{map,stat}}, \quad (7.2)$$

This becomes obvious since the amplitude estimator of the mapping method is systematically larger than the one obtained by the discrete Fourier transform  $\tilde{\epsilon}^{\text{map}} > \tilde{\epsilon}^{\text{DFT}}$ . The systematic bias is based on the fact, that in the case of the mapping method the number of bins of the asymmetry distribution has to be set. This leads to larger amplitude estimators and therefore to a smaller standard error of the phase (Fig. 6.5). In the following, further systematic effects of the phase determination are discussed.

### 7.1.1 Assumed Spin Tune

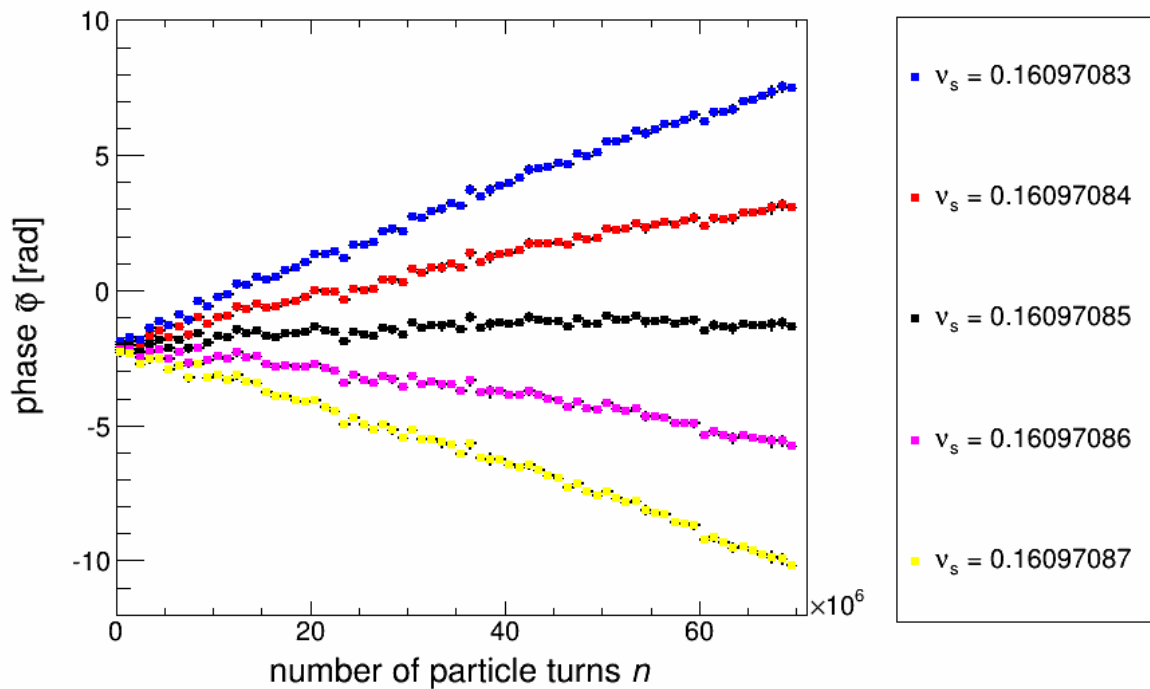


Figure 7.2: Turn depending phase for different assumed spin tunes. The variation of the assumed spin tune yields  $4 \cdot 10^{-8}$ , which is indicated by the values in the right box shown in different colors.

Both analysis methods are based on an assumed spin tune  $\nu_s^0$ , which is fixed for the whole cycle. In Eq. 6.33 it is stated that the turn depending phase estimator  $\tilde{\varphi}_s(n)$  depends linearly on  $\nu_s^0$ . Thus, in Fig. 7.2 five phase distributions are shown for different assumed spin tunes, where  $\nu_s^0$  varies in steps of  $1 \cdot 10^{-8}$ . One observes that the linear parameter changes in equidistant steps.

In order to estimate the systematic error of the phase caused by the choice of the assumed

spin tune, the results of  $\tilde{\varphi}_s(\nu_s^0)$  obtained for  $k_{\max} = 201 - 1$  different assumed spin tunes

$$\begin{aligned}\nu_s^0(k) &= \nu_s^0 - k \cdot \frac{\Delta\nu_s^0}{\Delta k} \\ &= -0.16097083 - k \cdot \frac{\Delta\nu_s^0}{\Delta k}, \quad \text{with integer index } k = 0, 1, \dots, k_{\max}\end{aligned}\quad (7.3)$$

are compared for the same cycle. The fraction  $\Delta\nu_s^0/\Delta k = 2 \cdot 10^{-10}$  corresponds to the spin tune change per increment by one of the integer index  $k$ . This yields to a total scan interval of  $\Delta\nu_s^0 k_{\max}/\Delta k = 4 \cdot 10^{-8}$ . Furthermore, the estimated phase value  $\tilde{\varphi}_s(n, k)$  depending on the turn number  $n$  and the assumed spin tune  $\nu_s^0(k)$  is corrected by the shift due to the variation of the assumed spin tune

$$\tilde{\varphi}_s^{\text{cor}}(n, k) = \tilde{\varphi}_s(n, k) - 2\pi n[\nu_s^0(k) - \nu_s^0(k=0)] \quad (7.4)$$

$$= \tilde{\varphi}_s(n, k) + 2\pi nk \frac{\Delta\nu_s^0}{\Delta k}. \quad (7.5)$$

The factor  $2\pi$  originates from Eq. 6.2, which describes the relation between the spin tune  $\nu_s$  and the phase  $\tilde{\varphi}_s$ .

For each macroscopic turn interval the arithmetic mean of  $\tilde{\varphi}_s^{\text{cor}}(n, k)$  is formed by summing over all assumed spin tunes and it serves as a reference value compared to the estimated one

$$\mu_{\tilde{\varphi}_s^{\text{cor}}}(n) = \frac{1}{201} \sum_{k=0}^{k_{\max}} \tilde{\varphi}_s^{\text{cor}}(n, k), \quad (7.6)$$

$$\Delta\tilde{\varphi}_s^{\text{cor}}(n, k) = (\tilde{\varphi}_s^{\text{cor}}(n, k) - \mu_{\tilde{\varphi}_s^{\text{cor}}}(n)) / \sigma_{\tilde{\varphi}_s^{\text{cor}}}^{\text{stat}}(n, k). \quad (7.7)$$

Here,  $\Delta\tilde{\varphi}_s^{\text{cor}}(n, k)$  denotes the difference between the corrected phase value and the arithmetic mean normalized by the statistical error of the phase  $\sigma_{\tilde{\varphi}_s^{\text{cor}}}^{\text{stat}}$ . In Fig. 7.3 the distribution of  $\Delta\tilde{\varphi}_s^{\text{cor}}$  based on 201 assumed spin tunes is shown. The red color corresponds to the results of the discrete Fourier transform and the blue color represents the mapping method. The statistical error of the phase shall be corrected by the standard deviation of the respective distribution

$$\sigma_{\tilde{\varphi}_s}^{\text{map}, \nu_s} = (\sigma_{\Delta\tilde{\varphi}_s^{\text{cor}}}^{\text{map}} + 1) \cdot \sigma_{\tilde{\varphi}_s}^{\text{map}, \text{stat}} = 1.092 \cdot \sigma_{\tilde{\varphi}_s}^{\text{map}, \text{stat}}, \quad (7.8)$$

$$\sigma_{\tilde{\varphi}_s}^{\text{DFT}, \nu_s} = (\sigma_{\Delta\tilde{\varphi}_s^{\text{cor}}}^{\text{DFT}} + 1) \cdot \sigma_{\tilde{\varphi}_s}^{\text{DFT}, \text{stat}} = 1.006 \cdot \sigma_{\tilde{\varphi}_s}^{\text{DFT}, \text{stat}}. \quad (7.9)$$

Each analysis is performed with the same data but a different assumed spin tune. Thus, the observed standard deviations  $\sigma_{\tilde{\varphi}_s}^{\text{map}, \nu_s} = 0.092 \pm 0.0012$  and  $\sigma_{\tilde{\varphi}_s}^{\text{DFT}, \nu_s} = 0.006 \pm 7 \cdot 10^{-5}$  are interpreted as a systematic bias inherent in each of the analysis methods. The results of the discrete Fourier transform are preferred since they show a more robust behavior. The mean values of each distribution  $\mu_{\tilde{\varphi}_s}^{\text{map}, \nu_s} = (0.51 \pm 17) \cdot 10^{-3}$  and  $\mu_{\tilde{\varphi}_s}^{\text{DFT}, \nu_s} = (7.5 \pm 10.1) \cdot 10^{-6}$  are compatible with zero. This indicates that the underlying systematic process is random nature.

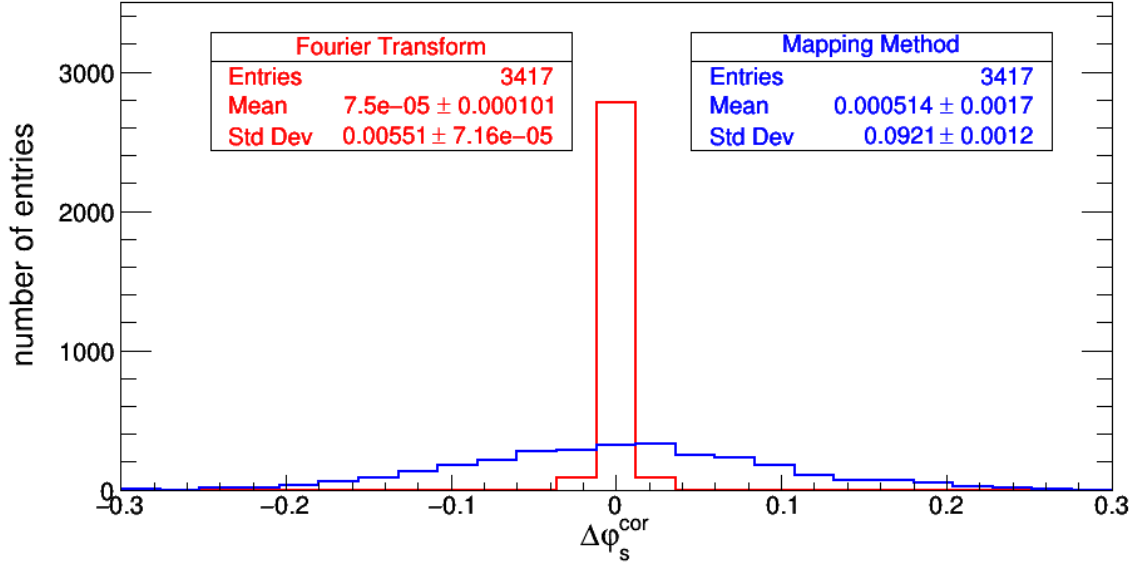


Figure 7.3: Phase deviation due to the variation of the assumed spin tune for the mapping method (blue) and the discrete Fourier transform (blue), respectively.

### 7.1.2 Number of Bins of the Asymmetry Distribution

To estimate the impact of the number of bins  $N_{\text{bins}}$  used for the asymmetry distribution (Fig. 4.3), the phase values obtained for different  $N_{\text{bins}}$  are compared. For this purpose the weighted arithmetic mean for each macroscopic turn interval is calculated

$$\mu_{\varphi_s}(n) = \sum_{N_{\text{bins}}=1}^{N_{\text{bins}}^{\text{max}}} \frac{\varphi_s(n, N_{\text{bins}})}{[\sigma_{\varphi_s}^{\text{stat}}(n, N_{\text{bins}})]^2} \cdot \left( \sum_{N_{\text{bins}}=1}^{N_{\text{bins}}^{\text{max}}} \frac{1}{[\sigma_{\varphi_s}^{\text{stat}}(n, N_{\text{bins}})]^2} \right)^{-1}, \quad (7.10)$$

where the sum of the sequences contains all addends until the maximum number of bins  $N_{\text{bins}}^{\text{max}} = 150$  is reached. A distribution of the differences between the phase value and the arithmetic mean normalized by the statistical error

$$\Delta\varphi_s^{N_{\text{bins}}}(n, N_{\text{bins}}) = \frac{\varphi_s(n, N_{\text{bins}}) - \mu_{\varphi_s}(n)}{\sigma_{\varphi_s}^{\text{stat}}(n, N_{\text{bins}})} \quad (7.11)$$

is shown for  $N_{\text{bins}} = 30$  in the left part of Fig. 7.4. The width  $\sigma_{\Delta\varphi_s}^{N_{\text{bins}}} = 0.074$  corresponds to the factor, which scales the statistical error considering systematic fluctuations of the analysis due to the choice of  $N_{\text{bins}}$ . Once again, the mean value of the distribution is not significantly different from zero, thus the fluctuations are totally random.

In the right part of Fig. 7.4 the widths of the respective distribution are shown for  $N_{\text{bins}} = [1, 150]$ . A clear minimum is located in the range of  $N_{\text{bins}} = [20, 50]$ . It is recommended to chose a number of bins within this interval to reduce the systematic effects and to minimize

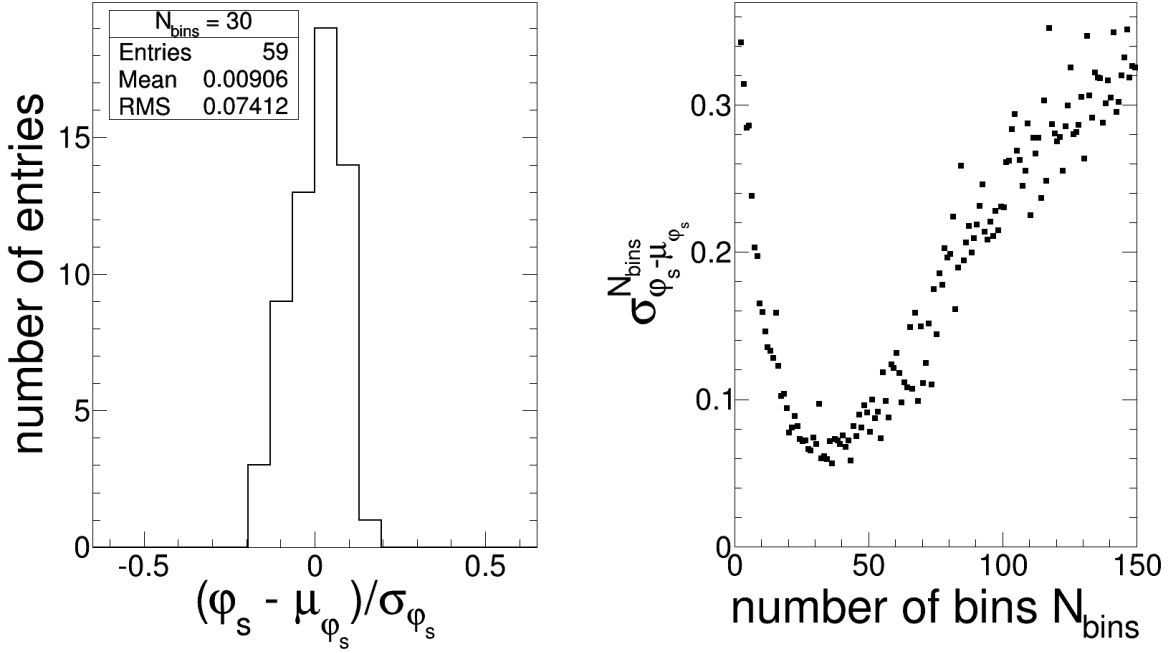


Figure 7.4: Left: Distribution of the difference between the phase and its arithmetic mean for  $N = 30$  normalized to the statistical error. Right: Standard deviation of the distribution shown on the left-hand side as a function of the number of bins of the asymmetry distribution.

the scaling factor of the statistical error, which yields approximately

$$\sigma_{\varphi_s}^{\text{map}, N_{\text{bins}}} = (\sigma_{\Delta\varphi_s}^{\text{map}, N_{\text{bins}}} + 1) \cdot \sigma_{\varphi_s}^{\text{map}, \text{stat}} \approx 1.07 \cdot \sigma_{\varphi_s}^{\text{map}, \text{stat}}. \quad (7.12)$$

### 7.1.3 Pull Distribution

In order to perform the analysis of each detector individually the counting rates  $N_X^{\pm}$  of the quadrants ( $X=U, D$ ) are formed according to Eq. 4.5

$$\epsilon_U(\varphi_s) = \frac{N_U^-(\varphi_s)}{N_U^+(\varphi_s)} = p_{\tilde{\zeta}} A_{y,U}^d \sin(\varphi_s + \tilde{\varphi}_U), \quad (7.13)$$

$$\epsilon_D(\varphi_s) = \frac{N_D^-(\varphi_s)}{N_D^+(\varphi_s)} = p_{\tilde{\zeta}} A_{y,D}^d \sin(\varphi_s + \tilde{\varphi}_D). \quad (7.14)$$

This yields one amplitude  $\tilde{\epsilon}_X = p_{\tilde{\zeta}} A_{y,X}^d$  respectively one phase  $\tilde{\varphi}_X$  ( $X=U, D$ ) estimator for each quadrant.

In Fig. 7.5 an example of the different phase determinations is given. The blue data points represent the up detector, whereas the phase distribution of the down detector is shown in red. In good approximation, the shift of the phase values is given by  $\tilde{\varphi}_s^U - \tilde{\varphi}_s^D \approx \pi$ , which is caused by the different azimuthal angles ( $\phi_U = 0$  and  $\phi_D = \pi$ ) stated in the definition of the spin depending cross section in Eq. 2.120. For comparison, the phase distribution obtained by

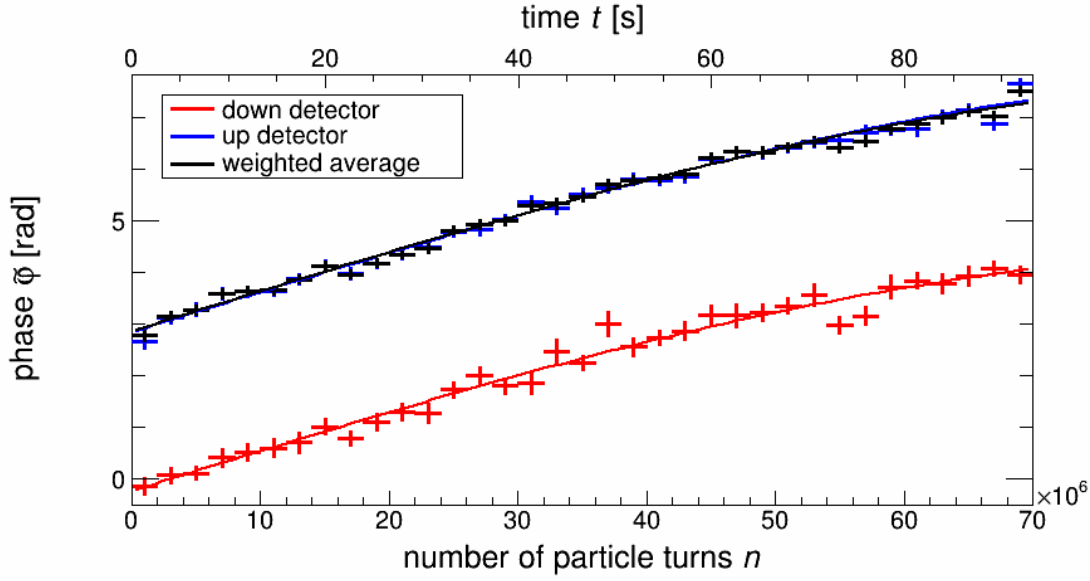


Figure 7.5: Comparison between the phase results of the individual detectors (up quadrant in blue and down quadrant in red) and the results obtained by the combination of both detector quadrants (black). (A.1)

calculating the asymmetry of both detectors  $\tilde{\varphi}_s$  is shown in black. Since the counting rate of the up detector  $N_U$  enters as the positive term to the asymmetry (Eq. 4.6), the phase distribution  $\tilde{\varphi}_s^U$  is almost identical to  $\tilde{\varphi}_s$ . Additionally, the error bars of the individual detectors are larger by a factor of approximately  $\sigma_{\tilde{\varphi}_s^{U,D}} \approx \sqrt{2}\sigma_{\tilde{\varphi}_s}$ , since the estimator of the phase standard error scales in good approximation with the reciprocal square root of the total number of detected events  $\sigma_{\tilde{\varphi}_s} \propto N^{-0.5}$ .

A bias, caused for example by systematic displacements of the detector quadrants, is studied by comparing the ratio of the difference between the individually estimated phase values and their statistical errors

$$g_{\tilde{\varphi}_s^U - \tilde{\varphi}_s^D} = \frac{|\tilde{\varphi}_s^U - \tilde{\varphi}_s^D| - \pi}{\sqrt{\sigma_{\tilde{\varphi}_s^U}^2 + \sigma_{\tilde{\varphi}_s^D}^2}}. \quad (7.15)$$

For this purpose, the systematic effects discussed in the previous section are taken into account by scaling the statistical error

$$\begin{aligned} \sigma_{\tilde{\varphi}_s}^{\text{map,tot}} &= \sqrt{(\sigma_{\tilde{\varphi}_s}^{\text{map},\nu_s})^2 + (\sigma_{\tilde{\varphi}_s}^{\text{map},N_{\text{bins}}})^2} \\ &= \left[ \sqrt{0.09^2 + 0.07^2} + 1 \right] \cdot \sigma_{\tilde{\varphi}_s}^{\text{map,stat}} \\ &= 1.11 \cdot \sigma_{\tilde{\varphi}_s}^{\text{map,stat}}, \end{aligned} \quad (7.16)$$

$$\begin{aligned} \sigma_{\tilde{\varphi}_s}^{\text{DFT,tot}} &= \sigma_{\tilde{\varphi}_s}^{\text{DFT},\nu_s} \\ &= 1.005 \cdot \sigma_{\tilde{\varphi}_s}^{\text{DFT,stat}}. \end{aligned} \quad (7.17)$$

Here it is assumed, that the systematic effects of the mapping method are independent and random nature.

The distribution of  $g_{\tilde{\varphi}_s^U - \tilde{\varphi}_s^D}$  corresponds to a pull-distribution and its width yields an estimator to what extent the statistical error has to be scaled. Fig. 7.6 shows the results of  $g_{\tilde{\varphi}_s^U - \tilde{\varphi}_s^D}$  for 10169 phase values obtained by the mapping method (blue) respectively the DFT method (red). The analyzed data is obtained from different experiments, which were performed during the beamtimes from 2013 to 2015. Thus, an extremely high significance is reached due to a long-term data acquisition.

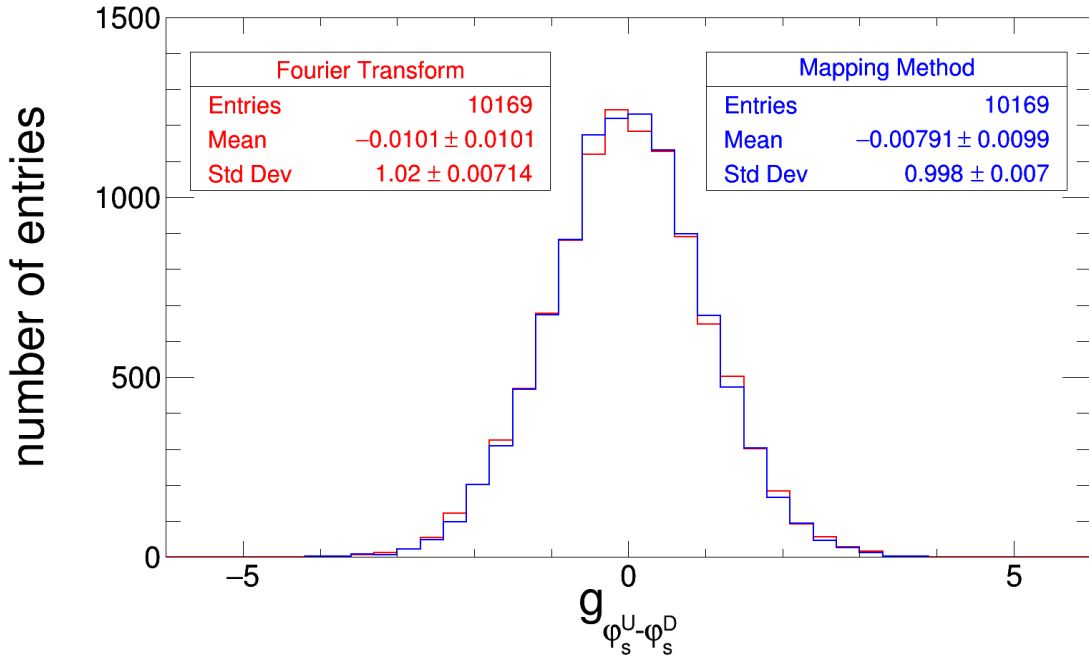


Figure 7.6: Pull distribution of the phase for to the up and down detector quadrants. The discrete Fourier transform is shown in red, whereas the result of mapping method corresponds to the blue color. (A.1)

The confidence intervals of both distributions are close to unity, thus the corrected statistical errors  $\sigma_{\tilde{\varphi}_s}^{\text{map,tot}}$  and  $\sigma_{\tilde{\varphi}_s}^{\text{DFT,tot}}$  provide reasonable results. However, they shall be corrected by

$$\sigma_{\tilde{\varphi}_s}^{\text{map,U,D}} = \sigma_{g_{\tilde{\varphi}_s^U - \tilde{\varphi}_s^D}}^{\text{map}} \cdot \sigma_{\tilde{\varphi}_s}^{\text{map,tot}} = 0.998 \cdot \sigma_{\tilde{\varphi}_s}^{\text{map,tot}}, \quad (7.18)$$

$$\sigma_{\tilde{\varphi}_s}^{\text{DFT,U,D}} = \sigma_{g_{\tilde{\varphi}_s^U - \tilde{\varphi}_s^D}}^{\text{DFT}} \cdot \sigma_{\tilde{\varphi}_s}^{\text{DFT,tot}} = 1.02 \cdot \sigma_{\tilde{\varphi}_s}^{\text{DFT,tot}}, \quad (7.19)$$

in order to incorporate systematics of the analysis methods. The mean values of both distributions  $\mu_{g_{\tilde{\varphi}_s^U - \tilde{\varphi}_s^D}}^{\text{DFT}} = -0.0101 \pm 0.0101$  and  $\mu_{g_{\tilde{\varphi}_s^U - \tilde{\varphi}_s^D}}^{\text{map}} = -0.0079 \pm 0.0099$  are compatible with null. This indicates that the phase difference based on the individual detectors is not systematically shifted and accordingly no systematic effects like geometric displacements of the detectors are observable.

#### 7.1.4 Conclusion

In the previous sections systematic effects of both analysis methods were discussed in order to estimate possible biases. Therefore, experimental data obtained during different beamtimes and from different years were used. The systematic errors were taken into account by scaling the statistical ones. The analyzed data contains a broad spectrum of different cycles within a time range of two years. Thus, it seems reasonable to estimate a systematic bias based on this data.

## 7.2 General Experimental Considerations

In order to determine the spin tune, which is defined as the spin revolutions around the invariant spin axis per particle turn in the ring, with the best possible accuracy, one has to ensure that the beam polarization lies completely in the horizontal plane. Thus the initially vertical polarized beam is tilted by the mean of a resonant RF solenoid. To monitor this process the cross ratio of the vertical polarization is specified according to Eq. 3.10.

### 7.2.1 Resonant Spin Flip

In order to ensure that the solenoid operates on the spin resonance a Froissart-Stora scan is performed followed by a fixed frequency scan. The Froissart-Stora scan provides a  $\pi$ -flip

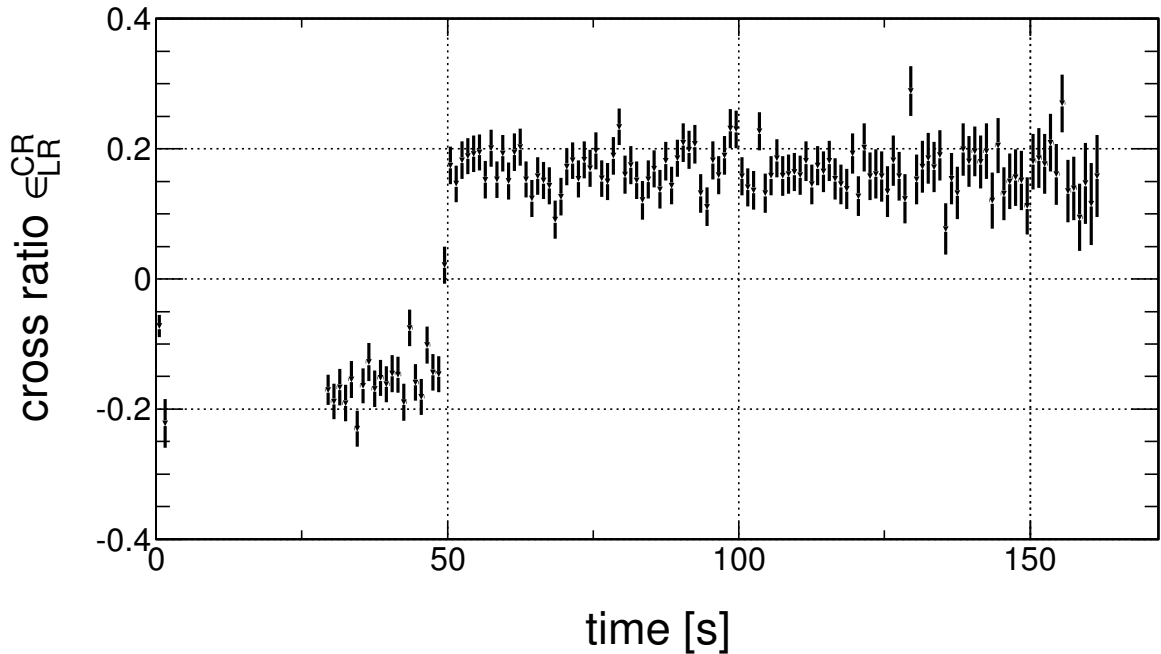


Figure 7.7: Cross ratio of a Froissart-Stora scan. ( A.1)

of the polarization by passing through a resonance of a magnetic device with a transverse magnetic field operating on the frequency of the spin oscillations. The ratio of the final  $p_f$  and initial  $p_i$  polarization is given by

$$\frac{p_f}{p_i} = 2e^{-\pi\epsilon^2/(2|\alpha|)} - 1, \quad (7.20)$$

where  $\epsilon$  is the resonance strength of the solenoid and  $\alpha$  denotes the speed of the passage across the resonance. For the adiabatic condition  $\epsilon^2/|\alpha| \gg 1$  there is almost no depolarization and a

total reversal of the polarization can be realized

$$\frac{p_f}{p_i} = -1. \quad (7.21)$$

The frequency of the RF solenoid is synchronized with the spin precession frequency  $f_{\text{sol}}^{\text{res}} = f_s + hf_{\text{RF}}$ . The harmonic is set to  $h = 1$  and it yields a first estimation of  $f_{\text{sol}}^{\text{res}}$ . Since the spin precession frequency is not constant on a time scale of days and in particular due to changes of the accelerator settings, the solenoid frequency, and the timings had to be observed and adjusted from time to time to provide an optimized spin flip into the horizontal plane.

### 7.2.2 Beam Revolution Period

The results of the turn based spin tune analysis are independent of the RF cavity frequency  $f_{\text{RF}}$ , since each event is unambiguously assigned to a turn number  $n$ . Nevertheless, it is important to study the revolution frequency of the beam  $f_{\text{beam}}$ , since latter defines the energy of the particles respectively the Lorentz factor  $\gamma$ , which is directly connected to the spin tune

$$\nu_s = G\gamma, \quad (7.22)$$

where  $G$  is the anomalous magnetic moment of the deuteron.

The period time of the beam  $T_{\text{beam}}$  is composed by two observables. First, the time signal of the RF cavity  $t_{\text{RF}}$ , which allows determining its period  $T_{\text{RF}} = t_{\text{RF},i+1} - t_{\text{RF},i}$ , acts like a baseline. In addition, the arrival time of the events  $t_{\text{ev}}$  with respect to the last COSY RF signal enables to specify the beam period

$$T_{\text{beam}} = T_{\text{RF}} + \Delta t_{\text{ev}}, \quad (7.23)$$

where  $\Delta t_{\text{ev}} = t_{\text{ev},i+1} - t_{\text{ev},i}$  denotes the deviation of the relative arrival time of two detected events. The relative spin tune change due to a variation of the beam period is given by

$$\frac{\Delta \nu_s}{\nu_s} = \frac{\Delta \gamma_{\text{beam}}}{\gamma_{\text{beam}}} = \frac{\beta_{\text{beam}}^2}{\eta_p} \frac{\Delta f_{\text{beam}}}{f_{\text{beam}}} = -\frac{\beta_{\text{beam}}^2}{\eta_p} \frac{\Delta T_{\text{beam}}}{T_{\text{beam}}}, \quad (7.24)$$

where  $\eta_p$  denotes the slip factor, which depends on the momentum compaction factor and the beam momentum.

In order to provide a quantitative value of  $\beta_{\text{beam}}^2/\eta_p$  the spin tune change  $\Delta \nu_s$  induced by a frequency shift of the COSY RF  $\Delta f_{\text{RF}}$  was investigated. Therefore, the initial COSY RF was changed after 30s of idle spin precession to a different value  $f_{s,\text{jump}} = \Delta f_{\text{RF}} + f_{s,\text{base}}$ . After additional 30s, the frequency was set back to the base value in order to be sensitive to any systematic effects like a time depending drift of the COSY RF or of the spin tune. The scan was performed in steps of  $\Delta f_{\text{RF}} \approx 0.15$  Hz and several cycles were taken for each setting. The results are shown in the upper plot of Fig. 7.8, where the spin tune jump is plotted versus the

frequency shift. A linear least squares fit to the data yields

$$\frac{\Delta\nu_s}{\Delta f_{\text{RF}}} = \frac{\beta_{\text{beam}}^2}{\eta_p} \frac{\nu_s}{f_{\text{RF}}} = \alpha_{\text{RF}}(\nu_s, f_{\text{RF}}) = (76.91 \pm 0.34) \text{ ns}. \quad (7.25)$$

The residuals in the lower part of Fig. 7.8 approve, that the linear model is a reasonable assumption and that the statistical errors of the spin tune shift are properly determined.

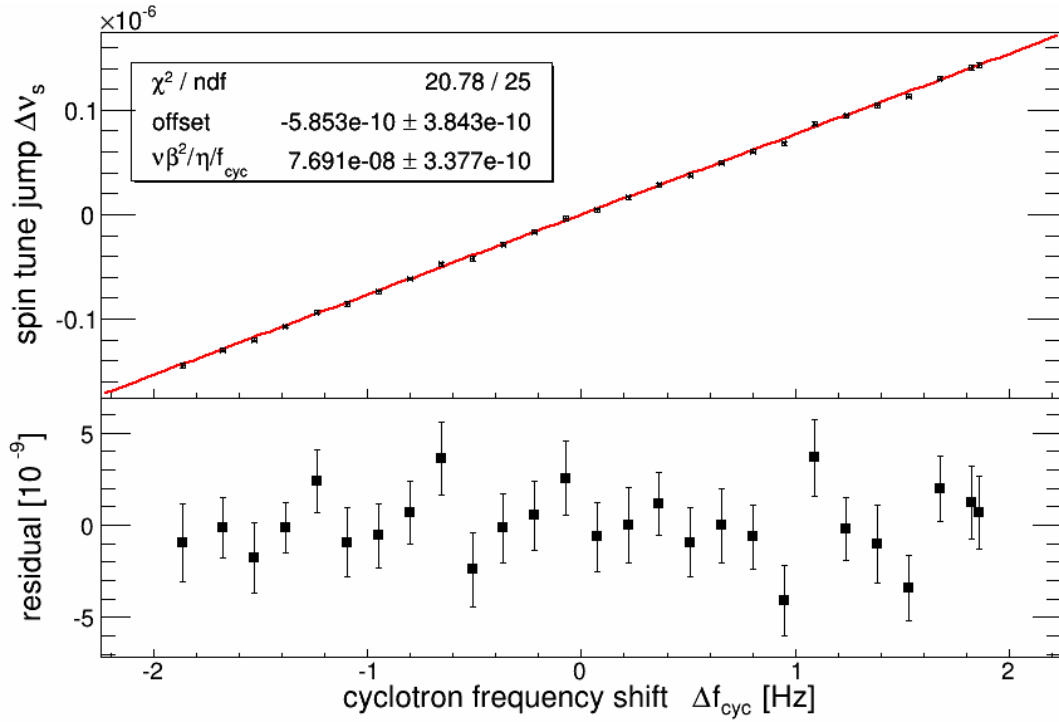


Figure 7.8: Upper plot: spin tune change  $\Delta\nu_s$  versus the shift of the COSY RF  $\Delta f_{\text{RF}}$ . A linear least squares fit is performed to the data and shown in red. Lower plot: residual of the data and the linear fit. (A.1)

Inserting the base values of the spin tune  $\nu_s = 0.16097416346 \pm 1.7 \times 10^{-9}$  and of the COSY RF  $f_{\text{RF}} = (750\,599.036 \pm 0.011)$  Hz allows determining the fraction

$$\frac{\beta_{\text{beam}}^2}{\eta_p} = \frac{f_{\text{RF}}}{\nu_s} \frac{\Delta\nu_s}{\Delta f_{\text{RF}}} = 0.3572 \pm 0.0015, \quad (7.26)$$

It depends on the COSY lattice since  $\eta_p$  is connected to the momentum compaction factor  $\alpha$ , which is a quantity defined by the settings of the storage ring. In conclusion, the spin tune change due to a shift of the COSY RF is linear over the whole scan interval. The stability of  $\omega_{\text{RF}}$  is studied in the upcoming section.

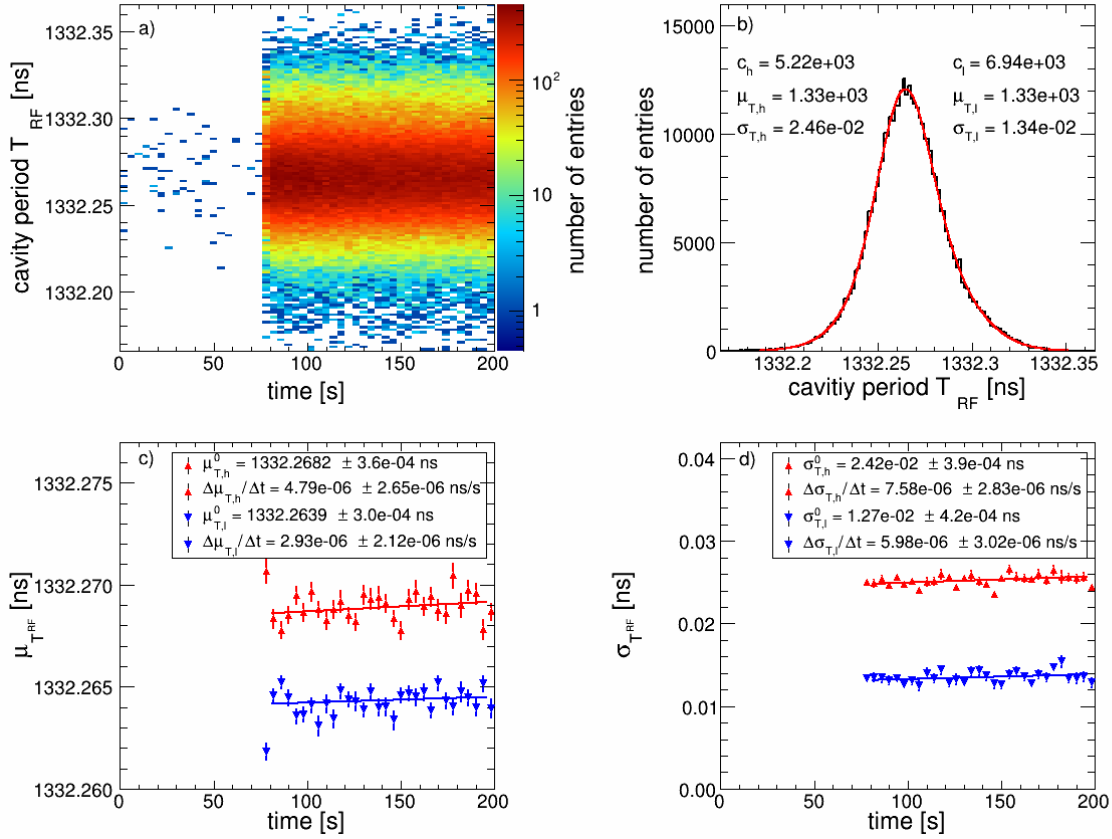


Figure 7.9: a) Time depending distribution of the RF cavity period  $T_{RF}$  for one cycle. The z-axis is chosen logarithmic. b) Y axis projection of the entire cycle. The red curve represents a least squares fit by a double Gaussian Eq. 7.26. c) Time depending mean values  $\mu_{T_{RF}}$  of the individual Gaussian distribution. The red and the blue curves represent a least squares fit by a linear function. d) Time depending widths  $\sigma_{T_{RF}}$  of the corresponding Gaussian distribution. Again, the curves represent a least squares fit by a linear function. (??)

### 7.2.3 RF Cavity Period

In this section, the drift of the COSY RF period  $T_{RF}$  during a cycle and in addition its long-term stability is studied. A time depending distribution of  $T_{RF}$  for a 200s cycle is shown in Fig. 7.11 a). In b) the vertical projection of the whole cycle is presented, where the red curve corresponds to a least squares fit by a double Gaussian

$$f(T_{RF}) = c_h e^{-\frac{1}{2} \left( \frac{T_{RF} - \mu_{T,h}}{\sigma_{T,h}} \right)^2} + c_l e^{-\frac{1}{2} \left( \frac{T_{RF} - \mu_{T,l}}{\sigma_{T,l}} \right)^2}. \quad (7.27)$$

Here,  $\mu_{T,h}$  and  $\mu_{T,l}$  are the mean values and  $\sigma_{T,h}$  and  $\sigma_{T,l}$  denote the width of the individual distributions, where the subscript h and l correspond to the distribution with the higher respectively lower mean period. One sees that both parameters deviate from each other, whereas the larger mean value yields a broader width. The time depending values of  $\mu_T$  and  $\sigma_T$  are shown in Fig. 7.11 c) respectively d). The difference between the individual mean values yields

$\Delta\mu_{T_{RF}} = \mu_{T,h} - \mu_{T,l} = 0.0054$  ns, which corresponds to a frequency shift of  $\Delta f_{RF} = -3.04$  Hz. Since the normalization parameters  $c_h$  and  $c_l$  are compatible with each other, it is assumed, that both frequencies contribute in equal parts to the beam momentum. If the change between both frequencies occurs fast compared to the time the beam needs to adapt the momentum, the beam energy yields exactly the mean value of both energies defined by  $\mu_{T,h}$  and  $\mu_{T,l}$ .

A linear least squares fit is performed in order to unfold a time depending drift of the COSY RF frequency. One observes, that the linear fit parameters of both Gaussian distributions  $\Delta\mu_T/\Delta t$  are slightly positive. The frequency shift within a 200 s interval is given by

$$\Delta f_{RF}^h(t = 200 \text{ s}) = -\frac{\Delta T_{RF}(t = 200 \text{ s})}{T_{RF}^2} = -\frac{\frac{\Delta\mu_{T,h}}{\Delta t} \cdot 200 \text{ s}}{(\mu_{T,h}^0)^2} = -(0.54 \pm 0.29) \text{ Hz}, \quad (7.28)$$

$$\Delta f_{RF}^l(t = 200 \text{ s}) = -\frac{\frac{\Delta\mu_{T,l}}{\Delta t} \cdot 200 \text{ s}}{(\mu_{T,l}^0)^2} = -(0.33 \pm 0.23) \text{ Hz}, \quad (7.29)$$

which corresponds to a spin tune change of

$$\Delta\nu_s^h(t = 200 \text{ s}) = \frac{\nu_s \beta_{beam}^2}{\eta_p} \frac{\Delta f_{beam}^h}{f_{beam}^h} = -(4.14 \pm 2.22) \times 10^{-8}, \quad (7.30)$$

$$\Delta\nu_s^l(t = 200 \text{ s}) = \frac{\nu_s \beta_{beam}^2}{\eta_p} \frac{\Delta f_{beam}^l}{f_{beam}^l} = -(2.53 \pm 1.76) \times 10^{-8}. \quad (7.31)$$

Consequently, a stable frequency of the COSY RF cavity is one important precondition in order to stabilize the spin tune over a whole cycle.

A long-term measurement of the COSY RF is shown in Fig. 7.10. One observes a fast and a slow oscillation. Thus, a least squares fit by the function

$$T_{RF}^{\text{fit}}(t) = T_{RF}^0 + T_{RF}^1 \sin(2\pi f_{\text{osci}}^{\text{short}} t + \varphi_{\text{osci}}^{\text{short}}) + T_{RF}^2 \sin(2\pi f_{\text{osci}}^{\text{long}} t + \varphi_{\text{osci}}^{\text{long}}), \quad (7.32)$$

is performed. The fit parameter associated to the fast oscillation corresponds to a daily pattern with  $f_{\text{osci}}^{\text{short}} = (1.0012 \pm 0.0003)$  days. Its phase  $\varphi_{\text{osci}}^{\text{short}}$  defines the time of the day when the maximum (2 h0 min) respectively minimum (14 h0 min) is reached. Consequently, in the case of a temperature correlation a maximum temperature would lead to a smaller frequency of the COSY RF.

The period of the slower oscillation yields  $f_{\text{osci}}^{\text{long}} = (17.919 \pm 0.008)$  days. The maximal spin tune change due to the drift of the COSY RF is specified by the amplitude parameter of the oscillations

$$\Delta f_{RF}^{\text{osci}} = \frac{2(T_{RF}^1 + T_{RF}^2)}{(T_{RF}^0)^2} \approx 0.5 \text{ Hz}, \quad (7.33)$$

$$\Rightarrow \Delta\nu_s^{\text{osci}} = 76.91 \text{ ns} \cdot f_{RF}^{\text{osci}} = 3.85 \cdot 10^{-8}, \quad (7.34)$$

where the calibration factor obtained from Fig. 7.8 is used. The amplitude of the daily spin tune variation is given by  $\Delta\nu_s^{\text{day}} \approx 1.65 \cdot 10^{-8}$ . One should note, that the statistical errors obtained by the least squares fit are not reasonable since the  $\chi^2$  is quite high. However, the

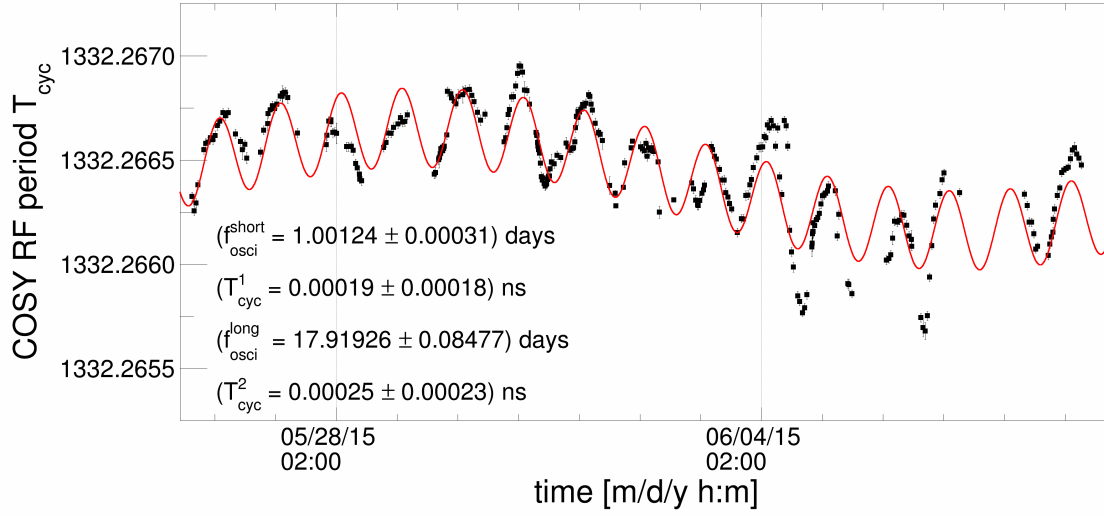


Figure 7.10: Long-term measurement of the COSY RF  $T_{RF}$ . The red curve represents a least squares fit with the function based on two independent oscillations  $T_{RF}^{fit}(t)$ .

daily pattern and the long term drift is clearly identified.

#### 7.2.4 Event Arrival Time

A time distribution of all events detected within a 200 s cycle is shown in Fig. 7.11 a) and b). The x-axis represents the time in cycle in seconds and the y-axis shows the arrival time of the detected event  $t_{ev}$  with respect to the last RF cavity timestamp  $t_{RF,n}$  in nanoseconds

$$t_{ev}^{t_{RF}} = t_{ev} - t_{RF,n}, \quad (7.35)$$

where  $n$  denotes the period number of the cavity RF in which the event is detected. For a better readability the z-axis is chosen logarithmic. The event distribution allows studying the longitudinal phase space of the particles since the longitudinal position of each particle in the beam is specified by  $t_{ev}^{t_{RF}}$  relative to the cavity position. Thus, the time scale of the y-axis can be substituted by the circumference of COSY.

The extraction onto the carbon target starts around  $t_{sol} = 80$  s. Simultaneously, the RF solenoid was switched on in order to flip the initially vertical polarization into the horizontal plane. The examples shown in Fig. 7.11 a) and b) were performed with two different conditions of cooling. In a) the electron cooler was activated during the whole cycle, whereas for b) no cooling was applied.

The data points in Fig. 7.11 c) represent the mean values  $\mu_{t_{ev}^{t_{RF}}}$  of each macroscopic time bin  $\Delta T_{mac}$  in Fig. 7.11 a) (red) and b) (blue). In the no cooling case a linear decreasing behavior of  $\mu_{t_{ev}^{t_{RF}}}$  is observed, whereas for the steadily cooled beam it stays constant. This indicates that the mean longitudinal position of the extracted particles moves over time relative to the location of the RF cavity. This corresponds to a mismatch of the COSY RF and the frequency of the detected particles, which might be explained by a higher momentum of the ensemble

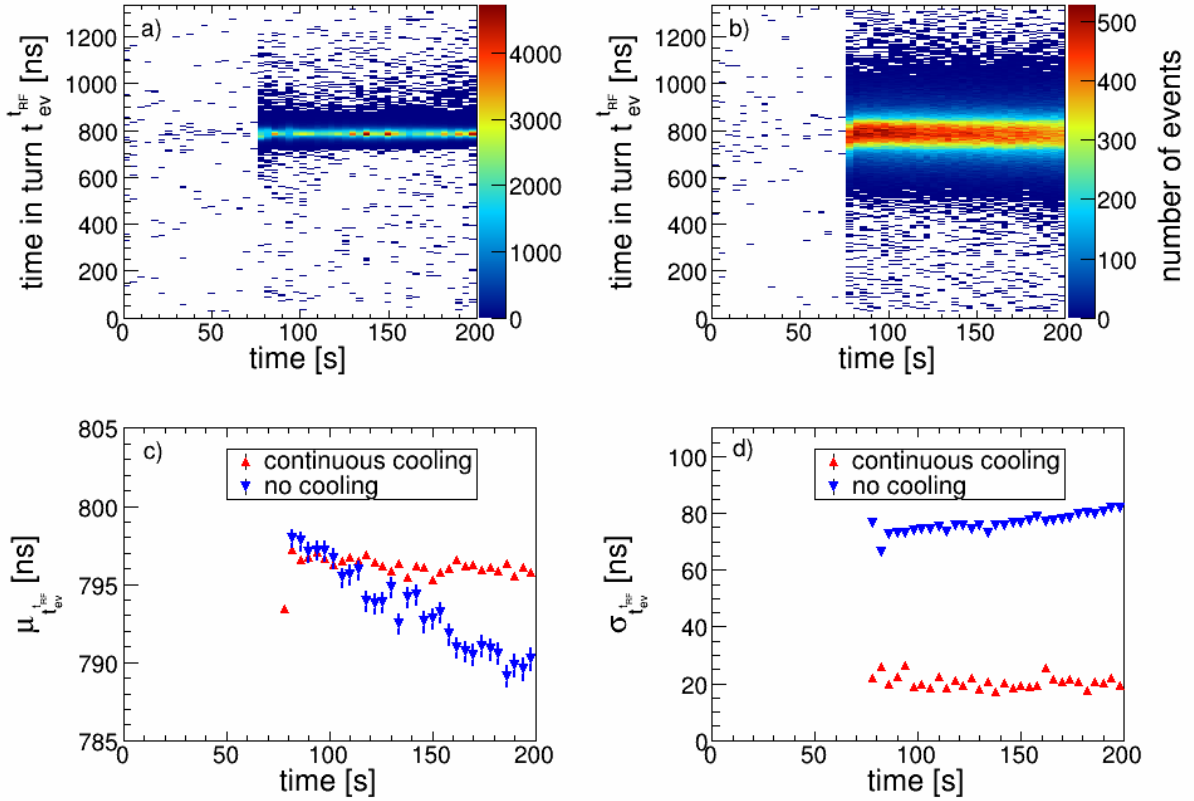


Figure 7.11: a) and b) Time in turn distribution  $t_{ev}^{t_{RF}}$  of all events during a 200 s cycle. a) was performed with continuous cooling and b) without any cooling. The scale of the z-axis is chosen logarithmic. In addition, the mean values (c) respectively the standard deviations (d) of  $t_{ev}^{t_{RF}}$  for each time bin are given. The data points in red correspond to the setup with a continuously cooled beam and the blue data points to a uncooled beam. ( ??

compared to the one defined by the RF cavity  $\Delta f_{beam} = f_{beam} - f_{RF}$ . The time depending frequency shift is given by the time derivative of  $\mu_{t_{ev}^{t_{RF}}}$  and in the case of no cooling it yields approximately

$$\frac{\Delta f_{beam}}{f_{beam}} = -\frac{\Delta T_{beam}}{T_{beam}} = -\frac{\partial \mu_{t_{ev}^{t_{RF}}}(t)}{\partial t} \approx 10^{-10}, \quad (7.36)$$

$$\Leftrightarrow \Delta f_{beam} = 10^{-10} f_{beam} \approx 0.75 \text{ mHz}. \quad (7.37)$$

For the constantly cooled beam the time derivative almost vanishes, which indicates that the frequency of the detected events is equal to the one provided by the cavity. In Fig. 7.11 d) the standard deviation  $\sigma_{t_{ev}^{t_{RF}}}$  of the respective time bin distribution is shown. For the cooled beam (red) the longitudinal spread of the particles stays constant since the electron cooler ensures that the momentum spread of the particles is small and almost time-invariant. The uncooled beam (blue) provides a larger standard deviation  $\sigma_{t_{ev}^{t_{RF}}}$  which increases over time, and the momentum spread grows linearly in good approximation. A decreasing arrival time

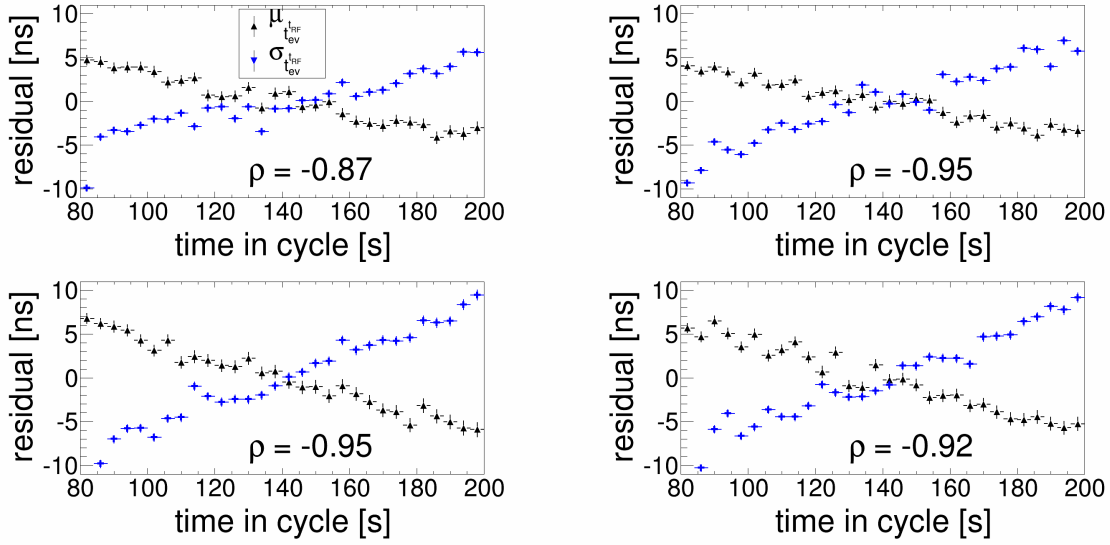


Figure 7.12: Four time depending distributions of the residuals obtained by subtracting the mean values of  $\mu_{t_{ev}^{t_{RF}}}^{\text{res}}$  (black) and  $\sigma_{t_{ev}^{t_{RF}}}^{\text{res}}$  (blue) from each data point. In addition, the Pearson correlation coefficients  $\rho$  based on both distributions are given. (A.1)

of the detected event with respect to the COSY RF signal induces an increasing longitudinal width of the beam. In order to quantify the correlation, the mean values  $\bar{\mu}_{t_{ev}^{t_{RF}}}$  and  $\bar{\sigma}_{t_{ev}^{t_{RF}}}$  of each distribution are subtracted from the respective data points

$$\mu_{t_{ev}^{t_{RF}},i}^{\text{res}} = \mu_{t_{ev}^{t_{RF}},i} - \bar{\mu}_{t_{ev}^{t_{RF}}}, \quad \text{with } \bar{\mu}_{t_{ev}^{t_{RF}}} = \frac{1}{N_{\text{bins}}} \sum_{i=1}^{N_{\text{bins}}} \mu_{t_{ev}^{t_{RF}},i}, \quad (7.38)$$

$$\sigma_{t_{ev}^{t_{RF}},i}^{\text{res}} = \sigma_{t_{ev}^{t_{RF}},i} - \bar{\sigma}_{t_{ev}^{t_{RF}}}, \quad \text{with } \bar{\sigma}_{t_{ev}^{t_{RF}}} = \frac{1}{N_{\text{bins}}} \sum_{i=1}^{N_{\text{bins}}} \sigma_{t_{ev}^{t_{RF}},i}, \quad (7.39)$$

where  $N_{\text{bins}}$  represents the number of time bins. Four different distributions of  $\mu_{t_{ev}^{t_{RF}}}^{\text{res}}$  (black) and  $\sigma_{t_{ev}^{t_{RF}}}^{\text{res}}$  (blue) are shown in Fig. 7.12. A strong negative correlation becomes obvious, whereas the Pearson product-moment correlation coefficient

$$\rho = \frac{\sum_{i=1}^{N_{\text{bins}}} \left( \mu_{t_{ev}^{t_{RF}},i} - \bar{\mu}_{t_{ev}^{t_{RF}}} \right) \left( \sigma_{t_{ev}^{t_{RF}},i} - \bar{\sigma}_{t_{ev}^{t_{RF}}} \right)}{\sqrt{\sum_{i=1}^{N_{\text{bins}}} \left( \mu_{t_{ev}^{t_{RF}},i} - \bar{\mu}_{t_{ev}^{t_{RF}}} \right)^2} \sqrt{\sum_{i=1}^{N_{\text{bins}}} \left( \sigma_{t_{ev}^{t_{RF}},i} - \bar{\sigma}_{t_{ev}^{t_{RF}}} \right)^2}} \quad (7.40)$$

yields values close to  $-1$ . Thus, a time depending longitudinal widening leads to a decreasing  $t_{ev}^{t_{RF}}$ .

### 7.3 Extraction Methods

In this section, the spin tune drift caused by different extraction methods will be studied. The experimental setup provides the bump extraction and the white noise extraction technique in order to realize an elastic scattering of the deuteron beam onto the carbon target. In the following, the results of both techniques are investigated.

#### 7.3.1 Vertical and Horizontal Bump Extraction

The bump extraction technique is based on steering the beam onto the carbon block by means of a magnetic dipole field. A radial field leads to a vertical and a vertical field to a radial displacement of the beam. After passing the target and two additional quadrupole magnets the beam is brought back to the reference orbit by a second magnetic dipole. Altogether the phase of the betatron oscillation advances by a half period. Thus, this method is called the local vertical or horizontal  $\pi$ -bump. A linear increasing and time depending magnetic field ensures that the beam is extracted entirely.

In Fig. 7.13 two examples of a spin tune phase distribution are shown, which are obtained by the magnetic bump extraction methods. The vertical bump corresponds to the blue data points and the horizontal one to the points given in magenta. For both methods, one observes a strong parabolic behavior, which corresponds to a significant linear spin tune change. A simple quadratic phase model is assumed, which leads to

$$\nu_s = \frac{1}{2\pi} \frac{d\varphi_s n}{dn} = \frac{1}{2\pi} (\varphi_{s,1} + 2\varphi_{s,2}n) . \quad (7.41)$$

The horizontal bump technique induces a negative spin tune drift, while the vertical bump corresponds to a positive one.

The corresponding interpolated spin tune based on Eq. 7.41 is shown in Fig. 7.14. Again, the same color scheme is used as given in Fig. 7.13. The respective spin tune drifts per particle turn yield

$$\frac{\Delta\nu_s^{\text{ver}}}{\Delta n} = (-1.03 \pm 0.01) \frac{10^{-15}}{\text{turn}} , \quad (7.42)$$

$$\frac{\Delta\nu_s^{\text{hor}}}{\Delta n} = (3.00 \pm 0.03) \frac{10^{-15}}{\text{turn}} . \quad (7.43)$$

For the horizontal extraction one observes a large positive spin tune drift, whereas the vertical bump provides a negative drift which is approximately 1/3 smaller. Two independent sources are candidates for this effect.

#### Magnetic Dipole Fields

Firstly, according to the Thomas-BMT equation 2.110 the magnetic fields of the kickers directly act on the spin motion. A radial magnetic field induces a vertical spin build up out of the horizontal plane. On average the spin vectors of the ensemble are distributed uniformly at the

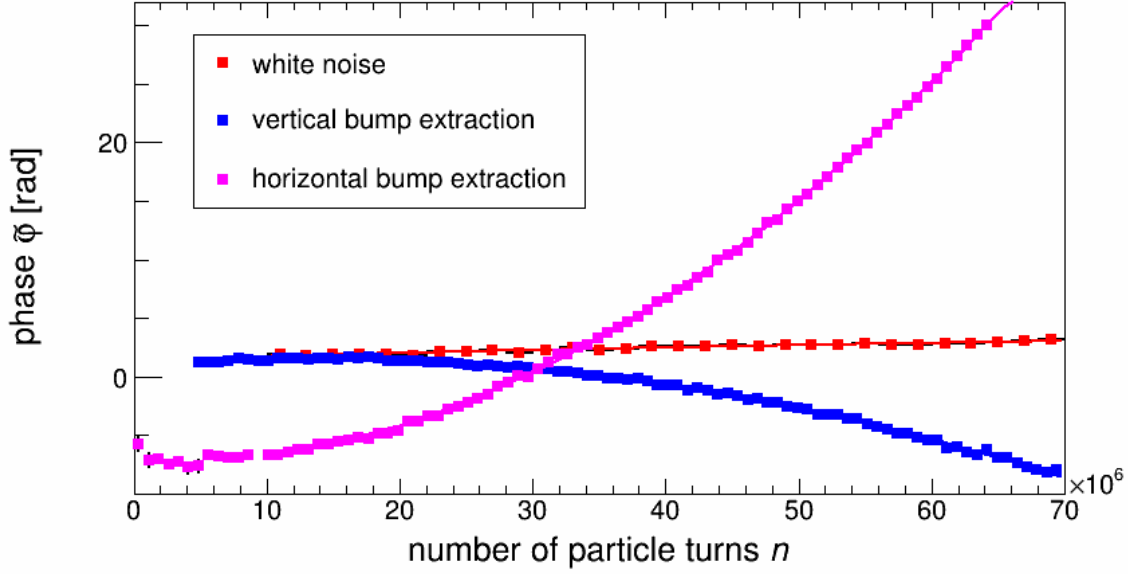


Figure 7.13: Comparison of the phase distributions based on white noise (red), vertical (blue) and horizontal (magenta) local bump extraction. (A.1)

kicker magnet and thus the expected spin build up vanishes since the kicks cancel out to zero. Consequently, no spin tune change should be observed due to radial magnetic fields.

Considering vertical dipole fields the spin vector will be rotated around the vertical axis according to the direction and the strength of the magnetic field, which leads to a kick of the spin

$$\varphi_s = v_s \phi_{\text{beam}} = \gamma G \phi_{\text{beam}}, \quad (7.44)$$

where  $\phi_{\text{beam}}$  denotes the angle between the vector of the initial beam momentum and the momentum vector at the extraction point. The two refocusing quadrupoles, which are located between the dipoles, provide a non-commutative compensation of the spin rotation. This leads to a time depending spin tune change. In particular, the spin vector is not completely returned to the initial state at the position of the detector, since it is not exactly located in the center of the magnetic dipoles.

### Path Lengthening

Additionally, the spin tune is changed by the path lengthening of the particle orbit due to the local bump. The relation between the relative change of the Lorentz factor and the orbit yields to

$$\frac{\Delta v_s^{\text{length}}}{v_s} = \gamma^2 \beta^2 \frac{\Delta L}{L}. \quad (7.45)$$

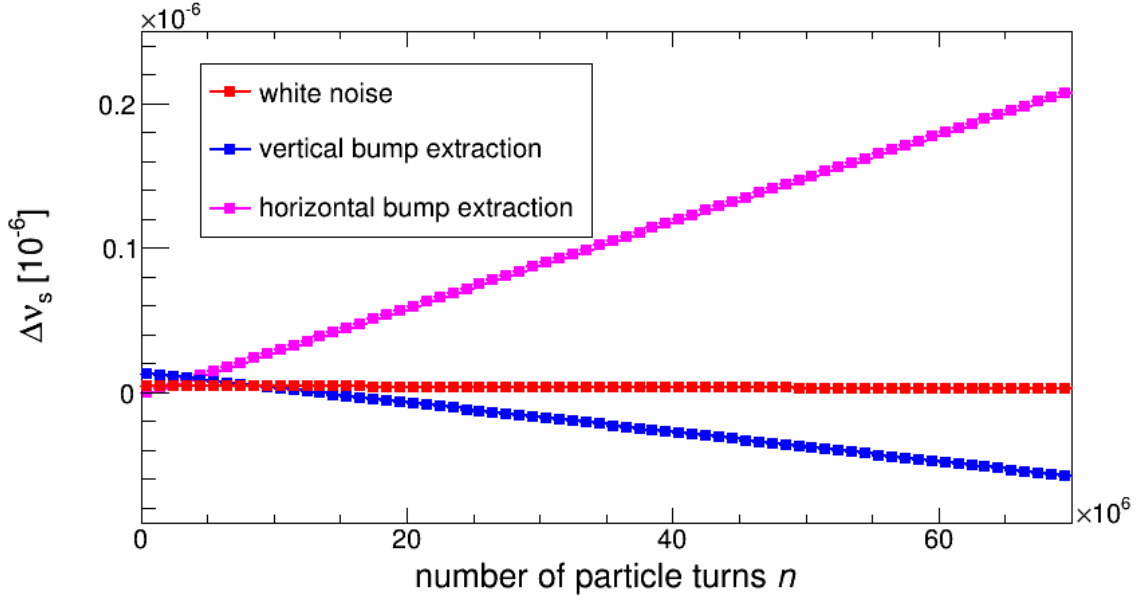


Figure 7.14: Interpolated spin tune obtained for the white noise extraction (red), the vertical (blue) and the horizontal (magenta) local bump extraction.

The so-called  $\pi$ -bump method provides a beam displacement within one-half of a betatron period. The betatron tune for COSY is generally given by about 3.6, which results in an orbit period length of  $L_{\text{COSY}}/3.6 = 50$  m, where  $L_{\text{COSY}} \approx 180$  m denotes the circumference of the complete ring. Since the bump is realized within a half period the total length between the two magnetic dipoles is  $L_{\text{bump}} = 25$  m.

In Fig. 7.15 a sketch of the local orbit bump is shown. The red curve represents the envelope of the betatron oscillation before the extraction starts  $\beta_z^{\text{max}}(t_{\text{ini}}) = 1$  mm. After switching on the magnetic dipole magnets the amplitude increases to a maximal displacement of  $\beta_z^{\text{max}}(t_{\text{fin}}) = 10$  mm, which is delineated by the blue line. To estimate the length difference of the particle orbit  $\Delta L$  one has to compare the arc lengths of the curvatures  $L_{\text{ini}}$  and  $L_{\text{fin}}$ , which can be calculated by

$$L(\beta_z^{\text{max}}) = \int_a^b \sqrt{1 + f'(x)} dx = \int_0^{L_{\text{bump}}} \sqrt{1 + \left(\frac{\pi \beta_z^{\text{max}}}{25}\right)^2 \cos^2\left(\frac{\pi}{25}x\right)} dx. \quad (7.46)$$

Here  $a = 0$  m and  $b = L_{\text{bump}} = 25$  m defines the x-axis interval and  $f(x) = \beta_z^{\text{max}} \sin(\pi/25x)$  is the functional form of the curve. The elliptic integral of second kind in Eq. 7.46 provides no analytical solution, however numerical calculation yields

$$\Delta L = L_{\text{fin}} - L_{\text{ini}} \approx 25.00001 \text{ m} - 25.0000001 \text{ m} = 10^{-5} \text{ m}. \quad (7.47)$$

Thus, the relative change of the spin tune due to vertical respectively horizontal path length-

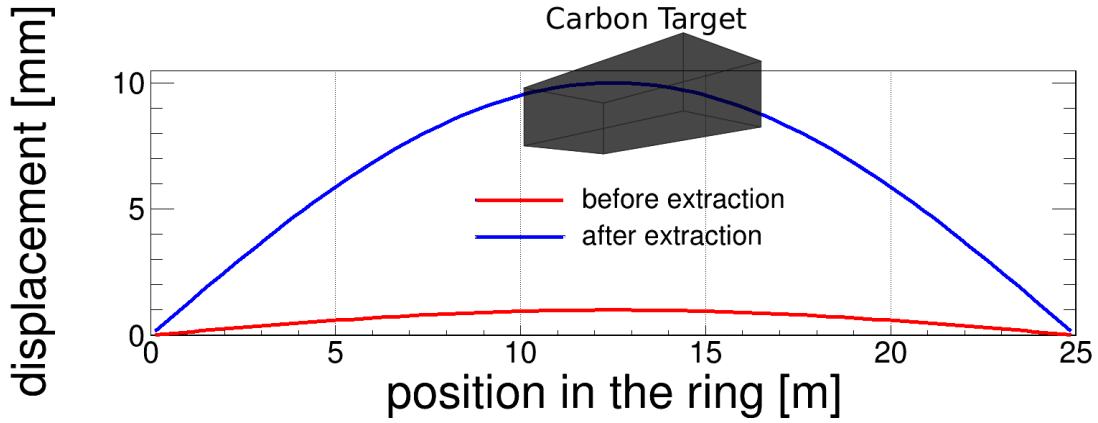


Figure 7.15: Sketch of the vertical respectively horizontal  $\pi$ -bump extraction. The red curve represents the betatron amplitude before and the blue one after extraction onto the carbon target.

ening is given by

$$\frac{\Delta\nu_s^{\text{length}}}{\nu_s} = \gamma^2 \beta^2 \frac{\Delta L}{L} = 0.268 \cdot \frac{10^{-5} \text{m}}{180 \text{m}} \approx 1.5 \cdot 10^{-8}. \quad (7.48)$$

This yields a spin tune shift of  $\Delta\nu_s^{\text{length}} = -0.1609 \cdot 1.5 \cdot 10^{-8} = -2.41 \cdot 10^{-9}$ . The results are one order of magnitude smaller than the measured one during a cycle for a vertically extracted beam  $\Delta\nu_s^{\text{ver}} = -8.16 \cdot 10^{-8}$ . One explanation for the deviation might be given by the quadrupole magnets, which are placed in between the two magnetic steerers to focus back the beam to the reference orbit. Particles with a larger betatron amplitude pass the quadrupole magnets more and more off-centered and will see a time depending change of the vertical component of the magnetic field, which leads to an additional non-commutative spin rotation.

### 7.3.2 White Noise Extraction

The white noise extraction is realized by a time depending vertical electrical field  $E_{\perp}(t)$ . This process heats the beam by enlarging the amplitude of the particle phase space. The field is generated by a superposition of several sinusoidal electrical wave signals with different frequencies. It is possible to connect the power supply of the electric plates to the so-called Schneider box, which measures the change of the beam current to provide a feedback in order to stabilize the extraction rate to a constant level during the whole cycle. Consequently, the number of detected events and therefore the statistical accuracy of the spin phase determination is constant for each macroscopic interval  $\Delta n$  and in the case of no depolarization.

A typical example of a phase distribution based on the white noise extraction is shown as the red data points in Fig 7.13. One observes a tiny quadratic drift of the phase, which corresponds to a small spin tune change, which is presented by the red curve in Fig. 7.14. In Sec. 4.4.1 it was shown, that under the assumption of a Rayleigh distributed spin tune the turn depending

phase change is described by

$$\varphi_s(n) = \varphi_0 + \frac{\pi}{2} - \arctan \left( \frac{\exp \left( (\sqrt{2}\pi\sigma_{R,\nu_s}n)^2 \right) - \operatorname{erfi} \left( \sqrt{2}\pi\sigma_{R,\nu_s}n \right)}{\sqrt{\pi}\sqrt{2}\pi\sigma_{R,\nu_s}n} \right), \quad (7.49)$$

where  $\operatorname{erfi}$  denotes the imaginary error function,  $n$  is the turn number and  $\sigma_{R,\nu_s}$  corresponds to the scale parameter of the Rayleigh distribution, i.e. the width of the spin tune distribution. Note that this model does not take into account any time depending systematic effects of the storage ring like variations of the magnetic fields or geometric beam fluctuations.

### 7.3.3 Conclusion

In the last sections three different extraction methods were discussed. In the case of the horizontal bumped technique a large spin tune change is observed since a time depending vertical magnetic field is applied, which directly manipulates the spin motion. The vertical extraction method shows a smaller but opposite spin tune change. Relating thereto the calculated spin tune drift induced by the path-lengthening is one order of magnitude too small in order to describe this effect. However, a non-perfectly aligned vertical magnetic field to the invariant spin axis contributes to an additional time depending spin tune drift. Finally, the white noise extraction based on a random electrical field generator yields the smallest spin tune change of all methods. Thus, this technique provides a minimal invasive extraction of the beam onto the carbon target.

## 7.4 Spin Tune Investigations (Beam time June/May 2015)

One of the main motivations of the beam time performed in May and June 2015 was the investigation of the spin coherence time  $\tau_{\text{SCT}}$ . Therefore, a polarized 0.97 GeV/c deuteron beam was injected into the storage ring and its polarization was tilted into the horizontal plane by means of the RF solenoid in order to realize an idle spin precession. The impact on the spin coherence time for different ring settings was studied by several measurement series. In the upcoming sections the results are discussed.

### 7.4.1 Variation within a Cycle

In the previous section the spin tune drift based on different extraction methods was discussed. It was shown that the white noise extraction corresponds to the minimally invasive technique. However, three additional processes cause a turn depending spin tune phase variation.

1. The depolarization of the spin ensemble leads to a non-linear drift of the spin tune phase if the spin tune distribution of the particles is assumed to be Rayleigh distributed. Note that this process does not change the spin tune of the reference particle itself.
2. If the beam period  $T_{\text{beam}}$  is not stable over time, the spin tune varies according to the considerations derived in section 7.2.3. The exact relation is experimentally determined and discussed in Eq. 7.25.
3. Time depending changes of the magnetic elements in the ring, which either varies the energy of the particle bunch or change the orbit of the beam, leads to additional spin tune variations.

The first process is estimated by the spin coherence time  $\tau_{\text{SCT}}$ , which can be determined simultaneously by the phase and amplitude spectrum. Note that the spin coherence time is correlated to the width of the spin tune distribution  $\sigma_{\text{R},\nu_s}$ . This allows identifying the functional form of the time depending spin tune phase based on the depolarization effect. The second item can be studied by the investigation of the RF cavity frequency. In order to investigate implications of the statement a very high precision of the orbit measurement and the currents in the bending dipoles is required.

### Depolarization

In chapter 6.5 it was shown, that the depolarization process can be described by the width of the spin tune distribution  $\sigma_{\text{R},\nu_s}$ . In the following, it is assumed that this parameter is time invariant  $\sigma_{\text{R},\nu_s}(n) = \sigma_{\text{R},\nu_s,0} = \text{const.}$ . Two cycles from different runs, which provides different spin coherence times, are shown in Fig. 7.16. The black data points represent estimated parameters obtained by the discrete turn Fourier transform. The color scale corresponds to the associated probability density functions derived in the previous chapters. The 68.3% confidence interval is represented by the black error bars. The gray curves show the result of a

global maximum likelihood fit, which minimizes the likelihood function

$$\mathcal{L} = \prod_{i=1}^N \tilde{p}_\varphi(\varphi_s(n_i; \boldsymbol{\theta}_\varphi); \tilde{\epsilon}_i, \tilde{\varphi}_{s,i}, \sigma_i) + \prod_{i=1}^N \tilde{p}_R(\epsilon(n_i; \boldsymbol{\theta}_\epsilon); \tilde{\epsilon}_i, \sigma_i). \quad (7.50)$$

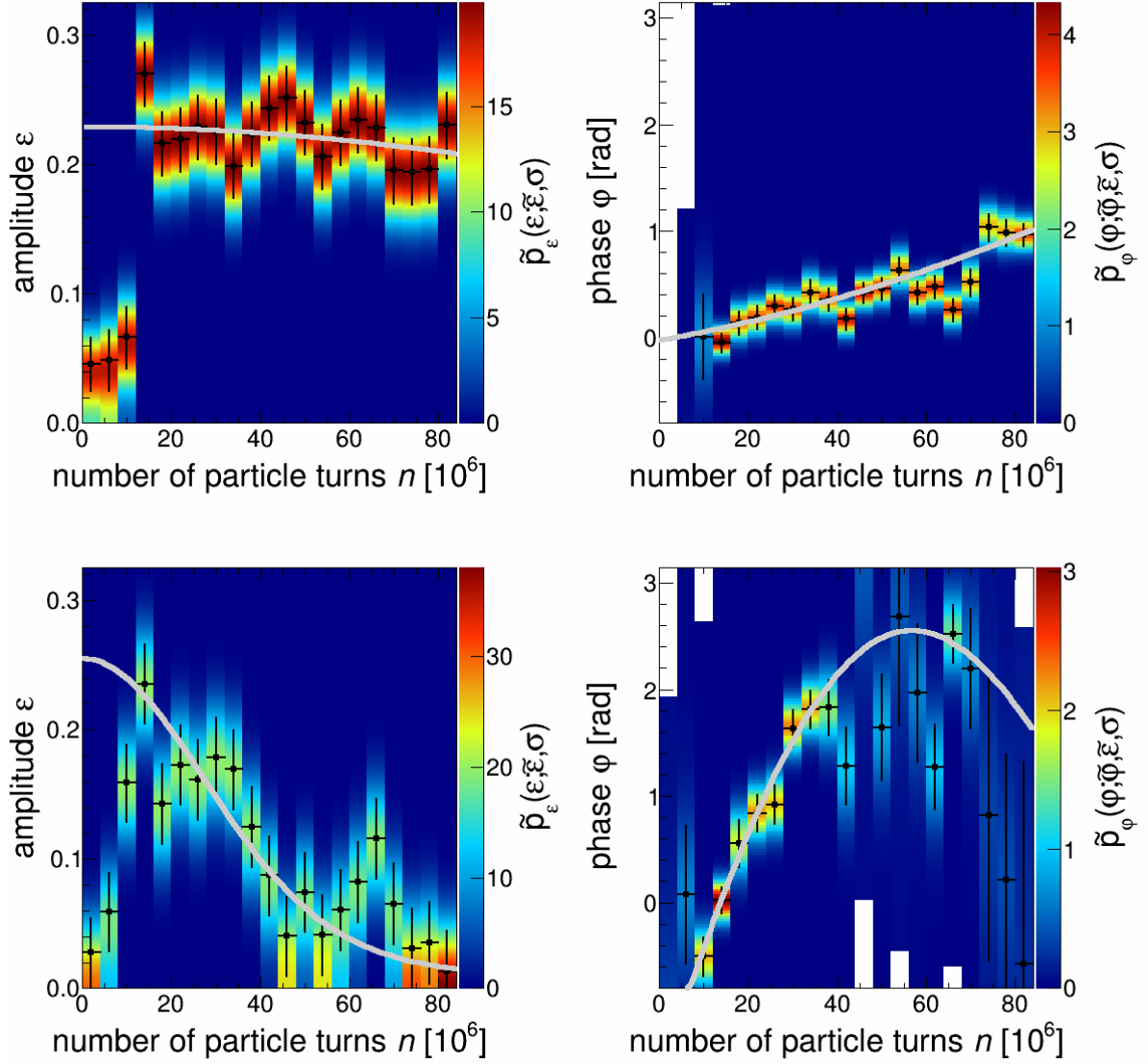


Figure 7.16: Turn depending amplitude and phase distribution for a long and short spin coherence time. The color scheme represents the probability density function according to the estimated values of the discrete turn Fourier transform. The gray curves correspond to a global maximum likelihood fit with the model functions derived in the previous chapters. (A.1)

The parameter vector reads  $\boldsymbol{\theta}_\varphi \in \{\sigma_{R,\nu_s,0}; \nu_{s,0}^{\text{ref}}, \nu_{s,1}^{\text{ref}}, \varphi_s^0\}$  and  $\boldsymbol{\theta}_\epsilon \in \{\sigma_{R,\nu_s,0} \epsilon_0\}$  and the numbers are given in table 7.1.

	long	short
$\epsilon_0$	$0.2295 \pm 0.0082$	$0.255 \pm 0.022$
$\varphi_s^0$	$(-1.59 \pm 0.25)$ rad	$(-3.25 \pm 0.38)$ rad
$\sigma_{R,\nu_s,0}$	$(1.26 \pm 0.34) \times 10^{-9}$	$(8.56 \pm 0.53) \times 10^{-9}$
$\nu_{s,0}^{\text{ref}}$	$(-0.38 \pm 1.65) \times 10^{-9}$	$(10.6 \pm 4.5) \times 10^{-9}$
$\nu_{s,1}^{\text{ref}}$	$(1.9 \pm 2.9) \times 10^{-17}$	$(-24.5 \pm 12.1) \times 10^{-17}$

Table 7.1: Parameters obtained by the global maximum likelihood fit based on the data for a long and short spin coherence time shown in Fig. 7.16.

The associated model function of the phase yields

$$\varphi_s(n; \boldsymbol{\theta}_\varphi) = \frac{\pi}{2} + \varphi_s^0 + 2\pi(\nu_{s,0}^{\text{ref}} n + \nu_{s,1}^{\text{ref}} n^2) - \arctan\left(\frac{e^{(\sigma_{\varphi_s} n)^2}}{\sigma_{\varphi_s} n} - \operatorname{erfi}(\sigma_{\varphi_s} n)\right), \quad (7.51)$$

with  $\sigma_{\varphi_s} = \sqrt{2}\pi\sigma_{R,\nu_s}$ . In addition, the amplitude yields

$$\epsilon(n; \boldsymbol{\theta}_\epsilon) = \epsilon_0 \left( \left[ 1 - \sqrt{\pi}\sigma_{\varphi_s} n e^{-(\sigma_{\varphi_s} n)^2} \operatorname{erfi}(\sigma_{\varphi_s} n) \right]^2 + \pi(\sigma_{\varphi_s} n)^2 e^{-2(\sigma_{\varphi_s} n)^2} \right)^{\frac{1}{2}}. \quad (7.52)$$

Both functions depend on  $\sigma_{\varphi_s}$ . In the first order, this quantity is coupled to the sextupole settings. Consequently, it is assumed to be constant for all cycles recorded within the same run. However, the linear drift of the reference spin tune  $\nu_{s,1}^{\text{ref}}$  can vary from cycle to cycle. It takes into account the variation of the beam frequency, the change of the current in the bending magnets or a drift of the beam orbit during a cycle. The ratio

$$r_{\nu_{s,1}^{\text{ref}}} = \frac{\nu_{s,1}^{\text{ref}}}{\sigma_{\nu_{s,1}^{\text{ref}}}} \quad (7.53)$$

is shown in Fig. 7.17 for 474 cycles. One observes a Gaussian distribution with negative mean and a standard deviation of  $\sigma_{r_{\nu_{s,1}^{\text{ref}}}} = 2.93 \pm 0.01$ . Thus, the decreasing reference spin tune corresponds to a significant statistical process. In the following sections, one possible source of this effect is discussed by investigating the period of the beam revolution in the ring.

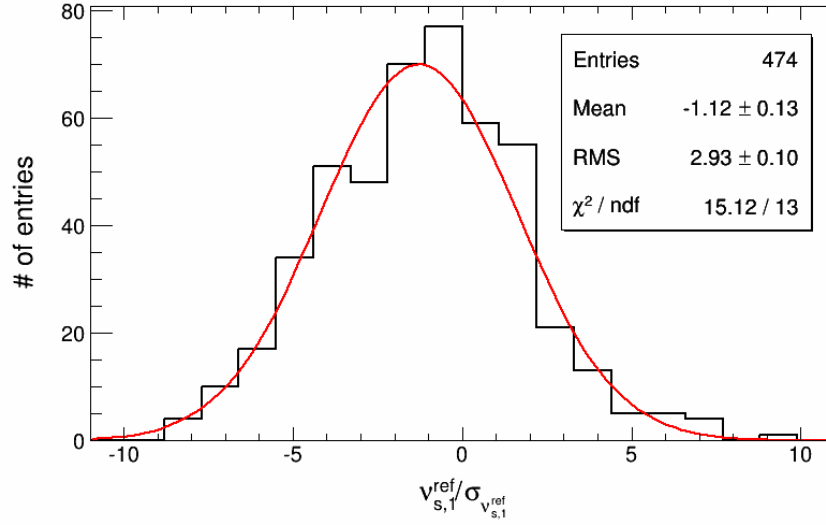


Figure 7.17: The ratio of the linear parameter of the reference spin tune and its standard deviation. In addition, a Gaussian function is shown based on a least squares fit. (A.1)

### Period of the Beam

The change of the reference spin tune induced by the drift of the beam frequency  $f_{\text{beam}}$  yields

$$\begin{aligned} \Delta v_s^{\text{ref}} &= \frac{\beta_{\text{beam}}^2}{\eta_p} \frac{v_s}{f_{\text{beam}}} \Delta f_{\text{beam}} \\ &= 0.3572 \frac{v_s}{f_{\text{beam}}} \Delta f_{\text{beam}}, \end{aligned} \quad (7.54)$$

where  $\eta_p$  is the slip factor and  $\beta_{\text{beam}}$  denotes the ratio of the particle velocity and the speed of light. In addition, the variation of the reference spin tune is given by the linear drift parameter

$$\begin{aligned} \Delta v_s^{\text{ref}}(n) &= v_{s,1}^{\text{ref}} n = \frac{\beta_{\text{beam}}^2}{\eta_p} \frac{v_s}{f_{\text{beam}}} \Delta f_{\text{beam}}(n) \quad (7.55) \\ \Rightarrow v_{s,1}^{\text{ref}} n &= \frac{\beta_{\text{beam}}^2 v_s}{\eta_p} \cdot \frac{\Delta f_{\text{beam}}(n)}{f_{\text{beam}}} \\ &= -\frac{\beta_{\text{beam}}^2 v_s}{\eta_p} \cdot \frac{\Delta T_{\text{beam}}(n)}{T_{\text{beam}}} \\ &= -\frac{\beta_{\text{beam}}^2}{\eta_p} \cdot \frac{\Delta T_{\text{beam}}(n)}{T_s}. \end{aligned} \quad (7.56)$$

The ratio yields  $\beta_{\text{beam}}^2/\eta_p = 0.3572$ . In addition, the period of the spin precession is given by  $T_s = T_{\text{beam}}/v_s \approx 8.28 \mu\text{s}$ .

The beam period is determined by two observables. In particular, the RF cavity period  $T_{\text{RF}}$  acts like a baseline. In addition, the difference between two event arrival times with respect to

the last RF cavity time stamp  $t_{\text{ev}}^{\text{RF}}$  is a measure of how much the beam period deviates from the beam frequency  $T_{\text{beam}}$

$$\Delta T_{\text{beam}} = \Delta T_{\text{RF}} + \frac{\Delta t_{\text{ev}}}{\Delta n} = \Delta T_{\text{RF}} + \frac{t_{\text{ev},i}^{\text{RF}} - t_{\text{ev},j}^{\text{RF}}}{n_i - n_j} \quad \text{with } i, j \in (1, \dots, N_{\text{ev}}). \quad (7.57)$$

The variable  $n$  corresponds to the turn number of the detected event, which is specified by the indices  $i$  and  $j$ .

### Event Arrival Time

Firstly, the arrival time of the event with respect to the last RF cavity signal  $t_{\text{ev}}^{\text{RF}}$  (Eq. 7.35) is studied. Inserting Eq. 7.57 into Eq. 7.56 yields

$$\nu_{s,1}^{\text{ref}} n = -\frac{\beta_{\text{beam}}^2}{\eta_{\text{p}}} \frac{\nu_{\text{s}}}{T_{\text{beam}}} \frac{\partial t_{\text{ev}}^{\text{RF}}(n)}{\partial n} \approx -4.32 \times 10^{-5} \frac{1}{\text{ns}} \cdot \frac{\partial t_{\text{ev}}^{\text{RF}}(n)}{\partial n}. \quad (7.58)$$

The values of the spin tune and the beam frequency are approximately given by  $\nu_{\text{s}} \approx 0.1609741$  and  $f_{\text{beam}} = 1/T_{\text{beam}} \approx 750\,599$  Hz. Thus, the reference spin tune correlates negatively to the arrival time of the detected event with respect to the last COSY RF signal. This makes perfect sense, since a particle, which reaches the detector at later times has less energy and consequently a smaller spin tune.

In Fig. 7.18 the turn depending event arrival time with respect to the last COSY RF signal is shown for six cycles within the same run. One observes a quadratic behavior of  $t_{\text{ev}}^{\text{RF}}$ . The parabolic least squares fits yield negative quadratic parameters in the order of  $5 \times 10^{-15}$  ns. This corresponds to a linear reference spin tune of

$$\nu_{s,1}^{\text{ref}} n = -4.32 \times 10^{-5} \frac{1}{\text{ns}} \times 2n \cdot t_{\text{ev},2}^{\text{RF}} \quad (7.59)$$

$$\Leftrightarrow \nu_{s,1}^{\text{ref}} = -4.32 \times 10^{-5} \frac{1}{\text{ns}} \times 2 \cdot \left( -5 \times 10^{-15} \text{ ns} \right) \approx 4.32 \times 10^{-19}. \quad (7.60)$$

This value is almost two orders of magnitude smaller than the statistical error of the linear parameter, which yields  $\approx 10^{-17}$  (table 7.1). Consequently, the experimental setup is not sensitive to observe a spin tune variation due to the change of  $t_{\text{ev}}^{\text{RF}}$ . Note that the relative change of the beam frequency based on the event arrival time yields

$$\frac{\Delta f_{\text{beam}}^{t_{\text{ev}}^{\text{RF}}}}{f_{\text{beam}}} = -\frac{\Delta T_{\text{beam}}^{t_{\text{ev}}^{\text{RF}}}}{T_{\text{beam}}} = -2 \frac{5 \times 10^{-15} \text{ ns} \cdot 100 \times 10^6}{1\,332 \text{ ns}} = -7.5 \times 10^{-10}, \quad (7.61)$$

during the measurement interval of  $100 \times 10^6$  turns.

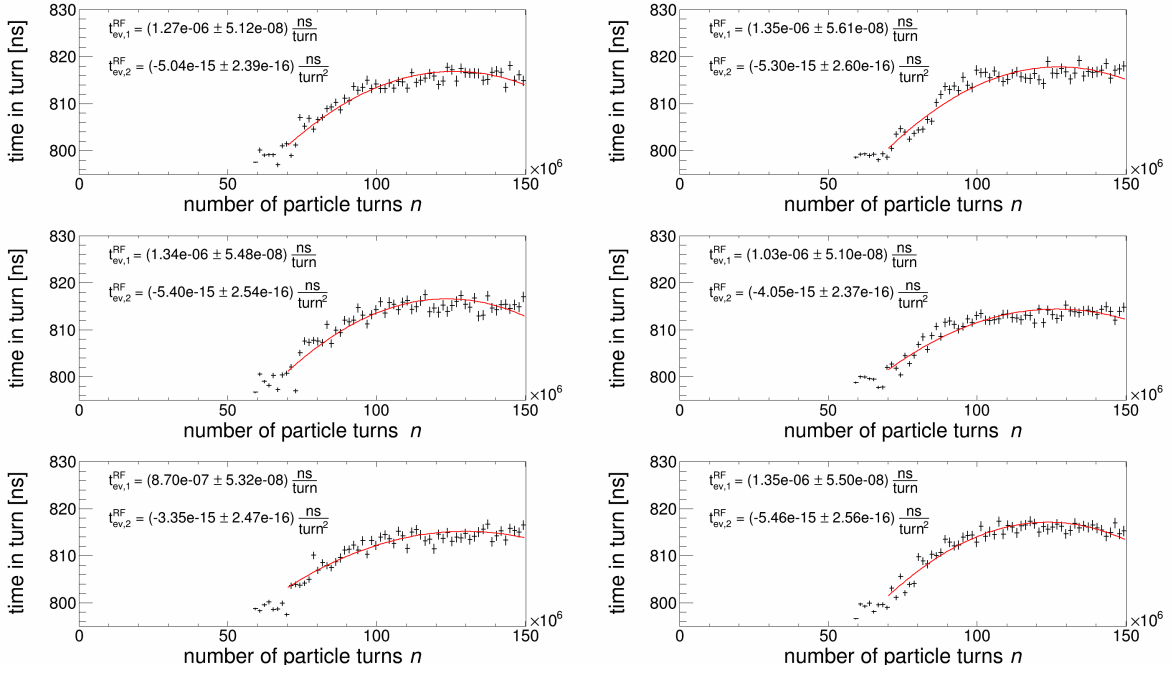


Figure 7.18: Turn depending event arrival time with respect to the last COSY RF time stamp for six cycles within the same run. The red curve corresponds to a parabolic least squares fit. ( A.1)

### RF Cavity Period

A turn depending drift of the RF cavity period causes a change of the reference spin tune, since the energy of the particle increases. Based on Eq. 7.56 and Eq. 7.57 the linear parameter is given by

$$\nu_{s,1}^{\text{ref}} n = -4.32 \times 10^{-5} \frac{1}{\text{ns}} \cdot \Delta T_{\text{RF}}(n). \quad (7.62)$$

Four examples of the turn depending spin tune phase and the corresponding cavity period are shown in Fig. 7.19. A linear increasing  $T_{\text{RF}}$  is observed. Thus, a least squares fit based on the function

$$T_{\text{RF}}(n) = T_{\text{RF}0} + T_{\text{RF}1} \cdot n, \quad (7.63)$$

is performed. In addition, the spin tune phase and the associated amplitude are fitted by a maximum likelihood function providing the linear reference spin tune drift parameter.

The values of  $T_{\text{RF}1}$  given in Fig. 7.19 are positive and in the order of  $T_{\text{RF}1} \approx 4 \times 10^{-12}$  ns. This corresponds to

$$\begin{aligned} \nu_{s,1}^{\text{ref}} &= -4.32 \times 10^{-5} \frac{1}{\text{ns}} \cdot \Delta T_{\text{RF}1} \\ &= 1.6 \times 10^{-16}, \end{aligned} \quad (7.64)$$

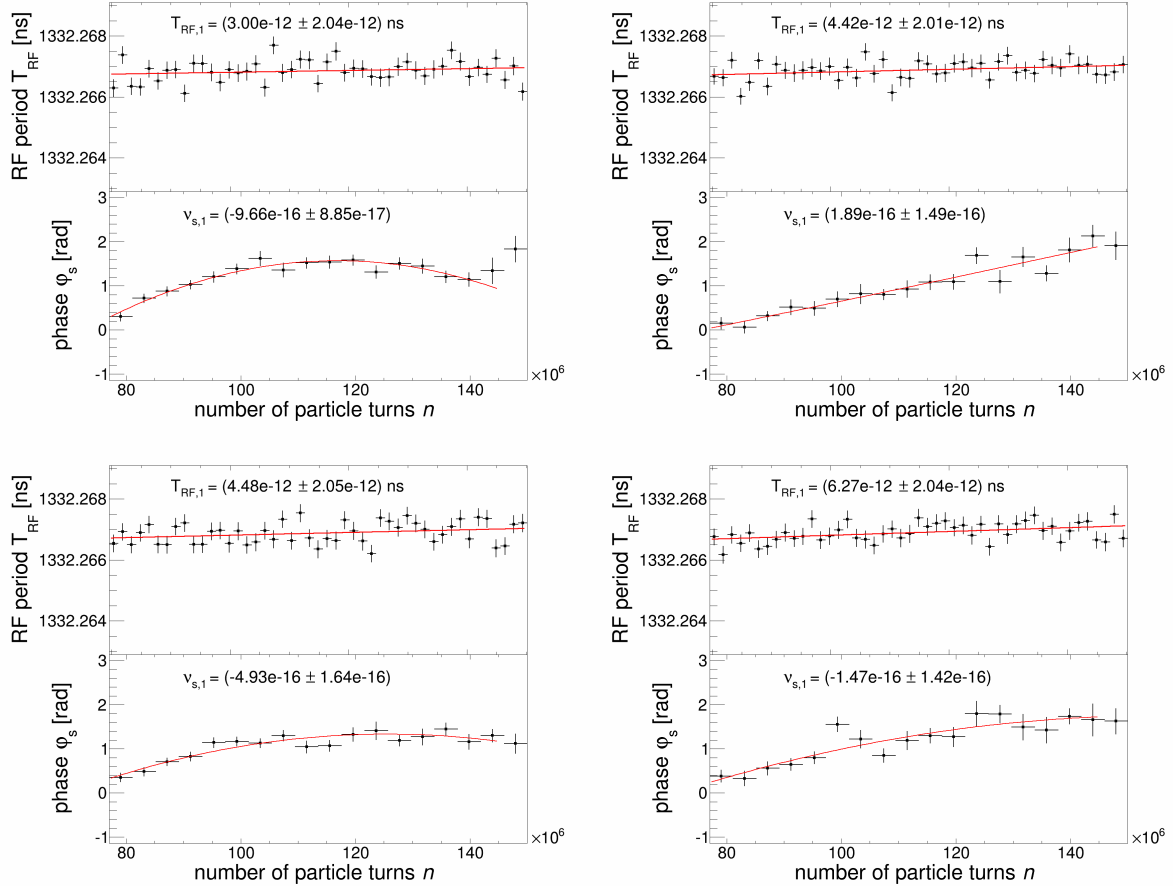


Figure 7.19: Phase and RF cavity distributions for 4 cycles. The red curve represents either a linear least squares fit (RF cavity) or a global maximum likelihood fit to the phase and the amplitude.

which is covered by the precision of the linear parameter. Note that the relative frequency change for a measurement interval of  $100 \times 10^6$  yields

$$\frac{\Delta f_{\text{beam}}^{\Delta T_{\text{RF}}}}{f_{\text{beam}}} = -\frac{\Delta T_{\text{beam}}^{\Delta T_{\text{RF}}}}{T_{\text{beam}}} = -\frac{4 \times 10^{-12} \text{ ns} \cdot 100 \times 10^6}{1332 \text{ ns}} \approx -3 \times 10^{-7}. \quad (7.65)$$

This number is more than 2 orders of magnitude larger than the effect based on the drift of the event arrival time.

In Fig. 7.20 the linear fit parameter of the RF cavity period and the linear drift parameter of the reference spin tune are shown for 100 cycles. On the one hand, one observes the day-night oscillation of  $T_{\text{RF},1}$ , whereas  $\nu_{s,1}^{\text{ref}}$  scatters randomly. The right-hand side of Fig. 7.20 shows the scatter plot of both quantities. It is obvious that the linear drift of the reference spin tune is not caused by a change of the RF cavity period since the correlation coefficient is close to zero.

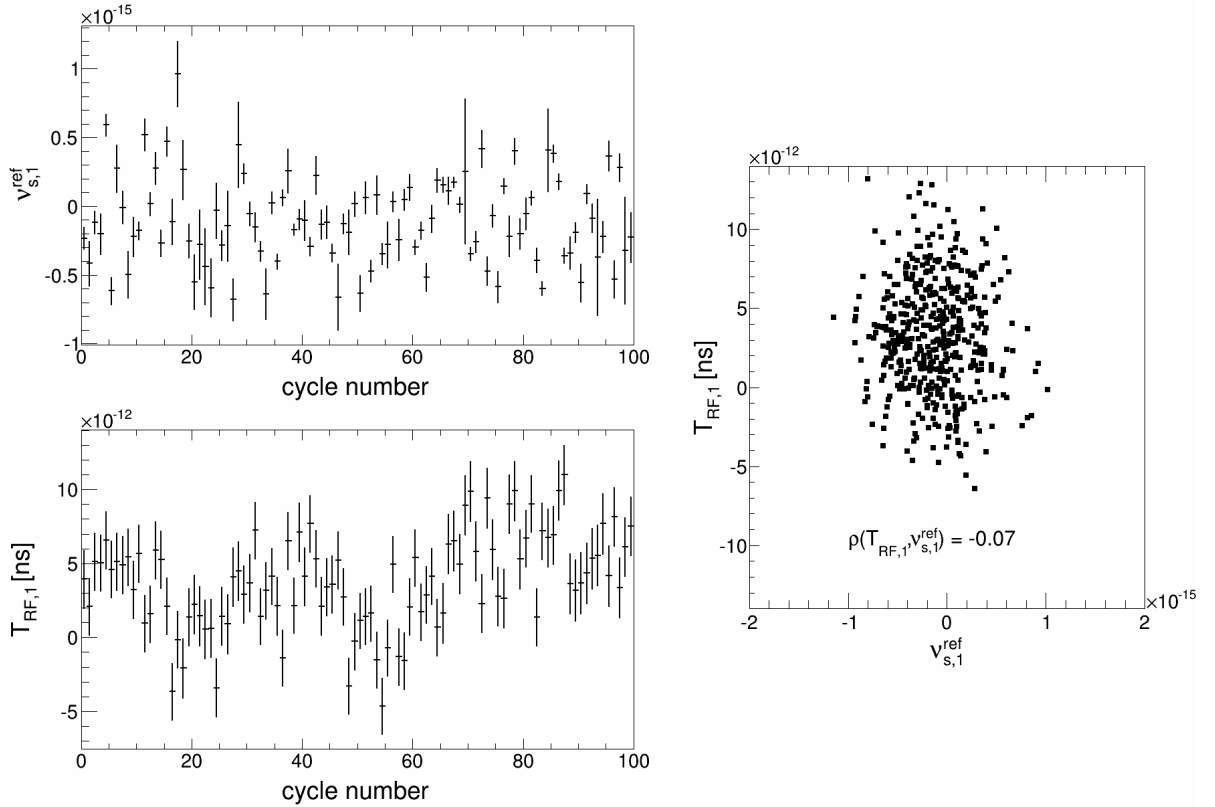


Figure 7.20: Linear fit parameter of the RF cavity period  $T_{RF,1}$  and linear drift parameter of the reference spin tune  $v_{s,1}^{ref}$  for 100 cycles. On the right-hand side the scatter plot of both quantities is shown.

## Conclusion

In the previous sections the turn dependent drift of the spin tune phase was investigated. It is found that the depolarization process, which assumes Rayleigh distributed spin tunes of the ensemble, is not sufficient to describe the measured phase change. Therefore, the turn dependent period of the beam, which is composed of the RF cavity period and the relative arrival time of the events, was studied

$$\Delta T_{\text{beam}}(n) = \Delta T_{\text{RF}}(n) + \frac{\partial t_{\text{ev}}(n)}{\partial n}. \quad (7.66)$$

The change of  $t_{\text{ev}}$  is almost three order of magnitudes too small in order to be determined by the spin tune measurement. In addition, there is no correlation between the linear drift parameter of the reference spin tune and the RF cavity has been detected. Thus, the additional quadratic behavior of the spin tune phase is caused by other underlying unknown systematics. Note that this process is random nature, which becomes obvious in Fig. 7.17, where the distribution of the ratio  $v_{s,1}^{ref}/\sigma_{v_{s,1}^{ref}}$  is shown. It is not possible to judge if the change of the RF cavity period is based on a true physical process or caused by a systematic drift of the TDC. In

the latter case, the spin tune phase would be unaffected because the turn dependent drift of  $T_{RF}$  originates from measurement issues of the DAQ. Another possible candidate of the linear spin tune drift is a time dependent change of the currents in the magnetic dipole magnets. However, no data is recorded for the magnetic fields of the bending magnets.

## 7.4.2 Long Term Stability

### Cycle to Cycle Fluctuations

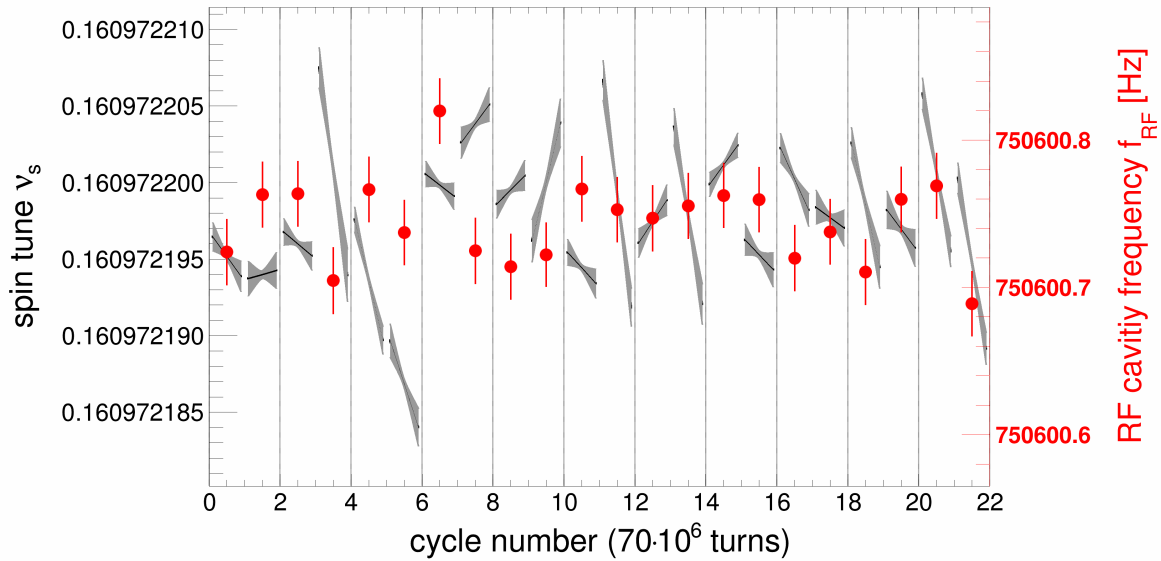


Figure 7.21: Spin tune distribution (black curves) for 22 cycles, which last for  $70 \cdot 10^6$  turns. All cycles are taken with the same sextupole settings. The red data points represent the mean of the RF cavity frequency obtained for the same measurement interval. The axis of the frequency is scaled by the factor determined in section 7.2.2. (A.1)

In the previous section, it was shown, that another unknown process beside of the depolarization and the RF cavity period drift causes a change of the spin tune phase during a cycle. The additional turn depending variation of  $\varphi_s$  is described by a quadratic function, which leads to a linear spin tune drift. In the following, the fluctuations of the spin tune from cycle to cycle within one run are investigated.

In Fig. 7.21 the turn depending interpolation of the spin tune is shown by the black curves for 22 cycles. Furthermore, the gray band represents the 68% confidence interval obtained by Gaussian error propagation. Since the sextupole settings of the investigated run provide a long spin coherence time  $\tau_{SCT} \approx 500$  s the phase change due to the depolarization is negligible. Consequently, the spin tune drift within a cycle originates basically from the unknown systematics and the spin tune interpolation yields a linear drift.

In addition, the cycle to cycle fluctuations of the RF cavity frequency  $f_{RF}$  are studied. A typical example of the  $T_{RF}$  distribution is shown in Fig. 7.9. Its mean value and its standard

deviation based on the same measurement interval as used for the spin tune phase determination are given by the red data points in Fig. 7.21. In order to compare the spin tune with  $f_{\text{RF}}$  the axis of the latter quantity is scaled by the factor determined in section 7.2.2

$$\Delta\nu_s = \frac{\beta_{\text{beam}}^2}{\eta_p} \frac{\nu_s}{f_{\text{RF}}} \Delta f_{\text{RF}} = 76.91 \text{ ns} \cdot \Delta f_{\text{RF}}. \quad (7.67)$$

The RF cavity frequency is stable within its error bars for the whole run, whereas the spin tune scatters significantly. In addition, the red data points do not coincide with the interpolated spin tune distributions, thus the jumps from cycle to cycle are not correlated to a change in the RF cavity frequency.

A possible explanation could be a variation of the magnetic field configuration of the ring from cycle to cycle. This fluctuation effects directly the spin tune, whereas the RF cavity period stays unchanged. A reason for this short-term variations might be, that the nominal value of the magnetic fields of the dipole magnets, which are ramped at the beginning of each cycle in order to accelerate the deuterons to the desired momentum, are not stable over time. Long term deviations of  $\nu_s^{\text{ref}}$  could arise from temperature variations, which should exhibit a day and night pattern. An additional source of a spin tune variation is given by the long-term stability of the cavity frequency, since the spin tune depends directly on  $f_{\text{RF}}$ .

### Run to Run Fluctuations

In order to study the spin tune variations due to different experimental setups, i.e. a change of the parameters of the components in the ring, the spin tune results recorded during a measurement period of more than two weeks are shown in Fig. 7.22. Each data point represents the reference spin tune of one cycle and the time axis shows the date in [month/day/year] and the time in [hour:minute]. The generic motivation of the experiment was to improve the spin coherence time by changing the sextupole magnets, which allowed a parasitical spin tune determination since the required idle horizontal spin precession was naturally provided. In addition, systematic effects caused by several ring devices were investigated, such as the electron cooler, the ionization beam profile monitor or the change of the dispersion using quadrupole magnets.

The first spin tune change in Fig. 7.22 a) is due to the realization of a horizontal orbit bump provided by the magnetic dipole steerers. This causes a clear jump of  $\Delta\nu_s^{\text{bump}} = 7 \times 10^{-7}$ , since the energy of the beam increases due to path lengthening and the vertical magnetic field of the steerers provides an additional spin kick to the horizontal spin precession. Before the orbit bump was applied the spin tune stayed almost constant over time. Another significant change of  $\nu_s$  becomes obvious as soon as the orbit correction based on the beam position monitors and the dipole steerers was applied during the beam preparation.

The impact of the quadrupole magnets on the spin tune can be studied by the data points located in the blue, green and red circles. First (blue) the quadrupole settings were set to arbitrary values. The green circles represent the case of minimized dispersion in the straight sections, whereas the red one corresponds to maximized dispersion. The dispersion was adjusted by changing the current in five quadrupole families.

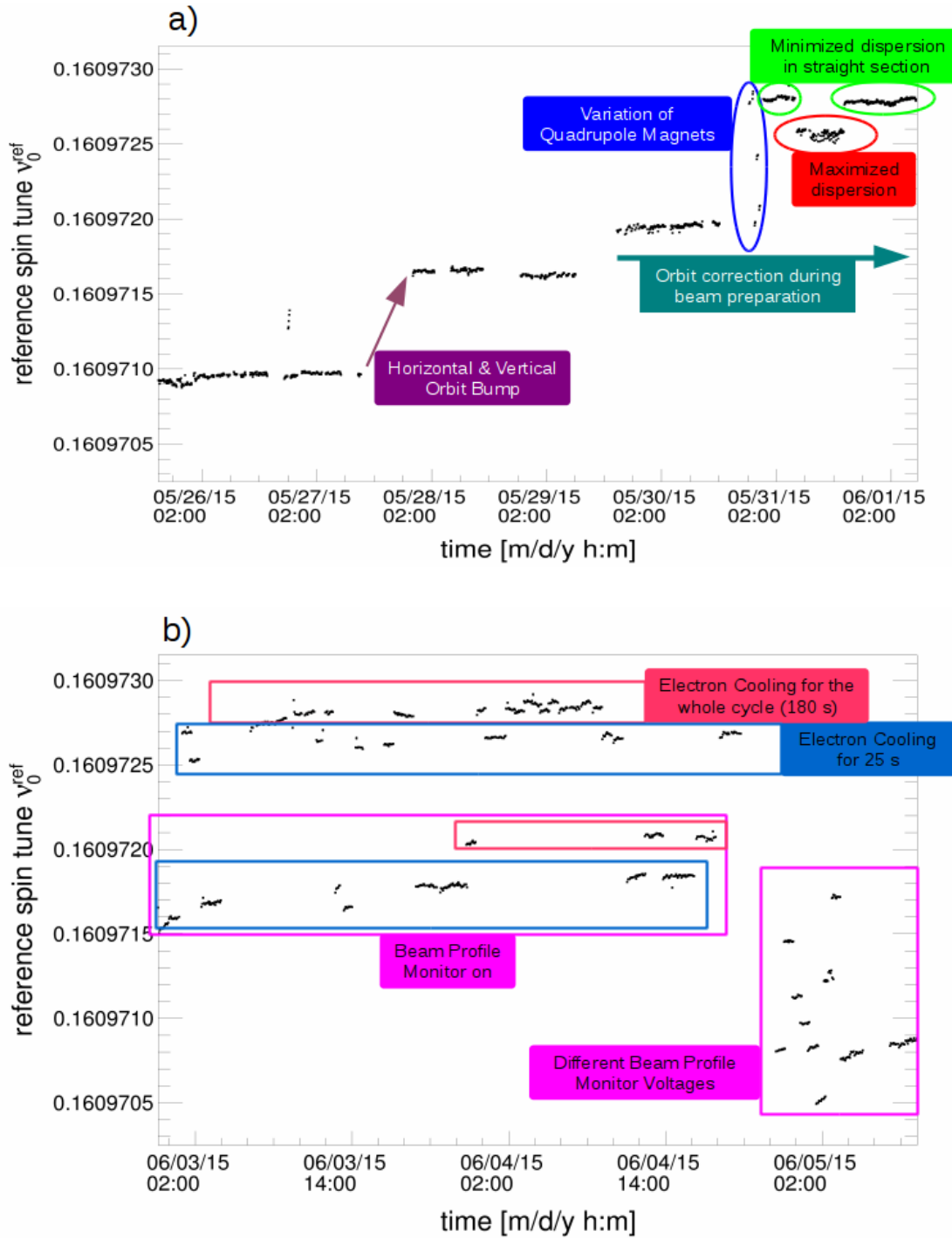


Figure 7.22: Long term spin tune measurement during the beam time in May/June 2015. Relevant changes of the devices in the ring are indicated by circles or rectangles. ( A.1)

In Fig. 7.22 b) the effect of the electron cooling and the application of the ion beam profile monitor can be investigated. The data points in the blue rectangles were taken for short cooling times  $t_{\text{cool}} = 25$  s, whereas the ones in the blue represent longer cases  $t_{\text{cool}} = 120$  s – 200 s. The corresponding spin tune change yields  $\Delta\nu_s^{\text{cool}} = 3 \times 10^{-7}$ . A longer cooling time leads to larger spin tune values. This indicates, that the momentum of the electrons is larger than the nominal momentum provided by the RF cavity and the deuterons are constantly adjusted by the energy of the electron cooler.

The ionization beam profile monitor decreases the spin tune, since the electric ion drift field perturbs the orbit of the beam. In fact, it is similar to an electric deflector. One observes that for higher voltages of the electrodes the decrease of the spin tune increases. Thus, the measurement of the spin tune represents a sensitive tool in order to determine any modifications of the beam orbit caused by the profile monitor.

### Day and Night Pattern and Sextupole Studies

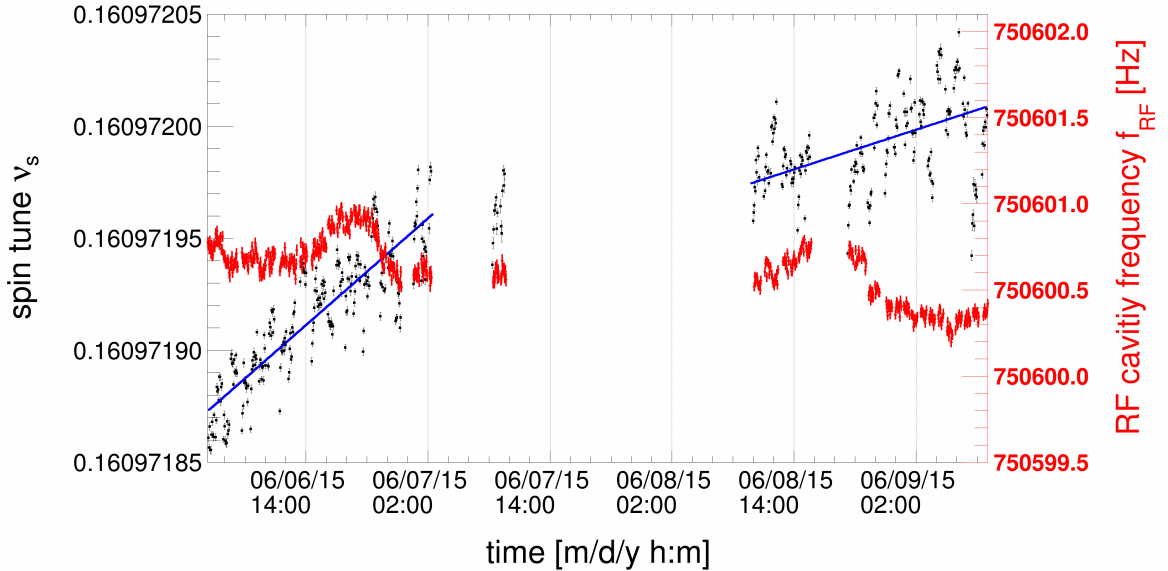


Figure 7.23: Spin tune and RF cavity frequency for a measurement interval where just the sextupole settings were changed. The scale between both quantity axes is given by  $\alpha_{\text{RF}}(\nu_s, f_{\text{RF}}) = 76.91$  ns. The blue lines represent a linear least squares fit to the spin tune. (A.1)

In section 7.2.3 it is shown that the RF cavity frequency performs a daily oscillation with an amplitude of  $\Delta f_{\text{RF}}^{\text{day}} = 0.1$  Hz. This corresponds to a spin tune change of  $\Delta\nu_s^{\text{day}} = 1.65 \times 10^{-8}$ . The red data points in Fig. 7.23 correspond to  $T_{\text{RF}}$ . The daily structure is clearly visible during the measurement interval, which lasts for more than three days. In addition, the corresponding spin tune distribution is shown in black. The axis is scaled by the factor  $\alpha_{\text{RF}}(\nu_s, f_{\text{RF}}) = 76.91$  ns in order to simplify the comparison of both quantities.

In the examined period only the sextupole settings were changed, thus no additional systematics should be visible. However, the spin tune increases linearly during the two macro-

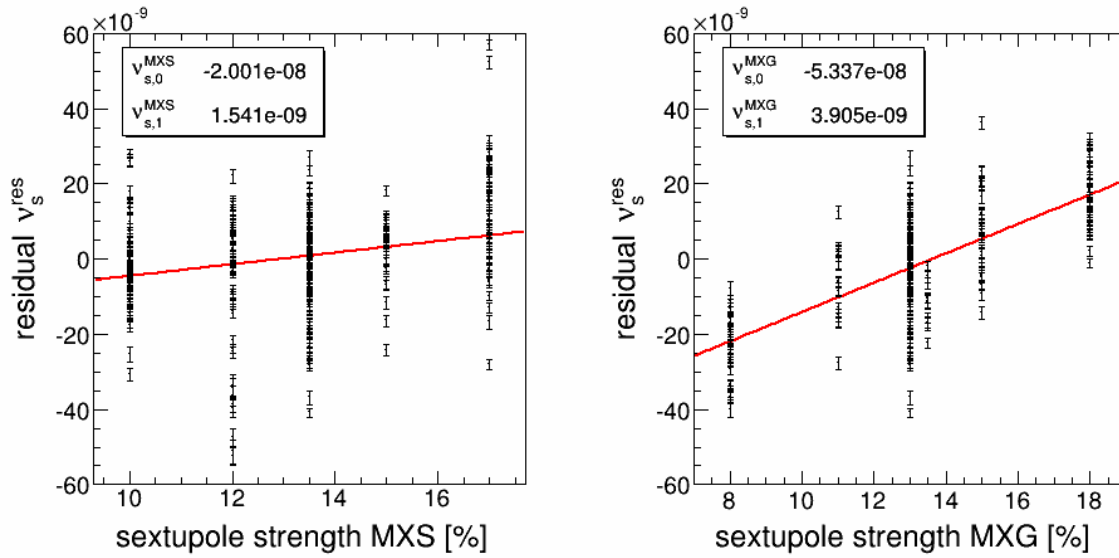


Figure 7.24: Residuals of the spin tune and the linear least squares fit given in Fig. 7.23. The results of two sextupole families are shown, whereas the red lines correspond to a linear least squares fit to the respective distribution.

scopic intervals. In addition, no correlation between the daily pattern of the RF cavity frequency is identified. Consequently, another unknown process leads to the linear spin tune change, which is indicated by the linear least squares fit in blue.

In order to study the impact of the sextupole magnets on the spin tune the two lines are used as a baseline. The residuals are shown in Fig. 7.24 as a function of the sextupole current, which is given in percentage of its maximal nominal value. In fact, two different sextupole families were investigated. The MXS magnets are located at large betatron amplitudes, whereas the MXG sextupoles are assembled at large dispersion. The red lines in Fig. 7.24 correspond to a linear least squares fit to the respective data. Note that the spin tune variations within the same run are in the order of  $\Delta v_s^{\text{run}} = 3 \cdot 10^{-8}$ . Thus, the width of each distribution obtained for one sextupole setting is relatively wide. However, in both cases, one observes a linear increasing spin tune for larger currents, whereas the MXG magnets yield an increased slope.

### 7.4.3 Long Cycle

In the previous section, the spin coherence time was determined to  $280 \times 10^6$  turns ( $\approx 370$  s) based on a cycle length of approximately 100 s. In order to prove that the requirement of an SCT of more than 1 000 s can be fulfilled, the measurement interval was extended to more than 800 s. Since the total number of polarized particles is basically invariant, the extraction rate was adapted in order to extract the beam for this longer period. The results of the amplitude distribution obtained for two cycles are shown in Fig. 7.25. One observes an almost constant polarization during the whole measurement time. A maximum likelihood fit to the data based

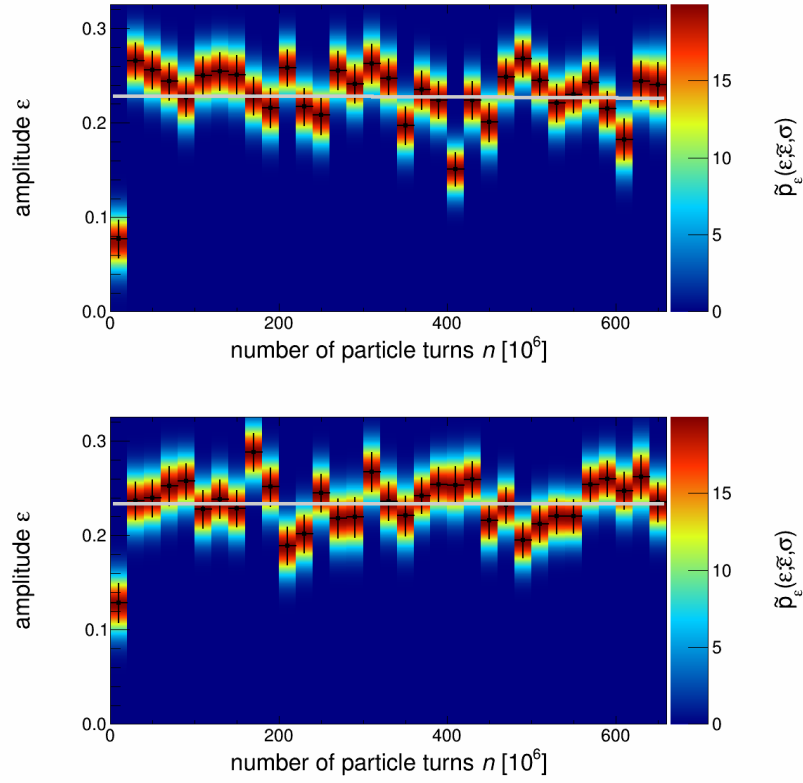


Figure 7.25: Two examples of long cycles with more than  $650 \times 10^6$  turns ( $\approx 860$  s). The spin tune width is estimated to  $\sigma_{R,\nu_s} = 5.49 \times 10^{-11}$  by means of a maximum likelihood fit based on the depolarization model. (A.1)

on the depolarization model yields a spin tune width of

$$\sigma_{R,\nu_s} = 5.49 \times 10^{-11}, \quad (7.68)$$

which corresponds to

$$\tau_{\text{SCT}} = 8486 \text{ s}. \quad (7.69)$$

This unprecedented spin coherence time was reached by beam bunching, electron cooling, sextupole field corrections, and the suppression of collective effects through beam current limits [45].

---

## Conclusion

---

In the scope of this thesis, a mathematical model of the spin tune analysis was derived in the context of feasibility studies of the JEDI collaboration towards an EDM experiment of charged elementary particles. In particular, two analysis methods were introduced. Firstly, the mapping method, which is discussed in [33], and secondly the discrete turn Fourier transform were investigated. It is pointed out that the latter one is more robust in terms of systematic effects and can be mathematically well described. Consequently, the final analysis uses the discrete turn Fourier transform in order to determine the phase and the amplitude of the spin precession in the horizontal plane. It was shown that the amplitude estimator is biased, whereas the phase of the spin tune can be estimated without bias by applying circular statistics. Making use of a naive Bayesian approach the probability density functions of the true values can be identified based on the estimators obtained by the turn discrete Fourier transform. Moreover, systematic effects of the analysis methods were estimated and discussed.

A statistical model explaining time depending depolarization effects and the spin tune drift was elaborated. This model has basically two parameters, the spin coherence time  $\tau_{\text{SCT}}$  and the time depending spin tune  $\nu_0(t)$ . Estimators for  $\tau_{\text{SCT}}$  and  $\nu_0(t)$  are determined by a maximum likelihood fit based on its probability density functions and the statistical model. This two quantities depend on the configuration of the electromagnetic field of the storage ring and the orbit of the particle beam. Consequently, its determination leads to a better understanding of the processes in the storage ring and can be used for systematic studies. As a result of this work, it was shown that the spin tune undergoes a significant quadratic drift during a experimental cycle. Unless it was not possible to determine the source of this process, several possibilities were excluded, like a time depending drift of the COSY RF or a relative longitudinal beam movement.

The spin tune is an ideal observable for long term stability measurements, since it correlates with tiny changes of the experimental environment. In this work, it was shown that for a cycle length of 100s and a constant event rate of 5000/s the spin tune can be determined with a statistical precision of  $10^{-10}$  [33]. On the one hand, this achievement allows to study systematic effects of the spin tune induced by the change of the COSY RF period. On the other hand, several experimental setups were examined, which investigated the spin tune jumps due to operational changes of the particular device in the machine. In addition, in [46] a new method to probe magnetic imperfections of storage rings is described making use of the very high statistical precision of the spin tune determination. Another application is given by the measurement of the dispersion of the machine, which is elaborated in the thesis of Fabian

Hinder. Finally, the phase observation can be used for a live feedback system, which corrects the spin phase in real time [47].

Furthermore, it is shown that the statistical sensitivity level of an intrinsic electric dipole moment of the deuteron of  $d < 10^{-29} e \text{ cm}$  requires a spin coherence time of 1 000 s. This requirement was met through a combination of beam bunching, electron cooling, sextupole field corrections, and the suppression of collective effects through beam current limits [45].

The exact design of the realization of an upcoming EDM experiments of charged particles is currently under fruitful discussion. One class of potential storage rings uses the spin tune not only as a variable to monitor systematic effects but also as a observable which is proportional to the EDM signal. This would increase the importance of a comprehensive understanding of the mechanisms which influence the spin movement of the particles. In the view of that fact, this thesis comprises crucial achievements towards a final experiment, which challenges an EDM limit of  $|d| < 10 \times 10^{-29} e \text{ cm}$  for charged elementary particles.

### A.1 List of Runs

In the following table the run numbers shown in the result chapter are given. In addition, the month and the year of the respective beam time is indicated.

Table A.1: List of runs dicussed in the result chapter

Figure	Beam Time	Run Number
7.5	May 2015	5117
7.6	May 2015	5093 - 5858
7.7	May 2015	5920
7.8	Nov 2015	6084 - 6175
7.9	May 2015	5097
7.11	May 2015	5097 and 5095
7.12	May 2015	5097
7.13	Feb 2013 and May 2015	1770, 2288 and 5117
7.16	May 2015	5183 and 5184
7.17	May 2015	5140 - 5190
7.18	May 2015	5097
7.21	May 2015	5189
7.22	May 2015	4982 - 5163
7.23	May 2015	5130 - 5163
7.25	May 2015	5924

## A.2 Integrals for Fisher Information for Spin Precession

The Fisher information of the probability density function based on the spin precession  $p_s(n)$  is given by

$$\mathcal{I}(\theta) = - \int_0^{\Delta n} \frac{\partial^2}{\partial \theta^2} \log p_s(n; \theta) p_s(n; \theta) \, dn, \quad (\text{A.1})$$

The second derivatives with respect to the individual parameters are given by

$$\frac{\partial^2}{\partial \varphi_s^2} \log p_s = - \frac{\epsilon [\epsilon + \sin(2\pi\nu_s n + \varphi_s)]}{(\epsilon \sin(2\pi\nu_s n + \varphi_s) + 1)^2}, \quad (\text{A.2})$$

$$\frac{\partial^2}{\partial \epsilon^2} \log p_s = - \frac{\sin^2(2\pi\nu_s n + \varphi_s)}{(\epsilon \sin(2\pi\nu_s n + \varphi_s) + 1)^2}, \quad (\text{A.3})$$

$$\frac{\partial^2}{\partial \nu_s^2} \log p_s = - \frac{\epsilon (2\pi n)^2 [\epsilon + \sin(2\pi\nu_s n + \varphi_s)]}{(\epsilon \sin(2\pi\nu_s n + \varphi_s) + 1)^2}, \quad (\text{A.4})$$

$$\frac{\partial}{\partial \varphi_s} \log p_s \frac{\partial}{\partial \epsilon} \log p_s = \frac{\epsilon \sin(2(\nu_s n + \varphi_s))}{(\epsilon \sin(2\pi\nu_s n + \varphi_s) + 1)^2}, \quad (\text{A.5})$$

$$\frac{\partial}{\partial \varphi_s} \log p_s \frac{\partial}{\partial \nu_s} \log p_s = - \frac{2\pi\epsilon^2 n \cos^2(2\pi\nu_s n + \varphi_s)}{(\epsilon \sin(2\pi\nu_s n + \varphi_s) + 1)^2}, \quad (\text{A.6})$$

$$\frac{\partial}{\partial \epsilon} \log p_s \frac{\partial}{\partial \nu_s} \log p_s = \frac{\pi\epsilon n \sin(2(2\pi\nu_s n + \varphi_s))}{(\epsilon \sin(2\pi\nu_s n + \varphi_s) + 1)^2}. \quad (\text{A.7})$$

$$(\text{A.8})$$

In order to solve the integral of Eq. A.1, the phase parameter can be set to zero  $\varphi_s = 0$  since for a large macroscopic turn interval  $\Delta n \gg 1$ , the phase averages out.

The analytical solution of the integrals for the respective parameter yields

$$\begin{aligned}
 \mathcal{I}(\varphi_s) &= \frac{1}{\Delta n} \int \frac{\epsilon [\epsilon + \sin(2\pi v_s n)]}{\epsilon \sin(2\pi v_s n) + 1} dn \\
 &= \frac{n}{\Delta n} - \frac{\sqrt{1-\epsilon^2} \arctan\left(\frac{\epsilon + \tan(\pi v_s n)}{\sqrt{1-\epsilon^2}}\right)}{\Delta n \pi v_s} + \text{const.}, \\
 \\
 \mathcal{I}(\epsilon) &= \frac{1}{\Delta n} \int \frac{\sin^2(2\pi v_s n)}{\epsilon \sin(2\pi v_s n) + 1} dn \\
 &= -\frac{n + \frac{\epsilon \cos(2\pi v_s n)}{2\pi v_s} - \frac{\arctan\left(\frac{\epsilon + \tan(\pi v_s n)}{\sqrt{1-\epsilon^2}}\right)}{\pi \sqrt{1-\epsilon^2} v_s}}{\Delta n \epsilon^2} + \text{const.}, \tag{A.9}
 \end{aligned}$$

$$\begin{aligned}
 \mathcal{I}(v_s) &= \frac{1}{\Delta n} \int \frac{\epsilon (2\pi n)^2 [\epsilon + \sin(2\pi v_s n)]}{\epsilon \sin(2\pi v_s n) + 1} dn \\
 &= \frac{1}{3\Delta n} \pi^2 \left[ 4n^3 + \frac{1}{\pi^3 v_s^3} \sqrt{1-\epsilon^2} \left( \right. \right. \\
 &\quad \left. \left. 2\pi v_s n [\text{Li}_2(\omega^-) - \text{Li}_2(-\omega^+)] \right. \right. \\
 &\quad \left. \left. + i\text{Li}_3(\omega^-) + i\text{Li}_3(-\omega^+) \right. \right. \\
 &\quad \left. \left. + 2\pi^2 v_s^2 n^2 i [\log(1-\omega^-) + \log(1+\omega^+)] \right) \right] + \text{const.},
 \end{aligned}$$

where  $\text{Li}_s(x)$  denotes the polylogarithm of  $s$ -th order and  $\log(x)$  is the natural logarithm. The quantities  $\omega^-$  and  $\omega^+$  are specified as

$$\omega^- = \frac{\epsilon e^{2i\pi n v_s}}{\sqrt{\epsilon^2 - 1} - i} \tag{A.10}$$

$$\omega^+ = \frac{\epsilon e^{2i\pi n v_s}}{\sqrt{\epsilon^2 - 1} + i} \tag{A.11}$$

Since the macroscopic turn interval is large  $\Delta n \gg \nu_s$ , following terms can be approximated

$$\begin{aligned} \arctan\left(\frac{\epsilon + \tan(\pi\nu n)}{\sqrt{1-\epsilon^2}}\right) &\approx \pi\nu_s n, \\ \cos(2\pi\nu_s n) &\approx 0 \text{ (oscillation)}, \\ \text{Li}_2(\omega^-) &\approx 0 \text{ (oscillation)}, \\ \text{Li}_2(\omega^+) &\approx 0 \text{ (oscillation)}, \\ \text{Li}_3(\omega^+) &\approx 0 \text{ (oscillation)}, \\ \text{Li}_3(\omega^-) &\approx 0 \text{ (oscillation)}, \\ \log(1-\omega^-) &\approx \begin{cases} 2\pi\nu_s n & \text{if } |i\frac{\epsilon}{\sqrt{\epsilon^2-1-i}}| > 1 \\ 0 & \text{if } |i\frac{\epsilon}{\sqrt{\epsilon^2-1-i}}| < 1 \text{ (oscillation)}, \end{cases} \\ \log(1+\omega^+) &\approx \begin{cases} 2\pi\nu_s n & \text{if } |i\frac{\epsilon}{\sqrt{\epsilon^2-1+i}}| > 1 \\ 0 & \text{if } |i\frac{\epsilon}{\sqrt{\epsilon^2-1+i}}| < 1 \text{ (oscillation)}. \end{cases} \end{aligned}$$

Thus, the definite integrals in Eq. A.9  $(0, \Delta n]$  are given by

$$\mathcal{I}(\varphi_s) = (1 - \sqrt{1-\epsilon^2}) \approx \frac{\epsilon^2}{2}, \quad (\text{A.12})$$

$$\mathcal{I}(\epsilon) = \frac{\frac{1}{\sqrt{1-\epsilon^2}} - 1}{\epsilon^2} \approx \frac{1}{2}, \quad (\text{A.13})$$

$$\mathcal{I}(\nu_s) = \Delta n^2 \frac{4\pi^2}{3} (1 - \sqrt{1-\epsilon^2}) \approx \frac{4\pi^2}{6} \Delta n^2 \epsilon^2, \quad (\text{A.14})$$

where the approximation is based on the Taylor series expand for small amplitudes  $\epsilon \ll 1$ .

The integral of the mixed derivatives are approximately given by

$$\mathcal{I}(\epsilon, \varphi_s) = \frac{1}{\Delta n} \int \frac{\epsilon \sin(2(\nu_s n))}{(\epsilon \sin(2\pi\nu_s n) + 1)} dn \approx 0, \quad (\text{A.15})$$

$$\mathcal{I}(\epsilon, \nu_s) = \frac{1}{\Delta n} \int \frac{\pi\epsilon n \sin(2(2\pi\nu_s n))}{(\epsilon \sin(2\pi\nu_s n) + 1)} dn \approx 0, \quad (\text{A.16})$$

$$\mathcal{I}(\varphi_s, \nu_s) = -\frac{1}{\Delta n} \int \frac{2\pi\epsilon^2 n \cos^2(2\pi\nu_s n)}{(\epsilon \sin(2\pi\nu_s n) + 1)^2} dn \approx \frac{\pi}{2} \Delta n \epsilon^2. \quad (\text{A.17})$$

### A.3 Integral of the bivariat Probability Density Function

The integration of  $p_{n,\nu_s}(n, \nu_s; \epsilon, \varphi_s, \sigma_{\nu_s}, \nu_s^{\text{ref}})$  with respect to the whole domain of the spin tune yields the marginal probability density function of the turn number

$$p_n(n) = \int_{\nu_s^{\text{ref}}}^{\infty} p_{n,\nu_s}(n, \nu_s) d\nu_s \quad (\text{A.18})$$

$$= \frac{1}{\Delta n} \left[ 1 + \epsilon \sin(2\pi\nu_s n + \varphi_s) + \sqrt{2}\pi^{3/2}\epsilon\sigma_{\nu_s} n e^{-2\pi^2\sigma_{\nu_s}^2 n^2} \times \right. \\ \left. \left( \cos(2\pi\nu_s n + \varphi_s) - \text{erfi}(\sqrt{2}\pi\sigma_{\nu_s} n) \sin(2\pi\nu_s n + \varphi_s) \right) \right] \quad (\text{A.19})$$

$$= \frac{1}{\Delta n} \left[ 1 + \epsilon \sin[\Omega_s(n)] + \sqrt{\pi}\epsilon\gamma_s(n)e^{-\gamma_s^2(n)} \left( \cos[\Omega_s(n)] - \text{erfi}[\gamma_s(n)] \sin[\Omega_s(n)] \right) \right] \\ = \frac{1}{\Delta n} \left[ 1 + \epsilon \left( \left[ 1 - \sqrt{\pi}\gamma_s(n)e^{-\gamma_s^2(n)} \text{erfi}(\gamma_s(n)) \right]^2 + \pi\gamma_s^2(n)e^{-2\gamma_s^2(n)} \right)^{\frac{1}{2}} \times \right. \\ \left. \sin \left[ \Omega_s(n) + \frac{\pi}{2} - \arctan \left( \frac{1 - \sqrt{\pi}\gamma_s(n)e^{-\gamma_s^2(n)} \text{erfi}(\gamma_s(n))}{\sqrt{\pi}\gamma_s(n)e^{-\gamma_s^2(n)}} \right) \right] \right] \quad (\text{A.20})$$

$$= \frac{1}{\Delta n} \left[ 1 + \epsilon \left( \left[ 1 - \sqrt{\pi}\gamma_s(n)e^{-\gamma_s^2(n)} \text{erfi}(\gamma_s(n)) \right]^2 + \pi\gamma_s^2(n)e^{-2\gamma_s^2(n)} \right)^{\frac{1}{2}} \times \right. \\ \left. \sin \left[ \Omega_s(n) + \frac{\pi}{2} - \arctan \left( \frac{e^{\gamma_s^2(n)}}{\sqrt{\pi}\gamma_s(n)} - \text{erfi}(\gamma_s(n)) \right) \right] \right], \quad (\text{A.21})$$

where  $\text{erfi}$  denotes the imaginary error function and  $\Omega_s(n) = 2\pi\nu_s n + \varphi_s$  represents the fundamental oscillation, with the phase  $\varphi_s$  and the spin tune  $\nu_s$ . The turn depending damping term is given by  $\gamma_s(n) = \sqrt{2}\pi\sigma_{\nu_s} n$  and it depends on the spin tune spread  $\sigma_{\nu_s}$ . A fundamental solution of the integral can be found in [48].

### A.4 Derivation of the Rician Distribution

Suppose two uncorrelated and Normal distributed parameters  $A \sim N(\mu_A, \sigma^2)$  and  $B \sim N(\mu_B, \sigma^2)$ , with the mean values  $\mu_A$  respectively  $\mu_B$  and the same standard deviations  $\sigma$ . Then the probability density function for the quantity  $\tilde{\epsilon} = \sqrt{\tilde{A}^2 + \tilde{B}^2}$  is given by the integral over the estimated phase  $\tilde{\varphi} = \text{atan2}(\tilde{B}, \tilde{A})$  of the joint probability density function of the two random variables  $\tilde{A}$

and  $\tilde{B}$ .

$$f(\tilde{\epsilon}, \tilde{\varphi}; \epsilon, \varphi) d\tilde{\epsilon} d\tilde{\varphi} = \frac{\tilde{\epsilon}}{2\pi\sigma^2} e^{-\frac{\tilde{\epsilon}^2 + \epsilon^2}{2\sigma^2}} \cdot e^{-\frac{2\tilde{\epsilon}\epsilon(\sin(\varphi)\sin(\tilde{\varphi}) + \cos(\varphi)\cos(\tilde{\varphi}))}{2\sigma^2}} d\tilde{\varphi} d\tilde{\epsilon} \quad (\text{A.22})$$

$$f(\tilde{\epsilon}; \epsilon, \varphi) d\tilde{\epsilon} = \frac{\tilde{\epsilon}}{2\pi\sigma^2} e^{-\frac{\tilde{\epsilon}^2 + \epsilon^2}{2\sigma^2}} \left[ \int_0^{2\pi} e^{-\frac{2\tilde{\epsilon}\epsilon(\sin(\varphi)\sin(\tilde{\varphi}) + \cos(\varphi)\cos(\tilde{\varphi}))}{2\sigma^2}} d\tilde{\varphi} \right] d\tilde{\epsilon} \quad (\text{A.23})$$

$$= \frac{\tilde{\epsilon}}{2\pi\sigma^2} e^{-\frac{\tilde{\epsilon}^2 + \epsilon^2}{2\sigma^2}} \left[ \int_0^{2\pi} e^{-\frac{2\tilde{\epsilon}\epsilon \cos(\varphi - \tilde{\varphi})}{2\sigma^2}} d\tilde{\varphi} \right] d\tilde{\epsilon} \quad (\text{A.24})$$

$$= \frac{\tilde{\epsilon}}{2\pi\sigma^2} e^{-\frac{\tilde{\epsilon}^2 + \epsilon^2}{2\sigma^2}} 2\pi I_0 \left( \frac{\tilde{\epsilon}\epsilon}{\sigma^2} \right) d\tilde{\epsilon} \quad (\text{A.25})$$

$$= \frac{\tilde{\epsilon}}{\sigma^2} e^{-\frac{\tilde{\epsilon}^2 + \epsilon^2}{2\sigma^2}} I_0 \left( \frac{\tilde{\epsilon}\epsilon}{\sigma^2} \right) d\tilde{\epsilon}. \quad \text{q.e.d.} \quad (\text{A.26})$$

Here the transformation into polar coordinates ( $\tilde{A} = \tilde{\epsilon} \sin(\tilde{\varphi})$  and  $\tilde{B} = \tilde{\epsilon} \cos(\tilde{\varphi})$ ) with the Jacobian  $J = \tilde{\epsilon}$  has been used.

## A.5 Probability Density Distribution of the Sum of Squared Random Variables

The 2nd moment estimator of the amplitude is given by

$$\hat{\epsilon}_{2\text{nd}} = \sqrt{\tilde{\epsilon}^2 - 2\sigma^2} \quad (\text{A.27})$$

$$\rightarrow \hat{\epsilon}_{2\text{nd}}^2 = \tilde{A}^2 + \tilde{B}^2 - 2\sigma^2, \quad (\text{A.28})$$

where  $\sigma = \sqrt{\frac{2}{N}}$  is the standard deviation depending on the number of detected events  $N$  and  $\tilde{\epsilon} = \sqrt{\tilde{A}^2 + \tilde{B}^2}$  is the estimated amplitude based on the estimated parameter  $\tilde{A}$  and  $\tilde{B}$  obtained by the mapping method respectively discrete Fourier transform. The probability density function of the sum of  $k$  squared and Normal distributed random variables

$$Z = \sum_{i=1}^k X_i^2 \quad (\text{A.29})$$

$$X_i \sim (\mu_{X_i}, \sigma^2), \quad (\text{A.30})$$

with same standard deviation but different expectation value is given by the noncentral chi squared distribution [49]

$$p(z; \lambda, \sigma, k) = \frac{1}{2\sigma^2} \left( \frac{z}{\lambda} \right)^{\frac{k}{2} - \frac{1}{2}} e^{-\frac{z+\lambda}{2\sigma^2}} I_{\frac{k}{2}-1} \left( \sqrt{\frac{\lambda z}{\sigma^2}} \right), \quad (\text{A.31})$$

where  $\lambda = \sum_{i=1}^k \mu_i^2$ .

In case of Eq. A.28 the parameters yield  $k = 2$  and  $\lambda = \epsilon^2 = \mu_A^2 + \mu_B^2$ , where  $\epsilon$  is the true

amplitude. Consequently, the pdf of  $\hat{\epsilon}_{2\text{nd}}^2$  is given by

$$p(\hat{\epsilon}_{2\text{nd}}^2; \epsilon, \sigma) = \frac{1}{2\sigma^2} e^{-\frac{\hat{\epsilon}_{2\text{nd}}^2 + \epsilon^2 + 2\sigma^2}{2\sigma^2}} I_0 \left( \frac{\sqrt{(\hat{\epsilon}_{2\text{nd}}^2 + 2\sigma^2)\epsilon^2}}{\sigma^2} \right) H(\hat{\epsilon}_{2\text{nd}}^2 + 2\sigma^2), \quad (\text{A.32})$$

where  $H$  denotes the Heaviside function. Fig. A.1 shows three examples of  $p(\hat{\epsilon}_{2\text{nd}}^2; \epsilon, \sigma)$  obtained for the same standard deviation  $\sigma = 0.1$  but different true amplitudes  $\epsilon = 0.05$  (red),  $\epsilon = 0.1$  (black),  $\epsilon = 0.2$  (blue). The area below each function is filled for  $\hat{\epsilon}_{2\text{nd}}^2 < 0$  in order to illustrate the integrated probability, that the 2nd moment estimator yields a physical meaningless result, i.e. the argument of the square root in Eq. A.27 becomes negative. Since this area increases for a decreasing true amplitude, the probability to obtain meaningful results reduces for smaller  $\epsilon$ .

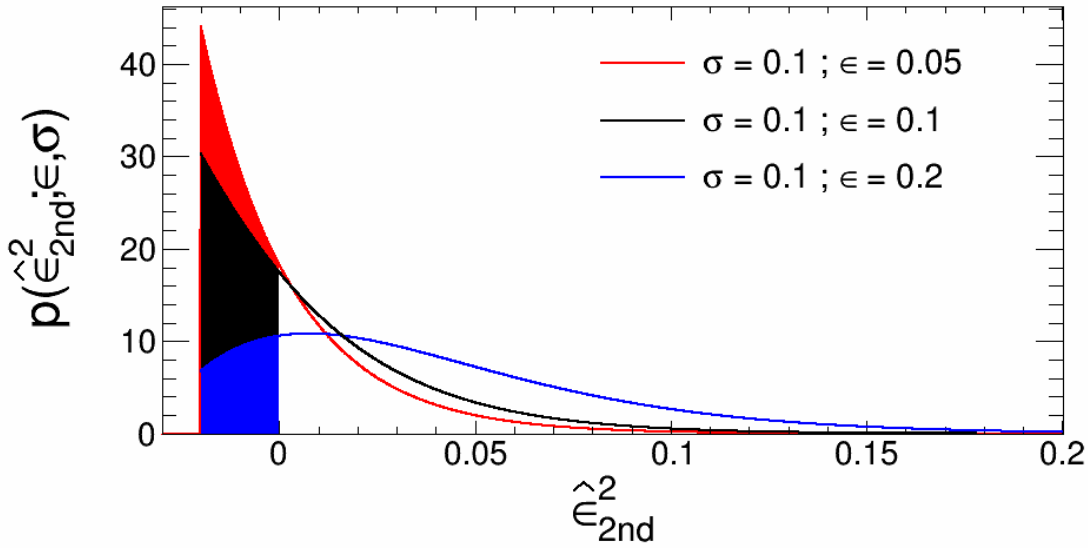


Figure A.1: Probability density function of the quadratic 2nd moment estimator  $p(\hat{\epsilon}_{2\text{nd}}^2; \epsilon, \sigma)$  for the same standard deviation  $\sigma = 0.1$  but different true amplitudes  $\epsilon = 0.05$  (red),  $\epsilon = 0.1$  (black),  $\epsilon = 0.2$  (blue). The filled area indicates the integrated probability, that the quadratic 2nd moment estimator assumes negative numbers.

## A.6 Integral of the Circular Moment Cosinus Term

The cosinus term of the first circular moment of the wrapped probability distribution 6.5 of the phase  $\tilde{\varphi}$  is given by

$$\hat{z}^1 = \frac{e^{-\frac{\epsilon^2}{2\sigma^2}}}{2\pi} \int_{-\pi}^{\pi} \left[ \cos(\tilde{\varphi}) - \frac{\sqrt{\pi}\epsilon \cos^2 \tilde{\varphi}}{\sqrt{2\sigma^2}} e^{\frac{\epsilon^2 \cos^2 \tilde{\varphi}}{2\sigma^2}} \operatorname{erfc} \left( \frac{\epsilon \cos \tilde{\varphi}}{\sqrt{2\sigma^2}} \right) \right] d\tilde{\varphi}, \quad (\text{A.33})$$

where  $\operatorname{erfc}$  denotes the complementary error function,  $\epsilon$  is the amplitude and  $\sigma$  represents the standard deviation based on the number of detected events. The first term of the integrand vanishes, since  $\int_{-\pi}^{\pi} \cos(\tilde{\varphi}) d\tilde{\varphi} = 0$ . Furthermore, an integration by the substitution

$$t = \cos \tilde{\varphi}, \quad (\text{A.34})$$

$$\tilde{\varphi} = \arccos t, \quad (\text{A.35})$$

$$\frac{d\tilde{\varphi}}{dt} = \frac{-1}{\sqrt{1-t^2}}, \quad (\text{A.36})$$

is performed. In order to avoid singularities the integration is executed piecewise

$$\hat{z}^1 = \int_{-\pi}^0 f(\tilde{\varphi}) d\tilde{\varphi} + \int_0^{\pi} f(\tilde{\varphi}) d\tilde{\varphi} = 2 \int_0^{\pi} d\tilde{\varphi} = 2 \int_1^{-1} \tilde{f}(t) dt = -2 \int_{-1}^1 \tilde{f}(t) dt, \quad (\text{A.37})$$

which is appropriate, since  $f(\tilde{\varphi})$  is even. This leads to

$$\hat{z}^1 = \frac{e^{-\frac{\epsilon^2}{2\sigma^2}}}{\pi} \int_{-1}^1 \frac{-t^2}{\sqrt{1-t^2}} \sqrt{\frac{\pi\epsilon^2}{2\sigma^2}} e^{t^2 \frac{\epsilon^2}{2\sigma^2}} \operatorname{erfc} \left( t \sqrt{\frac{\epsilon^2}{2\sigma^2}} \right) dt \quad (\text{A.38})$$

$$= \frac{e^{-k^2}}{\sqrt{\pi}} \int_{-1}^1 -\frac{t^2}{\sqrt{1-t^2}} k e^{t^2 k^2} \operatorname{erfc}(tk) dt, \quad (\text{A.39})$$

with  $k = \sqrt{\frac{\epsilon^2}{2\sigma^2}}$ . The complementary error function can be expressed in terms of the Kummer confluent hypergeometric function  $\operatorname{erfc}(x) = 1 - \frac{2x}{\sqrt{\pi}} {}_1F_1\left(\frac{1}{2}; \frac{3}{2}; -x^2\right)$

$$\hat{z}^1 = \frac{e^{-k^2}}{\sqrt{\pi}} \int_{-1}^1 -\frac{t^2}{\sqrt{1-t^2}} k e^{t^2 k^2} \left[ 1 - \frac{2tk}{\sqrt{\pi}} {}_1F_1\left(\frac{1}{2}; \frac{3}{2}; -(tk)^2\right) \right] dt \quad (\text{A.40})$$

$$= \frac{e^{-k^2}}{\sqrt{\pi}} \int_{-1}^1 \left[ -\frac{t^2 k e^{t^2 k^2}}{\sqrt{1-t^2}} + \frac{t^3}{\sqrt{1-t^2}} \frac{2k^2}{\sqrt{\pi}} {}_1F_1\left(\frac{1}{2}; \frac{3}{2}; -(tk)^2\right) \right] dt. \quad (\text{A.41})$$

The second term of the integrand yields zero, since  $\frac{t^3}{\sqrt{1-t^2}} \frac{2k^2}{\sqrt{\pi}} {}_1F_1\left(\frac{1}{2}; \frac{3}{2}; -(tk)^2\right)$  is odd. Consequently, the expression of A.41 simplifies to an elliptic integral

$$\hat{z}^1 = \frac{e^{-k^2}}{\sqrt{\pi}} \int_{-1}^1 -\frac{t^2 k e^{t^2 k^2}}{\sqrt{1-t^2}} dt \quad (\text{A.42})$$

$$= -\frac{\sqrt{\pi}}{2} k e^{-\frac{k^2}{2}} \left[ I_0\left(\frac{k^2}{2}\right) + I_1\left(\frac{k^2}{2}\right) \right], \quad (\text{A.43})$$

which is independent of  $t$  respectively the estimated phase  $\tilde{\varphi}$ . The final result is obtained by the backsubstitution of  $k$

$$\hat{z}^1 = \sqrt{\frac{\pi}{2}} \sqrt{\frac{\epsilon^2}{4\sigma^2}} e^{-\frac{\epsilon^2}{4\sigma^2}} \left[ I_0\left(\frac{\epsilon^2}{4\sigma^2}\right) + I_1\left(\frac{\epsilon^2}{4\sigma^2}\right) \right], \quad (\text{A.44})$$

where  $I_0$  and  $I_1$  are the modified Bessel function of first kind and zeroth respectively first order.

## A.7 Probability Density Function of the True Phase

The probability density function of the true phase based on the Bayes' theorem is given by

$$\begin{aligned}
 \tilde{p}_\varphi(\varphi; \tilde{\epsilon}, \tilde{\varphi}, \sigma) &= \int_0^\infty \tilde{p}(\epsilon, \varphi; \tilde{\epsilon}, \tilde{\varphi}, \sigma) d\epsilon \\
 &= \int_0^\infty \frac{p(\tilde{\epsilon}, \tilde{\varphi}; \epsilon, \varphi, \sigma) p(\epsilon)}{p(\tilde{\epsilon})} d\epsilon \\
 &= \int_0^\infty \frac{p(\tilde{\epsilon}, \tilde{\varphi}; \epsilon, \varphi, \sigma) \tilde{p}_R(\epsilon; \tilde{\epsilon}, \sigma)}{p_R(\tilde{\epsilon}; \epsilon, \sigma)} d\epsilon \\
 &= \int_0^\infty \frac{\frac{\tilde{\epsilon}}{2\pi\sigma^2} e^{-\frac{2\tilde{\epsilon}\epsilon \cos(\varphi - \tilde{\varphi})}{2\sigma^2}} \tilde{p}_R(\epsilon; \tilde{\epsilon}, \sigma)}{\frac{\tilde{\epsilon}}{\sigma^2} I_0\left(\frac{\tilde{\epsilon}\epsilon}{\sigma^2}\right)} d\epsilon \\
 &= \frac{1}{2\pi} \int_0^\infty \frac{e^{-\frac{2\tilde{\epsilon}\epsilon \cos(\varphi - \tilde{\varphi})}{2\sigma^2}} \tilde{p}_R(\epsilon; \tilde{\epsilon})}{I_0\left(\frac{\tilde{\epsilon}\epsilon}{\sigma^2}\right)} d\epsilon. \tag{A.45}
 \end{aligned}$$

Here, the expression of  $p(\epsilon)$  derived in Eq. 5.30 is used. Furthermore, the analytical representations in 5.2 and 5.3 enters, which yields a probability density function symmetric about the phase substitution  $\varphi \Leftrightarrow \tilde{\varphi}$ .



---

## Bibliography

---

- [1] M. S. Sozzi, *Discrete symmetries and CP violation: from experiment to theory*, Oxford Graduate Texts, New York, NY: Oxford Univ. Press, 2008, URL: <https://cds.cern.ch/record/1087897> (cit. on p. 1).
- [2] G. Branco, L. Lavoura and J. Silva, *CP Violation*, International series of monographs on physics, Clarendon Press, 1999, ISBN: 9780198503996, URL: <https://books.google.de/books?id=5PvpnQEACAAJ> (cit. on p. 2).
- [3] T. Gershon and V. V. Gligorov, *CP violation in the B system*, Reports on Progress in Physics **80.4** (2017) 046201, URL: <http://stacks.iop.org/0034-4885/80/i=4/a=046201> (cit. on p. 2).
- [4] V. Kostelecky, *Proceedings of the Fifth Meeting on CPT and Lorentz Symmetry, Bloomington, USA, 28 June - 2 July 2010*, World Scientific, 2011, ISBN: 9789814327671, URL: [https://books.google.de/books?id=ssH%5C\\_nQEACAAJ](https://books.google.de/books?id=ssH%5C_nQEACAAJ) (cit. on p. 4).
- [5] S. Atutov, R. Calabrese and L. Moi, *Trapped Particles and Fundamental Physics*, Nato Science Series II: Springer Netherlands, 2012, ISBN: 9789401004404, URL: <https://books.google.de/books?id=JRbtCAAAQBAJ> (cit. on p. 4).
- [6] A. Hocker and Z. Ligeti, *CP violation and the CKM matrix*, Ann. Rev. Nucl. Part. Sci. **56** (2006) 501–567, arXiv: hep-ph/0605217 [hep-ph] (cit. on p. 4).
- [7] M. C. Gonzalez-Garcia et al., *Global fit to three neutrino mixing: critical look at present precision*, JHEP **12** (2012) 123, arXiv: 1209.3023 [hep-ph] (cit. on p. 4).
- [8] S. A. R. Ellis and G. L. Kane, *Theoretical Prediction and Impact of Fundamental Electric Dipole Moments*, JHEP **01** (2016) 077, arXiv: 1405.7719 [hep-ph] (cit. on p. 4).
- [9] M. Pospelov and A. Ritz, *Electric dipole moments as probes of new physics*, Annals Phys. **318** (2005) 119–169, arXiv: hep-ph/0504231 [hep-ph] (cit. on p. 4).
- [10] F.-K. Guo and U.-G. Meissner, *Baryon electric dipole moments from strong CP violation*, JHEP **12** (2012) 097, arXiv: 1210.5887 [hep-ph] (cit. on p. 5).
- [11] C. A. Baker et al., *An Improved experimental limit on the electric dipole moment of the neutron*, Phys. Rev. Lett. **97** (2006) 131801, arXiv: hep-ex/0602020 [hep-ex] (cit. on p. 5).

- [12] Y. Filmus, *Two Proofs of the Central Limit Theorem* (2010),  
URL: <http://www.cs.toronto.edu/~yuvalf/CLT.pdf> (cit. on p. 9).
- [13] B. P. Carlin and T. A. Louis, *Bayes and Empirical Bayes Methods for Data Analysis*,  
London: Chapman & Hall, 1996 (ISBN: 0-412-05611-9) (cit. on p. 9).
- [14] E. Lehmann and G. Casella, *Theory of Point Estimation*, Springer Verlag, 1998,  
ISBN: 0387985026 (cit. on p. 11).
- [15] B. Everitt, *The Cambridge dictionary of statistics*,  
Cambridge, UK; New York: Cambridge University Press, 2002,  
ISBN: 052181099X 9780521810999, URL:  
[http://www.worldcat.org/search?qt=worldcat\\_org\\_all&q=052181099X](http://www.worldcat.org/search?qt=worldcat_org_all&q=052181099X)  
(cit. on p. 11).
- [16] E. Lehmann and J. Romano, *Testing Statistical Hypotheses*, Springer Texts in Statistics,  
Springer New York, 2008, ISBN: 9780387988641,  
URL: <https://books.google.de/books?id=Y7vSVW3ebSwC> (cit. on p. 11).
- [17] F. R. Hampel et al., *Robust Statistics - The Approach Based on Influence Functions*, missing,  
Wiley, 1986 (cit. on p. 11).
- [18] A. W. v. d. Vaart, *Asymptotic statistics*,  
Cambridge series in statistical and probabilistic mathematics,  
Autre tirage : 2000 (édition brochée), 2005, 2006, 2007,  
Cambridge (UK), New York (N.Y.): Cambridge University Press, 1998,  
ISBN: 0-521-78450-6, URL: <http://opac.inria.fr/record=b1127649>  
(cit. on p. 12).
- [19] B. R. Frieden, *Science from Fisher Information*, Cambridge Books Online,  
Cambridge University Press, 2004, ISBN: 9780511616907,  
URL: <http://dx.doi.org/10.1017/CBO9780511616907> (cit. on p. 12).
- [20] L. L. Cam, *Maximum likelihood: An introduction*, Intl. Stat. Rev **58** (1990) 153–171  
(cit. on p. 14).
- [21] “Front Matter”, *Statistics of Directional Data*, ed. by K. MARDIA,  
Probability and Mathematical Statistics: A Series of Monographs and Textbooks,  
Academic Press, 1972 iii–, URL: <http://www.sciencedirect.com/science/article/pii/B9780124711501500017>  
(cit. on p. 14).
- [22] N. I. Fisher, *Statistical analysis of circular data*, Réimpressions : 1995,  
Cambridge, England, New York NY USA: Cambridge University Press, 1993,  
ISBN: 0-521-35018-2, URL: <http://opac.inria.fr/record=b1126530>  
(cit. on pp. 15, 58, 59, 62).
- [23] M. Berz, K. Makino and W. Wan, *An Introduction to Beam Physics*.  
Series in high energy physics, cosmology, and gravitation, CRC Press, 2014  
I–XIV, 1–310, ISBN: 978-0-7503-0263-0 (cit. on p. 19).

- [24] M. Puchalski, J. Komasa and K. Pachucki,  
*Deuteron and triton magnetic moments from NMR spectra of the hydrogen molecule*,  
**92.2**, 020501 (2015) 020501, arXiv: 1505.07251 [physics.chem-ph] (cit. on p. 27).
- [25] B. v. Przewoski et al., *Analyzing powers and spin correlation coefficients for  $p + d$  elastic scattering at 135 and 200 MeV*, Phys.Rev.C **74** (2006) 064003 (cit. on p. 28).
- [26] S. Dymov et al.,  
*Analyzing powers and spin correlations in deuteron–proton charge exchange at 726 MeV*,  
Physics Letters B **744** (2015) 391–394, ISSN: 0370-2693, URL: <http://www.sciencedirect.com/science/article/pii/S0370269315002622>  
(cit. on p. 32).
- [27] M. Altmeier et al.,  
*Excitation Functions of the Analyzing Power in  $p \vec{p}$  Scattering from 0.45 to 2.5 GeV*,  
Phys. Rev. Lett. **85** (9 2000) 1819–1822,  
URL: <http://link.aps.org/doi/10.1103/PhysRevLett.85.1819>  
(cit. on p. 32).
- [28] M. Froissart and R. Stora,  
*Dépolarisation d'un faisceau de protons polarisés dans un synchrotron*,  
Nuclear Instruments and Methods **7** (1960) 297–305 (cit. on p. 34).
- [29] D. Prasuhn et al., *Electron and stochastic cooling at {COSY}*,  
Nuclear Instruments and Methods in Physics Research Section A: Accelerators,  
Spectrometers, Detectors and Associated Equipment **441.1–2** (2000) 167–174,  
ISSN: 0168-9002, URL: <http://www.sciencedirect.com/science/article/pii/S0168900299011286>  
(cit. on p. 34).
- [30] C. Boehme et al., “Gas Scintillation Beam Profile Monitor at COSY Jülich”,  
*Proceedings of the 2010 Beam Instrumentation Workshop, Santa Fe, USA, May 2-6, 2010*,  
Record converted from VDB: 12.11.2012, 2010,  
URL: <http://juser.fz-juelich.de/record/12789> (cit. on p. 34).
- [31] D. Eversmann, *Analysis of the Spin Coherence Time at the Cooler Synchrotron COSY*,  
MA thesis: RWTH Aachen University, 2013 (cit. on p. 35).
- [32] M. Mikirtychyants et al.,  
*The polarized H and D atomic beam source for {ANKE} at COSY-Jülich*,  
Nuclear Instruments and Methods in Physics Research Section A: Accelerators,  
Spectrometers, Detectors and Associated Equipment **721** (2013) 83–98, ISSN: 0168-9002,  
URL: <http://www.sciencedirect.com/science/article/pii/S0168900213003483>  
(cit. on p. 40).
- [33] D. Eversmann et al., *New Method for a Continuous Determination of the Spin Tune in Storage Rings and Implications for Precision Experiments*,  
Phys. Rev. Lett. **115** (9 2015) 094801,

- URL: <http://link.aps.org/doi/10.1103/PhysRevLett.115.094801>  
(cit. on pp. 41, 143).
- [34] *atan2*, URL: <http://en.cppreference.com/mwiki/index.php?title=cpp/numeric/math/atan2&oldid=79630> (visited on 30/04/2016) (cit. on p. 45).
- [35] S. W. Smith, *The Scientist and Engineer's Guide to Digital Signal Processing*, San Diego, CA, USA: California Technical Publishing, 1997, ISBN: 0-9660176-3-3 (cit. on p. 49).
- [36] M. Rosenthal, *Experimental Benchmarking of Spin Tracking Algorithms for Electric Dipole Moment Searches at the Cooler Synchrotron COSY* (2016) 132,  
URL: [http://collaborations.fz-juelich.de/ikp/jedi/public\\_files/theses/Thesis\\_MRosenthal.pdf](http://collaborations.fz-juelich.de/ikp/jedi/public_files/theses/Thesis_MRosenthal.pdf)  
(cit. on p. 57).
- [37] S. M. Guillaume Meurisse Pierre Hanna, ed.,  
*A New Analysis Method for Sinusoids+Noise Spectral Models*,  
pp.139–144, 2006. <hal-00307892>,  
Canada: Proceedings of the Digital Audio Effects (DAFx06) Conference, 2006  
(cit. on p. 66).
- [38] J. e. a. Sijbers, *Estimation of the Noise in Magnitude MR Images*, **16** (1998) 87–90  
(cit. on p. 68).
- [39] C. G. Koay and P. J. Basser,  
*Analytically exact correction scheme for signal extraction from noisy magnitude {MR} signals*,  
*Journal of Magnetic Resonance* **179.2** (2006) 317–322, ISSN: 1090-7807, URL: <http://www.sciencedirect.com/science/article/pii/S109078070600019X>  
(cit. on p. 69).
- [40] G. J. Feldman and R. D. Cousins,  
*A Unified approach to the classical statistical analysis of small signals*,  
*Phys. Rev.* **D57** (1998) 3873–3889, arXiv: physics/9711021 [physics.data-an]  
(cit. on p. 71).
- [41] A. Gelman et al., *Bayesian Data Analysis*, 1995 (cit. on p. 73).
- [42] N. I. Fisher, T. Lewis and B. J. J. Embleton, *Statistical analysis of spherical data*,  
Cambridge Univ Pr, 1993 (cit. on p. 85).
- [43] P. Berens, *CircStat: A MATLAB Toolbox for Circular Statistics*,  
*Journal of Statistical Software* **31.1** (2009),  
URL: <https://www.jstatsoft.org/index.php/jss/article/view/v031i10>  
(cit. on p. 86).
- [44] *Book Reviews*, *Journal of the American Statistical Association* **109.507** (2014) 1325–1337,  
eprint: <http://dx.doi.org/10.1080/01621459.2014.963405>,  
URL: <http://dx.doi.org/10.1080/01621459.2014.963405> (cit. on p. 91).

- 
- [45] G. Guidoboni et al., *How to Reach a Thousand-Second in-Plane Polarization Lifetime with 0.97-GeV/c Deuterons in a Storage Ring*, *Phys. Rev. Lett.* **117** (5 2016) 054801, URL: <https://link.aps.org/doi/10.1103/PhysRevLett.117.054801> (cit. on pp. 142, 144).
- [46] A. Saleev et al., *Spin tune mapping as a novel tool to probe the spin dynamics in storage rings* (2017), arXiv: 1703.01295 [physics.acc-ph] (cit. on p. 143).
- [47] N. Hempelmann et al., *Phase Locking the Spin Precession in a Storage Ring*, *Phys. Rev. Lett.* **119** (1 2017) 014801, URL: <https://link.aps.org/doi/10.1103/PhysRevLett.119.014801> (cit. on p. 144).
- [48] H. Bateman and S. of the Bateman Manuscript Project, *Higher transcendental functions. Volume I*, Préparé au California Institute of Technology, New-York, Toronto, London: McGraw-Hill Book Company, 1953 153, ISBN: 0-07-019545-5, URL: <http://authors.library.caltech.edu/43489/1/Volume%201.pdf> (cit. on p. 149).
- [49] M. Krishnan, *The Noncentral Bivariate Chi Distribution*, *SIAM Review* **9.4** (1967) 708–714, ISSN: 00361445, URL: <http://www.jstor.org/stable/2028301> (cit. on p. 150).



---

## List of Figures

---

1.1	Count sums $N_{U,D}^+(\varphi_s)$ and differences $N_{U,D}^-(\varphi_s)$ of Eq. 4.5 with $\varphi_s \in [0, 2\pi)$ using the counts $N_U(\varphi_s)$ and $N_D(\varphi_s)$ , shown in Fig. 4.1. The vertical error bars show the statistical uncertainties, the horizontal bars indicate the bin width. . . . .	6
2.1	Sketch of a co-moved Cartesian coordinate system, which is used to describe the particle motions in a planar accelerator. Its coordinates are called curvilinear.	17
2.2	Transverse linear particle motion specified by a phase space ellipse. The zero crossings and the extrema are expressed by the optical functions of the investigated particle . . . . .	21
3.1	Sketch of the COSY facility . . . . .	31
3.2	Sketch of the EDDA polarimeter . . . . .	32
3.3	The RF Solenoid . . . . .	34
3.4	a) Distribution of the period time of the RF cavity signal for a run of 200 s. b) Projection of the y-axis for the whole run. . . . .	36
3.5	Counting rates of each detector quadrant for a 200 s cycle. . . . .	37
3.6	Left-right asymmetry of individual polarization states and their cross-ratio for a typical 200 s cycle. . . . .	39
4.1	(a): Counts $N_U$ and $N_D$ after mapping the events recorded during a macroscopic turn interval of $\Delta n = 10^6$ turns into a spin phase advance interval of $4\pi$ . The vertical error bars show the statistical uncertainties, the horizontal bars indicate the bin width. . . . .	43
4.2	Count sums $N_{U,D}^+(\varphi_s)$ and differences $N_{U,D}^-(\varphi_s)$ of Eq. 4.5 with $\varphi_s \in [0, 2\pi)$ using the counts $N_U(\varphi_s)$ and $N_D(\varphi_s)$ , shown in Fig. 4.1. The vertical error bars show the statistical uncertainties, the horizontal bars indicate the bin width. . . . .	44
4.3	Measured asymmetry $\epsilon(\varphi_s)$ of Eq. 4.6 fitted with $\epsilon(\varphi_s)$ of Eq. 4.7 to extract amplitude $\tilde{\epsilon}$ and phase $\tilde{\varphi}$ , using the yields $N_{U,D}^{+,-}(\varphi_s)$ of Fig. 4.1 (b) for a single turn interval of $\Delta n = 10^6$ turns at a measurement time of $2.6 \text{ s} < t < 3.9 \text{ s}$ . . . . .	45
4.4	Upper two plots: distributions of the estimator of the parameter $A$ and $B$ based on random data analyzed by the discrete turn Fourier transform. The true amplitude value is set to $\epsilon = 0.05$ (red) and $\epsilon = 0.5$ (black), whereas the phase is fixed to $\varphi_s = -1$ . Lower plots: distribution of the amplitude and phase estimator obtained by $\tilde{A}$ and $\tilde{B}$ . . . . .	52

4.5	Left: wrapped probability density function of the phase for three different phase scale parameters (blue: $\sigma_{\varphi_s} = 1$ ; red: $\sigma_{\varphi_s} = 2$ ; black: $\sigma_{\varphi_s} = 3$ ). Right: average phase of the ensemble as a function of the phase scale parameter. . . . .	58
4.6	Joint bivariate probability density function of the turn number and the spin tune $p_{n,\nu_s}$ ( 4.57). The x-axis (number of particle turns) is cut into three intervals and each lasts for 50 turns. The size of the gaps is set to 25000 turns. The parameters are set to $\Delta n = 10^6$ turns, $\nu_s^{\text{ref}} = 0.1609$ , $\sigma_{R,\nu_s} = 10^{-4}$ , $\epsilon = 0.25$ and $\varphi_s = 0$ . The values on the y-axis are shifted by the reference spin tune $\nu_s^{\text{ref}}$ . . . . .	60
4.7	Marginal probability density function of the turn number $p_n(n)$ for the first 10000 particle turns with the parameters $\Delta n = 10^6$ turns, $\nu_s^{\text{ref}} = 0.1609$ , $\sigma_{R,\nu_s} = 10^{-4}$ , $\epsilon_0 = 0.25$ and $\varphi_s = 0$ . . . . .	61
4.8	Left: turn depending phase deviation of the ensemble from the reference particle for different spin tune spread parameters and the amplitude parameter $\epsilon = 0.25$ . Right: amplitude distribution . . . . .	63
5.1	Three examples of the Rice distribution with the standard deviation $\sigma = \sqrt{2/500}$ and different true amplitudes $\epsilon_1 = 0.05$ , $\epsilon_1 = 0.2$ , $\epsilon_1 = 0.5$ , which are represented by the vertical lines. Additionally, the first moments of each distribution are given. . . . .	67
5.2	The scale factor 5.16 of the amplitude variance as a function of the signal-to-noise ratio $\gamma_{\text{SNR}}$ . . . . .	69
5.3	Three log-likelihood functions 5.25 for different measured amplitudes $\tilde{\epsilon}$ with a standard deviation $\sigma^2 = 2/500$ . For the red and the blue curves, the maxima (best estimator) are located in the region $\epsilon > 0$ . The black curve decreases monotonically and yields $\tilde{\epsilon}_{\text{ML}} = 0$ . . . . .	71
5.4	Two examples of the construction of the Feldmann-Cousin confidence interval for $\epsilon = 0.1$ , $\epsilon = 0.4$ and $\sigma = 0.2$ . The blue area in the lower plots corresponds to the 68.3% confidence of the Rician distribution, whereas the colored curve in the upper plots represents the largest values of the likelihood ratio $R_R$ according to the 68% coverage. . . . .	72
5.5	Left: Two dimensional map of the Rice distribution 5.2 with standard deviation $\sigma = \sqrt{2/50}$ . In addition the most probable value of the true amplitude as a function of the estimated amplitude $\epsilon_{\text{best}}(\tilde{\epsilon})$ is shown in black. Right: Likelihood ratio 5.29 constructed according to the Feldmann-Cousin algorithm. The blue curve indicates the 68.3% confidence interval and the horizontal dashed white lines corresponds to the confidence interval of the respective estimated amplitude $\tilde{\epsilon}$ (vertical dashed white lines). The black curve represents the 68.3% coverage of the y-axis projection based on the Bayes' theorem. . . . .	73
5.6	Comparison between the amplitude likelihood ratio (black) and the probability density function of the true amplitude (red) obtained for a given $\tilde{\epsilon} = 0.1$ and $\tilde{\epsilon} = 0.4$ . The blue area represents 68.3% of the largest values of $R_R(\tilde{\epsilon}, \epsilon)$ . . . . .	74

5.7	Both plots show the different estimators of the amplitude normalized by the true one as a function of the reciprocal signal-to-noise ratio. The left-hand side illustrates a zoom of the plot on the right-hand side. The red data points correspond to the 2nd moment estimator $\hat{\epsilon}_{2\text{nd}}$ from Eq. 5.9. The the yellow ones are corrected by the scaling factor $\hat{\epsilon}_{2\text{nd,cor}}$ as shown in Eq. 5.20. The red curve represents the second order Taylor estimate of the 2nd moment estimator 5.10. The ML estimator 5.26 is shown in black and the blue band covers the 68.3% Feldmann-Cousin confidence interval 5.3. . . . .	75
5.8	The efficiency to obtain a physically meaningful estimator is shown as a function of the reciprocal signal-to-noise ratio for the three different approaches discussed in the previous sections (the 2nd moment in red, the corrected 2nd moment in yellow, the maximum likelihood in black). . . . .	77
5.9	Two examples of the turn depending amplitude spectrum $\tilde{\epsilon}$ for an idle spin precession in the horizontal plane, which lasts for $n = 70 \cdot 10^6$ turns ( $\approx 90$ s). The spin tune scan is performed from $\nu_{\text{min}}^{\text{scan}} = 0.1609655$ to $\nu_{\text{max}}^{\text{scan}} = 0.1609765$ , i.e. in a full range of $\Delta\nu_s^0 = 1.1 \cdot 10^{-5}$ . . . . .	79
5.10	The y-axis projection of the 3rd bin of the x-axis of Fig. 5.9. The red data points correspond to the mapping method and the blue ones represent the result obtained by the discrete Fourier transform. . . . .	79
5.11	Turn depending amplitude for two cycles from runs with different settings of the sextupole magnets. The red curve represents a maximum likelihood fit based on Eq. 5.44. The probability density function of the amplitude based on the measured amplitude is indicated by the color scheme. . . . .	82
6.1	Probability distributions for different true phases $\varphi_1 = 1; \varphi_2 = -\frac{\pi}{2}; \varphi_3 = \frac{\pi}{2}$ , but same standard deviation $\sigma^2 = \frac{2}{500}$ and amplitude $\epsilon = 0.05$ . . . . .	85
6.2	The plot on the left-hand side shows the probability density functions of the estimated phase $p_\varphi(\tilde{\varphi}; \epsilon, \varphi)$ for a given true amplitude $\epsilon = \sqrt{2} \cdot 0.2$ and a standard deviation $\sigma = \sqrt{2/500}$ . Additionally, the most probable value $\varphi_{\text{best}}(\tilde{\varphi})$ is given by the black line. On the right-hand side the likelihood ratio $R(\tilde{\varphi}, \varphi) = p(\tilde{\varphi}; \varphi) / p(\tilde{\varphi}; \varphi_{\text{best}})$ is shown. . . . .	88
6.3	Upper plot: the true phase value $\varphi$ is shown against the estimated one $\hat{\varphi}^{\text{circ}}$ . Lower plot: The 68.3% confidence interval obtained by the bounded (green) and unbounded (black) 2nd moment estimation based on directional statistics. The blue points represent the 2nd moment of the linear pdf and the red curve corresponds to the conventional estimation of standard deviation $\sigma_\varphi^{\text{con}} = \frac{1}{\gamma_{\text{SNR}}}$ . In magenta the result of the Feldmann-Cousin algorithm is shown. . . . .	90
6.4	Left: probability density function of the true signal-to-noise ratio given a measured one $\tilde{\gamma}_{\text{SNR}}$ . Right: corresponding pdf of the phase difference $\Delta\varphi = \varphi - \tilde{\varphi}$ denoted in Eq. 6.28. The black curves indicate the 68.3% confidence interval. . . . .	92
6.5	Confidence interval depending on the true $\sigma_{\tilde{\varphi}}(\gamma_{\text{SNR}})$ (green) and the estimated signal-to-noise ratio $\sigma_{\tilde{\varphi}}(\tilde{\gamma}_{\text{SNR}})$ (black). For comparison, the standard distribution of the discrete Fourier transform is shown in red. . . . .	93

6.6	Phase spectrum for a typical cycle based on spin tune scan. The initially wrapped phase is unwrapped by subtracting or adding $2\pi$ , which leads to a smooth phase distribution. . . . .	94
6.7	Left: vertical projections of the phase spectrum in Fig. 6.6 for different turn numbers. Right: horizontal projections for different assumed spin tune. . . . .	95
6.8	Turn depending phase distribution obtained for a fixed assumed spin tune. The red curve represents a maximum likelihood fit of the phase based on Eq. 6.35. . . . .	96
6.9	Contour plot of the two parameters $\Delta\omega_s$ and $\sigma_{R,\nu_s}$ . The 68.3% confidence interval is shown in blue, whereas the black line indicates the 95.4% confidence level. . . . .	97
6.10	Global maximum likelihood fit for the amplitude and phase spectrum based on the probability density functions derived in the previous chapters. The fit function provides turn depending parameters of the spin tune distribution. . . . .	101
6.11	Turn depending spin tune interpolation. The red color corresponds to the mean value of the spin tune and the blue color indicates the reference spin tune. . . . .	103
6.12	Statistical error of the interpolated spin tune as a function of the turn number $n$ . The red color corresponds to the mean value of the spin tune and the blue color indicates the reference spin tune. . . . .	105
7.1	The difference of the statistical error obtained by the mapping and the Fourier method. . . . .	108
7.2	Turn depending phase for different assumed spin tunes. The variation of the assumed spin tune yields $4 \cdot 10^{-8}$ , which is indicated by the values in the right box shown in different colors. . . . .	109
7.3	Phase deviation due to the variation of the assumed spin tune for the mapping method (blue) and the discrete Fourier transform (blue), respectively. . . . .	111
7.4	Left: Distribution of the difference between the phase and its arithmetic mean for $N = 30$ normalized to the statistical error. Right: Standard deviation of the distribution shown on the left-hand side as a function of the number of bins of the asymmetry distribution. . . . .	112
7.5	Comparison between the phase results of the individual detectors (up quadrant in blue and down quadrant in red) and the results obtained by the combination of both detector quadrants (black). (A.1) . . . . .	113
7.6	Pull distribution of the phase for to the up and down detector quadrants. The discrete Fourier transform is shown in red, whereas the result of mapping method corresponds to the blue color. (A.1) . . . . .	114
7.7	Cross ratio of a Froissart-Stora scan. ( A.1) . . . . .	116
7.8	Upper plot: spin tune change $\Delta\nu_s$ versus the shift of the COSY RF $\Delta f_{RF}$ . A linear least squares fit is performed to the data and shown in red. Lower plot: residual of the data and the linear fit. (A.1) . . . . .	118

7.9 a) Time depending distribution of the RF cavity period  $T_{\text{RF}}$  for one cycle. The z-axis is chosen logarithmic. b) Y axis projection of the entire cycle. The red curve represents a least squares fit by a double Gaussian Eq. 7.26. c) Time depending mean values  $\mu_{T_{\text{RF}}}$  of the individual Gaussian distribution. The red and the blue curves represent a least squares fit by a linear function. d) Time depending widths  $\sigma_{T_{\text{RF}}}$  of the corresponding Gaussian distribution. Again, the curves represent a least squares fit by a linear function. (?? . . . . . 119

7.10 Long-term measurement of the COSY RF  $T_{\text{RF}}$ . The red curve represents a least squares fit with the function based on two independent oscillations  $T_{\text{RF}}^{\text{fit}}(t)$ . . . . 121

7.11 a) and b) Time in turn distribution  $t_{\text{ev}}^{\text{RF}}$  of all events during a 200 s cycle. a) was performed with continuous cooling and b) without any cooling. The scale of the z-axis is chosen logarithmic. In addition, the mean values (c) respectively the standard deviations (d) of  $t_{\text{ev}}^{\text{RF}}$  for each time bin are given. The data points in red correspond to the setup with a continuously cooled beam and the blue data points to a uncooled beam. ( ?? . . . . . 122

7.12 Four time depending distributions of the residuals obtained by subtracting the mean values of  $\mu_{t_{\text{ev}}^{\text{RF},i}}^{\text{res}}$  (black) and  $\sigma_{t_{\text{ev}}^{\text{RF},i}}^{\text{res}}$  (blue) from each data point. In addition, the Pearson correlation coefficients  $\rho$  based on both distributions are given. (A.1) 123

7.13 Comparison of the phase distributions based on white noise (red), vertical (blue) and horizontal (magenta) local bump extraction. (A.1) . . . . . 125

7.14 Interpolated spin tune obtained for the white noise extraction (red), the vertical (blue) and the horizontal (magenta) local bump extraction. . . . . 126

7.15 Sketch of the vertical respectively horizontal  $\pi$ -bump extraction. The red curve represents the betatron amplitude before and the blue one after extraction onto the carbon target. . . . . 127

7.16 Turn depending amplitude and phase distribution for a long and short spin coherence time. The color scheme represents the probability density function according to the estimated values of the discrete turn Fourier transform. The gray curves correspond to a global maximum likelihood fit with the model functions derived in the previous chapters. (A.1) . . . . . 130

7.17 The ratio of the linear parameter of the reference spin tune and its standard deviation. In addition, a Gaussian function is shown based on a least squares fit. (A.1) . . . . . 132

7.18 Turn depending event arrival time with respect to the last COSY RF time stamp for six cycles within the same run. The red curve corresponds to a parabolic least squares fit. ( A.1) . . . . . 134

7.19 Phase and RF cavity distributions for 4 cycles. The red curve represents either a linear least squares fit (RF cavity) or a global maximum likelihood fit to the phase and the amplitude. . . . . 135

7.20 Linear fit parameter of the RF cavity period  $T_{\text{RF},1}$  and linear drift parameter of the reference spin tune  $\nu_{s,1}^{\text{ref}}$  for 100 cycles. On the right-hand side the scatter plot of both quantities is shown. . . . . 136

7.21	Spin tune distribution (black curves) for 22 cycles, which last for $70 \cdot 10^6$ turns. All cycles are taken with the same sextupole settings. The red data points represent the mean of the RF cavity frequency obtained for the same measurement interval. The axis of the frequency is scaled by the factor determined in section 7.2.2. (A.1) . . . . .	137
7.22	Long term spin tune measurement during the beam time in May/June 2015. Relevant changes of the devices in the ring are indicated by circles or rectangles. (A.1) . . . . .	139
7.23	Spin tune and RF cavity frequency for a measurement interval where just the sextupole settings were changed. The scale between both quantity axes is given by $\alpha_{\text{RF}}(\nu_s, f_{\text{RF}}) = 76.91 \text{ ns}$ . The blue lines represent a linear least squares fit to the spin tune. (A.1) . . . . .	140
7.24	Residuals of the spin tune and the linear least squares fit given in Fig. 7.23. The results of two sextupole families are shown, whereas the red lines correspond to a linear least squares fit to the respective distribution. . . . .	141
7.25	Two examples of long cycles with more than $650 \times 10^6$ turns ( $\approx 860 \text{ s}$ ). The spin tune width is estimated to $\sigma_{R, \nu_s} = 5.49 \times 10^{-11}$ by means of a maximum likelihood fit based on the depolarization model. (A.1) . . . . .	142
A.1	Probability density function of the quadratic 2nd moment estimator $p(\hat{\epsilon}_{2\text{nd}}^2; \epsilon, \sigma)$ for the same standard deviation $\sigma = 0.1$ but different true amplitudes $\epsilon = 0.05$ (red), $\epsilon = 0.1$ (black), $\epsilon = 0.2$ (blue). The filled area indicates the integrated probability, that the quadratic 2nd moment estimator assumes negative numbers. . . . .	151

---

## List of Tables

---

2.1	Magnetic properties of the proton, deuteron, electron and muon. . . . .	27
4.1	Mean value and the standard deviation of the estimated amplitude and phase compared to the true ones . . . . .	53
4.2	First and second of the estimated amplitude and phase compared to the true ones	55
6.1	Parameters obtained by the global maximum likelihood fit based on the data shown in Fig. 6.10. . . . .	102
7.1	Parameters obtained by the global maximum likelihood fit based on the data for a long and short spin coherence time shown in Fig. 7.16. . . . .	131
A.1	List of runs dicussed in the result chapter . . . . .	145